THESIS

This is to certify that the

dissertation entitled

Synthesis and Characterization of Polymer/Inorganic Intercalation Compounds

presented by

Yu-Ju Liu

has been accepted towards fulfillment
of the requirements for

Ph D. degree in **Chemistry**

Major professor

Date 7/6/94

SYNTHESIS AND CHARACTERIZATION OF POLYMER/INORGANIC INTERCALATION COMPOUNDS

By

Yu-Ju Liu

A DISSERTATION

Submitted to
Michigan State University
in partial fulfillment of the requirements
for the degree of

DOCTOR OF PHILOSOPHY

Department of Chemistry

1994

ABSTRACT

SYNTHESIS AND CHARACTERIZATION OF POLYMER/INORGANIC INTERCALATION COMPOUNDS

By

Yu-Ju Liu

Poly(ethylene-oxide), poly(vinylpyrrolidone), poly(propylene-oxide) and methyl-cellulose have been intercalated in $V_2O_5 \cdot nH_2O$ xerogel by mixing aqueous polymer solutions with aqueous V_2O_5 gels followed by slow drying. Various phases of the polymer/V_2O_5 materials were prepared by changing the stoichiometric conditions. Irradiation with UV or visible dramatically changes the electronic structure of V_2O_5 framework and results in enhanced electrical conductivity. The conductivity decreases as the polymer content increases. The thermopower data are consistent with a n-type semiconductor.

The reaction of V_2O_5 xerogel with $C_6H_5NH_3I$ in a 1:4 molar ratio in CH_2Cl_2 for 2 days yielded (anilinium)$_{0.4}V_2O_5 \cdot 0.4H_2O$ **1**. Exposure to air resulted in an intra-lamellar polymerization to form $\{1/n(\text{-}C_6H_4NH\text{-})_n\}_{0.4}V_2O_5.0.4H_2O$ **2**. Magnetic susceptibility measurements showed a μ_{eff} of 1.3 BM for **1** and 0.87 BM for **2**. The electrical conductivity of **2** (10^{-3} S/cm) is higher than that of **1** (10^{-5} S/cm) while the thermopower of **2** (-100 μV/K) is smaller than that of **1** (-20 μV/K).

$A_xV_2O_5 \cdot nH_2O$ xerogels (A = K and Cs, $0.05 < x < 0.6$) were synthesized by reacting V_2O_5 xerogel with various amounts of KI and CsI in

acetone under N_2 for 3 days. X-ray diffraction and FT-IR indicated that the pristine V_2O_5 framework is preserved. The magnetic behavior of the $A_xV_2O_5 \cdot nH_2O$ phases is best described as Curie-Weiss type coupled with temperature independent paramagnetism (TIP). The Curie constant and EPR peak-width of the $A_xV_2O_5 \cdot nH_2O$ materials show a maximum value at x ~ 0.3. Charge transport studies indicate a thermally activated semiconductor. Optical diffuse reflectance spectra are reported.

Aniline and N-phenyl-1,4-phenylenediamine (PPDA) were intercalated in $HUO_2PO_4 \cdot 4H_2O$ (HUP), α-$Ti(HOPO_3)_2 \cdot H_2O$ (TiP) and α-$Zr(HOPO_3)_2 \cdot H_2O$ (ZrP) to form precursors for polymerization. Thermal treatment at 130°C in air resulted in an intralamellar polymerization of aniline and PPDA to polyaniline. The formation of polyaniline was confirmed by spectroscopy, EPR and magnetic susceptibility. X-ray diffraction data indicated a monolayer of polyaniline in HUP and TiP, and a bilayer of polyaniline in ZrP. All materials are insulators. The MW of the polyaniline was estimated by gel permeation chromatography.

To My Love, Jui-Sui (Alice) and To My Parents, Chen-Hwa and Yu-Chai

ACKNOWLEDGMENT

The research in this dissertation would not have been successful without the assistance and support of many sincere persons. Foremost, I would like to thank my research advisor Mercouri G. Kanatzidis for his patience, wise guidance and support. I also thank the other members of my committee : Professor J.L. McCracken, Professor J.A. Cowen for discussion of magnetic susceptibility and Professor T.J. Pinnavaia for his helpful comments as a second reader.

I would like to thank Professor C.R. Kannewurf, D.C. DeGroot and J.L. Schindler for charge transport measurements, Dr. W. Hirpo for ^{7}Li NMR measurements and discussion and Dr. J.-H. Liao for assistance on ORTEP graphs. Many thanks go to all members in the Kanatzidis group for their friendship and stimulating research ideas.

In addition, I would like to acknowledge Center for Fundamental Materials Research, the Department of Chemistry, Michigan State University, and National Science Foundation for financial support during my graduate career.

Most importantly, I would like to give my deepest appreciation to my mother, wife and brother for their encouragement and support .

TABLE OF CONTENTS

LIST OF TABLES

LIST OF FIGURES

LIST OF SCHEMES

ABBREVIATIONS

TGA : Thermogravmetric Analysis.

DSC : Differential Scanning Calorimetry.

GPC : Gel Permeation Chromatography.

SEM : Scanning Electron Microscopy

EPR : Electron Paramagnetic Resonance.

PEO : Poly(ethylene-oxide).

PPG : Poly(propylene-oxide).

PVP : Poly(vinylpyrrolidone).

PANI : Poly(aniline).

PPDA : N-phenyl-1,4-phenylenediamine

CHAPTER I

INTRODUCTION

1.1. General Introduction.

The first report of an intercalation compound was inadvertently described by Schafhäutl more than 150 years ago when he reported his observations on attempting to dissolve graphite in sulfuric acid.[1] However, the development of the chemistry started from 1926 when Fredenhagen *et al.* described the uptake of potassium vapor into graphite.[2] Intercalation is a term to describe the reversible insertion of guest species into host matrix without changing structural integrity of the host. Literally, it refers to the act of inserting into a calendar some extra interval of time. However, the term is used loosely even for irreversible reactions. Generally, the host matrices include materials with three-dimensional frameworks, two-dimensional frameworks and one-dimensional chains, as summarized in Scheme 1.1. They can be organic, inorganic or organometallic compounds with insulating, semiconducting and metallic properties. Guest species can be intercalated into hosts via ion-exchange[3], acid-base chemistry[4], coordination chemistry[5] and redox reactions.[6]

For a long time, interests in intercalation chemistry (host-guest chemistry) were primarily focused on the properties of host materials.[7-10] The role of guest species was merely to insert into host matrices and modify the properties of these hosts. The guest species were usually metal ions and small molecules. The intercalation of macromolecules was comparatively few and most studies concentrated on clay materials due to the important applications in agriculture and industry.[11] For instance, polymers such as poly(vinyl alcohol), hydrolyzed polyacrylonitrile and polysaccharides are used as "soil conditioners" because they can improve the stability of soil aggregates.[12] The use of finely divided clays as a "filler" incorporated into

1. Three-dimensional framework hosts

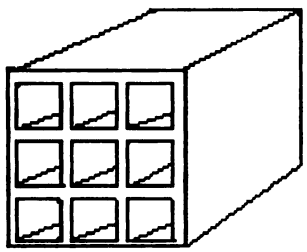

Structure is composed of a 3-D matrix which contains isolated or inter-connected channels. Intercalation is severely restricted to guest species whose dimensions are smaller than that of the channels.
Examples: Zeolites, Pyrochlores, Proteins.

2. Two-dimensional framework hosts

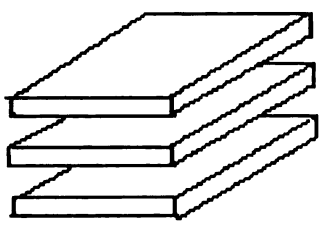

The structure of hosts are composed of 2-D layer units. They have a high structural flrxibility with respect to the uptake or exchange of guest species by expansion of interlayer spacing.

Examples:
Clays
Hydrous oxides ($M(HPO_4)_2nH_2O$, M = Zr, Ti, Sn),
Alkali oxometallates ($ATiMO_5$, A = K, Cs; M = Ta, Nb)
Transition metal dichalcogenides (MQ_2, Q= S, Se, Te),
Teansition metal oxides [MoO_3, A_xMO_2(M = Fe, Co),
MOCl (M= Fe,Y)]
Graphites

3. One-dimensional chain hosts

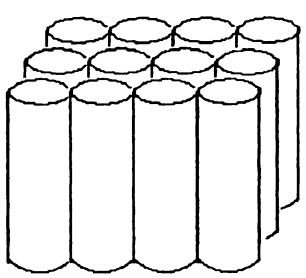

Host matrices are composed of 1-D chains separated by van der Waals gaps or counterions. They possess a high structural flexibility with respect to the uptake or exchange of guest species with different size and geometry. However, they also have poor structural stability toward intercalation. Compounds belonging to the category are comparatively few.
Examples:
Transition metal trichalcogenides MQ_3 (M = Ti, Zr, Hf)
$LiMo_3Se_3$

Scheme 1.1. Three types of host stuctures.

polymer matrices such as poly(vinyl chloride) (PVC) and polyethylene to improve physico-mechanical properties has also been widely studied and applied in industry.[13] The paper industry is one of the largest users of clays, especially kaolinites which serve as both filling and coating agents to improve the brightness, color, opacity and printability of the sheet. The incorporation of naturally occurring polymers such as proteins, enzymes, and viruses into clays has been investigated as well.[14] The studies essentially involve the use of clays for separation and stabilization of these natural species, and the modification of their activities.

In recent decades, the remarkable electrical, optical, mechanical properties of conjugated polymers together with the wide range of their potential technological applications have received considerable research attention.[15] Among the many known polymers, polyacetylene, polyaniline (PANI), polypyrrole, polythiophene, poly(phenylenevinylene) and poly(phenylenesulfide) have been studied the most. Generally, the research objects involve the fundamental understanding of charge transport and its relationship with lattice structure, improvement of processibility and pursuit of high conductivity. The conductivity of the polymers is primarily limited by their slow carrier mobility (10^{-4}-10^{-5} $cm^2/V \cdot sec.$) which results from low crystallinity and structural defects.[16] With the goal of aligning polymer chains and thus achieving higher carrier mobility, several methods have been designed such as physically stretching polymer films,[17] and chemically preparing polymers in liquid crystal solvents and microporous membranes.[18] One particular way is to form these polymers within the crystalline and confined environment of an inorganic inclusion host. Thus, control of conformation, linearity, cross-linking, alignment, and interchain electronic processes is possible, if the so-called topotactic principle is obeyed. In

addition to these, the direct structural characterization of polymers by crystallographic methods may also be possible.

In the early 1970s, Mortland and Pinnavaia first observed the formation of conjugated polymers within confined host lattices. When the Cu^{2+} exchanged clay was exposed to benzene vapor, poly(p-phenylene) was formed in the galleries of clays.[19] A decade later, Soma *et al.* reported the polymerization of the benzene and thiophene in Cu^{2+}- and Fe^{3+}- exchanged montmorillonites.[20] A variety of spectroscopic techniques suggested the formation of doped conducting polymers. However, these studies mainly focus on spectroscopic properties rather than on structural and electrical properties. The study of topochemical reactions started from Day and Tieke in 1982-3.[21] They have polymerized aminodienes and -diynes in layered $CdCl_4$ by UV and γ-ray irradiation, see Scheme 1.2.

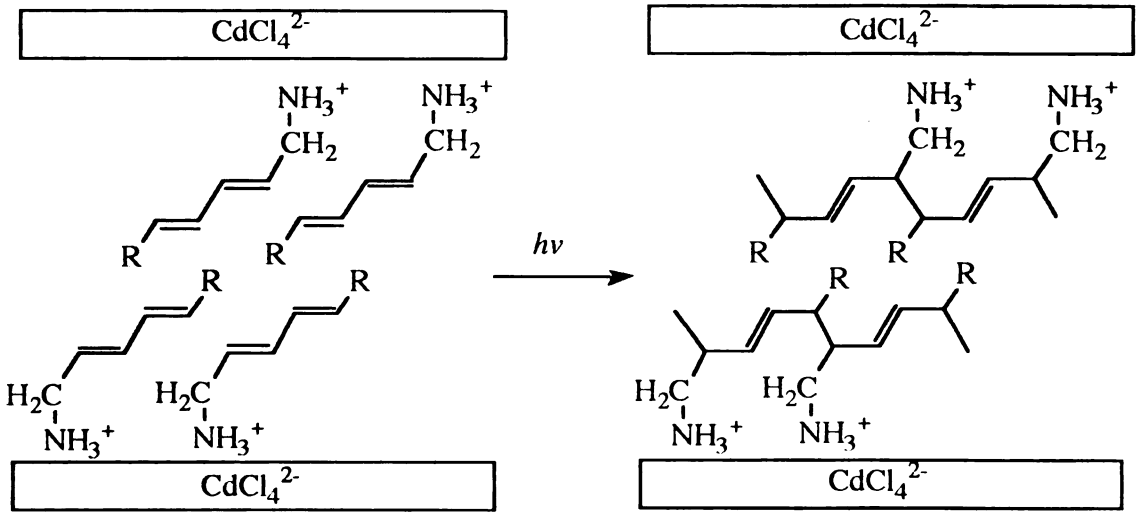

Scheme 1.2. 1.4-addition polymerization in layered $CdCl_4$ (ref 21).

However, the development of the intercalation of conducting polymers started from the late 1980s. Kanatzidis and coworkers in 1987 reported the *in-situ* oxidative polymerization and intercalation of pyrrole in lamellar

FeOCl (the Fe^{3+} center acts as an oxidant to accept electrons released from pyrrole).[22] The resulting polypyrrole/FeOCl (Scheme 1.3.) showed room temperature electrical conductivity of 1 S/cm. This remarkable reaction opened a new way to encapsulate conducting polymers inside the interlayer space of inorganic host lattices from their corresponding monomers. In the following several years, our group has extended this field of research to other conducting polymers such as polyaniline, polythiophene and polyfuran, and other host materials[23] such as V_2O_5 xerogel. The properties of these materials are intriguing, as described later.

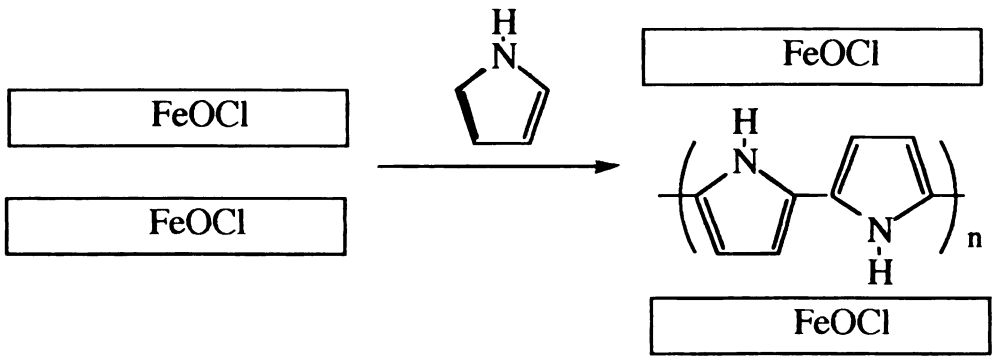

Scheme 1.3. The *in-situ* polymerization/intercalation of pyrrole in FeOCl (ref 22).

The same method has also been used by other groups in different host materials. The *in-situ* polymerization of pyrrole in channels of 3-D $[(Me_3Sn)_3Fe^{III}(CN)]_x$ was accomplished by Fisher and coworkers in 1989.[24] The room temperature conductivity for the polypyrrole intercalated compound is only $7x10^{-5}$ S/cm which is much lower than that of doped polypyrrole, but much higher than that of $[Li_{0.3}(Me_3Sn)_3Fe^{II}_{0.3}Fe^{III}_{0.7}(CN)]_x$.

Matsubayashi *et al.* recently reported the *in situ* oxidative polymerization of anilinium, 3-methylpyrrole and 3,4-dimethylpyrrole in $VOPO_4 \cdot 2H_2O$.[25] In these reactions, the V^{5+} centers act as an oxidizing agent to oxidatively polymerize these monomers. The net expansion is 8.7 Å and 9.7 Å for poly(3-methylpyrrole) and poly(3,4-dimethylpyrrole) intercalates respectively, consistent with pyrrole planes approximately perpendicular to the layers.

The electrochemical polymerization of intercalated aniline in montmorillonite was first observed by Inoue and coworkers.[26] Clay-modified electrodes intercalated with aniline were electrolyzed gavanostatically at 20 μAcm^{-2} in 2 M HCl. As the reaction proceeded, the electrode gradually turned blue, consistent with the formation of polyaniline. However, no spectroscopic data were described. The polymerization process is very slow and incomplete. The product, PANI/montmorillonite, showed a net interlayer expansion of only 3.4 Å, suggesting that the phenyl rings of PANI are parallel to the silicate sheets. This materials remains essentially uncharacterized.

Insertion of poly(phenylene vinylene) (PPV) in MoO_3 has been obtained by Nazar and coworkers by ion exchange of Li_xMoO_3 with the precursor of PPV, poly(*p*-xylylene-α-dimethylsulfoxonium) chloride, followed by heat treatment to eliminate dimethylsulfide to form PPV (Scheme 1.4.).[27] The 5.6 Å interlayer expansion observed is consistent with a monolayer of PPV in the galleries with the aromatic ring plane nearly perpendicular to the oxide sheets. The material shows room-temperature conductivity of 0.5 S/cm which is one order of magnitude higher than that of alkali doped MoO_3.

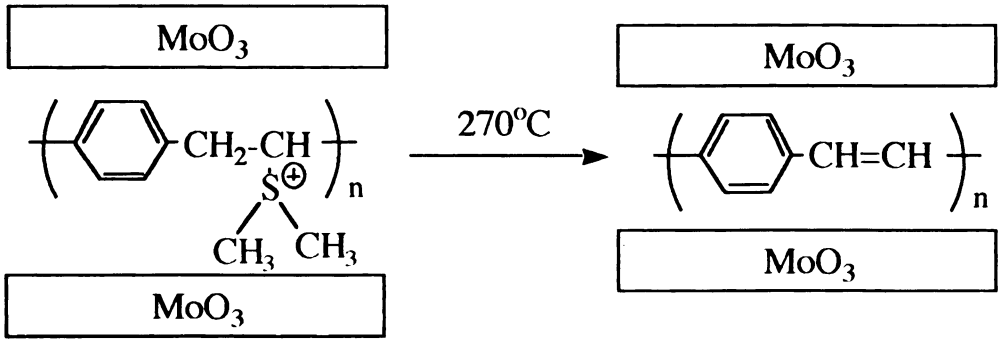

Scheme 1.4. Intralamellar thermal conversion of PPV precursor to PPV (ref 27).

The first report of formation of conjugated polymers in 3-D structures such as zeolites instead of 2-D layered hosts was made by Chao *et al.* who observed the polymerization of pyrrole in Fe^{3+} and Cu^{2+} exchanged zeolite Y.[28] The resulting materials were insulating which was explained by insufficient amount of polymer in the zeolite to dominate the electrical properties of the materials.

Bein and coworkers have also worked on the zeolite systems. In 1989, they reported the polymerization of intercalated anilinium in zeolite channels by addition of an external oxidant, $(NH_4)_2S_2O_8$.[29a] Using zeolites containing Cu^{2+} and Fe^{3+} ions, they have also accomplished the *in-situ* polymerization of pyrrole and thiophene inside the 3-D framework.[29b-d] However, these materials are insulating since the conducting polymer is embedded in an insulating three-dimensional host and cannot be accessed electrically. Recently, they reported the encapsulation of non-charged polymers as well. Acrylonitrile adsorbed in zeolite was polymerized with radical initiators. Pyrolysis of the intrazeolite poly(acrylonitrile) led to the formation of a ladder polymer shown in Scheme 1.5.[30]

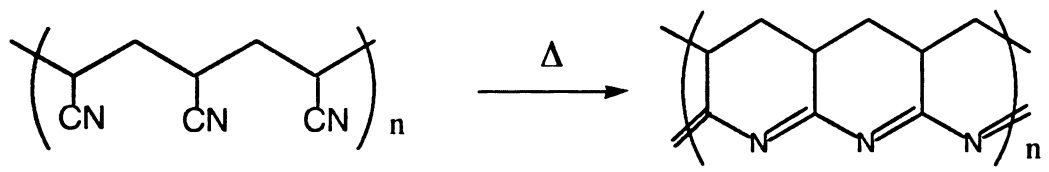

Scheme 1.5. Intrazeolite polymerization of acrylonitrile (ref 30).

Similar experiments on zeolite systems were also made by the researchers at Du Pont.[31] They have used the pentasil zeolites such as ZSM-5 and Na-β as supporting matrices in which short-chain oligomers of polythiophene were inserted, oxidatively doped to the conducting state, and finally spectroscopically characterized. They have successfully observed the evolution of the electronic structure of doped polythiophene from monomer, to oligomer, to polymer.

The intercalation of polymers also provides access to the preparation of novel polymer-ceramic nanocomposites in which the host layers are well dispersed in polymer matrices. These nanocomposites can exhibit excellent physical and mechanical properties which are superior to those of individual components. Okada and coworkers reported that ε-caprolactam was thermally polymerized in the interlayer spacing of montmorillonite yielding a nylon-6/clay hybrid (Scheme 1.6.).[32a] X-ray and TEM measurements revealed that the silicate layers were well dispersed in the nylon-6 matrix at an average distance of 214 Å. Compared to nylon-6 , the composite showed excellent physical properties. For example, tensile strength increased from 69 MPa for nylon-6 to 107 MPa for the composite.

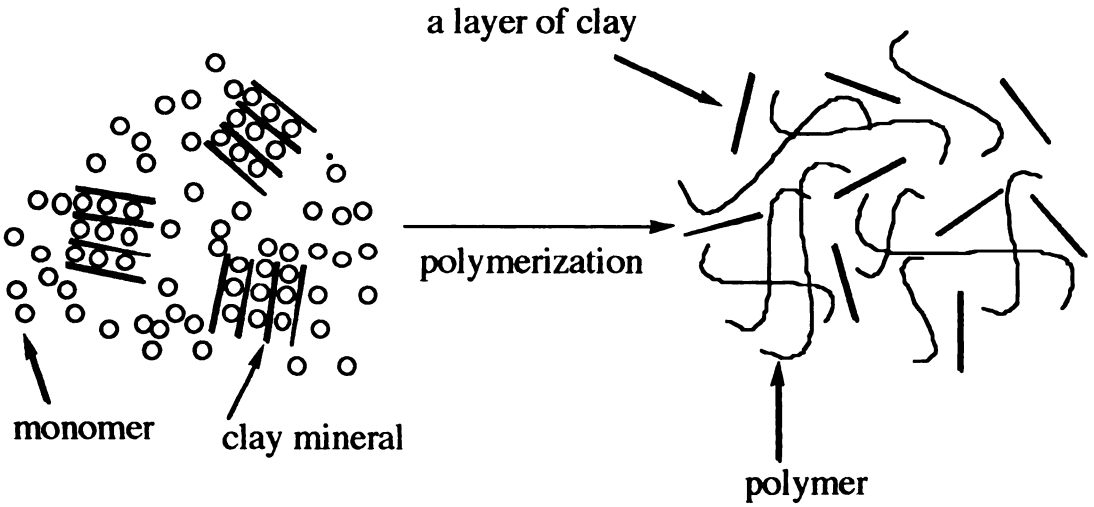

Scheme 1.6. A conceptive picture of polymerization in the presence of clay (ref 32a).

They have also investigated rubber/montmorillonite and polyimide/montmorillonite hybrids.[32b,c] The latter composite reveals excellent gas barrier and low thermal expansion properties.

The Pinnavaia group at Michigan State University has studied the polyether/clay system.[33a] Epoxy resin monomers were intercalated into smectite clays followed by the thermal polymerization to polyether at 120-200°C. The average distance between clay plates was about 200 Å. They have also achieved the polyimide/clay system which shows similar properties with one reported by Okada.[33b]

A research group at Cornell University used Cu^{2+} exchanged mica-type layered silicates as host materials for intercalative polymerization of aniline (Scheme 1.7.).[34] The resulting PANI-hybrid was insulating but became conducting when appropriately doped. Four-probe electrical conductivity measurements showed a value of 0.05 S/cm. This nanocomposite is not the same type as those found on dispersion of single layers in a continuous polymer matrix. However, the PANI-hybrid still

showed modified fracture toughness, storage modulus with respect to individual components. They also found that the hybrid was more oriented than the pristine host, probably due to the reorganization of the silicate layers to maximize the interactions between the polymer and the host.

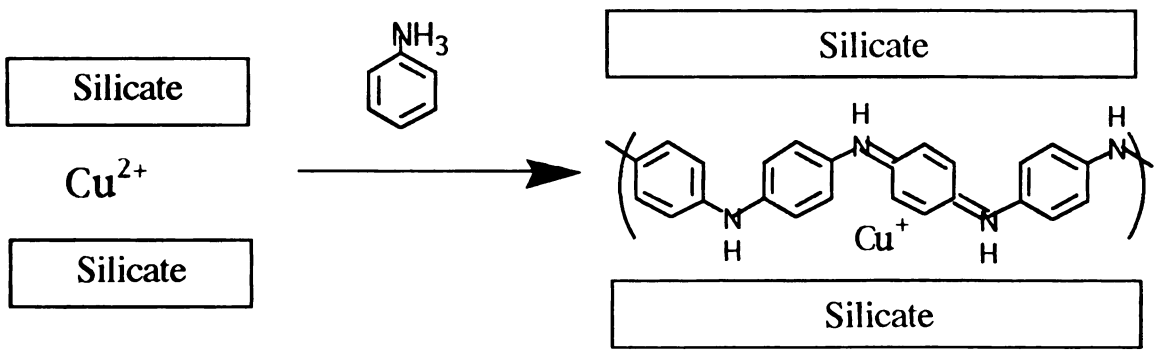

Scheme 1.7. Intercalation of polyaniline in the silicate galleries (ref 34).

Recently, they pressed a mixture of organically modified silicates and polymers into a pellet, and heated the pellet at an appropriate temperature producing a intercalated polymer/silicate hybrid. For polystyrene-hybrid, the gallery height increase of 7 Å corresponded to a monolayer of nearly planar polymer chains.[34c]

During the past several years, our group has investigated in detail the intercalative redox polymerization of organic molecules (e.g. aniline, pyrrole, 2,2'-bithiophene and terfuran) in layered FeOCl and V_2O_5 xerogel.[17] The resulting materials are composed of alternating conducting polymers and semiconducting oxide layers, and possess intriguing electrical properties arising from the combination of the two electrically active but chemically diverse components. For instance, the charge carriers can switch from electrons to holes, and the conductivity can increase from semiconducting-like to metallic by varying the polymer loading. Recently, we extended our interests to insulating polymers such as poly(ethylene-

oxide) (PEO), poly(vinylpyrrolidone) (PVP), poly(propylene glycol) (PPG), and methyl cellulose. We have found that the V_2O_5 xerogel is an excellent host not only for oxidative polymer intercalation but also for the direct intercalation of water-soluble insulating polymers.[35] The resulting nanocomposites show interesting physical and chemical properties (chapter 2 &3).

Although the inclusion of conjugated polymers in V_2O_5 xerogel has been well studied in the aspect of synthesis and property, the reaction mechanism and the interactions between the polymers and the framework are not clear yet. To approach the first issue, we intercalated anilinium into the V_2O_5 and observed its slow conversion to polyaniline upon oxidation (chapter 4).[36] To approach the second issue, it is important to understand the nature and properties of the reduced V_2O_5 framework alone. For this objective, we prepared a series of reduced V_2O_5 xerogels, $M_xV_2O_5$ (M = K, Cs), and studied their optical, magnetic and electrical properties as a function of x (chapter 5).[37]

The known host materials which have sufficient oxidizing power to initiate the intercalative polymerization are only a few. In order to expand this field to other ordered host materials which have limited redox properties, we must find the proper conditions under which intercalated monomers can be polymerized, not necessarily by the host, but by external power . We are interested in building up general methodologies to produce conjugated polymers in layered or spatially confined environments. We have found that ambient oxygen can successfully polymerize aniline to polyaniline in layered uranyl phosphate, α-zirconium phosphate and α-titanium phosphate (chapter 6).[38]

1.2. Description of Host and Guest Materials Used in the Work

1.2.1 Host Materials

a) Layered Vanadium Pentoxide Xerogel ($V_2O_5.1.8H_2O$)

Porous $V_2O_5 \cdot nH_2O$ gels have been known for more than a century.[39] They can be easily prepared by pouring molten V_2O_5 into water[40] or by hydrolysis and condensation of $VOCl_3$,[41] $VO(OR)_3$,[42] or metavanadic acid[43] via a sol-gel process.

The structure of V_2O_5 xerogel has been widely investigated for the past decade by X-ray diffraction,[44] electron microscopy,[45] neutron diffraction,[46] etc. X-ray diffraction indicates that the V_2O_5 xerogel is a layered material with an interlayer spacing of 11.5 Å. Electron microscopy shows that the gels are composed of long ribbon-like particles with typical planar dimensions of 1000 x 10 nm. Recently, cryogenic electron microscopy further suggests that small threads (100 x 2 nm) are formed first in the early stages of sol-gel process.[45] They grow lengthwise and assemble with others edge by edge to form ribbon-like particles. X-ray absorption near-edge structure (XANES) spectra reveal that the vanadium atom is in a approximately square-pyramidal geometry as in crystalline V_2O_5.[47] Extended X-ray absorption fine structure (EXAFS) data[48] in the layer stacking direction show a strong oscillation corresponding to V=O bonds with bond length of 1.58 Å, indicating that the V=O bonds point out the layers. Two weak oscillations associated with vanadium and oxygen are also observed at 2.7 and 3.7 Å. The first one is assigned to the distance between vanadium and water, suggesting that the vanadium center is weakly bonded by water. The second oscillation is attributed to the distance

between vanadium and oxygen of the nearest V=O group in the adjacent pyramid. The EXAFS data performed on the other two directions also show that V-O distance is from 1.78 to 2.02 Å and V-V distances are 3.1 and 3.3 Å which correspond to edge sharing and corner sharing of [VO_5] units, respectively. These data suggest that the square-pyramidal [VO_5] units share their edges and corners with other units to form a 2-D ribbon. One-dimensional Patterson function calculated from x-ray data in the layer axis show a strong maximum at 2.8 Å. Livage contributes the maximum to a non-planar V-V linkage from adjacent V_2O_5 units that leads to a corrugated ribbon model as shown in Figure 1.1.[44,49] The intra-ribbon structure is closely related to orthorhombic V_2O_5 (Figure 1.2). The interlayer regions are filled with water molecules which form hydrogen bonds with other water molecules or coordinate to vanadium centers. Recently, Oka proposed that the ribbons consist of two V_2O_5 slabs facing each other with a separation of 2.8 Å close to $M_xV_2O_5$[24] (M = Na, K) as shown in Figure 1.3.[50] The single V_2O_5 sheet is composed of edge and corner sharing of [VO_5] units with the vanadyl groups on the same side of the sheet (Figure 1.4.). Although most work refers to Livage's model[44-8, 51-2], the density measurements strongly prefer Oka's model, see Table 1.1.

V_2O_5 xerogel is an acidic and highly oxidizing host material. The protons between the layers can be exchanged with cations or neutralized with bases.[51] The vanadium (V^{5+}) atoms of the framework can be reduced by reducants[52] such as iodide. It shows n-type semiconductor behavior arising from electrons hopping between V^{4+}/V^{5+} centers.[53] The room temperature conductivity is around 10^{-5} S/cm.

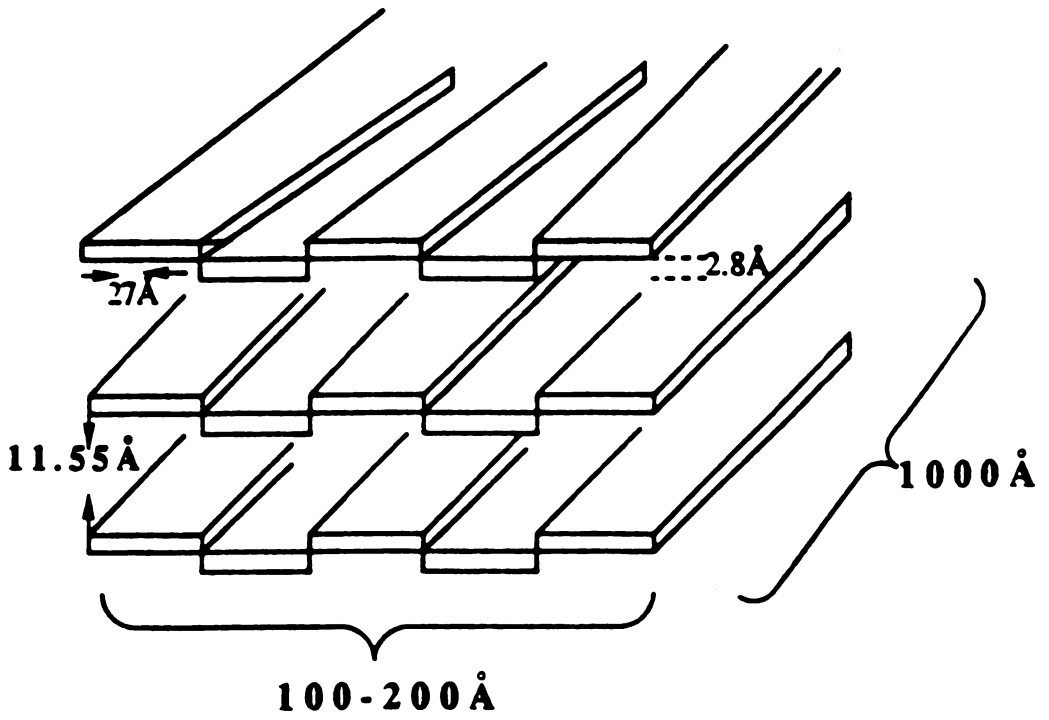

Figure 1.1. Schematic representation of V_2O_5 fibril organization and approximate dimensions. (proposed by Livage *et al.*)

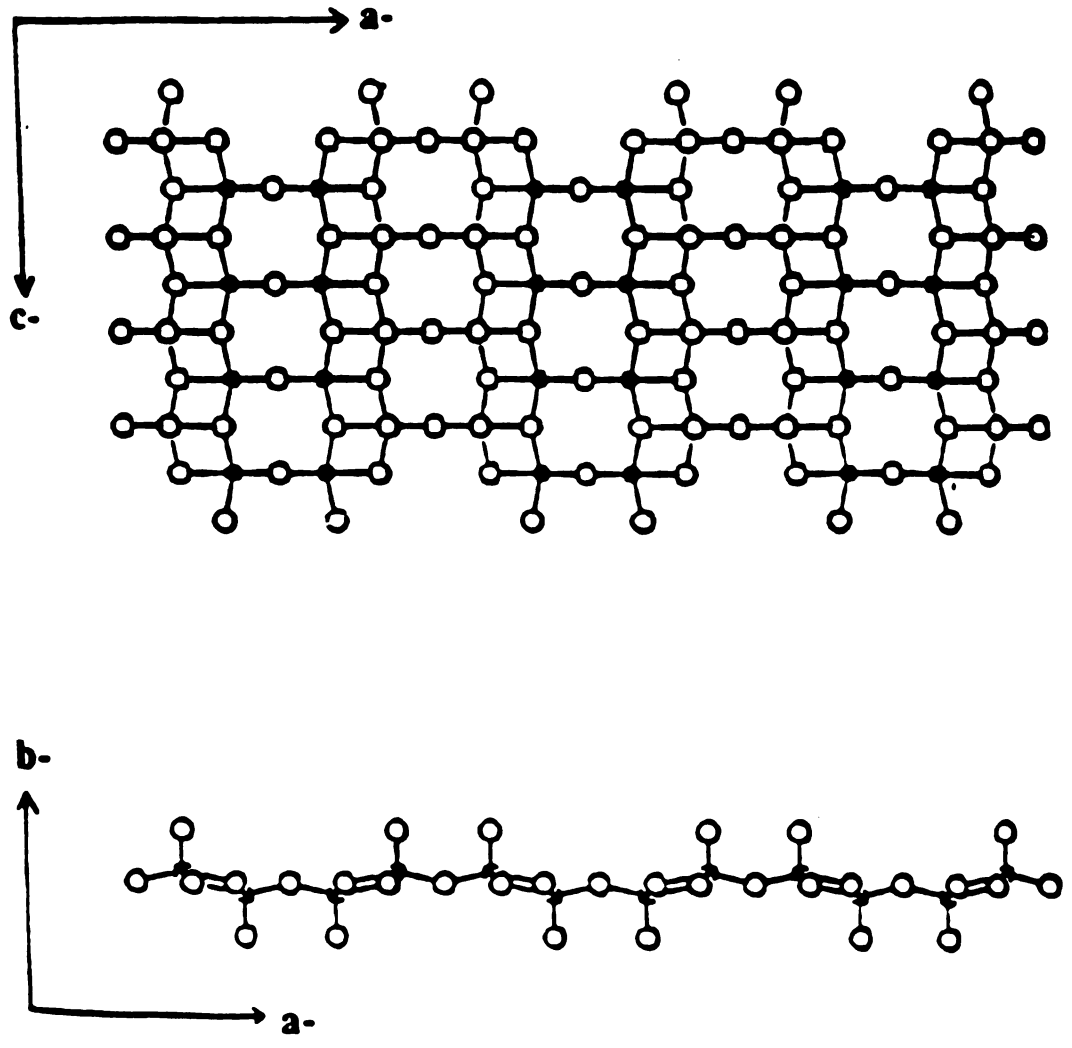

Figure 1.2. Two views of the structure of a V_2O_5 layer in orthorhombic vanadium oxide. Open circles: oxygen. Solid circles: vanadium.

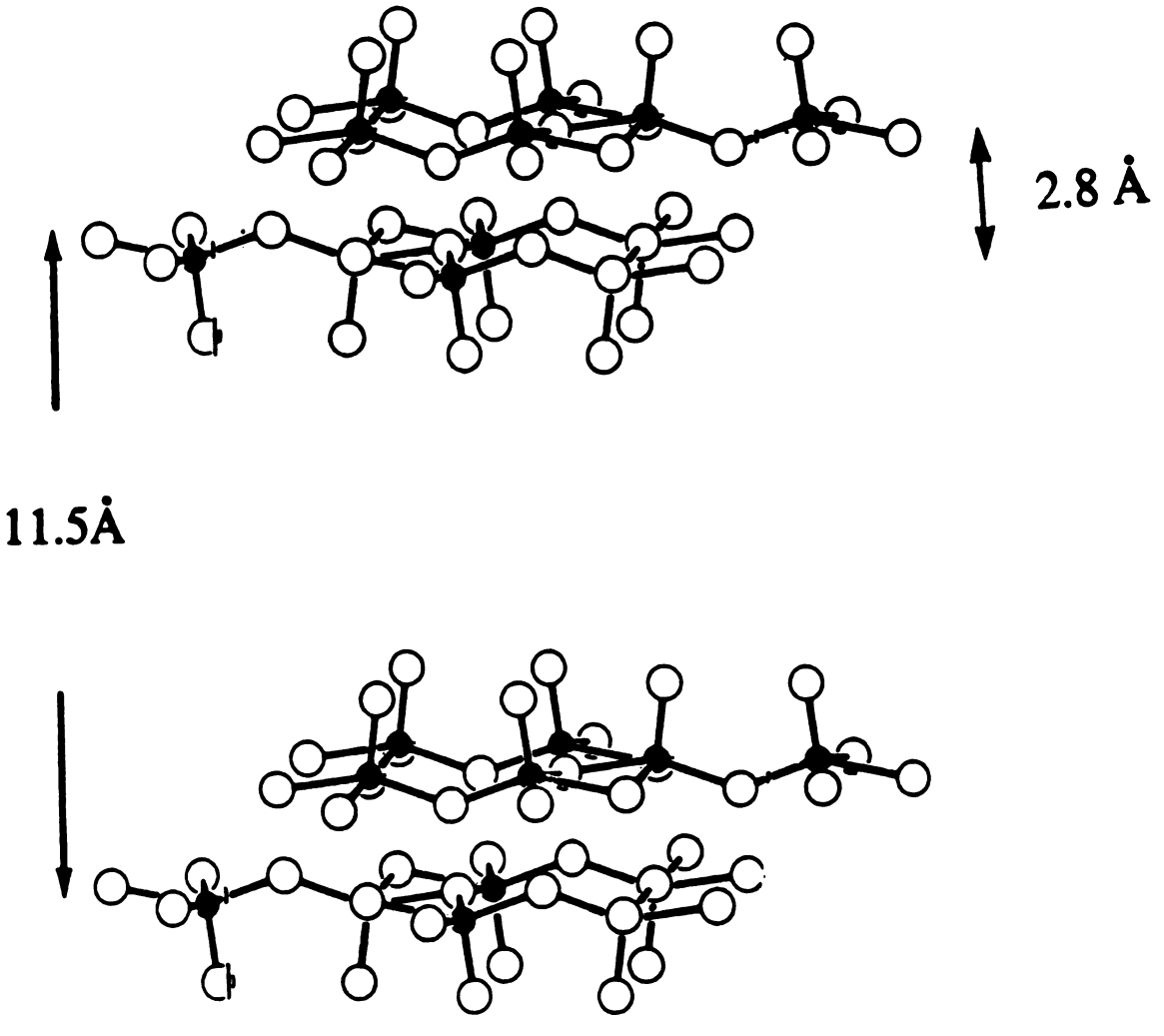

Figure 1.3. The structure of V_2O_5 xerogel (proposed by Oka *et al.*). Open circles: oxygen. Solid circles: vanadium.

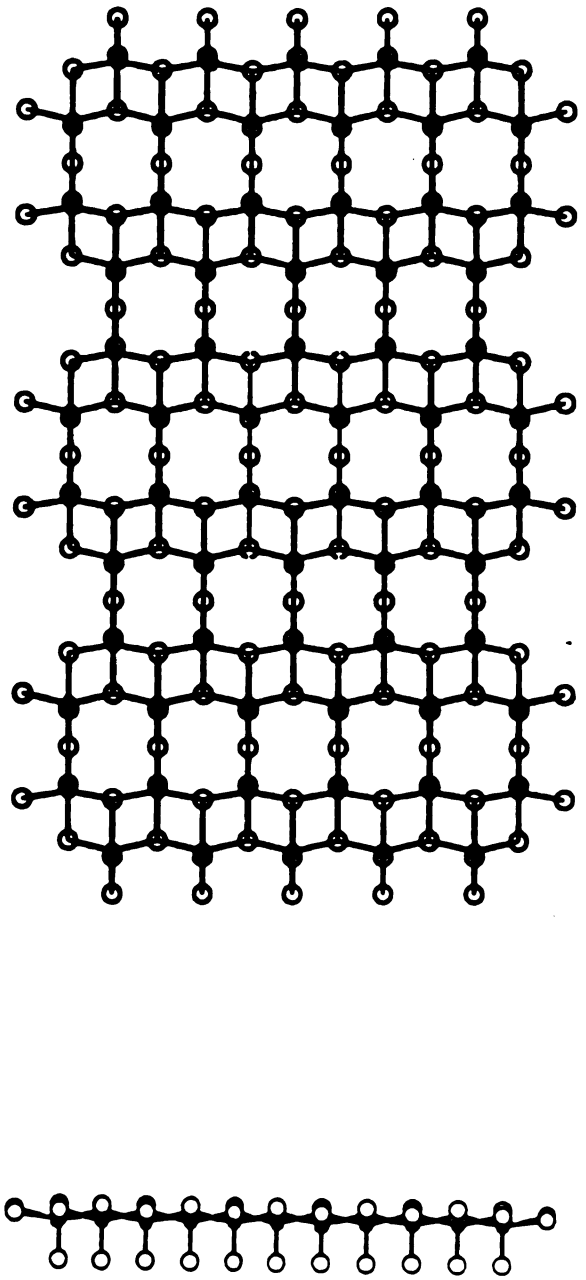

Figure 1.4. Two views of the structure of a V_2O_5 sheet (proposed by Oka *et al.*). Solid circles: vanadium. Open circles: oxygen.

Table 1.1. Calculated and Measured Densities of $V_2O_5 \cdot 1.08DMSO$ and $(PEO)_{1.0}V_2O_5 \cdot 0.7H_2O$

	Density (g/cm^3)		
Compound	Calculated from Livage's model	Calculated from Oka's model	Measured value
$V_2O_5 \cdot 1.08DMSO$[a]	1.18	2.35	2.25
$(PEO)_{1.0}V_2O_5 \cdot 0.7H_2O$[b]	~1.1	~2.2	~2.3

[a]Reported by Oka and co-workers. [b]Material synthesized in this thesis.

b) Layered Hydrogen Uranyl Phosphate (HUP)

Hydrogen uranyl phosphate $HUO_2PO_4 \cdot 4H_2O$ is a bright yellow layered material with an interlayer distance of 8.69 Å.[54] The crystal adopts a tetragonal structure (P4/ncc) with cell parameters of a = 6.995Å and c = 17.491Å. The layers consist of dumbbell-shaped uranyl ions (UO_2^{2+}) with the uranium center further coordinated by four equatorial oxygen atoms of four PO_4^{3-} tetrahedra. The PO_4^{3-} tetrahedron and uranyl ions link into two-dimensional sheets as shown in Figure 1.5. The galleries consist of two water hydrogen bonded layers, roughly one-fourth of which are protonated. The H^+ atoms in the galleries can be exchanged with cations including mono-, di and tri-valent species or neutralized with bases such as amines.[36]

HUP exhibits high proton conductivity, which has led to its use in miniature fuel cells and electrochromic displays.[55] The ac conductivity reaches 0.4 S/m at 290 K measured parallel to the layers.[55b] The activation energy is 31±3 kJ/mole. HUP also exhibits rich electronic absorption and

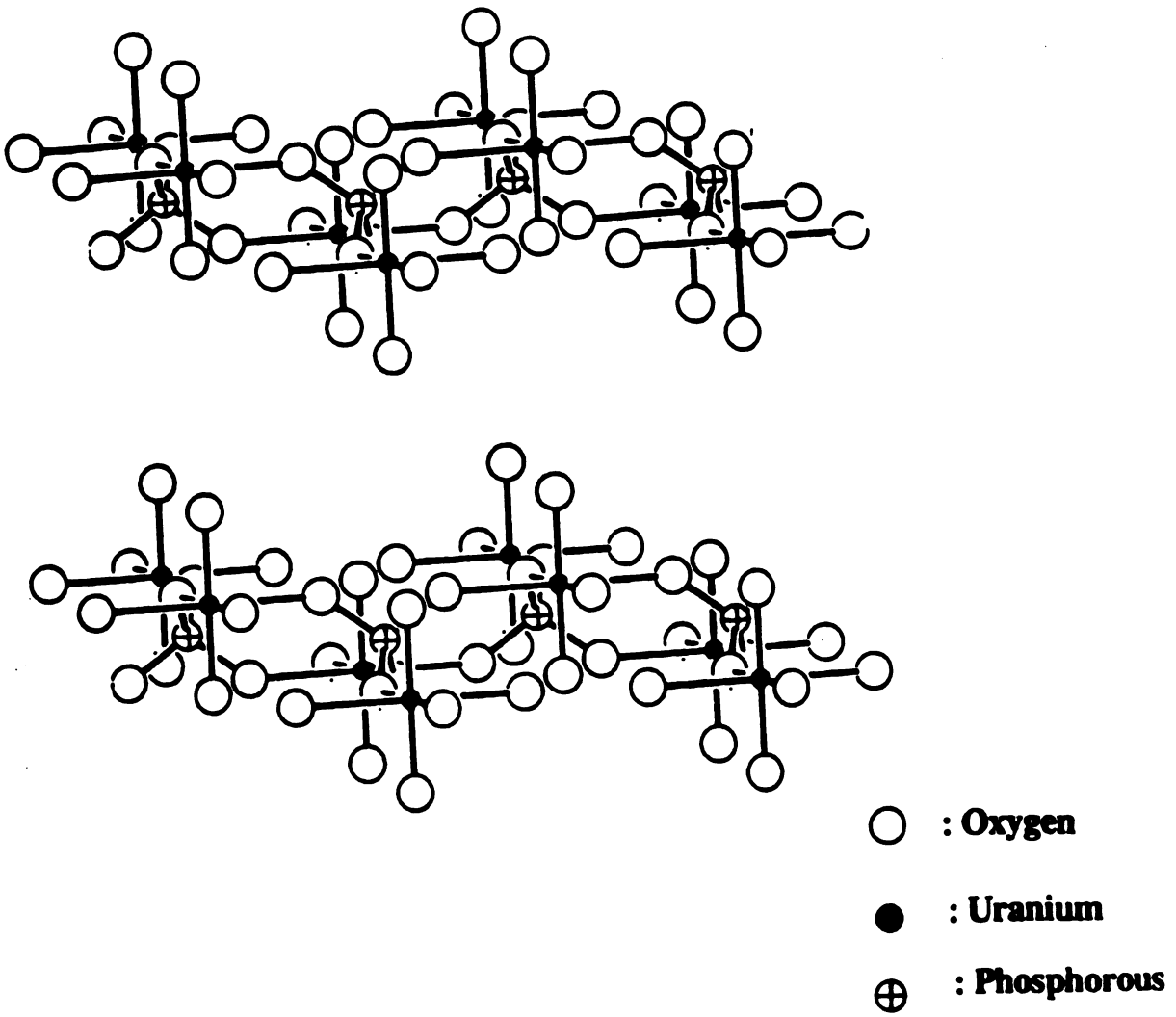

Figure 1.5. The structure of uranyl phosphate ($HUO_2PO_4.4H_2O$).

emission spectra. The yellow solid emits intense yellow-green photoluminescence with UV or near UV excitation. Spectral features indicate that the electronic transition are dominated by the UO^{2+} moiety.[56] The photoluminescence properties depend on guest excited-state properties and on host-guest interactions. For example, the intercalation of n-$C_8H_{17}NH_2$ totally quenches the emission.[56a]

c) α-Zirconium Phosphate [$Zr(HOPO_3)_2 \cdot H_2O$]

Amorphous zirconium phosphate has been known for a long time.[57] Its good ion-exchange properties and high resistance toward temperature and radiation attracted considerable attention. In 1964, its crystalline phase was prepared and structurally characterized by Clearfield and co-workers.[58] α-zirconium phosphate (α-ZrP) is a white crystalline powder prepared either by adding concentrated H_3PO_4 to $ZrOCl_2$ solution in presence of HF or refluxing its gels in concentrated phosphoric acid. It is a layered material with an interlayer spacing of 7.6 Å (Figure 1.6.). The crystal is monoclinic with a = 9.06(2), b = 5.297(1), c = 15.414(3) and β = 101.71(2)°. The layers consist of zirconium atoms lying slightly above and below the mean plane and coordinated by phosphate groups located alternatively above and below the plane as shown in Figure 1.7. Three oxygen atoms of each phosphates are bound to three different zirconium atoms and the fourth oxygen bears a proton and points into the interlayer space. Thus each zirconium atom is octahedrally coordinated by six oxygen atoms. The interlayer regions are composed of a monolayer of water molecules, forming hydrogen bonds with the phosphate groups.

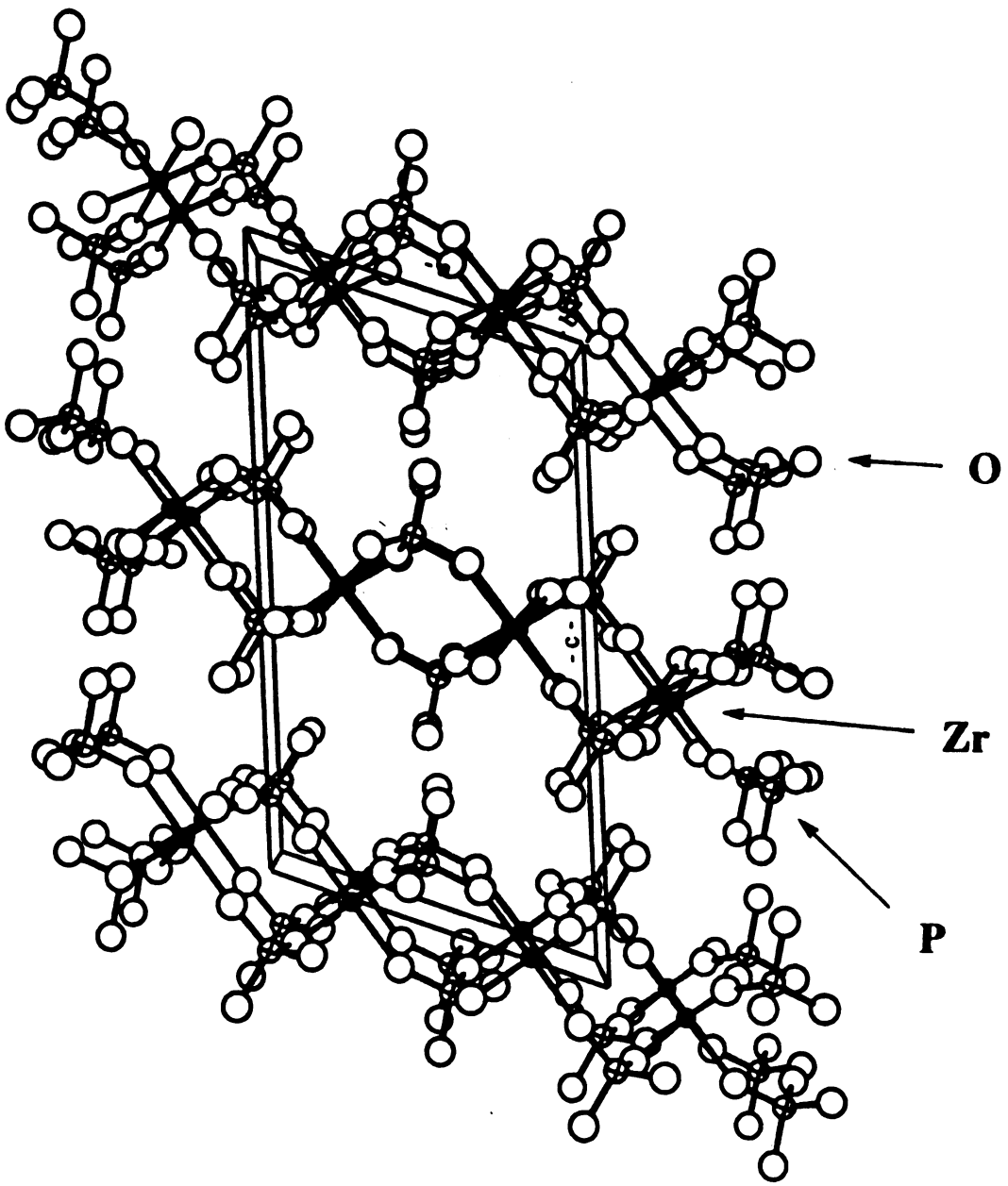

Figure 1.6. The crystal structure of α-$Zr(HPO_4)_2 \cdot H_2O$. View perpendicular to the b-axis.

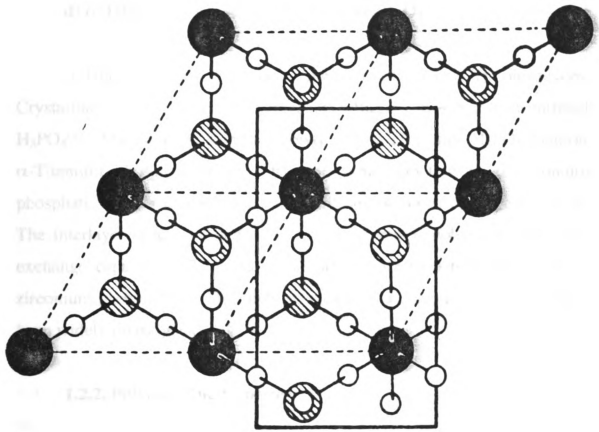

Figure 1.7. Projection of a layer of α-zirconium phosphate in the ab plane. Solid circles : Zr. Open circles : O. Shaped circles : P.

α-Zirconium phosphate exhibits a rich and varied intercalation chemistry.[59] This arises from the high acidity and weak forces between layers. Organic molecules (such as amines, alcohols, glycols) and metal ions have been intercalated into α-ZrP via ion-exchange and acid-base reactions.

d) α-Titanium Phosphate [$Ti(HOPO_3)_2 \cdot H_2O$]

α-Titanium phosphate is a member of group(VI) phosphates. Crystalline α-TiP can be synthesized by refluxing its gel in concentrated H_3PO_4[60]. The gel is prepared by slowly adding $TiCl_4$ into H_3PO_4 solution. α-Titanium phosphate (α-TiP) has the same structure as α-zirconium phosphate. It is a layered compound with an interlayer distance of 7.6 Å. The interlayer space is filled with a layer of water molecules. The ion-exchange capacity is 7.76 meq/g, slightly higher than 6.64 meq/g of α-zirconium phosphate.[61] The application on ion-exchange and catalyst have been widely investigated.[59,61-2]

1.2.2. Polymer Guest Species

a) Polyaniline (PANI)

Polyaniline, probably the oldest synthetic organic polymer, has been know for over a century.[63] It is currently of great interest because of the ability to control its electronic and optical properties through changes in protonation and oxidation.[64] Polyaniline consists of head-to-tail coupling of aniline molecules and can be prepared as a film by electrochemical oxidation or as a powder by chemical methods.[65] Depending on the oxidation states, PANI has three forms, named "leucoemeraldine", "emeraldine", and

"pernigraniline".[66] The leucoemeraldine form is composed of reduced repeat units, 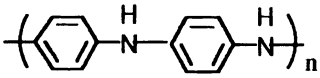 , the emeraldine form consists of alternative reduced and oxidized repeat units, 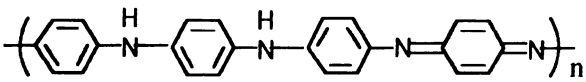 and the pernigraniline from is composed of oxidized repeat units, 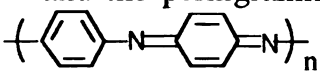 . The relationships between these forms are shown in Figure 1.8. Among them, emeraldine is the most interesting best studied. It is insulating (10^{-10} S/cm) at its neutral state but becomes highly conductive (200 S/cm) after protonation. The structural, electrical, optical and magnetic properties of the emeraldine form have been extensively studied by several types of spectroscopy[67], X-ray diffraction[68], nuclear magnetic resonance (NMR)[69] and electrical conductivity.[70] Optical spectroscopy of the emeraldine base (unprotonated) shows a π-to-π^* gap of 3.8 eV and an exciton absorption of ~2 eV, while the emeraldine salt (protonated) has no 2 eV absorption, but instead exhibits two new absorptions at 1.4 and 2.9 eV, assigned to polaron bands.[67] The emeraldine base (prepared by extracting bulk emeraldine base with THF and NMP) is proposed to be isostructural to poly(*p*-phenylene sulfide) and poly(*p*-phenylene oxide).[68] Charge transport studies show the metallic nature of the islands formed, and the conduction occurs via charging-energy-limited tunneling between the islands.[70] The molecular weight (MW) of PANI depends on the preparation conditions.[71] The PANI prepared chemically has average MW between 66,000-78,000. However, by lowering the aniline concentration and polymerization temperature, the MW (M_W) in excess of 400,000 has been obtained. Thermogravimetric analysis has shown that the emeraldine base is much more stable than the protonated

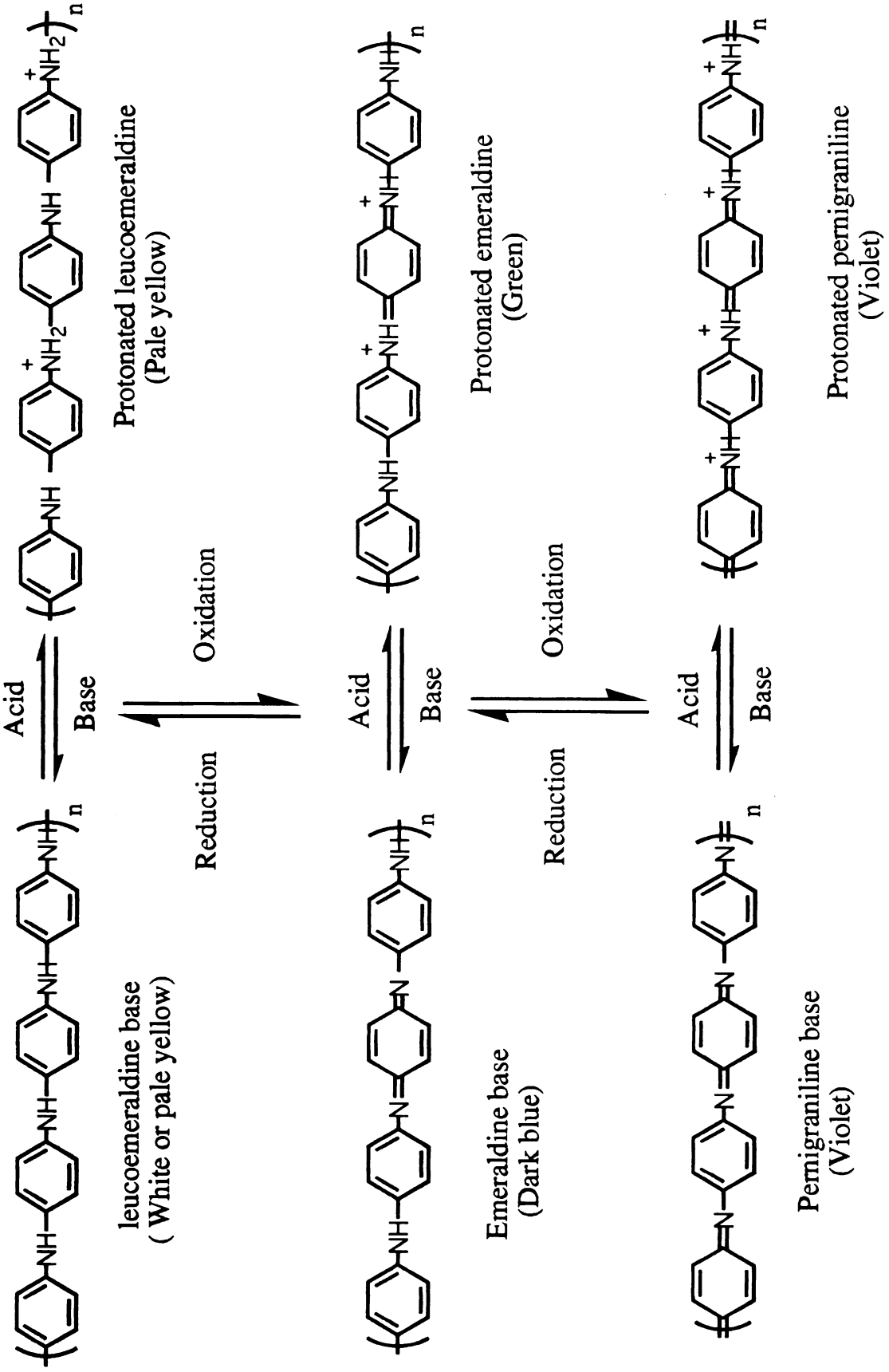

Figure 1.8. Different phases of polyaniline

form.[72] The base form decomposes at 450°C while the protonated form (when anion is chloride) decomposes at 100-250°C due to the loss of HCl.

The application of these interesting optical and electrical properties to batteries,[73] acid/base indicators,[74] corrosion inhibitors,[75] electrochromic materials[76] and microelectronic devices[77] has received a great deal of attention. The first commercial product, a 3-V coin-sized primary battery, appeared in 1987. It was manufactured by a joint venture Bridgestone and Seiko in Japan. An anti-corrosive coating to protect steel against salt is expected to be commercialized in the near future.[78]

b) Poly(ethylene-oxide) (PEO)

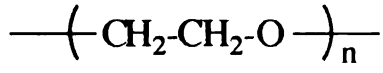

Poly(ethylene-oxide), the simplest structure of water-soluble polymers, is a semicrystalline material with ~70% of the bulk being crystalline and the remaining present as an amorphous phase.[70] Pristine PEO adopts a helical conformation with seven monomer units and a thread of 19.3 Å per unit as shown in Figure 1.9. Under stretching or pressure, a planar zigzag conformation of PEO is observed in which the repeat unit contains two monomers with a period of 7.12 Å.[71] The polymer is quite stable chemically. In air, peroxide formation and UV chain cleavage are responsible for a slow molecular weight decrease over months. The melting point of the crystalline phase is T_m ~ 65°C and the glass transition temperature is T_g ~ -60°C.

PEO has received a lot of attention because of its ability to complex various salts giving solid polymer electrolytes (SPE).[72] The maximum

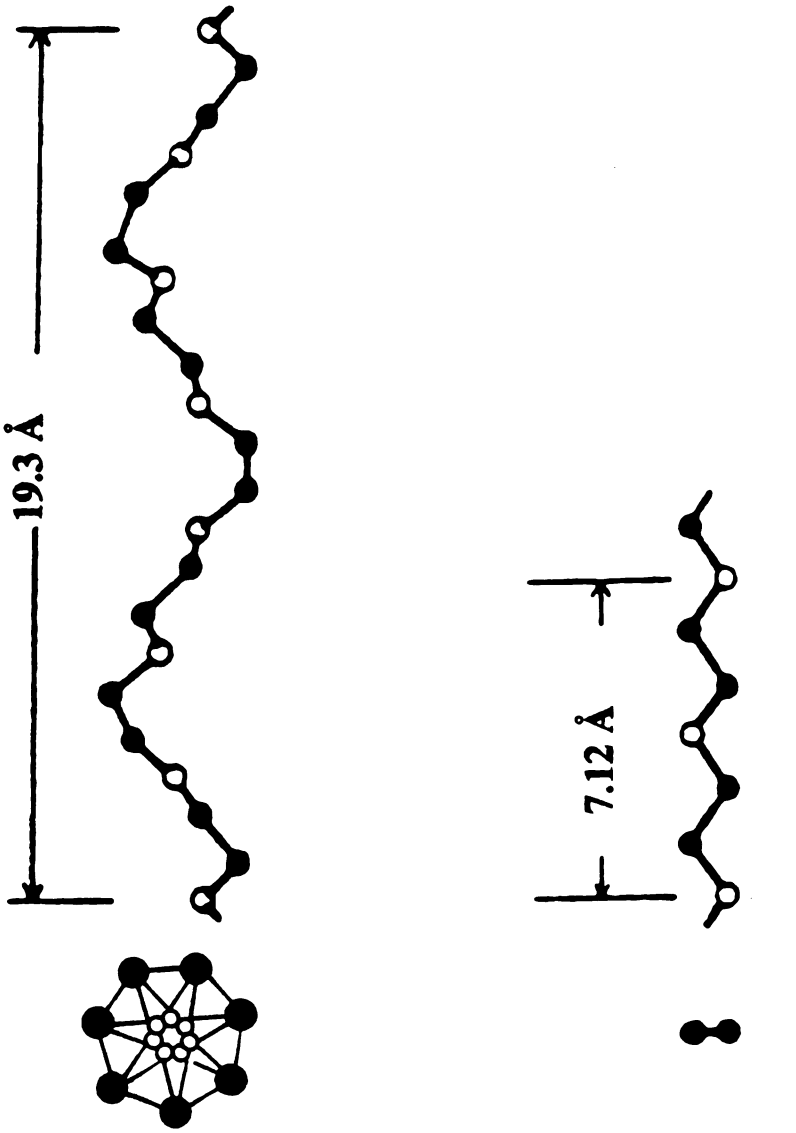

Figure 1.9. Know conformation of poly(ethylene-oxide). Open circles : O. Solid circles: CH_2.

stoichiometry of the complexes depends on the size of cations and anions. For example, the small cations (Li^+ and Na^+) give a 3(monomer unit) : 1 (cation) adduct while potassium and ammonium salts tend to keep the 4:1 ratio. In addition, large anions such as ClO_4^- and AsF_6^- form a 6:1 complex. Systematic studies of ionic conductivity versus composition and temperature for various salts have been extensively reported.[72] The amorphous elastomeric phases in PEO electrolytes are responsible for the ionic conductivity. Usually, the conductivity is in the range of 10^{-3}-10^{-4} S/cm at 100°C, and falls to 10^{-6}-10^{-8} S/cm at room temperature.

The application of PEO-based electrolytes on solid-state batteries and electrochromic devices has motivated most of the research in the field.[72] Technologically, SPE makes it possible to manufacture all-solid state cells without the difficulties generally associated with the use of liquid electrolytes such as safety and environmental stability. In addition, thin films can be easily achieved with SPE. This results in a more reversible electrochemical process and a higher overall energy efficiency.

c) Poly(propylene-oxide) (PPO) / poly(propylene-glycol) (PPG)

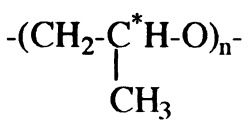

PPO has the same backbone structure as PEO.[79,82] while PPO has true asymmetric carbon atoms. Crystalline PPO is isotactic and the molecular chains have a slightly distorted planar zigzag conformation. Atactic PPO is completely amorphous and is known to dissolve alkali metal salts to form amorphous polymer electrolytes. PPO shows much weaker

solvating property than PEO, and thus electrolytes capable of complex formation are limited to lithium and sodium salts. This is thought to be due to the fact that negative effect of the steric hindrance exerted by the methyl groups which predominates over the increased donor power of the oxygen atoms. Ionic conductivity of the PPO-alkali metal salt complexes is comparable with that of the PEO complexes in the range of 10^{-5} S/cm.

d) Poly(vinylpyrrolidone) (PVP)

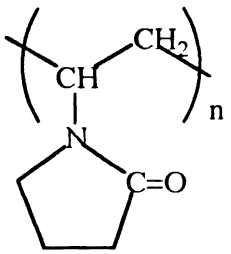

PVP is a polar polymer with a T_g of 453K.[79,82] It is an important commercial polymer with a large number of uses. It is readily soluble in water and many organic solvents, and is compatible with many plasticizers, inorganic salts and other resins. Bulk PVP is fully amorphous and hygroscopic but highly stable. The most important applications of PVP are in pharmaceuticals and cosmetics. It is also capable of dissolving lithium salts but this produces poorly conducting films.[72]

e) Methyl cellulose

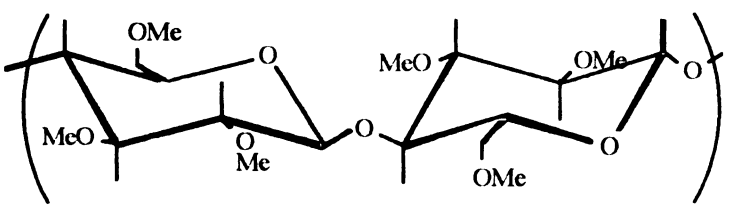

Methyl cellulose is a derivative of cellulose and water-soluble.[79,82] Cellulose is the most abundant of all naturally occurring organic compounds found in wood, seed, leaf etc. Chemically, it is a polysaccharide, consisting with glucose anhydride units linked together through the 1 and 4 carbon atoms with a β-glucosidal linkage. Crystalline cellulose adopts a straight chain conformation.[82] The two anhydroglucose units are nearly co-planar with the -CH_2OH side chains in successive units occurring on opposite sides of the chain. Large amounts of cellulose and its derivatives are used in films, plastics, protective coatings, adhesives and in many other important industrial products.

LIST OF REFERENCES

LIST OF REFERENCES

(1) Schafhäutl, C. *J. Prakt. Chem.* **1841**, 23, 298-330.

(2) Fredenhagen, K.; Cadenbach, G. *Z. Anorg. Allg. Chem.* **1926**, 158, 249-263.

(3) Clearfield, A.; Hagiwara, H. *J. Inorg. Nucl. Chem.* **1978**, 40, 907-914.

(4) Fritz Weigel; Gunter Hoffmann *J. Less-Common Met.* **1976**, 44, 99-123.

(5) Johnson, J.W.; Jacobson, A.J.; Brody, J.F.; Rich, S.M. *Inorg. Chem.* **1982**, 21, 3820-3825.

(6) Murphy, D.W.; DiSalvo, F.J.; Hull, G.H.; Waszczak, J.V. *Inorg. Chem.* **1976**, 15(1), 17-21.

(7) (a) Wittingham, M.S.; Jacobson, A.J. *Intercalation Chemistry* Academic Press, New York, 1982. (b) Schollhorn, R. *Angew. Chem. Int. Ed. Engl.* **1980**, 19, 983-1003. (c) Levy, F.A. *Intercalated Layered Materials,* Holland, **1979**. (d) Friend, R.H.; Yoffe, A.D. *Adv. Phys.* **1987**, 36, 1-94. (e) Bernard, L.; McKelvy, M.; Glaunsinger, W.; Colombet, P. *Solid State Ionics* **1985**, 15, 301-310.

(8) (a) Eichinger, G.; Besenhard, J.O. *J. Electroanal. Chem.* **1976**, 72, 1-31. (b) Whittingham, M.S. *J. Solid State Chem.* **1979**, 29, 303-310. (c) Abraham, K.M. *J. Power Sources* **1981**, 7, 1-43.

(9) (a) Colton, R.J.; Guzman, A.M.; Rabalais, J.W. *Acc. Chem. Res.* **1978**, 11,170-176. (b) Bange, K.; Gambke, T. *Adv. Mater.* **1990**, 2, 10-22. (c) Talledo, A.; Andersson, A.M.; Granqvist, C.G. *J. Appl. Phy.* **1991**, 69(5), 3261-5.

(10) (a) Boersma, M.A. *Catal. Rev.* **1974**, 10, 243-280. (b) Pinnavaia, T.J.; Farzanch, F. *Inorg. Chem.* **1983**, 22, 2216. (c) Baiker, A.; Dollenmeier, P.; Glinski, M.; Reller, A.; Sharma, V.K. *J. Catal.* **1988**, 111, 273-285. (d) Figueras, F. *Catal. Rev.* **1988**, 30, 457-499 (e) Wang, M.C. *Clay&Clay Minerals* **1991**, 39, 202-210.

(11) Theng, B.K.G. "*Formation and Properties of Clay-polymer Complexes*" Elsevier/Notth-Holland Inc., N.Y. **1979**.

(12) (a) Greenland, D.J. *J. Colloid Sci.* **1963**, 18, 647-664. (b) Bear, F.E. *Soil Sci.* **1952**, 73, 419-492.

(13) (a) Murry, T.P. *Clay&Clay Minerals*, **1963**, 10, 291-298. (b) Schwarz E.C. United States Patent 4017452.

(14) (a) Fraser, M.J. *J. Pharmacy and Pharmacology* **1957**, 9, 497-521. (b) Malaren , A.D. *Can. J. Soil Sci.* **1970**, 50, 97-109.

(15) (a) "*The Physics and Chemistry of Low Dimensional Solids*" Bechgaard, K.; Anderson, J.R.; Alcacer, L., Ed. D. Reidel Publishing Co. **1980**. (b) Marks, T.J. *Science* **1985**, 227, 881-889. (c) "*Handbook of Conducting Polymers*"; Skotheim, T.A., Ed.; Marcel Dekker : New York, **1986**; Vol 1 and 2. (d) Huang, W.-S.; Humphrey, B.D.; MacDiarmid, A.G. *J. Chem. Soc. Faraday Trans* **1986**, 82, 2385-2400. (e) Kanatzidis, M.G. *Chemical & Engineering News* **1990,** 68, 36-54.

(16) (a) Shirakawa, H.; Ikeda, S. *Syhth. Met.* **1979/1980**, 1, 175-184. (b) Cao, Y.; Smith, P.; Heeger, A.J. *Synth. Met.* **1991**, 41-43, 181-184. (c) Bryce, M.R.; Chissel, A.D.; Gopel, J.; Kathirganathan, P.; Parker, D. *Synth. Met.* **1991**, 39, 397-400.

(17) (a) Fisher, J.E.; Yang, X.; Scherr, E.M.; Capjipe, V.B.; MacDiarmid A.G. *Synth. Met.* **1991**, 41-43, 661-664. (b) Gustasson G.; Inganas, O.; Stafatrom, S.; Osterholm, H.; Laakso, J. *Synth. Met.* **1991**, 41-43, 593-596. (c) Monkman, A.P.; Adams, P. *Synth. Met.* **1991**, 40, 87-96.

(18) (a) Martin, C.R.; Van Dyke, L.S.; Cai, Z.; Liang, W. *J. Am. Chem. Soc.* **1990**, 112,8976-8977. (b) Aldissi, M. *J. Polym. Sci. Polym. Lett. Ed.* **1985**, 23, 167-170.

(19) Mortland M.M.; Pinnavaia, T.J. *Nature* **1971**, 229, 75-77.

(20) (a) Soma, Y.; Soma, M.; Harada, I. *Chem. Phys. Lett.* **1983**, 99, 153-156. (b) Soma, Y.; Soma, M.; Furukawa, Y.; Harada, I. *Clay&Clay Minerals* **1987**, 35, 53-59.

(21) (a) Day, P.; Ledsham, R.D. *Mol. Cryst. Liq. Cryst.* **1982**, 86, 163-174. (b) Tieke, B. *Mol. Cryst. Liq. Cryst.* **1983**, 93, 119-145

(22) Kanatzidis, M.G.; Tonge, L.M.; Marks, T.J.; Marcy, H.O.; Kannewurf, C.R. *J. Am. Chem. Soc.* **1987**, 109, 3797-3799.

(23) (a) Wu, C.-G.; Kanatzidis, M.G.; Marcy, H.O.; DeGroot, D.C.; Kannewurf, C.R. *Polym. Mat. Sci. Eng.* **1989**, 61, 969-973. (b) Kanatzidis, M.G.; Wu, C.-G.; Marcy, H.O.; DeGroot, D.C.; Kannewurf, C.R. *Chem. Mater.* **1990**, 2(3), 222-224. (c) Wu, C.-G.; Marcy, H.O.; DeGroot, D.C.; Schindler, J.L.; Kannewurf, C.R.; Leung, W.-Y.; Benz, M.; LeGoff, E.; Kanatzidis, M.G. *Synth. Met.* **1991**, 41-43, 797-803. (d) Wu, C.-G.; Marcy, H.O.; DeGroot, D.C.; Schindler, J.L.; Kannewurf, C.R.; Kanatzidis, M.G. *Synth. Met.* **1991**, 41-43, 693-698.

(24) Brandt, P.; Fisher, R.D.; Martinez, S.E.; Calleja, R.D. *Angew. Chem. Int. Ed. Engl.* **1989**, 28, 1265-1266.

(25) (a) Nakajima, H.; Matsubayashi, G. *Chem. Lett.* **1993**, 423-426. (b) Nakajima, H.; Matsubayashi, G. *J. Phy. chem.* in press.

(26) Inoue H.; Yoneyama, H. *J. Electroanal. Chem.* **1987**, 233, 291-295.

(27) Nazar, L.F.; Zang, Z.; Zinkwege, D. *J. Am. Chem. Soc.* **1992**, 114, 6239-6240.

(28) Chao, T.H.; Erf, H.A. *J. Catal.* **1986**, 100, 492-499.

(29) (a) Enzel P.; Bein, T *J. Phys. Chem.* **1989**, 93, 6270-6272. (b) Enzel P.; Bein, T *J. Chem. Soc. ,Chem. Commun.* **1989**, 1326-1327. (c) Bein, T ; Enzel P. *Synth. Met.* **1989**, 29, 163-168. (d) Bein, T ; Enzel P. *Mol. Cryst. Liq. Cryst.* **1990**, 181, 315-324.

(30) Enzel P.; Bein, T. *Chem. Mater.* **1992**, 4, 819-824.

(31) Caspar, J.V.; Ramamurthy, V.; Corbin, D.R. *J. Am. Chem. Soc.* **1991**, 113, 600-610.

(32) (a) Okada, A.; Kawasuki, M.; Usuki, A.; Kojima, Y.; Kurauchi, T.; Kamigaito, O. *Mat. Res. Soc. Symp. Proc.* **1990**, 171, 44-50. (b) Yano, K.; Usuki, A.; Okada, A.; Kurauchi, T.; Kamigaito, O. *Polymer Preprints*, **1991**, 32, #1, 65. (c) Okada, A.; Fukumori, K.; Usuki, A.; Kojima, Y.; Kurauchi, T.; Kamigaito, O. *Polymer Preprints*, **1991**, 32, #3, 540.

(33) (a) Kaviratna, P.D.; Lan, T.; Pinnavaia, T.J. *Polymer Preprints*, **1994**, 35(1), 788-789. (b) Lan, T.; Kaviratna, P.D.; Pinnavaia, T.J. *Polymer Preprints*, **1994**, 35(1), 823-824.

(34) (a) Mehrotra, V.; Giannelis, E.P. *Solid State Ionics* **1992**, 51, 115-122. (b) Mehrotra, V.; Giannelis, E.P. *Solid State Commun.* **1991**, 77, 155-

158. (c) Vaia, R.A.; Ishii, H.; Giannelis, E.P. *Chem. Mater.* **1993**, 5, 1694-1696.

(35) (a) Liu, Y.-J.; DeGroot, D.C.; Schindler, J.L.; Kannewurf, C.R.; Kanatzidis, M.G. *Chem. Mater.* **1991**, 3, 992-994. (b) Liu, Y.-J.; DeGroot, D.C.; Schindler, J.L.; Kannewurf, C.R.; Kanatzidis, M.G. *Adv. Mater.* **1993**, 5(5), 369-372.

(36) Liu, Y.-J.; DeGroot, D.C.; Schindler, J.L.; Kannewurf, C.R.; Kanatzidis, M.G. *J. Chem. Soc., Chem. Commun.* **1993**, 593-596.

(37) Liu, Y.-J.; Cowen, J. A.; Kaplan, T.; DeGroot, D. C.; Schindler J.; Kannewurf, C. R.; Kanatzidis, M. G. "Investigation of the Vanadium Oxide Xerogel Bronzes: $A_xV_2O_5 \cdot nH_2O$ (A = K and Cs)", in preparation.

(38) Liu, Y.-J.; Kanatzidis, M.G. *Inorg. Chem.* **1993**, 32(14), 2989-2991.

(39) Ditle, A. *Seances Acad. Sci.* **1885**, 101, 6987-6989.

(40) (a) Mullier, E.Z. *Chem. Ind. Kolloide* **1911**, 8, 302-307. (b) Mullier E.Z. *Chem. Ind. Kolloide* **1904**, 8, 1098-1104.

(41) Wegelin, G.Z. *Chem. Ind. Kolloide* **1912**, 11, 25-28.

(42) Prandtl, W.; Hess, L. *Z. Anorg. Allg. Chem.* **1913**, 82, 103-129.

(43) Lemerle, J.; Nejem, L.; Lefebvre, J. *J. Inorg. Nucl. Chem.* **1980**, 42, 17-20.

(44) Legendre, J.-J.; Aldebert, P.; Baffier, N.; Livage, J. *J. Colloid Interface Sci.* **1983**, 94(1), 84-89.

(45) (a) Legendre, J.J., Livage, J. *J. Colloid Interface Sci.* **1983**, 94, 75-83. (b) Bailey, J.K.; Pozarnsky, G.A.; Mecartney, M.L. *J. Mater. Res.* **1992**, 7(9), 2530-2537.

(46) Aldebert, P.; Haesslin, H.W.; Baffier, N.; Livage, J. *J. Colloid Interface Sci.* **1984**, 98(2), 484-488.

(47) Stizza, S.; Benfatto, M.; Bianconi, A.; Garcia, J.; Mancini, G.; Natoli, C.R. *J. Phys.* **1986**, 47-C8, 691-696.

(48) (a) Stizza, S.; Davoli, I.; Benfatto, M. *J. Non-Cryst. Solids* **1987**, 95-96, 327-334. (b) Stizza, S.; Mancini, G.; Benfatto, M.; Natoli, C.R.; Garcia, J.; Bianconi, A. *Phys. Rev. B* **1989**, 40, 12229-12236.

(49) Livage, J. *Chem. Mater.* **1991**, 3, 573-593.

(50) (a) Yao T.; Oka, Y.; Yamamoto, N. *Mat. Res. Bull.* **1992**, 27, 669-675. (b) Yao T.; Oka, Y.; Yamamoto, N. *J. Mater. Chem.* **1992**, 2(3), 331-336. (c) Yao T.; Oka, Y.; Yamamoto, N. *J. Mater. Chem.* **1992**, 2(3), 337-340.

(51) (a) Bouhaouss, A.; Aldebert, P. *Mater. Res. Bull* **1983**, 18, 1247-1256. (b) Casal, B.; Ruiz-Hitzky, E.; Crespin, M.; Tinet, D.; Galvan, J.C. *J. Chem. Soc., Faraday Trans* **1989**, 86, 4167-4177. (c) Masbah, H.; Tinet, D.; Crespin, M.; Erre, R.; Setton, R.; Van Damme, H. *J. Chem. Soc. Chem. Commun.* **1985**, 935-936.

(52) (a) Aldebert, P.; Baffier, N.; Gharbi, N.; Livage, J. *Mater. Res. Bull* **1981**, 16, 949-955. (b) Erre, R.; Masbah, H.; Crespin, M.; Van Damme, H.; Tinet, D. *Solid State Ionics*, **1990**, 37, 239-251.

(53) Bullot, J.; Cordier, P.; Gallais, O.; Gauthier, M.; Livage, J. *J. Non-Cryst. Solids* **1984**, 68, 135-146.

(54) (a) Morosin, B. *Phys. Lett.* **1978**, 65A, 53-54. (b) Shilton, M.G.; Howe, A.T. *J. Solid State Chem.*. **1980**, 34, 137-147. (c) Lloyd, M.H.; Bischoff, K.; Peng, K.; Nissen, H.U.; Wessicken, R. *J. Inorg. Nucl. Chem.*. **1976**, 38, 1141-1147.

(55) .(a) Howe, A.T.; Shilton, M.G. *J. Solid State Chem.* **1979**, 28, 345-361. (b) Howe, A.T.; Shilton, M.G. *J. Solid State Chem.* **1980**, 34, 149-155. (c) Howe, A.T.; Shffield, S.H.; Childs, P.E.; Shilton, M.G. *Thin Solid Films* **1980**, 67, 365.

(56) (a) Olken, M.M.; Biagioni, R.N.; Ellis, A.B. *Inorg. Chem.* **1983**, 22, 4128-4134. (b) Hunsberger, L.R.; Ellis, A.B. *Coord. Chem. Rev.* **1990**, 97, 209-224.

(57) (a) von Hevesey, G.; Kimura, K. *J. Am. Chem. Soc.* **1925**, 47, 2540-2544. (b) Amphlett, C.B. "*Inorganic Ion Exchange*", Elsevier, Amsterdam, **1964**.

(58) Clearfield, A.; Smith, G.D. *J. Colloid Interface Sci.* **1969**, 3(3), 431-436.

(59) (a) Clearfield, A. *Comments Inorg. Chem.* **1990**, 10, 89-128. (b) Alberti, G. *Acc. Chem. Res.* **1978**, 11, 163-170. (c) Clearfield, A. *Chem. Rev.* **1988**, 88, 125-148. (d) Alberti, G.; Costantino, U. *J. Mol. Catal.* **1984**, 27, 235-250.

(60) Alberti, G.; Cardini-Galli, P.; Costantino, U; Torracca, E. *J. Inorg. Nucl. Chem.* **1967**, 29, 571-578.

(61) Clearfield, A.; Thakur, D.S. *Appl. Catal.* **1986**, 26, 1-26.

(62) Allulli, S.; Ferragina, C.; La Ginestra, A.; Massucci, M.A.; Tomassina, N. *J. Inorg. Nucl. Chem.* **1977**, 39, 1043-1048.

(63) Letherby, H. *J. Chem. Soc.* **1862**, 15, 161-163.

(64) (a) MacDiarmid, A.G.; Somasiri, N.L.; Salaneck, W.R.; Lundstroem, L.; Liedberg, B.; Hassan, M.A.; Erlandsson, R.; Konrasson, P. Springer series in solid state science V63 Springer, Berlin, 1985. (b) Huang, W.-S.; Humphrey, B.D.; MacDiarmid, A.G. *J. Chem. Soc. Faraday*

Trans. **1986**, 82, 2385-2400. (c) MacDiarmid A.G.; Epstein, A.J. *Faraday Discuss Chem. Soc.* **1989**, 88, 317-332.

(65) (a) Mohilner, D.M. Adams, R.N. Argersinger, Jr., W. J. *Am. Chem. Soc.* **1962**, 84, 3618-3622. (b) Geniès, E.M.; Lapkowski, M.; Penneau, J.F. *J. Electroanal. Chem.* **1988**, 249, 97-107.

(66) MacDiarmid, A.G.; Chiang, J.-C.; Halpern, M.; Huang, W.-S.; Mu, S.-L.; Somasiri, N.L.D.; Wu, W.; Yaniger, S.I. *Mol. Cryst. Liq. Cryst.* **1985**, 121, 173-180.

(67) (a) Ohsaka, T.; Ohnuki, Y.; Oyama, N. *J. Electroanal. Chem.* **1984**, 161, 399-405. (b) Furukawa, Y.; Ueda, F.; Hyodo, Y.; Harada, I.; Nakajima, T.; Kawagoe, T. *Macromolecules* **1988**, 21, 1297-1305. (c) Harada, I.; Furukawa, Y.; Ueda, F. *Synth. Met.* **1989**, 29, E303-E312. (d) Bloor, D.; Monkman, A. *Synth. Met.* **1987**, 21, 175-179.

(68) Pouget J.P.; Józefowicz, M.E.; Epstein, A.J.; Tang, X.; MacDiarmid, A.G. *Macromolecules* **1991**, 24, 779-789.

(69) (a) Kaplan, S.; Conwell, E.M.; Richter, A.F.; MacDiarmid, A.D. "*Solid State NMR of Polymers*" Mathias, L. Eds., Plenum Press, N.Y. **1991**. (b) Kaplan, S.; Conwell, E.M.; Richter, A.F.; MacDiarmid, A.D. *J. Am. Chem. Soc.* **1988**, 110, 764-768.

(70) (a) Zuo, F.; Angelopoulos, M.; MacDiarmid, A.G.; Epstein, A.J. *Phys. Rev. B*, 36, 3475. (b) Wnek, G.E. *Synth. Met.* **1986**, 15, 213-218. (c)

Lundberg, B.; Salaneck, W.R.; Lundström, I. *Synth. Met.* **1987**, 21, 143-147.

(71) (a) Abe, M.; Ohtani, A.; Umemoto, Y.; Akizuki, S.; Ezoe, M.; Higuvhi, H.; Nakamoto, K.; Okuno, A.; Noda, Y. *J. Chem. Soc. Chem. Commun.* **1989**, 1736-1738. (b) Geniès, E.M.; Noël, P. *Synth. Met.* **1992**, 46, 285-292. (c) Scherr, E.M.; MacDiarmid, A.G.; Manohar, S.K.; Masters, J.G.; Sun, Y.; Tang, X.; Druy, M.A.; Glatkowski, P.J.; Cajipe, V.B.; Fischer, J.E.; Cromack, K.R.; Jozefowicz, M.E.; Ginder, J.M.; McCall, R.P.; Epstein, A.J. *Synth. Met.* **1991**, 41-43, 735-738. (d) Hsu, C.-H.; Peacock, P.M.; Flippen, R.B.; Manohar, S.K.; MacDiarmid, A.G. *Synth. Met.* **1993**, 60, 233-237.

(72) (a) Kulkarni, V.G.; Campbell, L.D.; Mathew, W.R. *Synth. Met.* **1989**, 30, 321-325. (b) Hagiwara, T.; Yamaura, M.; Iwata, K. *Synth. Met.* **1988**, 25, 243-252. (c) Yue, J.; Epstein, A.J.; Zhong, Z.; Gallangher, P.K.; MacDiarmid, A.G. *Synth. Met.* **1991**, 41-43, 765-768.

(73) Kitani, A.; Kaga, M.; Sasak, K. *J. Electrochem. Soc.* **1988**, 2491-2496.

(74) Syed, A.A.; Dinesan, M.K. *Synth. Met.* **1990**, 36, 209-215.

(75) (a) Mengoli, G.; Musiani, M.M.; Pelli, B.;Vecchi, E. *J. Appl. Polym. Sci.* **1983**, 28, 1125-1136. (b) Noufi, R.; Nozik, A.J.; White, J.; Warren, L.F. *J. Electrochem. Soc.* **1982**, 129(10), 2261-2265.

(76) Akhtar, A.; Weakliem, H.A.; Paiste, R.M.; Gaughan, K. *Synth. Met.* **1988**, 26, 203-208.

(77) (a) Paul, E.W.; Ricco, A.J.; Wrighton, M.S. *J. Phys. Chem.* **1985**, 89, 1441-1447. (b) Chao, S.; Wrighton M.S. *J. Am. Chem. Soc.* **1987**, 109, 6627-6631.

(78) Schoch, K.F.; Saunders, H. *IEEE Spectrum* , **1992**, 52-55.

(79) Molyneux, P. in *Water-Soluble Synthetic Polymers* ; CRC press, Inc.: New York, **1983** Vols. 1, 2.

(80) (a) Takahashi, Y.; Sumita, I.; Tadokoro, H. *J. Polym. Sci. Polym. Phys. Ed.* **1973**, 11, 2113-2122. (b) Takahashi, Y.; Sumita, I.; Tadokoro, H. *J. Polym. Sci. Polym. Phys. Ed.* **1981**, 19, 1153-1155.

(81) "*Polymer Electrolyte Reviews*" McCallum, J.R., Vincent, C.A., Eds.; Elsevier Applied Science: London, **1987** and **1989** Vols. 1, 2.

(82) Ott, E.; Spurlin, M. in *High Polymers*; Interscience Publishers, Inc., New York, **1954** Vol. 5.

CHAPTER II

SYNTHESIS, STRUCTURE AND REACTIONS OF POLY(ETHYLENE-OXIDE)/V_2O_5 INTERCALATION COMPOUNDS

ABSTRACT

Intercalation and structural characterization of poly(ethylene-oxide) (PEO) in layered V_2O_5 xerogel, its physicochemical properties and lithium ion redox intercalation are reported. The synthesis of PEO/V_2O_5 composites is achieved by simply mixing aqueous solutions of PEO with aqueous V_2O_5 gels. After slow water evaporation, a PEO/V_2O_5 intercalate is formed. Various phases of PEO/V_2O_5 composites are obtained by just changing the stoichiometric conditions. The interlayer distance of $PEO_xV_2O_5 \cdot nH_2O$ varies from 13.2 Å, at $x = 0.5$ to 16.8 Å at $x = 1.0$, to 17.6 Å at $1 < x < 3$, and to 18.3 Å at $x \geq 3$. However, bulk PEO phase is found when $x > 2.0$. One-dimensional electron density calculations based on X-ray diffraction data (perpendicular to layers) show that the composites contain a monolayer of PEO molecules when $x < 1$ and bilayers when $x \geq 1$. The conformation of PEO chains between the layers is a planar zigzag. These intercalation compounds are water swellable and light sensitive. The photo-induced reaction dramatically changes the electronic structure of V_2O_5 which results in enhanced electrical conductivity and decreased solubility. The conductivity decreases as the PEO content increases. The thermopower data and increased magnetic susceptibility of the irradiated products are consistent with the increased V^{4+} concentration and a n-type semiconductor. By reaction with lithium iodide, the PEO/V_2O_5 composites can be intercalated with lithium. Variable temperature ^7Li solid state NMR studies of the Li/PEO/V_2O_5 materials are reported.

2.1. Introduction

In recent years, the synthesis of polymer/inorganic nanocomposites has received considerable attention[1-3]. These materials, in principle, can possess electrical, optical and mechanical properties which may not be achieved with each component separately. V_2O_5 xerogel is a very reactive layered host material.[4] It can be intercalated by either cation-exchange, acid-base chemistry and redox reactions. In the past several years, we have reported that monomers (i.e. aniline, pyrrole and bithiophene) can be oxidatively polymerized and intercalated into the intralamellar space of the host.[5] Recently, we successfully used the swelling properties of the gels in water to open a way to directly intercalate water-soluble polymers[6] such as poly(ethylene-oxide) (PEO).

PEO has the simplest structure of water-soluble polymers. Its complexes with salts can be solid electrolytes and have attracted considerable research attention because they are promising for applications in solid state batteries and electrochromic devices.[7] Systematic studies of ionic conductivity versus composition and temperature for various salts have been extensively investigated. However, the studies of the PEO complex inside a constrained environment such as the galleries of 2-D inorganic hosts were comparatively rare.[8-11] Ruiz-Hitzky *et al.* reported that phyllosilicates containing Li^+ and Na^+ ions can act as host materials for PEO intercalation.[8] The resulting materials show higher ionic conductivities than those for the parent alkali-exchanged silicates. The similar method was also applied to layered transition metal chalcogenides, MPS_3 (M = Mn, Cd).[9] Recently, encapsulation of PEO into MoS_2 was accomplished by taking advantage of the exfoliation property of this

dichalcogenide.[10,11] This intercalation compound showed very high electrical conductivity (0.1 S/cm) due to structural distortion of MoS_2.

Preliminary results for $(PEO)_{0.5}V_2O_5 \cdot nH_2O$ phases have been reported earlier.[6a] The composite material showed interesting photo-sensitivity and could accept Li^+ ions in the framework by the redox reaction with LiI. Further investigation led to the synthesis of several PEO/V_2O_5 phases with varying polymer loading. Here, we report the synthesis, structural characterization and systematic investigation of the chemical and physical properties as a function of PEO loading. We also report the synthesis of Li^+ intercalated phases and the studies of their properties by ^7Li NMR spectroscopy.

2.2. Experimental Section

2.2.1. Materials

Poly(ethylene-oxide), with molecular weight (MW) of $1x10^5$ and $5x10^6$, LiI and $NaVO_3$ were purchased from Aldrich Chemical Co., Milwaukee, WI and were used without further purification.

2.2.2. Measurements

Infrared spectra were collected from 4000 to 400 cm^{-1} with a resolution of 4 cm^{-1} on a Nicolet 740 FT-IR spectrometer. Samples were recorded in pressed KBr matrixes or as free standing films under N_2 flow.

X-ray diffraction was carried out on a Rigaku rotating anode X-ray powder diffractometer, Rigaku-Denki/RW400F2 (Rotaflex), at 45KV and 100mA with a scintillation counter detector and a graphite monochromator to yield Cu Kα (wavelength 1.54184 Å) radiation. Data were collected at

room temperature over the range $2° \leq 2\theta \leq 100°$ in increments of 0.01°. Samples were directly coated on X-ray sample slides for reflection mode measurements. For transmission mode measurements, composite films were taped on a sample slide with a hole in the center. The sample slide was perpendicular to the X-ray beam and the detector collected data from 2° to 60° in 2θ with a speed of 1°/min. The coherence length was determined from the half width of peaks using the Scherrer formula[12] :

$$L_{hkl} = K\lambda/B\cos\theta$$

L is the coherence length along the Miller indices (hkl), λ is the wavelength of the X-rays used, K is Scherrer's constant and has a value of 0.9, θ is the Bragg angle, and B is the peak width at half-height in radians.

Thermogravimetric analysis (TGA) was performed on a Shimadzu TGA-50. Typically 5-10 mg of sample was heated in a quartz crucible in air from room temperature to 1000°C at the rate of 5°C/min.

Electron Paramagnetic Resonance (EPR) spectroscopy was obtained using a Varian E-4 spectrometer operating at 9.5 GHz (X band) and at room temperature. Solid samples were scanned from 2700 to 3700 gauss at 8 gauss field modulation and 0.03 second time constant. The g value was obtained with reference to the standard diphenylpycrilhydrazine (DPPH).

Magnetic susceptibility measurements were done on a MPMS Quantum Design SQUID system (Superconducting Quantum Interference Device) with a magnetic field of 5000 gauss. A known quantity of sample was placed in a plastic bag and purged with Ar gas. Data were collected with an ascending ramp from 5K to 300K and then corrected for the diamagnetic components which were obtained from the literature.[13]

Scanning Electron Microscopy (SEM) was done with JEOL-JSM 35 CF microscope at an accelerating voltage of 20 KV. Samples were glued to

the microscopic sample holder with conducting graphite paint.

Direct-current electrical conductivity and thermopower measurements were performed in the usual four-probe geometry with 60 mm and 25 mm gold wires used for the current and voltage electrodes respectively.[14] Thermoelectric power measurements were made by using a slow ac technique with 60 mm gold wires serving to support and conduct heat to the sample, as well as to measure the voltage across the sample resulting from the applied temperature gradient.[15]

Optical diffuse reflectance spectra were measured at room temperature with a Shimadzu UV-3101PC double beam, double monochromator spectrophotometer. Samples were placed above $BaSO_4$ on a sample holder. $BaSO_4$ powder was used as a reference. The absorption spectrum was calculated from the reflectance data using the Kubelka-Munk function: $\alpha/S=(1-R)^2/2R$. R is the reflectance, α is the absorption coefficient and S is the scattering coefficient which is practically wavelength independent when the particle size is larger than 5 μm.[16]

^{7}Li NMR spectra were recorded on a Varian 400 MHz instrument using a wide line Varian probe equipped with a variable temperature (VT) control, at a frequency of 155.45 MHz. All samples were run with a repetition delay time of 1 sec with typical 90° pulse of 2.8 μs.

One-dimensional Patterson function and electron density (ED) calculations were based on the X-ray reflection data. Six *00l* reflections were used for the V_2O_5 xerogel out to d_{008} = 1.43 Å, ten reflections were used for $(PEO)_{0.5}V_2O_5{\cdot}nH_2O$ out to d_{0010} = 1.35, twelve reflections were used for $(PEO)_{1.0}V_2O_5{\cdot}nH_2O$ out to d_{0013} = 1.34 and eleven reflections were used for $(PEO)_{1.5}V_2O_5{\cdot}nH_2O$ out to d_{0012} = 1.42 Å. The intensities were obtained from the integrated peak areas. The structure factors, *F*, of

these reflections were derived from their intensities and corrected by Lorentz-polarization effects, see eq (2.1)

$$|F(l)| = (I/Lp)^{1/2} \tag{2.1}$$

where I is the peak intensity and Lp is Lorentz-polarization effects.

$$Lp = (1+\cos^2 2\theta)/(\sin^2\theta\cos\theta) \tag{2.2}$$

The $|F(l)|^2$ values for V_2O_5 xerogel, $PEO_{0.5}V_2O_5{\cdot}nH_2O$, $PEO_{1.0}V_2O_5{\cdot}nH_2O$ and $PEO_{1.5}V_2O_5{\cdot}nH_2O$ are shown in Tables 2.1, 2.2, 2.3 and 2.4, respectively. The 1-D Patterson functions were calculated according to eq (2.3).

$$P(z) = 2/c \sum_{l} |F(l)|^2 \cos(2\pi l z) \tag{2.3}$$

The functions were synthesized from z = 0.0 to 1.0 in increments of 0.01 for all materials.

The signs of the structure factors were directly obtained from the scattering contributions of the V_2O_5 framework. This assumes that the scattering contribution from the intercalated PEO is relatively small. The structure factors for the V_2O_5 framework alone were calculated as follows. Atomic scattering factors for vanadium and oxygen were determined by eq (2.4)

$$f(\theta) = [\sum_{i=1}^{4} a_i \exp(-b_i\lambda^{-2} \sin^2\theta) + c\,] \exp(-B \sin^2\theta / \lambda^2) \tag{2.4}$$

Table 2.1. X-ray Diffraction Data and $|F(l)|^2$ for $V_2O_5 \cdot nH_2O$ xerogel

(hkl)	d(obsd). (Å)	d(calcd). (Å)	Intensity (count)	$\|F(l)\|^2$
001	11.41	11.41	18566	42.58
003	3.81	3.81	1707	37.08
004	2.86	2.86	552	22.28
005	2.29	2.29	458	30.52
007	1.63	1.64	58	8.73
008	1.44	1.43	54	11.11

Table 2.2. X-ray Diffraction Data and $|F(l)|^2$ for $(PEO)_{0.5}V_2O_5 \cdot nH_2O$

(hkl)	$d_{(obsed)}$ (Å)	$d_{(calcd)}$ (Å)	Intensity (count)	$\|F(l)\|^2$
001	13.22	13.25	28892	49.285
002	6.70	6.63	1820	12.262
003	4.44	4.43	2708	42.617
004	3.33	3.33	1188	34.381
005	2.67	2.67	997	46.832
006	2.22	2.23	568	40.539
007	1.92	1.91	45	4.548
008	1.66	1.68	93	13.366
009	1.48	1.49	87	16.651
0010	1.33	1.35	31	7.630

Table 2.3. X-ray Diffraction Data and $|F(l)|^2$ for $(PEO)_{1.0}V_2O_5 \cdot nH_2O$

(hkl)	$d_{(obsed)}$ (Å)	$d_{(calcd)}$ (Å)	Intensity (count)	$\|F(l)\|^2$
001	16.80	16.86	5.587e+5	588.69
002	8.56	8.45	1.177e+5	481.72
004	4.28	4.25	6.350e+4	1077.40
005	3.42	3.41	3.239e+4	887.83
006	2.84	2.85	2.738e+4	1121.20
007	2.44	2.44	2.323e+4	1333.10
008	2.14	2.14	1.365e+4	1064.60
009	1.90	1.91	3.000e+3	310.22
0010	1.70	1.72	4.914e+3	667.31
0011	1.55	1.57	8.049e+3	1368.20
0012	1.43	1.44	3.635e+3	760.91
0013	1.32	1.34	1.258e+3	317.49

Table 2.4. X-ray Diffraction Data and $|F(l)|^2$ for $(PEO)_{1.5}V_2O_5 \cdot nH_2O$

(hkl)	$d_{(obsed)}$ (Å)	$d_{(calcd)}$ (Å)	Intensity (count)	$\|F(l)\|^2$
001	17.58	17.56	2.269e+6	2181.7
002	8.74	8.75	5.516e+5	2166.2
004	4.27	4.34	2.334e+5	3988.4
005	3.44	3.46	1.184e+5	3188.2
006	2.87	2.88	8.289e+4	3320.5
007	2.46	2.46	8.596e+4	4845.7
008	2.15	2.14	3.434e+4	2640.8
009	1.90	1.90	6.001e+3	617.6
0010	1.71	1.70	5.954e+3	793.6
0011	1.56	1.54	1.217e+4	2029.3
0012	1.44	1.42	9.282e+3	1884.5

where the values of a_i, b_i and c for each element were obtained from the literature.[17] B is a temperature parameter and assumed to be 2.0 for every element. The structure factors were calculated according to eq (2.5)

$$F(l) = \sum_{j=1}^{N} 2f_j \cos(2\pi l z_j) \qquad (2.5)$$

where f_j is the scattering factor of j atom (obtained from eq (2.4)) and z_j is its fractional coordinate on the c-axis. Here, Oka's model was used. The fractional coordinates (z_j) of V and O in the V_2O_5 framework are shown in Table 2.5.

Table 2.5. z Parameters of V and O for the PEO/V_2O_5 Compounds

	z parameter	
	$VO_{1.5}$ sheet	O sheet
$PEO_{1.0}V_2O_5 \cdot nH_2O$	0.0833	0.179
$PEO_{1.5}V_2O_5 \cdot nH_2O$	0.0796	0.171

The $F(l)_{calcd}$ values for $PEO_{1.0}V_2O_5 \cdot nH_2O$ and $PEO_{1.5}V_2O_5 \cdot nH_2O$ are shown in Tables 2.6 and 2.7, respectively. The 1-D electron densities were obtained from eq (2.6).

$$\rho(z) = (1/L)\,[F_0 + 2\sum_{l} F_l \cos(2\pi l z)] \qquad (2.6)$$

L is the length of the repeat unit and F_0 is the zeroth-order structure factor. The electron densities of the PEO/V_2O_5 materials were calculated

Table 2.6. Observed and Calculated Structure Factors for $(PEO)_{1.0}V_2O_5 \cdot nH_2O$

(hkl)	$\|F(l)\|_{(obsd)}$*	$F(l)^a_{(calcd)}$	$F(l)^b_{(calcd)}$
001	10.676	25.662	21.970
002	9.657	2.844	9.433
004	14.442	-11.629	-12.311
005	13.110	-17.245	-13.023
006	14.733	-12.758	-15.905
007	16.065	-15.866	-15.581
008	14.357	-10.739	-10.050
009	7.750	2.463	3.034
0010	11.366	5.745	3.981
0011	16.276	4.248	5.708
0012	12.137	4.224	4.024
0013	7.840	2.586	1.934

[a] Includes scattering of V_2O_5 only. [b] Includes contributions of V_2O_5 and PEO; R = 0.38, K = 0.44. R calculated as $R = \sum(|K|F_o|-|F_c||)/\sum(K|F_o|)$.
*Corrected by K.

Table 2.7. Observed and Calculated Structure Factors for $(PEO)_{1.5}V_2O_5 \cdot nH_2O$

(hkl)	$\|F(l)\|_{(obsd)}$*	$F(l)^a_{(calcd)}$	$F(l)^b_{(calcd)}$
001	11.210	30.451	19.171
002	11.170	10.002	12.183
004	15.157	-9.513	-12.670
005	13.551	-11.794	-11.794
006	13.830	-15.177	-13.937
007	16.707	-16.060	-15.621
008	12.333	-11.003	-13.748
009	5.965	-2.713	0.647
0010	6.761	3.361	1.197
0011	10.812	5.147	5.626
0012	10.419	4.201	4.731

[a] Includes scattering of V_2O_5 only. [b] Includes contributions of V_2O_5 and PEO; R = 0.293, K = 0.24. *Corrected by K.

by using t

from the A

-0.2 to 1

checked t

contribut

amounts

possible

molecu

of (PE

Namel

not co

meta

The

exc

Up

A

by using the $|F(l)|_{obsd}$, obtained from eq (2.1), with the signs, obtained from the $F(l)_{calcd}$. The electron density maps were synthesized from z = -0.2 to 1.2 in increments of 0.01. The signs of the phases were also checked by recalculation of the electron densities, including the scattering contributions of the PEO molecules. In the recalculation, the exact amounts of PEO molecules (based on elemental analysis) with different possible conformations and positions were used. Before and after the PEO molecules were included, the signs of the phases were consistent in the case of $(PEO)_{1.0}V_2O_5 \cdot nH_2O$, but slightly different in $(PEO)_{1.5}V_2O_5 \cdot nH_2O$. Namely, one reflection sign changed in $(PEO)_{1.5}V_2O_5 \cdot nH_2O$ but this did not consequently change the ED pattern.

2.2.3. Preparation of V_2O_5 Xerogel

V_2O_5 xerogel was prepared by a reported method.[18] Sodium metavanadate, 4 g (32.8 mmol) was dissolved in 250 ml of distilled water. The resulting solution was eluted through a column packed with H^+ ion-exchange resin (Dowex-50X2-100) forming a pale-orange solution HVO_3. Upon standing, the HVO_3 polymerized to a red V_2O_5 gel in several days. After evaporation of excess water, a film of V_2O_5 xerogel was formed.

2.2.4. Preparation of $(PEO)_xV_2O_5 \cdot nH_2O$

Aqueous solutions of 0.01 M V_2O_5 gels mixed with a stoichiometric amount of PEO (M.W.= $1x10^5$), were stirred overnight in the dark. The PEO/V_2O_5 molar ratio was varied from 0.5 to 5.0 in increments of 0.5. The resulting red mixture was cast into a film by evaporation of water at room temperature on a flat surface without further washing. High molecular weight PEO (MW = $5x10^6$) was also used and gave rise to

similar in

molecula

2.

A

light so

exposed

in CH

and c

by S

were

2.3

1

c

r

I

similar intercalation compounds. Most data on this paper were from low molecular weight PEO.

2.2.5. Photoreaction of $(PEO)_xV_2O_5 \cdot nH_2O$

A medium-pressure Hg lamp filtered by Pyrex glass was used as a light source. $PEO_xV_2O_5 \cdot nH_2O$ films coated on a piece of glass slide were exposed to this light source in air for 12 hours.

2.2.6. Preparation of $Li_y(PEO)_xV_2O_5 \cdot nH_2O$

An amount of 0.5 g of $PEO_xV_2O_5$ film reacted with 2 equivalent LiI in CH_3CN for 3 days. The resulting blue product was washed with CH_3CN and dried in air. No trace of iodine or iodide were detected in the product by SEM/EDS microprobe analysis. The compositions of these materials were determined by elemental analysis.

2.3. Results and Discussion

2.3.1. Structure of V_2O_5 Xerogel

V_2O_5 xerogel is a lamellar material with an interlayer distance of 11.5 Å. Livage *et al.* proposed that the V_2O_5 layers are composed of corrugated ribbons with a step of 2.8 Å,[19] see Figure 2.1a, and the intra-ribbon structure is closely related to single layers of orthorhombic V_2O_5. Recently, Oka *et al.* proposed a different structure in which the layers consist of two V_2O_5 sheets facing each other at a distance of 2.8 Å according to the structure of $M_xV_2O_5$[20] (M = Na, K) as shown in Figure 2.1b. Most studies reported to date seem to prefer Livage's model.[4,19] However, density measurements for $V_2O_5 \cdot 1.08DMSO$ and

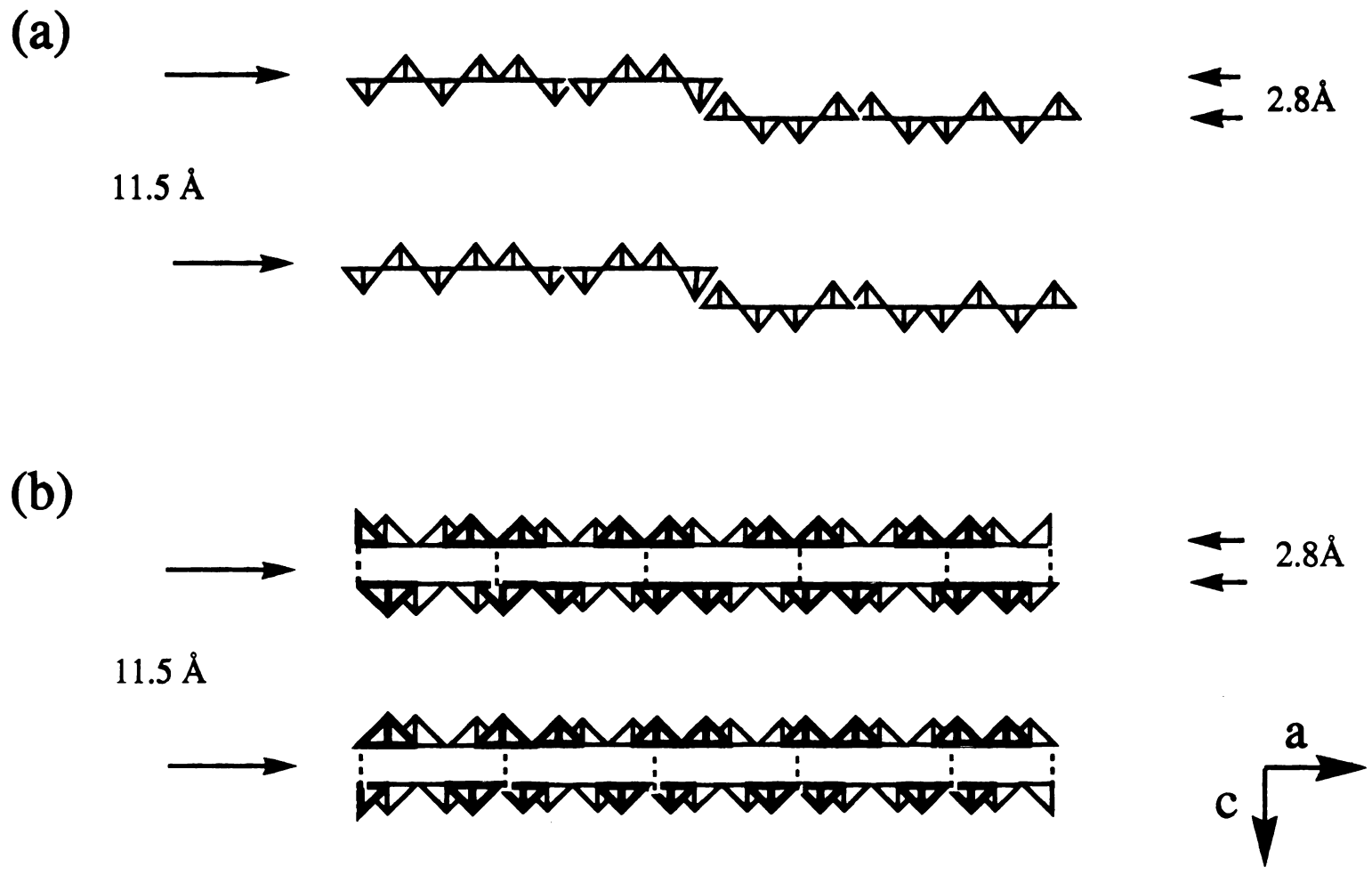

Figure 2.1. Schematic illustration of the proposed structure of V_2O_5 xerogel projected onto the ac plane : (a) from Livage *et al.*, (b) from Oka *et al.*

$(PEO)_{1.0}V_2O_5{\cdot}0.7H_2O$, shown in Table 2.8, are consistent with Oka's model.

2.3.2. Characterization of $(PEO)_xV_2O_5{\cdot}nH_2O$ Phases

A series of $(PEO)_xV_2O_5{\cdot}nH_2O$ nanocomposite intercalates with x = 0.5 to 5.0 were prepared. Depending on x, several phases were identified by the X-ray diffraction. Figure 2.2 shows typical X-ray diffraction patterns in which *00l* reflections dominate. The phase with x = 0.5 has been reported with an interlayer spacing of 13.2 Å. As x increases , the interlayer distance increases from 16.8 Å at x = 1.0 to 18.3 Å at x = 5 as summarized in Table 2.9. The net V_2O_5 interlayer expansion is from 4.5 Å at x = 0.5 to 9.6 Å at x = 5.0. The coherence length along the layer stacking direction, as estimated from the Scherrer formula, decreases from 90 Å when x = 0.5 to 60 Å when x = 4. Scanning electron micrographs of these PEO/V_2O_5 composites are shown in Figure 2.3. After intercalation, the surface becomes distinctly corrugated, consistent with the decreased crystallinity. Compared with V_2O_5 xerogel, these composite films show much improved mechanical flexibility which becomes more noticeable as the PEO content increases. All of the phases absorb moisture reversibly which causes a further 2 Å expansion in the interlayer distance. However, these highly hydrated forms of $(PEO)_xV_2O_5{\cdot}nH_2O$ show poor crystallinity or consist of mixed phases. Materials with high MW PEO ($5.0x10^6$) were also prepared and they generally show an improved crystallinity in the layer stacking direction. For example, the coherence length of $(PEO)_{0.5}V_2O_5{\cdot}nH_2O$ increases to 112 Å, a value higher than that of V_2O_5 xerogel itself.

Even though a large amount of PEO can be intercalated, in fact,

Table 2.8. Calculated and Measured Densities for $(DMSO)_{1.08}V_2O_5$ and $(PEO)_{1.0}V_2O_5 \cdot 0.7H_2O$.

	Density (g/cm^3)		
Compound	Livage	Oka	Measured value
$V_2O_5 \cdot 1.08DMSO$*	1.18	2.35	2.25
$(PEO)_{1.0}V_2O_5 \cdot 0.7H_2O$	1.1	~2.2	~2.3

*Copy from ref 20.

Figure
(b) (P

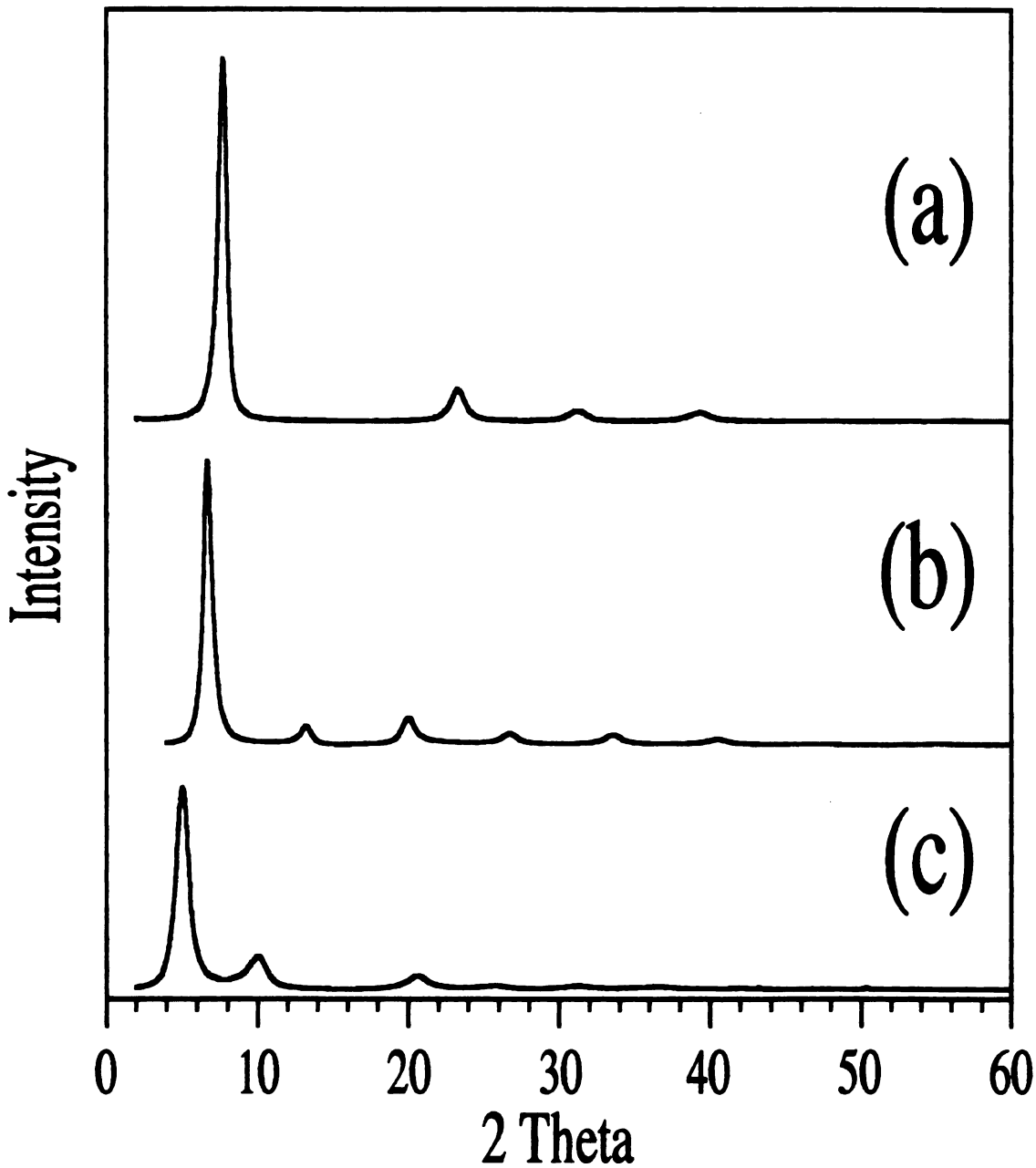

Figure 2.2. X-ray powder diffraction patterns of films of (a) V_2O_5 xerogel, (b) $(PEO)_{0.5}V_2O_5{\cdot}nH_2O$ and (c) $(PEO)_{1.5}V_2O_5{\cdot}nH_2O$.

Table 2.9. Summary of Interlayer Distance, Net Expansion and Coherence Length for $(PEO)_xV_2O_5 \cdot nH_2O$

Molar ratio (PEO/V_2O_5)	Interlayer distance (Å)	Net expansion[1] (Å)	Coherence length[2] (Å)
0*	11.5	2.8	100
0.5	13.2	4.5	90
0.8	13.2	4.5	90
1.0	16.8	6.9	88
1.2	17.2	8.5	70
1.4	17.4	8.7	77
1.5	17.6	8.9	75
2.0	17.6	8.9	75
2.5	17.6	8.9	70
3.0	~18.3	9.6	65
4.0	~18.3	9.6	60
5.0	~18.3	9.6	60

[1]The thickness of the V_2O_5 layer is 8.7 Å. [2]Along the layer stacking axis.

*V_2O_5 xerogel.

a) *n* is ~1-1.6 for the phases with $x < 1$ and 0.5-1.0 for the phases with $x \geq 1$.

(A)

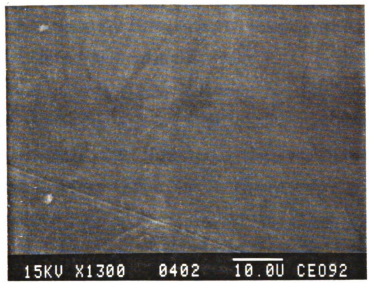

(B)

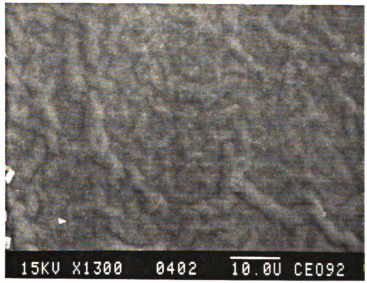

Figure 2.3..Scanning Electron Micrographs of (a) V_2O_5 xerogel (b) $(PEO)_{0.5}V_2O_5 \cdot nH_2O$.

when the PEO/V_2O_5 molar ratio reaches five, considerable amount of PEO was found outside the layers as a separated phase. We observed bulk crystalline PEO by X-ray diffraction. By washing out the excess PEO with CH_3CN, we found that materials with $x < 2$ show no significant composition changes by TGA, indicating no significant amount of un-intercalated PEO. For $x \geq 2$, after washing, the final product always shows x in a range of ~2.0. However, washing also decreases the interlayer spacing from 18.3 Å to 17.5 Å, for the phases with $x > 2.5$, implying that some intercalated PEO might be washed out. Thus, we cannot precisely determine the maximal PEO loading in the V_2O_5 framework from the CH_3CN washing experiments. FT-IR spectroscopy indicates that an accumulation of the bulk PEO phase exists from $x > 2$.

After PEO intercalation, the structural integrity of the V_2O_5 framework is maintained as confirmed by the infrared spectroscopic data and X-ray diffraction. Three strong vibrations at 1010, 750, and 570 cm^{-1}, due to the framework, and two intense electronic UV/Vis transitions at 270 nm and 380 nm, due to the ligand-to-metal electron transfer, were observed. These values are nearly identical to those of V_2O_5 xerogel.[18,21] However, the intercalated PEO shows some structural modifications. In the region of the CH_2 stretching absorption, a strong band at 2880 cm^{-1} and two weak bands at lower wavenumber observed in bulk PEO, change into two well-defined bands at 2910 and 2878 cm^{-1}. In the region of 1500 to 1100 cm^{-1}, no significant energy shifts are observed, but the relative intensities between absorptions are different and the band shapes become broader. Below 1100 cm^{-1}, the absorptions are mainly shielded by the strong vibrations of the V_2O_5 framework. These small but significant changes are due to steric interactions between the confined PEO and the

framew

B

on sub

contains

plane st

that the

of V_2O

intercal

structu

2

S

to scatt

to dete

axis.

and ele

structu

correct

determi

specific

polyme

one-din

are sho

functior

c-axis.

at 2.8 Å

(projecte

framework.

Because of the preferred orientation of PEO/V_2O_5 composite films on substrates, X-ray diffraction in the regular reflection mode only contains the *00l* set of reflections. The *hk0* set, which derives from the in-plane structure, can be only observed in the transmission mode. We found that the transmission patterns of all PEO/V_2O_5 phases are identical with that of V_2O_5 xerogel, as shown in Figure 2.4. This further confirms that the intercalation is topotactic and does not disrupt the two-dimensional V_2O_5 structure.

2.3.3. Structure of $(PEO)_xV_2O_5.nH_2O$

Since a relatively large number of *00l* reflections are observed due to scattering from planes perpendicular to the stacking axis, we attempted to determine the structure of the intercalated species projected on the c-axis. This is possible by calculating one-dimensional Patterson functions and electron-density maps from the observed intensities. Assuming the structural model for the vanadium oxide part of the structure is known and correct, the projection of the PEO structure on the c-axis may be determined from difference electron-density maps. This could yield specific information about the orientation and structure of the intercalated polymer, or at least eliminate certain conformational possibilities. The one-dimensional Patterson functions, calculated from the *00l* reflections, are shown in Figure 2.5 along the layer axis (defined as the c-axis). This function derives from the projected structure of $(PEO)_xV_2O_5{\cdot}nH_2O$ on the c-axis. The 1-D Patterson function of V_2O_5 xerogel itself shows two peaks at 2.8 Å and 4.5 Å. The strong peak at 2.8 Å is assigned to the V-V vector (projected on the c-axis) from two adjacent V_2O_5 layers and the peak at 4.5

Figur
xerog

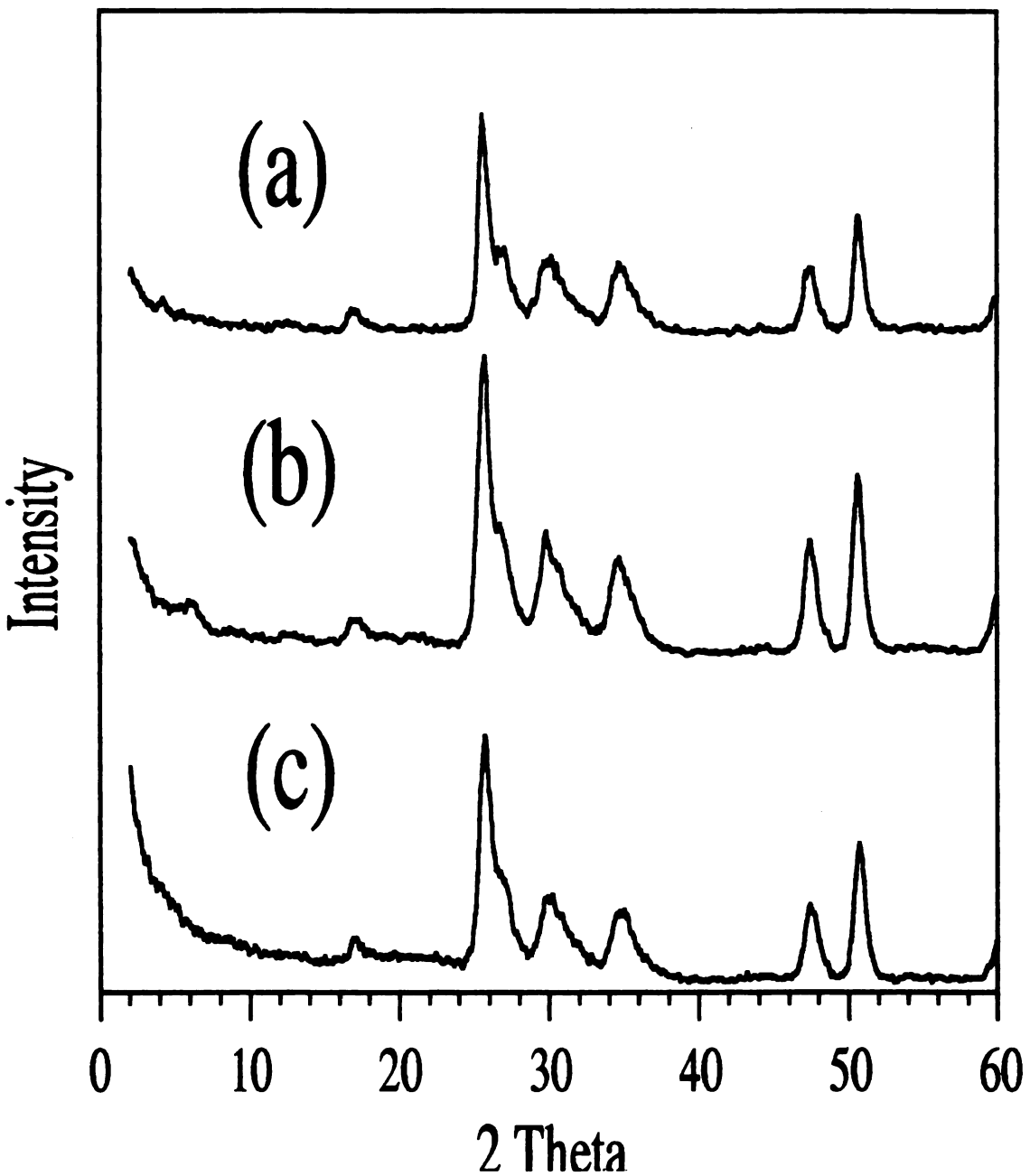

Figure 2.4. Transmission mode of X-ray diffraction patterns for (a) V_2O_5 xerogel, (b) $(PEO)_{0.5}V_2O_5{\cdot}nH_2O$ and (c) $(PEO)_{1.5}V_2O_5{\cdot}nH_2O$.

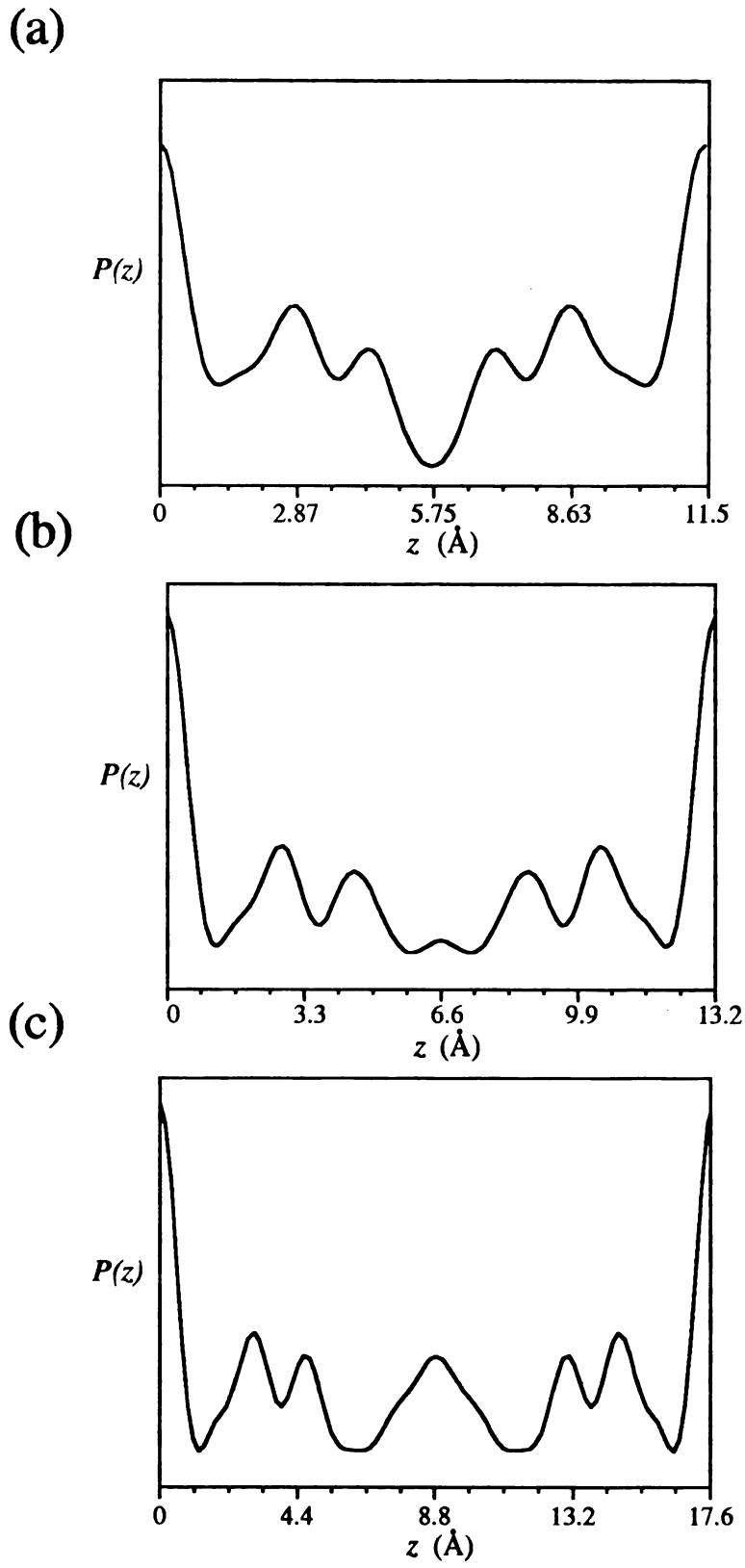

Figure 2.5. One-dimensional Patterson functions along the interlayer c-axis of (a) V_2O_5 xerogel, (b) $(PEO)_{0.5}V_2O_5{\cdot}nH_2O$ and (3) $(PEO)_{1.5}V_2O_5{\cdot}nH_2O$.

À is
PEO
fram
(PE
grad
vect
thes
and
regi
whi
is i
cha

fu
Fi
la
h
A
c
(
I

Å is due to the V-O vector involving oxide atoms and water.[18a] These PEO intercalates preserve the original peaks associated with the V_2O_5 framework and show a new broad peak centered at 6.6 Å for $(PEO)_{0.5}V_2O_5{\cdot}nH_2O$ and 8.8 Å for $(PEO)_{1.5}V_2O_5{\cdot}nH_2O$. Its intensity gradually increases with PEO loading indicating that the peak is due to the vector between vanadium atoms and atoms in PEO. The appearance of these peaks confirms that the internal structure of the V_2O_5 layers is intact and indicates that PEO is positioned at interlayer regions, not at intralayer regions. This agrees with the spectroscopic and X-ray diffraction data which show that the structure of the host is undoubtedly unchanged. This is important in the following 1-D electron density calculations for the characterization of the PEO conformation

In a previous study we showed that the interlayer expansion as a function of PEO content does not vary linearly, but shows plateaus, see Figure 2.6, indicating that the intercalation of PEO is either a layer-by-layer process or subject to a conformation change from a planar zigzag to a helix. For example, $(PEO)_{0.5}V_2O_5{\cdot}nH_2O$ has a net expansion of only 4.5 Å which is too small for a helical structure suggesting that the PEO conformation must be close to a planar zigzag. However, $(PEO)_xV_2O_5{\cdot}nH_2O$ phases with $x \geq 1$ have a net expansion of 8 Å or higher which is compatible either with two layers of polymer chains with a planar zigzag conformation, or one layer of helical PEO. In order to probe the polymer conformation, 1-D electron density (ED) maps were calculated along the layers stacking direction.

Ideally, if PEO has a helical conformation the 1-D ED map along the c-axis should show a broad peak between the layers, see Figure 2.7a. If PEO has a planar-zigzag conformation, the 1-D ED map can show several

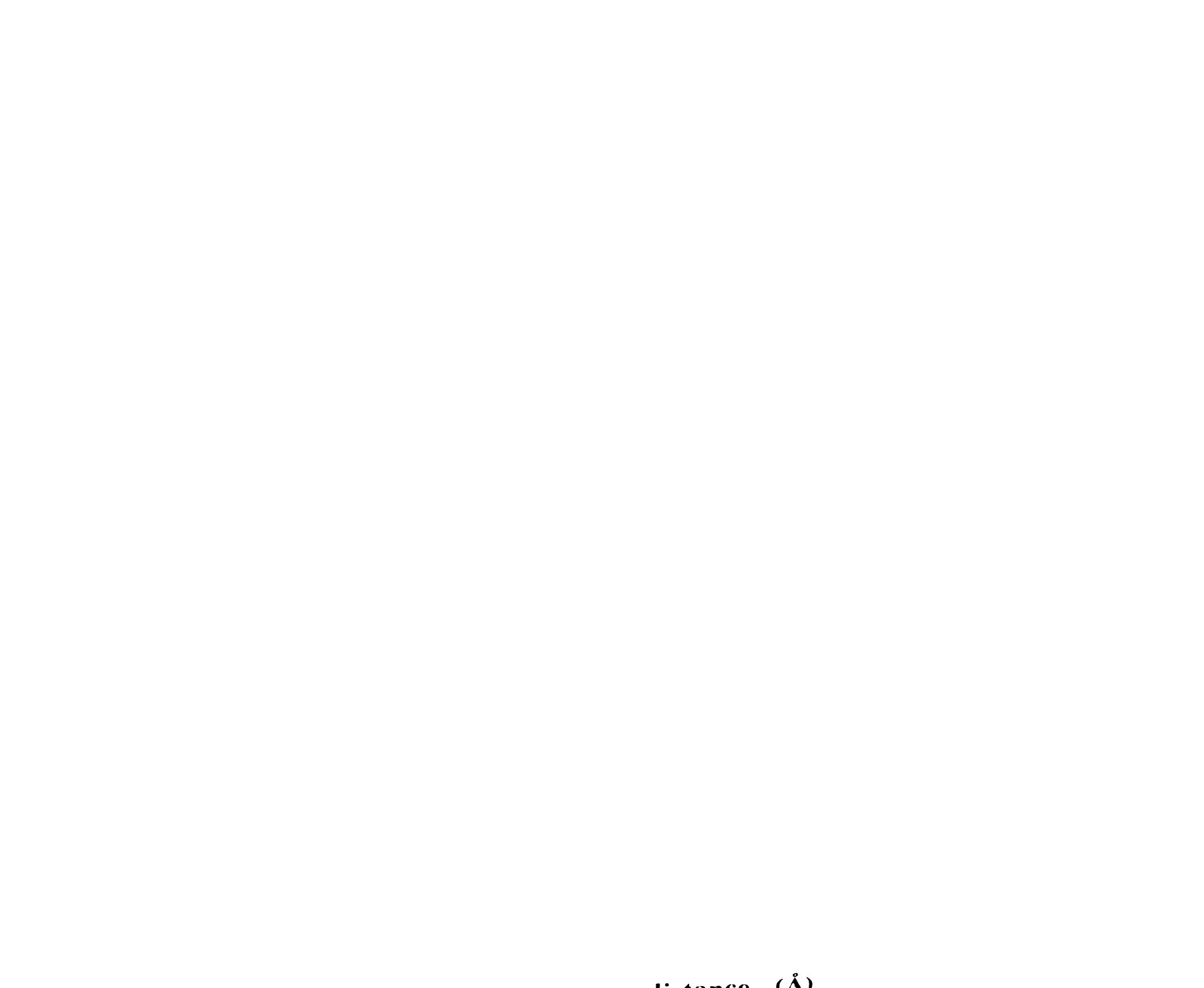
Distance (Å)

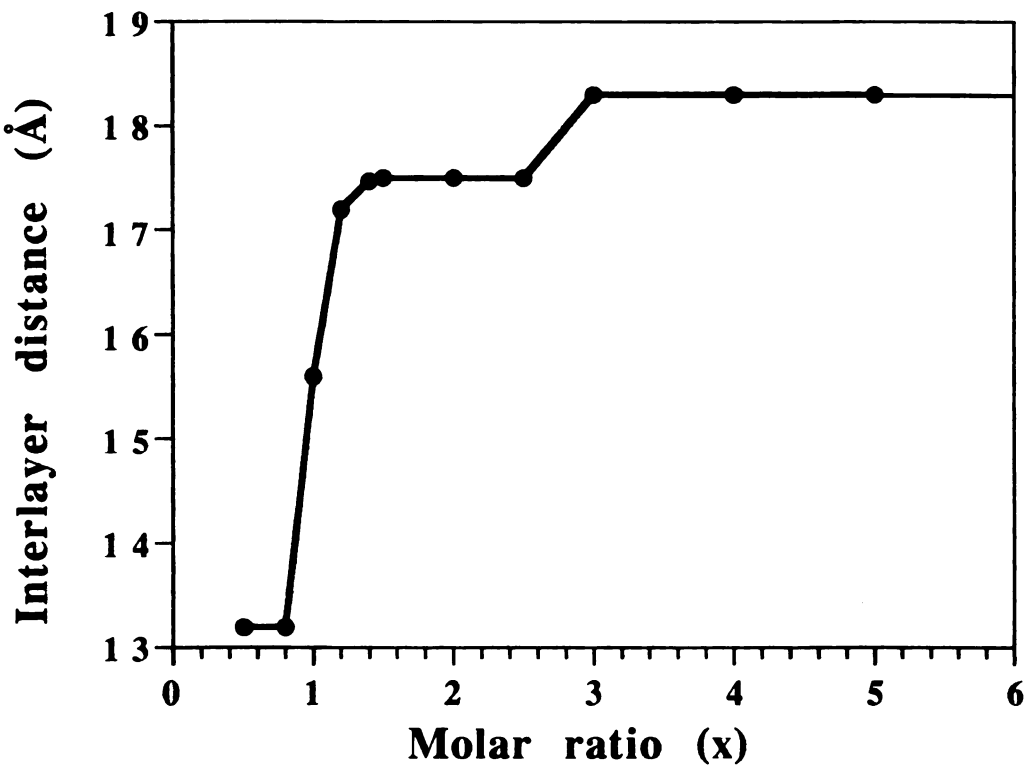

Figure 2.6. Variation of interlayer distance as a function of x for $(PEO)_xV_2O_5{\cdot}nH_2O$.

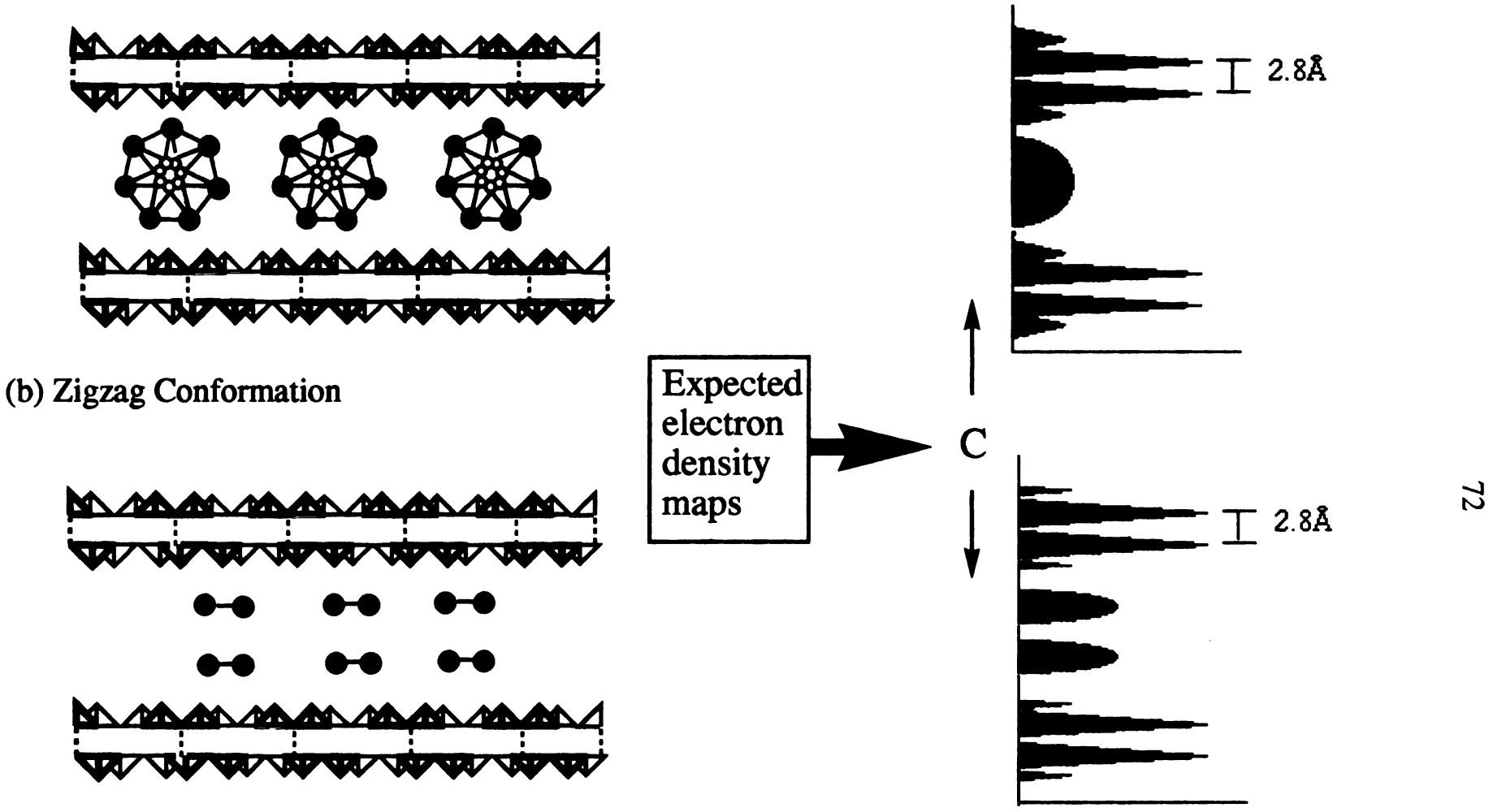

Figure 2.7. Schemes of a helical (a) and planar-zigzag (b) PEO conformation in V_2O_5 framework and their expected electron density projections along the layer stacking direction (depicted from Oka's model).

patterns which depend on the packing arrangement of the polymer chains. For example, if the plane containing the zigzag chain is parallel to the V_2O_5 layer, the 1-D ED map should show two peaks symmetrically disposed from the middle as shown in Figure 2.7b. On the other hand, if the plane is perpendicular to the V_2O_5 sheet, the 1-D ED map should show 4 peaks (Figure 2.8a). In this case, the distance between peaks due to a single polymer chain should be less than 0.9 Å. Another possibility is that the PEO bilayer structure is arranged in a zigzag-like fashion. In this case, 1-D electron density map will also show 4 peaks (Figure 2.8b). Of course, there are still many possibilities. The 1-D ED calculation of $(PEO)_{1.0}V_2O_5{\cdot}nH_2O$ phase, based on Oka's model, is shown in Figure 2.9. As expected, the distance of the adjacent V_2O_5 planes is ~2.8 Å and the V=O bond is ~1.6 Å. Four ED peaks due to PEO are observed between the layers and the average distance between adjacent peaks is ~ 2.0 Å. This suggests that the intercalated PEO has a zigzag bilayer structure and its chain conformation is close to a planar-zigzag[22] as depicted in Figure 2.8b. This PEO conformation is dramatically different from the coil conformation proposed in systems where the intercalation is based on the affinity of PEO toward alkali ions. An attempt to produce helical PEO by additional incorporation of Li salt such as $LiClO_4$ and $LiCF_3SO_3$ in the preparation did not succeed. Based on the X-ray diffraction, the product is a mixture of V_2O_5 and/or PEO/V_2O_5 as well as a Li salt complex with PEO. At low PEO levels, we believe that the driving forces for PEO/V_2O_5 stabilization are van der Waals interactions and hydrogen bonds which are maximized when the polymer is fully extended (i.e. zigzag conformation). The 1-D ED map of $(PEO)_{1.5}V_2O_5{\cdot}nH_2O$ was also calculated and shows a similar pattern with $(PEO)_{1.0}V_2O_5{\cdot}nH_2O$, indicating that the intercalated

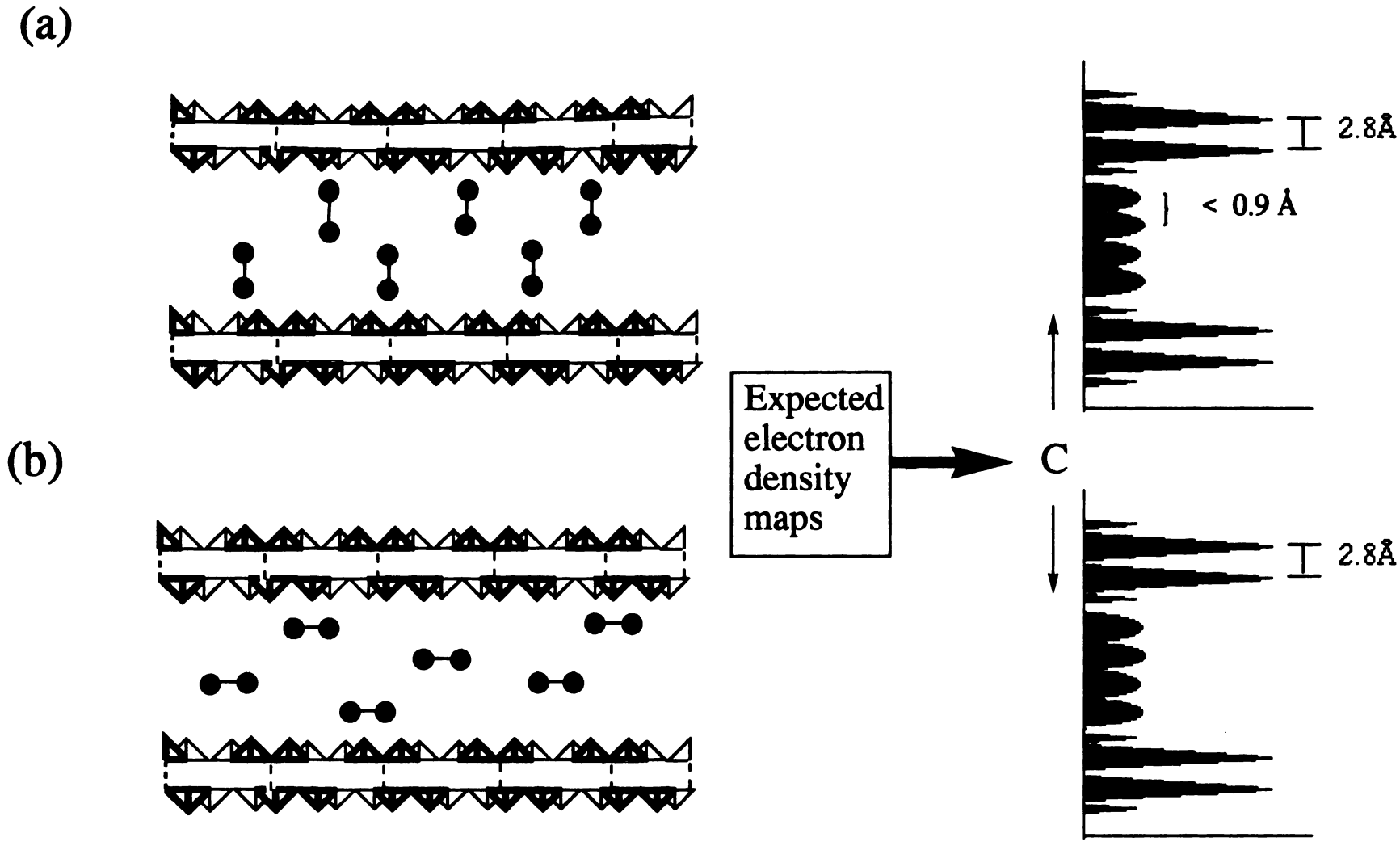

Figure 2.8. Schemes of two arrangements of planar-zigzag PEO chains in V_2O_5 framework and their expected electron density projections along the layer stacking direction : (a) the plane containing the polymer chain perpendicular to the V_2O_5 sheet and (b) the plane parallel to the V_2O_5 sheet and the PEO bilayer structure arranged in a zigzag-like fashion. (View along the polymer chain).

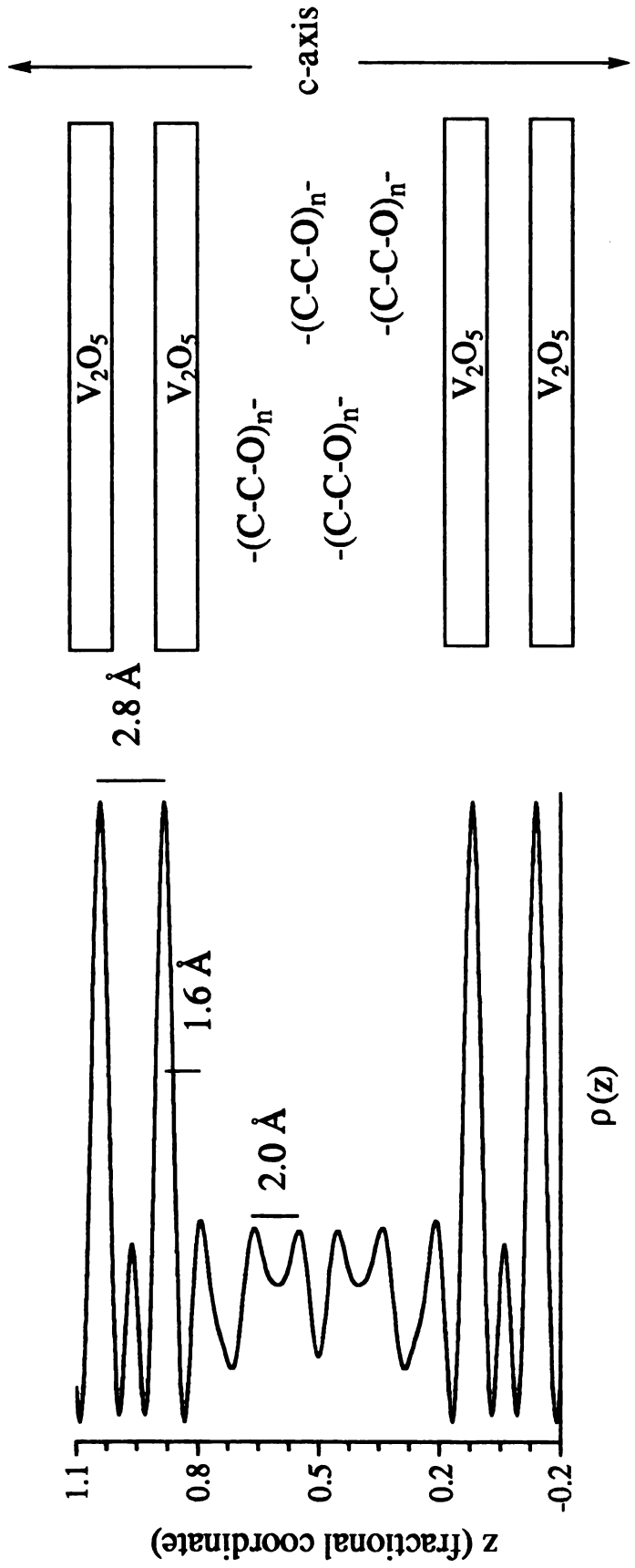

Figure 2.9. Projection of the electron density of $(PEO)_{1.0}V_2O_5{\cdot}nH_2O$ calculated from Oka's model and illustrations of the deduced arrangement of PEO in the interlayer space.

PEO molecules still have a double layer arrangement. The ED calculations of the phases with x > 1.5 are not reliable due to low crystallinity and insufficient numbers of observed reflections. Thus, the PEO intercalation is a layer-by-layer insertion without any conformational change from a zigzag to a helix.

2.3.4. Photoreaction of $(PEO)_xV_2O_5 \cdot nH_2O$

The $(PEO)_xV_2O_5 \cdot nH_2O$ materials are light-sensitive and turn blue when they stand in room light for several weeks. Exposure to a medium-pressure Hg lamp causes the materials to turn blue in an hour. The color change is due to a light-induced redox reaction in which the PEO is oxidized by the vanadium oxide framework. The infrared spectra of irradiated samples show a new very weak absorption around 1700 cm^{-1}, indicating that the PEO molecules probably are oxidized to aldehyde or even acid. The vibration of V=O slightly shifts down to ~ 1000 cm^{-1}, consistent with increased number of V^{4+} centers.[23] Except for these, we do not observe significant changes in the position and shape of infrared absorption peaks of the PEO and vanadium oxide framework, suggesting only minor structural changes in the framework. The irradiation slightly decreases the interlayer spacing, see Table 2.10, due to some water expulsion from the layers caused by the reduction of the V_2O_5 framework which make it more hydrophobic.

The redox nature of the photoreaction is confirmed by the increased magnetic susceptibility and enhanced intensity of the material's EPR signal. Figure 2.10 shows variable-temperature magnetic susceptibility data for fresh and irradiated samples in which the irradiated material shows a higher value than the fresh material. This confirms more V^{4+} centers in

Table 2.10. X-ray Diffraction and Magnetic Data of Irradiated $(PEO)_xV_2O_5 \cdot nH_2O$ Compounds

x	Color	d-spacing decrement (Å)	EPR (gauss)	μ_{eff}[1] (BM)	$\chi_{(TIP)}$† (emu/mole)
0.5	blue	0.2	400*	0.73	1.28×10^{-4}
1.0	blue	2.2	hyperfine	0.81	1.55×10^{-4}
1.5	blue	1.2	hyperfine	0.77	1.36×10^{-4}

*Peak-to-peak width.

†TIP: Temperature Independent Paramagnetism.

[1]μ_{eff} was calculated from $\chi_{(Curie\text{-}Weiss)}$ component.

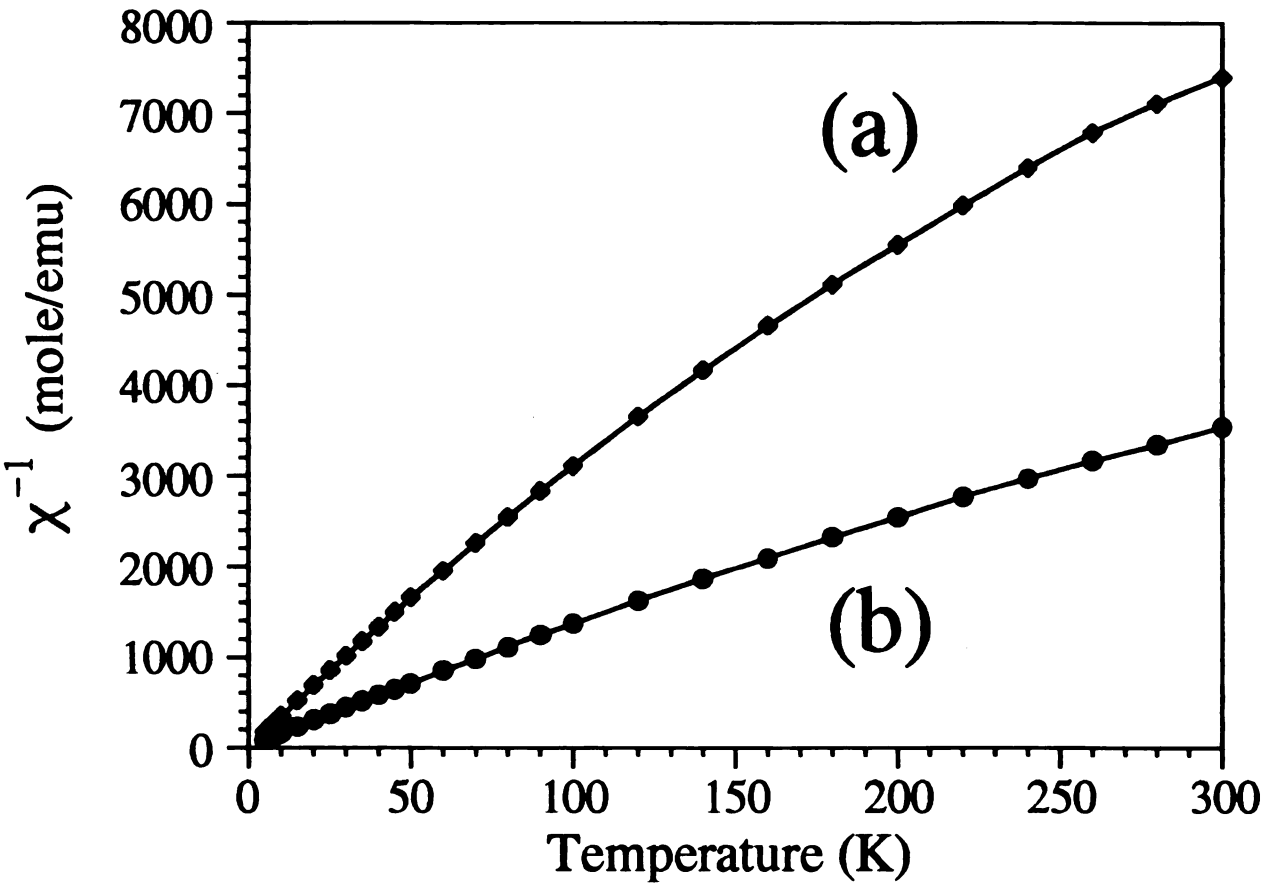

Figure 2.10. Magnetic susceptibility of (a) fresh and (b) irradiated $(PEO)_{0.5}V_2O_5{\cdot}nH_2O$ as a function of temperature.

the framework upon irradiation. The magnetic susceptibility (χ_m) decreased with rising temperature but there is no linear relationship between the inverse χ_m and temperature. We found that the magnetic behavior can be interpreted as Curie-Weiss type with a small amount of van Vleck temperature-independent paramagnetism (TIP),[24] shown in Figure 2.11. The un-irradiated PEO/V_2O_5 compounds have an average μ_{eff} (calculated from $\chi_{(Curie\text{-}Weiss)}$) of ~0.3-0.4 BM at room temperature. After 12 h of irradiation, the μ_{eff} increases to 0.7-0.8 BM because of the increased V^{4+} concentration, see Table 2.10.

Before irradiation, the EPR hyperfine structure is observed in the spectra of PEO/V_2O_5 materials due to $(V{=}O)^{2+}$ impurities (S=1/2, I=7/2) in an axially distorted crystal field.[25] After irradiation, for example in $(PEO)_{0.5}V_2O_5{\cdot}nH_2O$, the increased V^{4+} concentration causes a gradual disappearance of the original hyperfine splitting and a gradual appearance of a broad peak (due to V^{4+}-V^{4+} exchange interactions) as shown in Figure 2.12. The g value is ~1.96. Surprisingly, this is not the case in $(PEO)_xV_2O_5{\cdot}nH_2O$ materials with $x \geq 1$. Even though the μ_{eff} of the PEO-rich materials is slightly higher than that of $PEO_{0.5}V_2O_5{\cdot}nH_2O$, indicating higher V^{4+} concentration in the former, the EPR hyperfine structure still persists, suggesting that the average V^{4+} concentration in the PEO-rich materials is lower than that in $(PEO)_{0.5}V_2O_5{\cdot}nH_2O$. One possible explanation for this is that some of V^{4+} centers, probably in the form of VO^{2+}, diffuse between the layers and are magnetically isolated by coordination to PEO. The existence of VO^{2+} species has been proposed in the reduced V_2O_5 xerogels.[26]

Optical diffuse reflectance spectra of the irradiated materials contain a new very broad absorption band centered at 1400 nm, see Figure 2.13,

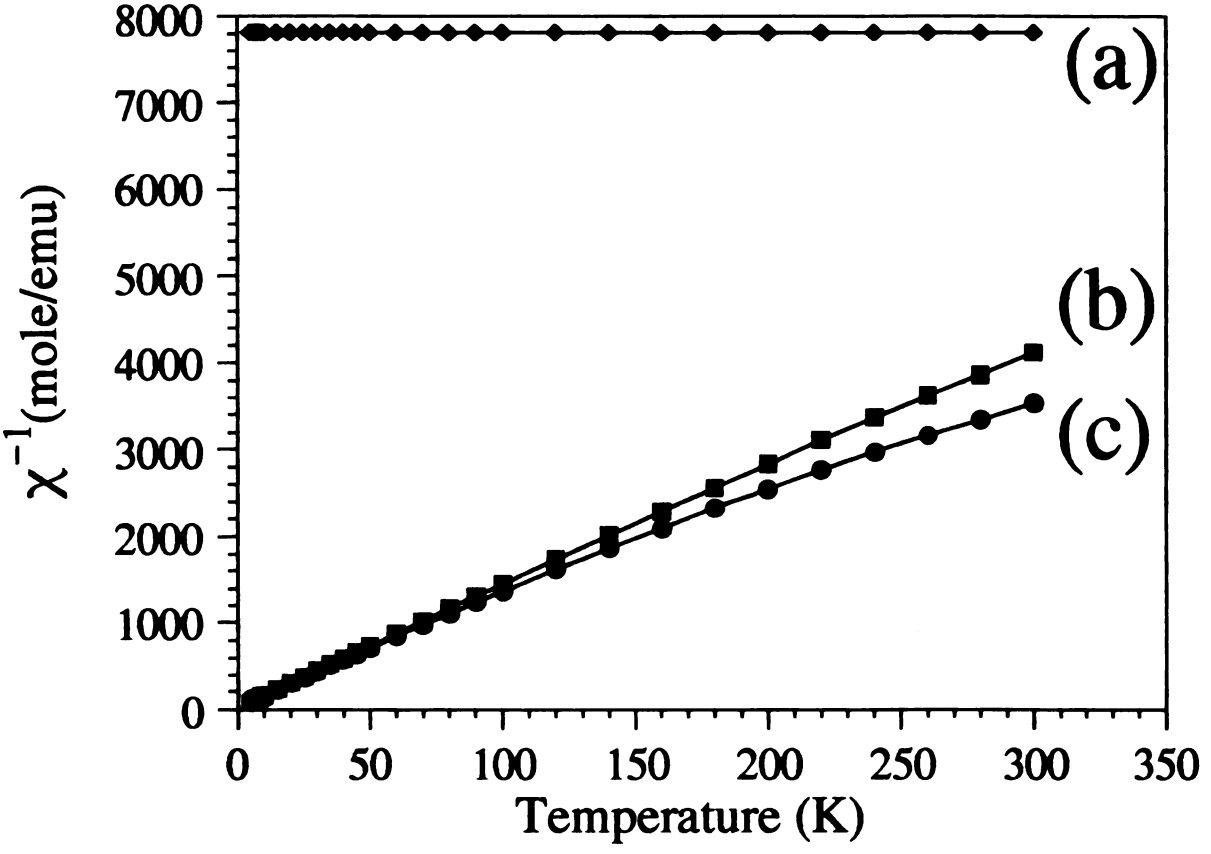

Figure 2.11. Inverse magnetic susceptibility of irradiated $(PEO)_{0.5}V_2O_5{\cdot}nH_2O$ as a function of temperature : (a) $\chi_{(TIP)}$, (b) $\chi_{(Curie\text{-}Weiss)}$ and (c) $\chi_{(measured)}$. ($\chi_{(measured)} = \chi_{(Curie\text{-}Weiss)} + \chi_{(TIP)}$)

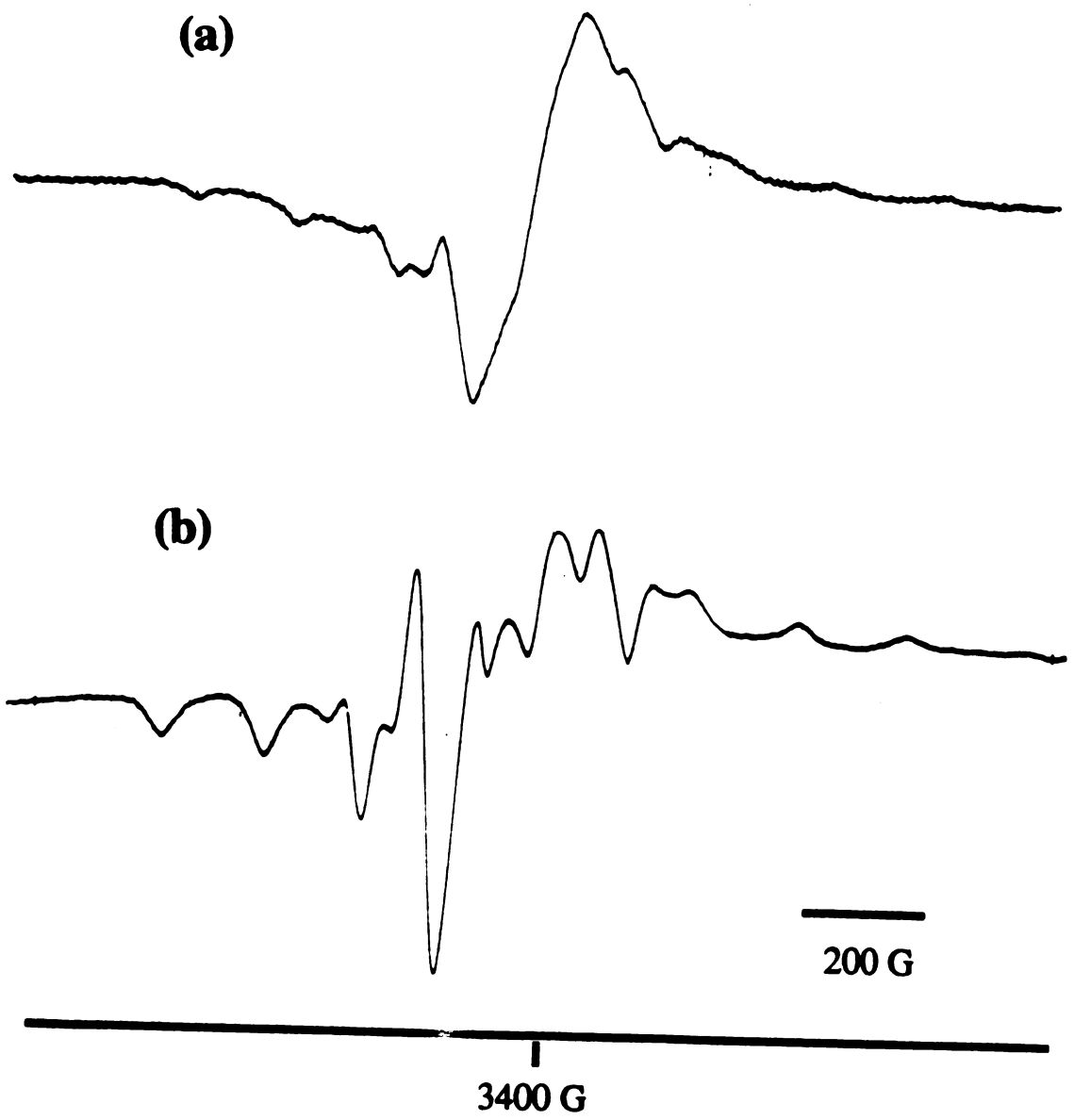

Figure 2.12. Room temperature EPR spectra of irradiated (a) $(PEO)_{0.5}V_2O_5{\cdot}nH_2O$ and (b) $(PEO)_{1.5}V_2O_5{\cdot}nH_2O$.

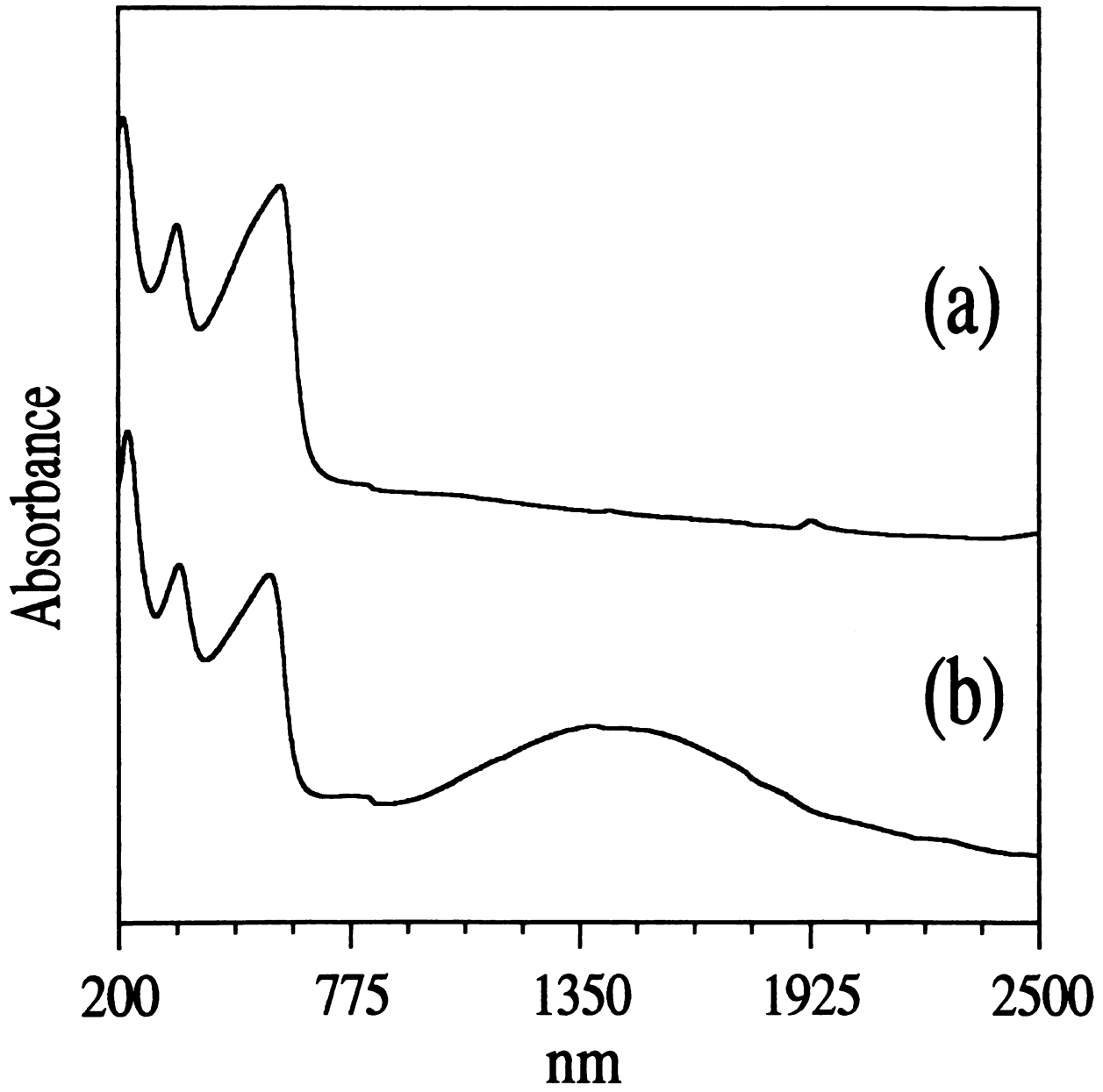

Figure 2.13. Optical absorption spectra of un-irradiated (a) and irradiated (b) $(PEO)_{0.5}V_2O_5{\cdot}nH_2O$.

which is due to an intervalence electronic transition associated with the mixed valence V^{4+}/V^{5+} framework.[27] The appearance of this band is consistent with the increased number of V^{4+} centers in the V_2O_5 framework and indicates charge transfer from the polymer to the V_2O_5 framework.

2.3.5. Charge Transport Properties

The irradiated samples show diminished solubility in water and enhanced electrical conductivity as listed in Table 2.11. The irradiated $(PEO)_{0.5}V_2O_5{\cdot}nH_2O$ has nearly two orders magnitude increased conductivity, up to 10^{-2} S/cm at room temperature. The irradiated $(PEO)_{1.5}V_2O_5{\cdot}nH_2O$ has a lower conductivity of $5x10^{-4}$ S/cm, probably because of the increased spatial separation of the conductive V_2O_5 layers which increases the barrier of electron transport through the material. The conductivity as a function temperature is shown in Figure 2.14a and is consistent with a thermally activated charge transport as in many small-polaron conductors,[28] where the transport is due to carriers hopping. Thermoelectric power data, shown in Figure 2.14b, confirm the non-metallic nature of these systems. The Seebeck coefficients are negative with large values and decrease with falling temperature. This indicates n-type thermally activated charge transport. The Seebeck coefficient of $(PEO)_{0.5}V_2O_5{\cdot}nH_2O$ is less negative than those of the PEO-rich materials, consistent with the higher conductivity of the former.

2.3.6. Alkali Ion Intercalation

As mentioned above, the intercalation of PEO does not change the structure and electronic state of V_2O_5 framework. In other words, the

Table 2.11. Room Temperature Electrical Conductivity and Thermoelectric Power of Unirradiated and Irradiated $(PEO)_xV_2O_5 \cdot nH_2O$ Materials

	Conductivity σ (S/cm)		Thermopower (μV/K)
x	Un-irradiated	Irradiated	Irradiated
0.5	10^{-4}	10^{-2}	-140
1.0	10^{-5}	10^{-3}	-150
1.5	10^{-6}	$5x10^{-4}$	-160

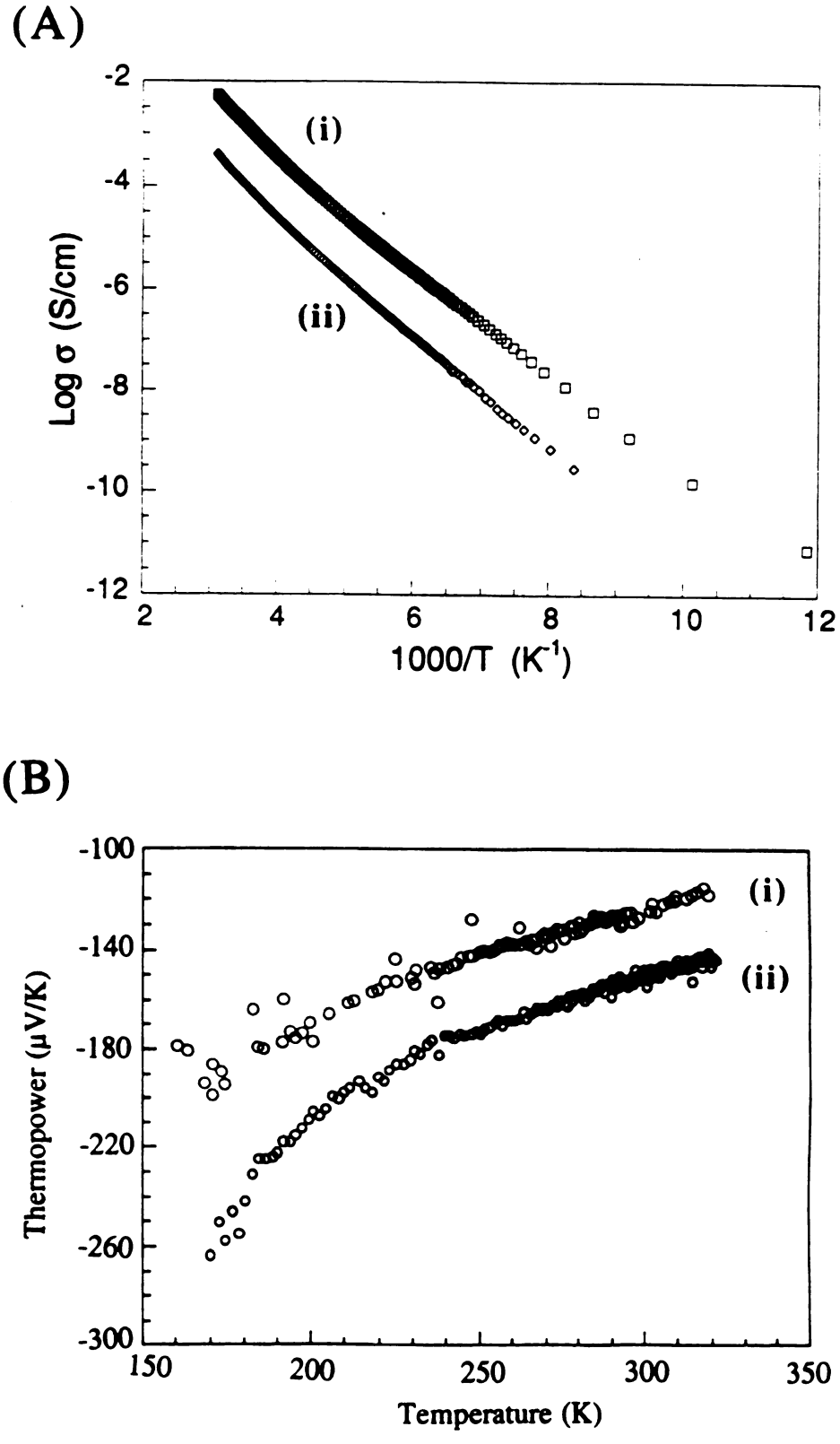

Figure 2.14. (a) Four-probe variable temperature electrical conductivity data of films of irradiated (i) $(PEO)_{0.5}V_2O_5{\cdot}nH_2O$ and (ii) $(PEO)_{1.5}V_2O_5{\cdot}nH_2O$, and (b) Thermoelectric power data of films of irradiated (i) $(PEO)_{0.5}V_2O_5{\cdot}nH_2O$ and (ii) $(PEO)_{1.0}V_2O_5{\cdot}nH_2O$.

PEO/V_2O_5 compounds preserve the oxidation ability of the V_2O_5 framework and thus are good hosts for further redox intercalation. By reaction with lithium iodide, we are able to intercalate lithium ions to the PEO/V_2O_5 phases according to eq (2.7).

$$yLiI + (PEO)_xV_2O_5{\cdot}nH_2O \longrightarrow Li_y(PEO)_xV_2O_5{\cdot}mH_2O + y/2\ I_2 \qquad (2.7)$$

The redox intercalation reduces the V_2O_5 framework and produces iodine as a byproduct which is detected spectroscopically. The reduced framework acquires a blue color and increased magnetic susceptibility. The infrared spectra of $Li_y(PEO)_xV_2O_5{\cdot}nH_2O$ compounds show no significant changes from those prior to intercalation. The compositions and X-ray diffraction data of the $Li_y(PEO)_xV_2O_5{\cdot}nH_2O$ compounds are listed in Table 2.12. The intercalation decreases the interlayer distance and the crystallinity in the c crystallographic direction. For example, the average coherence length decreases by 15 Å to 60-70 Å. Regardless of y in $Li_y(PEO)_{0.5}V_2O_5{\cdot}nH_2O$ compounds, the net interlayer height is always much less than 8 Å, which is the expected van der Waals diameter of a PEO helix containing Li^+ cations. This suggests that the incorporation of Li^+ ions does not change the conformation of PEO from a zigzag to a helix. This is possible that the Li^+ ions are solvated by hydrated water and do not bind to PEO or that the bonding mode between the PEO and the Li^+ ions must be such that a coiled structure is avoided. However, the net expansion of 7.7 Å in the $Li_y(PEO)_{1.5}V_2O_5{\cdot}nH_2O$ implies that the PEO may either preserve the double zigzag conformation or change to a coiled structure in the presence of Li^+ ions. The Li^+ intercalated products do not show a sufficient number of 00l reflections in the X-ray pattern to warrant

Table 2.12. Composition, Net Expansion and Coherence Length of $M_y(PEO)_xV_2O_5 \cdot nH_2O$

x	M	y	Net interlayer expansion (Å)	Coherence Length (along c-axis) (Å)
0.5	Li	0.18	4.3	76
1.0	Li	0.04*	5.4	46
1.5	Li	0.17	7.7	60

*Prepared by using large pieces of PEO/V_2O_5 films and no stirring during the reaction.

a meaningful electron density calculation as was done in the case of PEO/V_2O_5 above. Thus, the conformation of PEO and the chain arrangement in $Li_y(PEO)_xV_2O_5 \cdot nH_2O$ could not be probed by this technique.

2.3.7. ^{7}Li NMR Studies

The $Li_y(PEO)_xV_2O_5 \cdot nH_2O$ materials were examined with variable temperature wide-line ^{7}Li NMR spectroscopy in the hope of probing the state and coordination of Li^+ in the galleries. Regardless of the Li^+ or PEO content, the samples showed just one signal of first order quadrupolar transition with no significant satellite peaks. The change in width at half height ($\Delta\upsilon_{1/2}$) versus temperature for different samples is shown in Figure 2.15. In general, a similar trend of a decrease in $\Delta\upsilon_{1/2}$ with increasing temperature is observed in all samples. Typically, $\Delta\upsilon_{1/2}$ decreases gradually but slowly with increasing temperature, and then a significant narrowing of the lines are observed in the temperature range of 220 to 320 K, after which the line narrowing again gradually increases. As long as the temperature remains below 350 K, above which the vanadium oxide framework begins to decompose, this behavior is reversible for many cooling and heating cycles.

The range of change in $\Delta\upsilon_{1/2}$ with increasing temperature is influenced by the amount of PEO in the layer. Even though all the intercalates studied with or without PEO behave similarly, where line narrowing of the signals takes place with increasing temperature, the sample with the lowest PEO load, $Li_{0.18}(PEO)_{0.5}V_2O_5 \cdot nH_2O$, shows the highest width in the lower temperature region (< 240 K). The one with the highest PEO load but with about the same amount of Li,

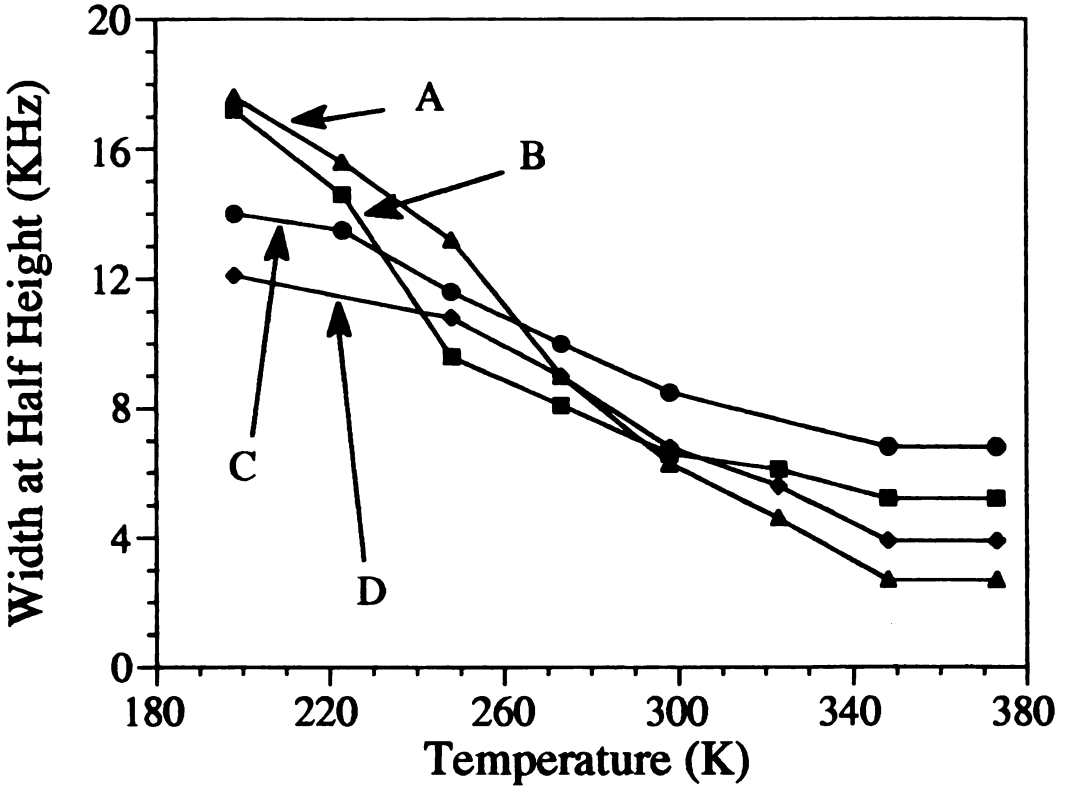

Figure 2.15. Width at half height versus temperature of ^{7}Li NMR signals for samples, (A) $Li_{0.18}(PEO)_{0.5}V_2O_5{\cdot}nH_2O$, (B) $Li_{0.2}V_2O_5{\cdot}nH_2O$, (C) $Li_{0.04}(PEO)_{1.0}V_2O_5{\cdot}nH_2O$, (D) $Li_{0.17}(PEO)_{1.5}V_2O_5{\cdot}nH_2O$.

$Li_{0.17}(PEO)_{1.5}V_2O_5{\cdot}nH_2O$, shows a much narrower signal at < 240 K studied. Though both samples have similar $\Delta\upsilon_{1/2}$ at 280 K, at higher temperatures, the situation is reversed and the sample with the highest PEO shows a higher $\Delta\upsilon_{1/2}$. In both cases the signals are symmetric with no indication of different lithium environments at all temperatures studied. This observation may suggest that the sites that the Li ions can occupy in the general framework are very much affected by the presence of PEO which also imposes limitations on their mobility probably via coordination. The sample with an intermediate PEO load but with the lowest lithium content $Li_{0.04}(PEO)_{1.0}V_2O_5{\cdot}nH_2O$, shows an intermediate line narrowing in the low temperature region. Thus below *ca* 280 K regardless of the amount of lithium load, the higher the PEO content the wider the signals. The lithium in these samples can either be coordinated exclusively to PEO or be in a mixed PEO/water environment or it may exist in two different environments, one exclusively coordinated to PEO and one exclusively coordinated to water. Of course, it is also possible that framework oxide ions may be involved in Li^+ coordination, although we believe this is unlikely when PEO and water are also present. The distribution of these different Li^+ environments would depend on the PEO and water contents in the material. For example, low PEO contents may not be sufficient to fully complex the Li^+. Distribution of the Li^+ sites may also depend on the temperature. For example, at higher temperature a more homogeneous lithium environment may be achieved through thermal equilibration and ion hopping. The fact that we observe only one signal suggests, but does not prove, that the Li^+ ions are primarily in one type of environment. The materials exhibiting asymmetric ^{7}Li-NMR lines may indeed contain substantial number of lithium ions in different sites. For the purpose of

comparison, we examined $Li_{0.2}V_2O_5 \cdot nH_2O$ (no PEO) which contains the highest load of Li^+. The spectrum of this material undergoes a similar line narrowing with increasing temperature, see Figure 2.15. Interestingly, this sample with the highest lithium content shows a signal with a broader base at all temperatures, perhaps suggesting different Li^+ sites. With increasing temperature a significant amount of asymmetry is also observed while the broader base is also retained. With the most reduced state of the V_2O_5 layer, the asymmetry of the signals in this sample is an indication of symmetrical Li^+ environments overlapping with some unsymmetrical sites which induce an electric field gradient (efg) around the Li nuclei. The substantial line narrowing observed in the spectra of all materials with increasing temperature is also consistent with enhanced ion mobility and ion-conductivity in these systems. Ion mobility will lead to changes in the local movement of the Li^+ ions. An increase in temperature presumably leads to an increase in the mobility or exchange frequency of lithium. A similar observation of line narrowing of lithium NMR signals with increasing temperature has been reported earlier for $(PEO)_8LiClO_4$ and $Li_{1+x}V_3O_8$.[29] Furthermore, other qudrupolar nuclei like sodium, when complexed to PEO, have been shown to undergo a similar line narrowing transition with temperature.[30]

The spin lattice relaxation time T1 at room temperature measured by the spin recovery technique shows 117 ms for $Li_{0.18}(PEO)_{0.5}V_2O_5 \cdot nH_2O$ and 131 ms for $Li_{0.17}(PEO)_{1.5}V_2O_5 \cdot nH_2O$. These T1 values are in the same range with values reported earlier for Li salts of PEO.[31] The larger T1 in the latter material suggest that the relaxation of lithium in the layer is also influenced by the amount of PEO in the layer and may reflect a more extensive coordination of lithium by PEO.

Attempts to extract chemical shift information for different samples were mostly inconclusive mainly because of the extremely wide signals (in the range of KHz). Yet at room temperature, a recognizable trend of chemical shift variations were observed for the samples with different reduced states of the V_2O_5 layer. The sample with the maximum load of Li^+ and, hence with the most reduced V_2O_5 layer, shows the most up-field Li chemical shift of *ca* -25 ppm (compared to LiCl value of 0). Likewise the sample with the least Li^+ content shows the most down-field Li chemical shift of ca -7.6 ppm., while the one with an intermediate load of Li^+ shows a chemical shift of -14 ppm. It is to be noted that the signals observed here are symmetric singlets with no indication of significantly different Li^+ environments which would be evident if some of the lithium were associated with just PEO and some with water or V_2O_5. Furthermore, the trend of chemical shift change with degree of reduction of the V_2O_5 layer is probably due to paramagnetic contact or pseudo-contact shifts exerted on the Li^+ nucleus.

2.4. Conclusion

A variety of new PEO/V_2O_5 nanocomposite phases have been obtained. The use of water-swellable V_2O_5 gels as a host material has opened a way for intercalation of water-soluble polymers. The intercalation of poly(vinylpyrrolidone) (PVP), poly(propylene-glycol) (PPG) and methyl-cellulose in V_2O_5 xerogel have been reported earlier.[6b] The intercalation of PEO to $V_2O_5 \cdot nH_2O$ xerogel produces new materials with interesting lithium redox intercalation and photochemical properties. The photochemical properties are similar but not identical to those in other

polymer/V_2O_5 systems. For instance, although all polymer/V_2O_5 systems are sensitive to light, the sensitivity decreases in the order of PPG > PEO ~ methyl-cellulose > PVP. The magnitude of increase in electrical conductivity upon irradiation is associated with polymer loading. The findings can lead to the production of inclusion compounds with controlled light sensitivity and electrical conductivity.

We have prepared several $Li_y(PEO)_xV_2O_5{\cdot}nH_2O$ phases and studied them by ^7Li NMR spectroscopy. Although the results do not prove that the Li^+ ions are coordinated by PEO, lithium ions appear to be mobile at higher temperature which could impart good ionic conductivity to the composite materials.

LIST OF REFERENCES

LIST OF REFERENCES

(1) (a) Giannelis, E.P. in press " *Materials Chemistry : An Emerging Subdiscipline*". (b) Yano, K.; Usuki, A.; Okada, A.; Kurauchi, T.; Kamigaito, O. *Polymer Preprints*, **1991**, 32, #1, 65. (c) Okada, A.; Fukumori, K.; Usuki, A.; Kojima, Y.; Kurauchi, T.; Kamigaito, O. *Polymer Preprints*, **1991**, 32, #3, 540.

(2) (a) Day, P.; Ledsham, R.D. *Mol. Cryst. Liq. Cryst.* **1982**, 86, 163-174. (b) Tieke, B. *Mol. Cryst. Liq. Cryst.* **1983**, 93, 119-145. (c) Pillion, J.E.; Thompson, M.E. *Chem. Mater.* **1991**, 3, 777-779. (d) Enzel, P.; Bein, T. *Chem. Mater.* **1992**, 4, 819-824.

(3) (a) Kanatzidis, M.G.; Tonge, L.M.; Marks, T.J. *J. Am. Chem. Soc.* **1987**, 109, 3797-3799. (b) Kanatzidis, M.G.; Wu, C.-G. ; Marcy, H.O.; Kannewurf, C.R. *Adv. Mater.* **1990**, 2, 364-366.

(4) (a) Bouhaouss, A.; Aldebert, P. *Mater. Res. Bull* **1983**, 18, 1247-1256. (b) Casal, B.; Ruiz-Hitzky, E.; Crespin, M.; Tinet, D.; Galvan, J.C. *J. Chem. Soc., Far. Trans* **1989**, 86, 4167-4177. (c) Masbah, H.; Tinet, D.; Crespin, M.; Erre, R.; Setton, R.; Van Damme, H. *J. Chem. Soc. Chem. Commun*, **1985**, 935-936. (d) Erre, R.; Masbah, H.; Crespin, M.; Van Damme, H.; Tinet, D. *Solid State Ionics*, **1990**, 37, 239-251.

(5) (a) Kanatzidis, M.G.; Wu, C.-G.; Marcy, H.O.; Kannewurf, C.R. *J.*

Am. Chem. Soc. **1989**, 111, 4139-4141. (b) Wu, C.-G.; Kanatzidis, M.G.; Marcy, H.O.; DeGroot, D.C.; Kannewurf, C.R. *Polym. Mat. Sci. Eng.* **1989**, 61, 969-973. (c) Kanatzidis, M.G.; Wu, C.-G.; Marcy, H.O.; DeGroot, D.C.; Kannewurf, C.R. *Chem. Mater.* **1990**, 2(3), 222-224.

(6) (a) Liu, Y.-J.; DeGroot, D.C.; Schindler, J.L.; Kannewurf, C.R.; Kanatzidis, M.G. *Chem. Mater.* **1991**, 3, 992-994. (b) Liu, Y.-J.; DeGroot, D.C.; Schindler, J.L.; Kannewurf, C.R.; Kanatzidis, M.G. *Adv. Mater.* **1993**, 5(5), 369-372.

(7) *Polymer Electrolyte Reviews* McCallum, J.R., Vincent, C.A., Eds.; Elsevier Applied Science: London, **1987** and **1989** Vols. 1, 2.

(8) (a) Ruiz-Hitzky, E.; Aranda, P. *Adv. Mater.* **1990**, 2, 545-547. (b) Ruiz-Hitzky, E.; Aranda P.; Casal, B. *J. Mater. Chem.* **1992**, 2(5), 581-582. (c) Aranda, P.;Ruiz-Hitzky, E. *Chem. Mater.* **1992**, 4, 1395-1403.

(9) Lagadic, I.; Léaustic, A.; Clément, R. *J. Chem. Soc. Chem. Commun.* **1992**, 1396-1397

(10) Bissessur R.; Kanatzidis, M.G.; Schindler, J.L.; Kannewurf, C.R. *J. Chem. Soc. Chem. Commun.* **1993**, 1582-1585.

(11) Ruiz-Hitzky, E.; Jimenez, R.; Casal B.; Manriquez, V.; Ana, A.S. *Adv. Mater.* **1993**, 5(10), 738-741.

(12) Klug, H.P.; Alexander, L.E. "*X-ray Diffraction Procedures for Polycrystalline and Amorphous Materials*"; John Wiley & Sons: New York, 1962; 491-538.

(13) Boudreaux, E.A.; Mulay, L.N. "*Theory and Applications of Molecular Paramagnetism*" ,John Wiley & Sons: New York, 1976.

(14) Lyding, J.W.; Marcy, H.O.; Marks, T.J.; Kannewurf, C.R. *IEEE Trans. Instrum. Meas.* **1988**, 37, 76-80.

(15) Marcy, H.O.; Marks, T.J.; Kannewurf, C.R. *IEEE Trans. Instrum. Meas.* **1990**, 39, 756-760.

(16) (a) Wendlandt, W. W.; Hecht, H. G. "*Reflectance Spectroscopy*", Interscience Puplishers, **1966**. (b) Kotüm, G. "*Reflectance Spectroscopy*", Springer Verlag, New York, **1969**. (c) Tandon, S. P.; Gupta, J. P. *Phys. Stat. Solidi* **1970**, 38, 363-367.

(17) "*International Tables for X-ray Crystallography*", The Kynoch Press, English, **1974**.

(18) Lemerle, J.; Nejem, L.; Lefebvre, J. *J. Inorg. Nucl. Chem.* **1980**, 42, 17-20.

(19) (a) Legendre, J.-J.; Aldebert, P.; Baffier, N.; Livage, J. *J. Colloid Interface Sci.* **1983**, 94(1), 84-89. (b) Livage, J. *Chem. Mater.* 1991, 3, 573-593.

(20) (a) Yao T.; Oka,Y.; Yamamoto, N. *Mat. Res. Bull.* **1992**, 27, 669-675. (b) Yao T.; Oka,Y.; Yamamoto, N. *J. Mater. Chem.* **1992**, 2(3), 331-336. (c) Yao T.; Oka,Y.; Yamamoto, N. *J. Mater. Chem.* **1992**, 2(3), 337-340.

(21) Abello, L.; Husson, E.; Repelin, Y.; Lucazeau, G. *J. Solid State Chem.* **1985**, 56, 379-389.

(22) (a) Takahashi, Y.; Sumita, I.; Tadokoro, H. *J. Poly. Sci. Polym. Phys. Ed.* **1973**, 11, 2113-2122. (b) Takahashi, Y.; Sumita, I.; Tadokoro, H. *J. Poly. Sci. Polym. Phys. Ed.* **1981**, 19, 1153-1155.

(23) Ruiz-Hitzky, E.; Casal, Blanca *J. Chem. Soc., Faraday Trans. 1*, **1986**, 82, 1597-1604.

(24) (a) Drago, R.S. "*Physical Methods in Chemistry*" W.B. Sanders Co.: Philadelphia, **1977**. (b) Liu, Y.-J.; Kanatzidis, M.G. in preparation.

(25) Sanchez, C.; Babonneau, F.; Morineau, R.; Livage, J.; *Bullot, J. Philos. Mag. B*, **1983**, 3, 279-290.

(26) Babonneau, F.; Barboux, P.; Josien, F.A.; Livage, J. *J. Chim. Physique* **1985**, 82, 761-766.

(27) (a) Bullot, J.; Cordier, P.; Gallais, O.; Gauthier, M. *J. Non-Cryst. Solids* **1984**, 68, 123-134. (b) Livage, J.; Jolivet, J.P.; Tronc, E. *J.*

Non-Cryst. Solids **1990**, 121, 35-39.

(28) Bullot, J.; Cordier, P.; Gallais, O.; Gauthier, M.; Livage, J. *J. Non-Cryst. Solids* **1984**,68, 135-146.

(29) (a) Wang, G.; Roos, J.; Brinkmann, D.; Pasquali, M.; Pistoia, G. *J. Phys. Chem. Solids*, **1993**, 54, 851-855. (b) Gang, W.; Roos, J.; Brinkmann, D.; Capuano, F.; Croce, F.; Scrosati, B. *Solid State Ionics*, **1992**, 53-56, 1102-1105. (c) Tanzella, F. L.; Bailey, W.;Frydrych, D.; Farrigton, G. C.; Story, H. S. *Solid State Ionics*, **1981**, 5, 681-684. (d) Killis, A.; LeNest, J. F.; Gandini, A.; Cheradame, H.; Cohen-Addad, J. P. *Polymer Bulletin*, **1982**, 6, 351-358. (e) Wintersgill, M. C.; Fontanella, J. J.; Calame, J. P.; Greenbaum, S. G.; Andeen, C. G. *J. Electrochem. Soc.* **1984**, 131, 2208-2209.

(30) Greenbaum, S. G. *Solid State Ionics*, **1985**, 15, 259-262.

(31) Sondregger, M.; Roos, J.; Mali, M.; Brinkmann, D. *Solid State Ionics*, **1992**, 5, 849-852.

CHAPTER III

INTERCALATION OF V_2O_5 XEROGEL WITH POLY(VINYLPYRROLIDONE), POLY(PROPYLENE-GLYCOL) AND METHYL-CELLULOSE

ABSTRACT

Intercalation of poly(vinylpyrrolidone) (PVP), poly(propylene-glycol) (PPG) and methyl-cellulose in V_2O_5 xerogel is reported. The polymer/V_2O_5 intercalation compounds were synthesized by mixing the polymers with V_2O_5 xerogel in water. The products are obtained after water evaporation, as red composite films. Different composite phases of varying polymer/V_2O_5 ratios can be produced. All polymer/V_2O_5 materials are light sensitive. Upon exposure to a medium-pressure Hg lamp filtered by Pyrex glass, the red composites turn blue in several hours. This light-induced redox reaction which results in increased number of V^{4+} in the vanadium oxide framework results in the increased number of charge carriers and leads to higher electrical conductivity in these materials. This change can be monitored by EPR and magnetic susceptibility measurements.

3.1. Introduction

In recent years, the synthesis of new polymer/inorganic intercalation compounds has attracted considerable interest[1-4]. In the previous chapter, we have shown that PEO can be intercalated into V_2O_5 xerogel[5,6] and phases with varying PEO loading can be readily prepared by simply changing the stoichiometric ratios. Further exploration shows that, besides PEO, other water-soluble polymers such as poly(vinylpyrrolidone) (PVP)[7], poly(propylene-glycol) (PPG)[7] and methyl-cellulose[7], can be similarly intercalated into V_2O_5 xerogel. We found that the intercalated polymer content, the interlayer distance, and the photo-sensitivity of the products strongly depend on the particular polymer. In this chapter, we describe the synthesis of several new polymer/V_2O_5 intercalation compounds, their chemical and physical properties and we compare them to the PEO/V_2O_5.$n$$H_2O$ materials.

3.2. Experimental

3.2.1. Materials

Poly(vinylpyrrolidone), with molecular weight (MW) of 10^4, poly(propylene glycol), with MW of 10^3, and methyl-cellulose, with MW of $6.3x10^3$, were purchased from Aldrich Co., Milwaukee, WI and were used without further purification.

3.2.2. Physicochemical Methods

See chapter two.

3.2.3. Preparation of V_2O_5 Xerogel

See chapter two.

3.2.4. Preparation of (polymer)$_x$$V_2O_5$.$n$$H_2O$ Intercalation Compounds

The preparation of the polymer/V_2O_5 materials was carried out by mixing aqueous polymer solutions with a V_2O_5 solution in various stoichiometries. The polymer/V_2O_5 molar ratios varied from 0.5 to 5.0 for PVP, 0.5 to 3 for PPG, and 0.05 to 0.5 for methyl-cellulose. The average increment of the molar ratio is 0.5 for the first two polymers and 0.1 for the last polymer. The resulting mixture was stirred at room temperature for several hours and then poured onto a flat surface. After slow water evaporation at room temperature, a red film was formed. All manipulations were done with as much exclusion of light as possible. The fresh films are soluble in water. The water content n (analyzed by thermogravimetric analysis) is ~0.4-0.5 for PVP, ~0.2-0.4 for PPG, and ~0.3-0.6 for methyl-cellulose.

3.2.5. Photo-reaction

The (polymer)$_x$$V_2O_5$.$n$$H_2O$ were irradiated as described in chapter two.

3.3. Results and Discussion

3.3.1. Characterization of (polymer)/V_2O_5 Phases

Poly(vinylpyrrolidone)

A series of new phases of $(PVP)_xV_2O_5{\cdot}nH_2O$ were prepared. These phases are characterized by the different interlayer distances in the V_2O_5. When the molar ratio x was less than 1, mixed phases were found. For example, when x = 0.2, the d-spacing is the same as vanadium oxide (i.e. 11.5 Å) with a shoulder at low 2θ angle. When x = 0.5, two phases with interlayer separation of 19.7 Å and 14.3 Å were found. However, when x ~ 1, a single phase, based on X-ray diffraction, was obtained with an interlayer spacing of 22.4 Å, as shown in Figure 3.1. Three strong (00l) diffraction peaks were observed, consistent with a lamellar nature. As x increases, the interlayer distance increases from 22.4 Å when x = 1 to 43 Å when x = 5 as shown in Figure 3.2. The net V_2O_5 interlayer expansion is from 13.66 Å at x = 1.0 to 29.13 Å at x = 3.0. The crystallinity (1.e. long range order) of the composite decreases as the polymer loading increases. The coherence length along the layer stacking direction, as estimated from the Scherrer formula, decreases from 57 Å when x = 1.0 and 45 Å when x = 3. All of the composite phases are red in color as the V_2O_5 xerogel. The infrared spectrum of intercalated PVP exhibits a significant shift in the C=O vibration from 1670 cm^{-1} to 1640 cm^{-1} which we ascribe to hydrogen bonding with co-intercalated water[8]. Compared with V_2O_5 xerogel, these composite films are more brittle.

Poly(propylene-glycol)

In the $(PPG)_xV_2O_5{\cdot}nH_2O$ system, we observed only two types of interlayer distances despite the several x values examined. A typical X-ray diffraction pattern with x = 0.5 is shown in Figure 3.3. The interlayer distance is 16.87 Å when x = 0.5 and increases to 17.7 Å when

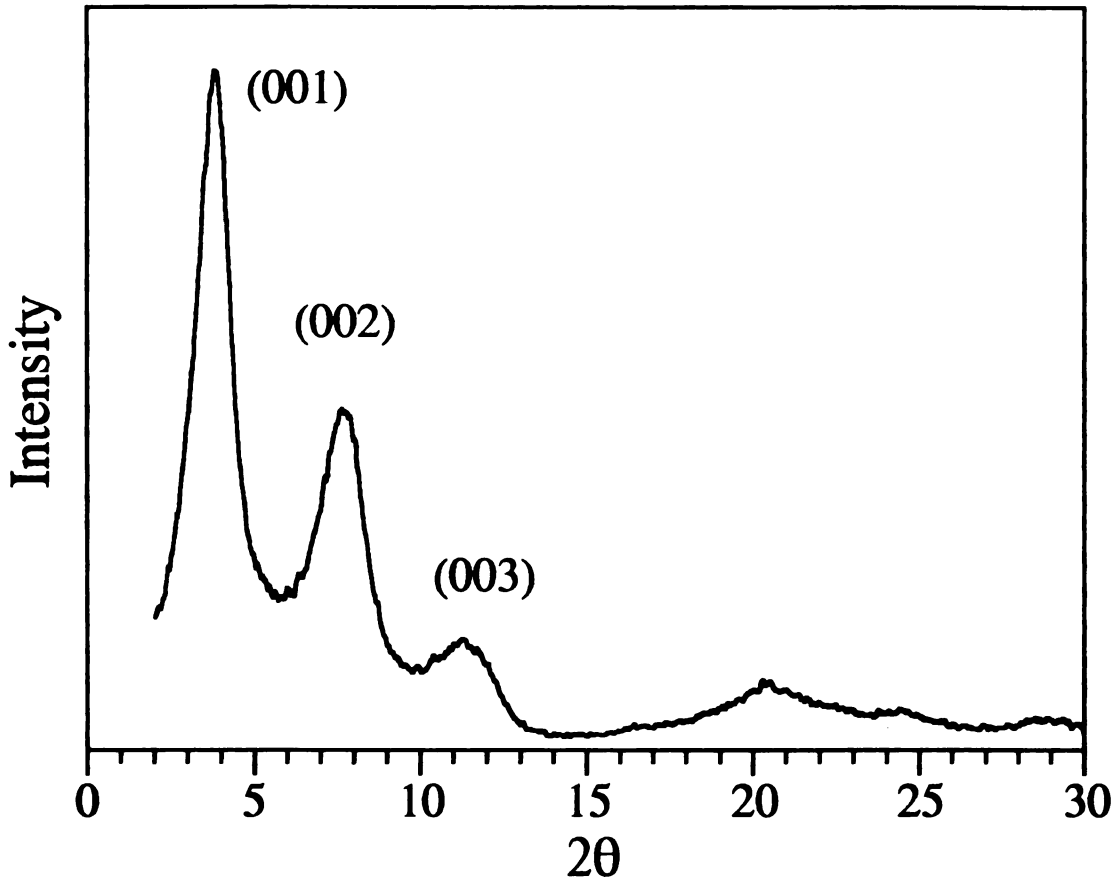

Figure 3.1. X-ray diffraction pattern of $(PVP)_{1.0}V_2O_5{\cdot}nH_2O$ film .

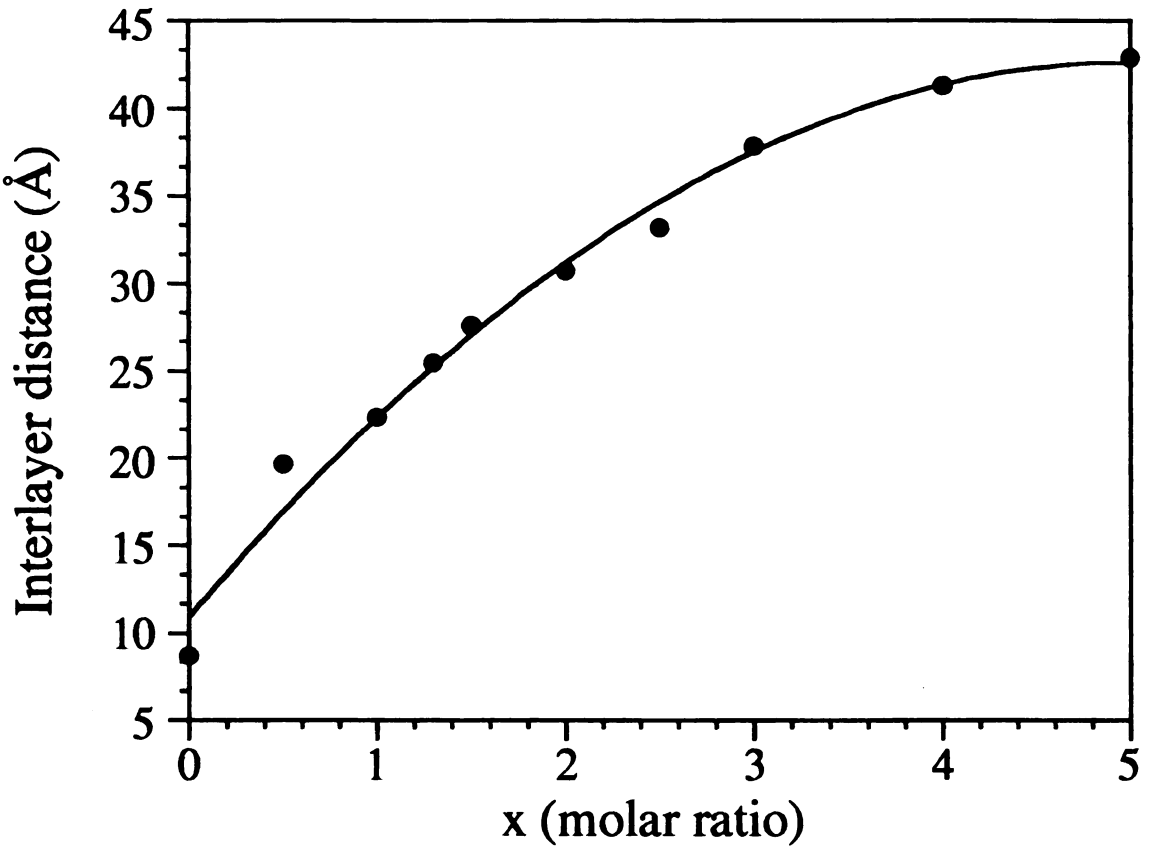

Figure 3.2. Variation of the interlayer distance as a function of x for $(PVP)_xV_2O_5{\cdot}nH_2O$.

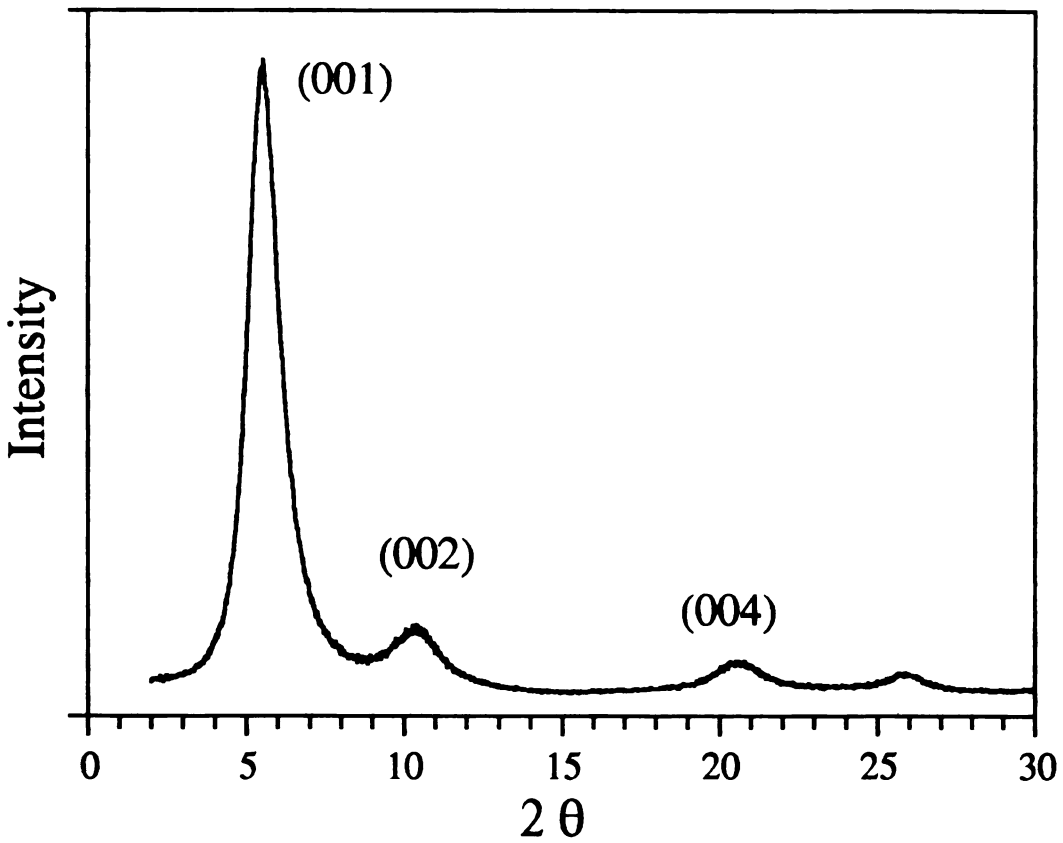

Figure 3.3. X-ray diffraction pattern of $(PPG)_{0.5}V_2O_5 \cdot nH_2O$ film.

x = 2.0. At higher polymer loading it remains constant as shown in Figure 3.4. The net expansion varies from 8.17 Å at x = 0.5 to 9.26 Å at x = 3.0 consistent with the presence of only two phases. The coherence length perpendicular to the stacking direction decreases from 92 Å at x = 0.5 to 78 Å at x = 3.0. Infrared spectroscopy suggests that PPG retains its chemical identity in the V_2O_5 layers. Compared with V2O5 xerogel, these composite films are similar in texture as the one described above.

Methyl-cellulose

Various intercalate phases could also be prepared using methyl-cellulose. X-ray diffraction of (methyl-cellulose)$_{0.05}V_2O_5 \cdot nH_2O$ is shown in Figure 3.5. The interlayer spacing increases from 14.02 Å when x = 0.05 to 18.3 Å when x = 0.35 as shown in Figure 3.6. The net expansion varies from 5.32 Å at x = 0.05 to 9.6 Å at x = 0.35. The coherence length perpendicular to the layers decreases from 71 Å when x = 0.05 to just 38 Å when x = 0.35, suggesting a lower degree of stacking order in the polymer-rich phase. Infrared spectroscopic data of the intercalated methyl-cellulose are similar to those of the free polymer. The only difference is the vibration at 947 cm^{-1} which shifts to 910 cm^{-1}. This vibration was assigned to the C-H deformation of methyl groups[7b]. However, both absorptions co-exist at x > 0.2. Unlike the materials described above, all phases of methyl-cellulose are mechanically flexible.

In order to probe the internal structure of the V_2O_5 layers in these compounds, we performed X-ray diffraction experiments with the main beam perpendicular to the layers (transmission mode). As shown in Figure 3.7, the X-ray diffraction patterns of the inclusion products are identical to that of pristine V_2O_5 xerogel confirming that the intralayer

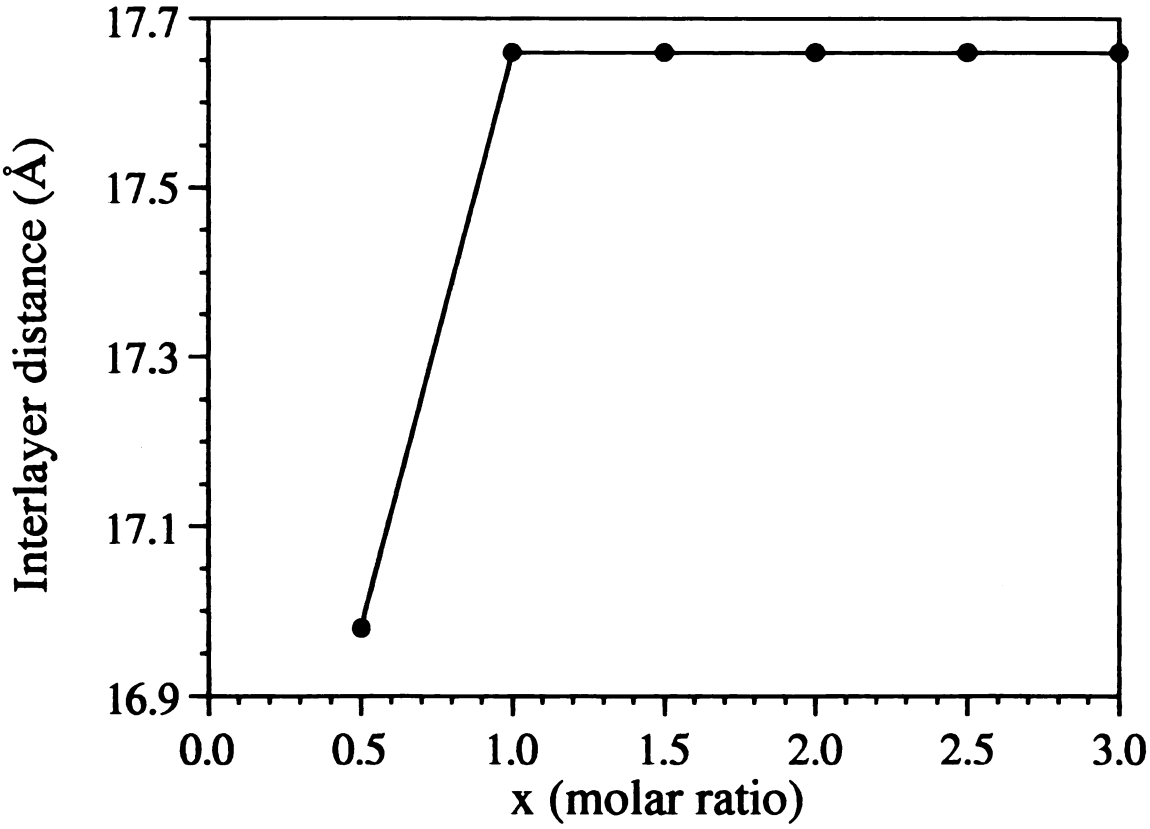

Figure 3.4. Variation of the interlayer distance as function of x for $(PPG)_xV_2O_5 \cdot nH_2O$.

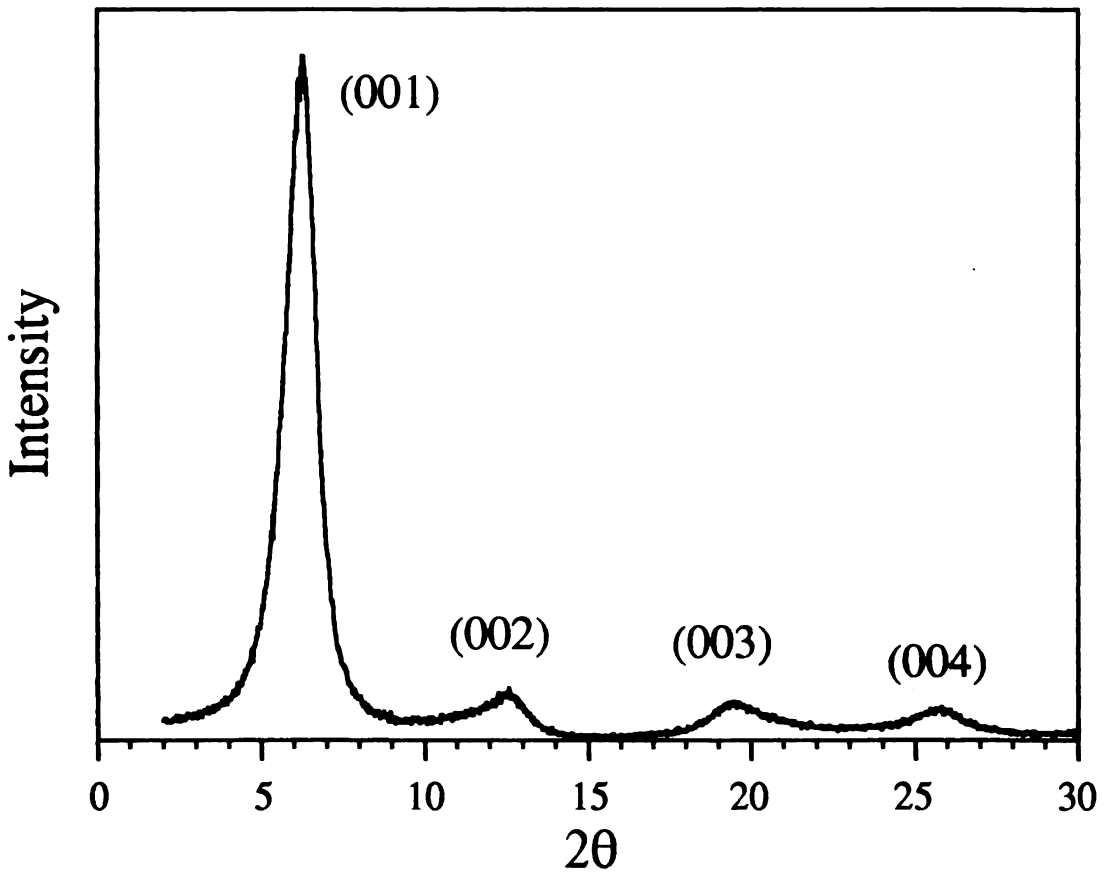

Figure 3.5. X-ray diffraction pattern of (methyl-cellulose)$_{0.05}V_2O_5 \cdot nH_2O$ film.

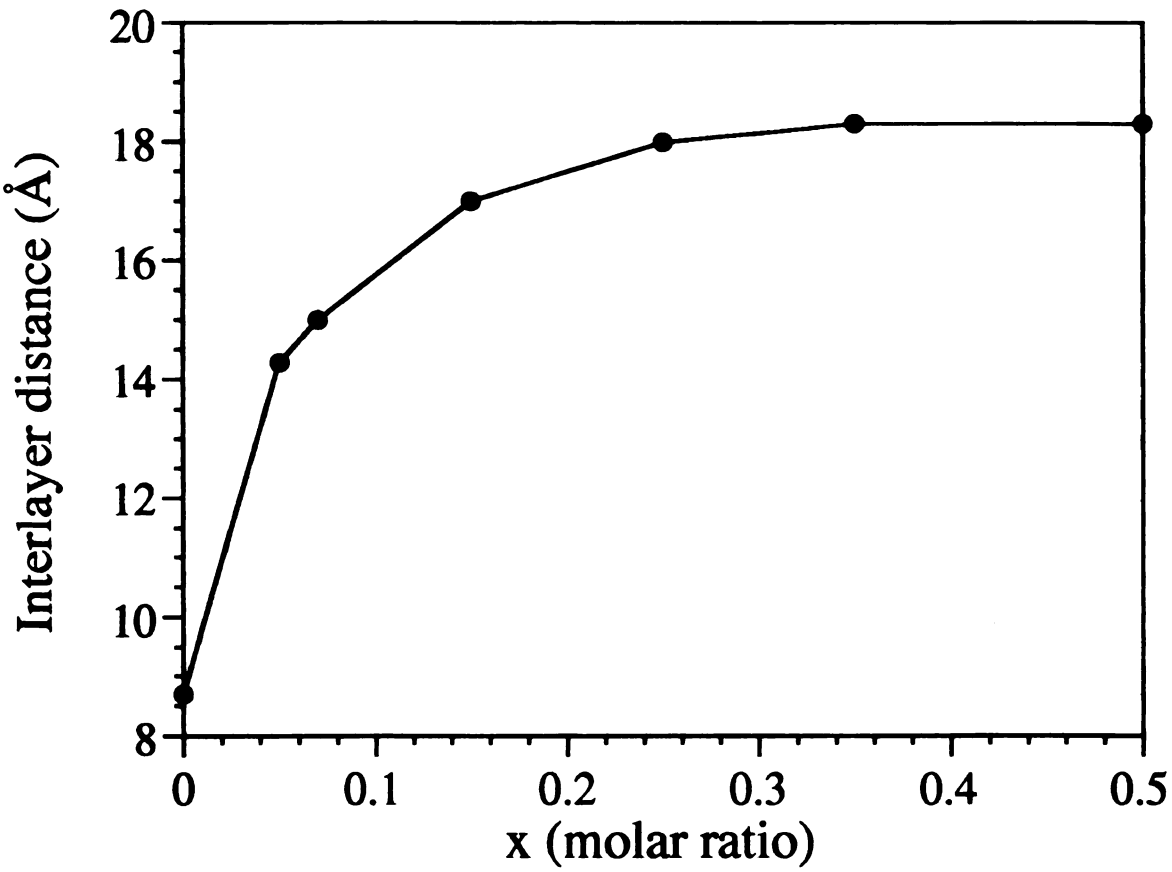

Figure 3.6. Variation of the interlayer distance as a function of x for (methyl-cellulose)$_x$$V_2O_5$·$nH_2O$.

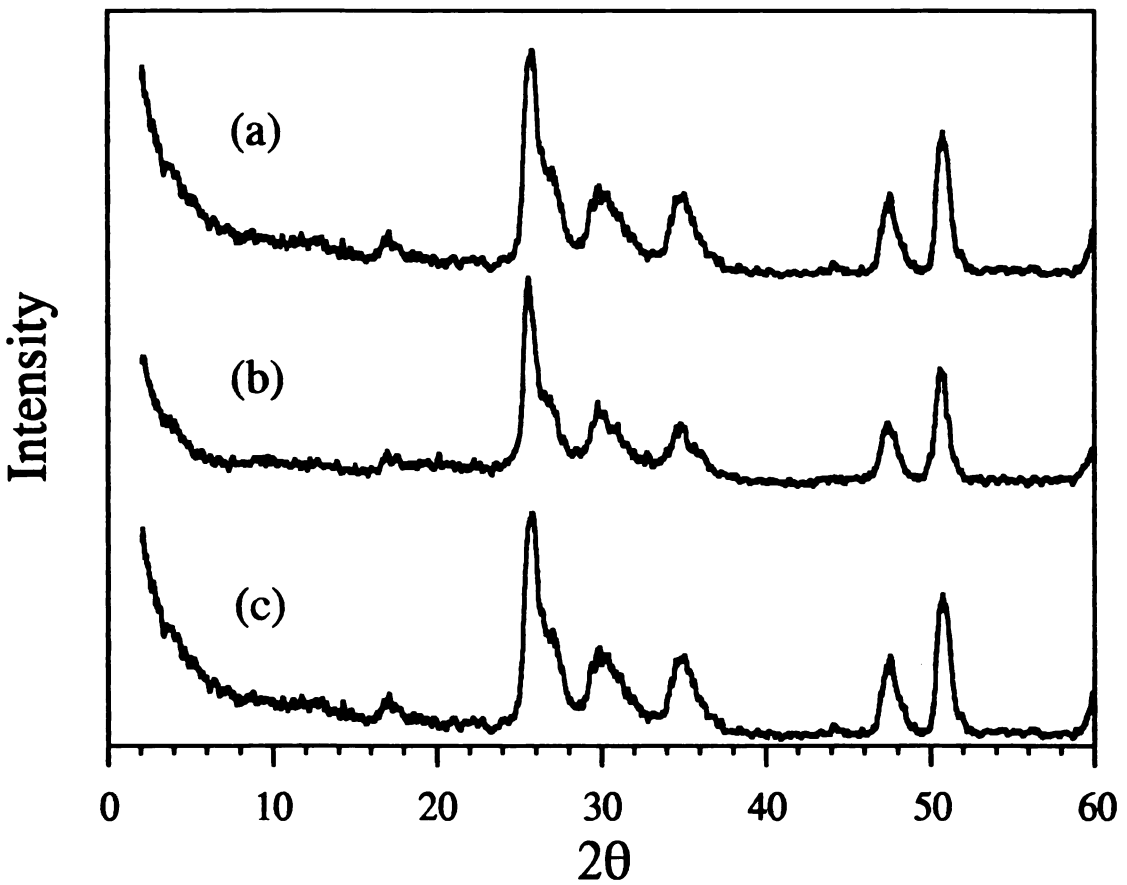

Figure 3.7. Transmission-mode X-ray diffraction patterns of films of (a) (methyl-cellulose)$_{0.05}$$V_2O_5$.$n$$H_2O$, (b) (PVP)$_{1.0}$$V_2O_5$.$n$$H_2O$ and (c) V_2O_5 xerogel.

framework of V_2O_5 is structurally preserved[9]. This is also consistent with infrared data which show that the characteristic stretching vibration peaks of the vanadium oxide framework (1014, 750, 496 cm^{-1} respectively)[10] are present in all compounds.

Thin films of the polymer/V_2O_5 composites (coated on quartz slides) showed two optical absorption bands at 380 and 260 nm, again, identical to that of pristine $V_2O_5 \cdot nH_2O$ films[11]. A typical absorption spectrum is shown in Figure 3.8. The above data confirm that the compounds reported here are true inclusion compounds with no significant interaction or charge transfer between the host and the guest. The constant interlayer distance of the materials with PPG and methyl-cellulose at high x values may indicate that some polymer molecules are outside the layers.

3.3.2. Photo-sensitivity

A characteristic property of these composites is their response to light, particularly of the PPG system. When the red PPG/V_2O_5 films are exposed to room light, their surface turns green within two days. On the other hand, the color change for the other two polymers takes several weeks. However, exposure of these materials to a medium-pressure Hg lamp (filtered by Pyrex glass) dramatically changes the red color to blue in several hours with the PPG/V_2O_5 showing the faster response. The slowest response was exhibited by the PVP. This blue color is due to a light-induced redox reaction where the polymers presumably are oxidized by the vanadium oxide, mentioned in the PEO/V_2O_5 system. For instance, the C-O bond of PPG is probably cleaved and oxidized to aldehyde or even acid, a process which releases at least two electrons to

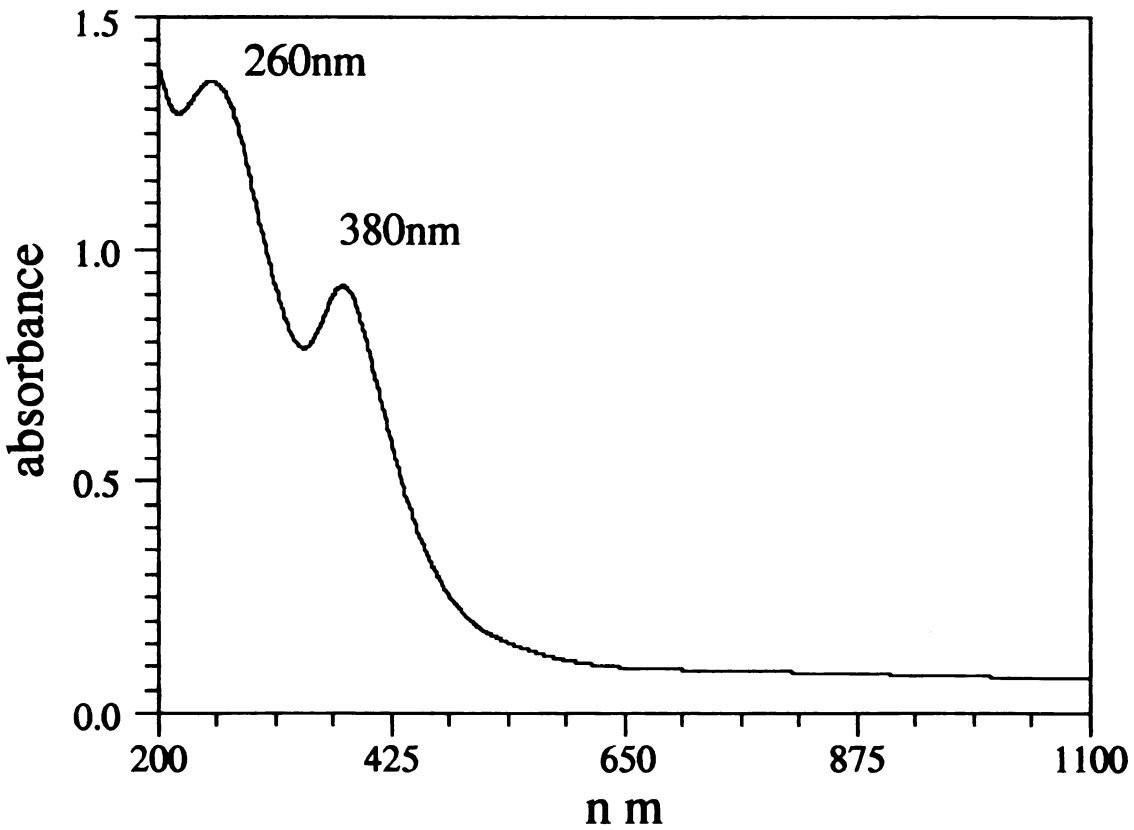

Figure 3.8. Absorption spectrum of $(PVP)_{1.0}V_2O_5.nH_2O$ film (transmission mode).

the V_2O_5 framework. The charge on V_2O_5 is presumably balanced by protons. The infrared spectra of the irradiated compounds show no significant changes suggesting that most of the polymer remains intact and that the number of oxidation sites remains small. However, the formation of V^{4+} atoms by this process can be easily detected by EPR spectroscopy and magnetic susceptibility measurements. As the irradiation time increases, the EPR signal intensity increases and the original hyperfine structure from ^{51}V ($I = {}^{7}/_{2}$) nucleus gradually weakens, yielding a new broad resonance in (methyl-cellulose)$_{0.05}V_2O_5.nH_2O$ as shown in Figure 3.9. The g value is 1.96 and the broad resonance is about 150 G which is due to the exchange interaction of V^{4+} centers[12,14]. However, the hyperfine structure still persists in polymer-rich materials such as $(PVP)_3V_2O_5.nH_2O$ and (methyl-cellulose)$_{0.35}V_2O_5.nH_2O$. This phenomenon has already been explained in the PEO/V_2O_5 system. This may be due to some of $(V{=}O)^{2+}$ centers diffusing between the layers and becoming magnetically isolated by polymers, stabilized by coordination either to oxygen atoms in the polymers and/or water molecules.

The increase in the number of spins is also confirmed by the magnetic susceptibility measurement as shown in Figure 3.10, where the irradiated samples show much higher magnetic susceptibility. The fresh sample is paramagnetic due to the presence of V^{4+} impurities. The paramagnetic behavior can be interpreted as a Curie-Weiss type with a small temperature independent Van Vleck paramagnetism (TIP). The TIP term is originated from the second order Zeeman effect[13] which will be explained in chapter four. The spin-only effective magnetic moment (μ_{eff}, calculated from the Curie-Weiss component) and $\chi_{(TIP)}$ of several materials are summarized in Table 3.1. The μ_{eff} increases from 0.3~0.4

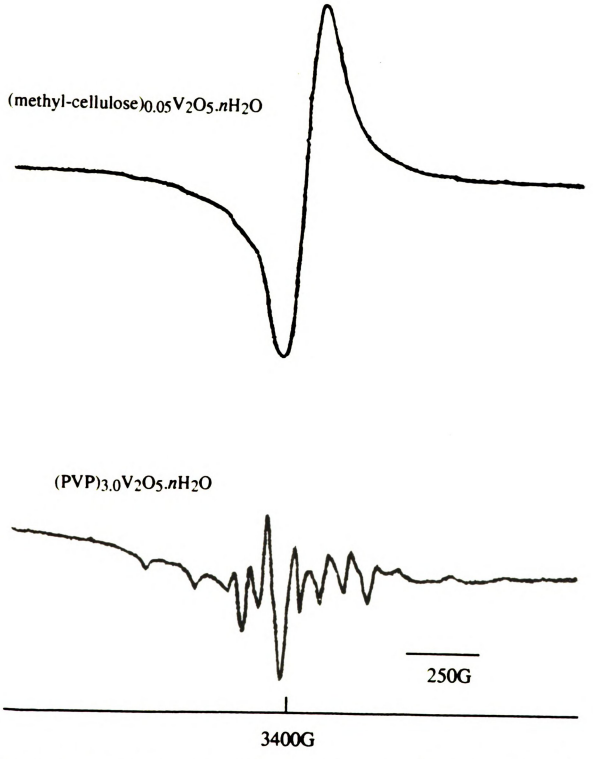

Figure 3.9. Electron paramagnetic resonance of irradiated samples. (irradiation time : 12 h)

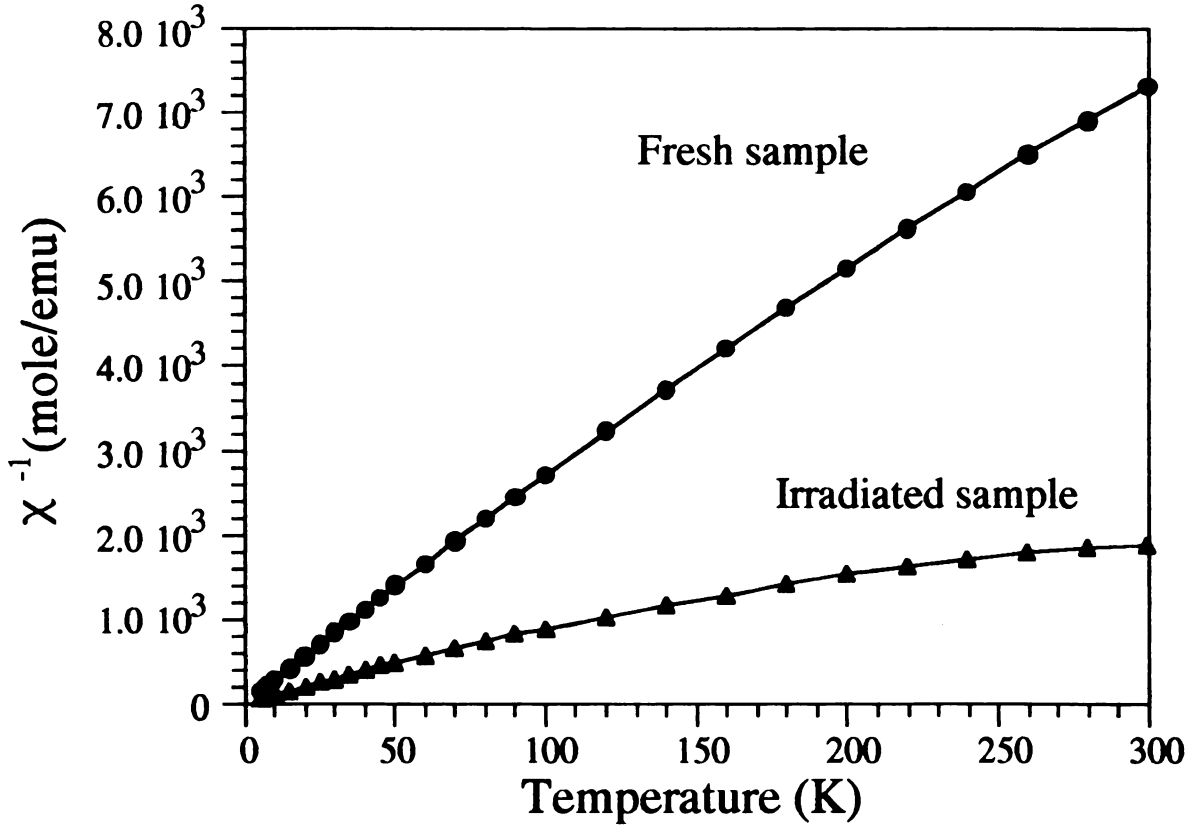

Figure 3.10. Variable temperature magnetic susceptibility of $(PVP)_{1.0}V_2O_5{\cdot}nH_2O$.

Table 3.1. Magnetic Data of Irradiated (Polymer)$_x$$V_2O_5$·$nH_2O$

Polymer	x	μ_{eff} (BM)	χ(TIP) (emu/mole)	d-spacing contraction (Å)
PVP	0.5	0.84	2.3×10^{-4}	~0
PVP	3.0	0.71	2.0×10^{-4}	2.1
Methyl-cellulose	0.05	0.60	4.0×10^{-5}	0.7
Methyl-cellulose	0.35	0.9	4.1×10^{-5}	1.7
PPG	0.5	0.8	1.4×10^{-4}	0.6

BM, in the un-irradiated samples, to ~0.7-0.8 BM after 12 h irradiation and the value is independent of the polymer type and its loading. The 0.7-0.8 BM corresponds to ~10% of V^{4+} centers in the framework, suggesting that less than 5% of the polymer chains are oxidized. This small amount of polymer oxidation is consistent with the unchanged infrared spectra of the irradiated materials. Under the same irradiation conditions, no changes are seen in the pristine $V_2O_5 \cdot nH_2O$.

The irradiated materials also contain a new very broad electronic absorption band centered at 1400 nm which increases in intensity as the irradiation proceeds and is due to an intervalence transition associated with the V^{4+} to V^{5+} centers[14] as shown in Figure 3.11. The appearance of this absorption band is consistent with the increase of V^{4+} concentration in the vanadium oxide framework and further confirms the electron transfer from the polymer to the V_2O_5 framework. The X-ray diffraction patterns of irradiated compounds still show strong (00l) reflections but the interlayer distance is decreased somewhat. The magnitude of the contraction increases with polymer loading, see Table 3.1. For example, in the case of (methyl-cellulose)$_x$$V_2O_5$ compounds, the contraction is 0.7 Å at x = 0.05 and 1.7 Å at x = 0.35. This may be due to the expulsion of a small amount of water from the material upon reduction of V_2O_5 framework and possible conformational changes in the oxidized polymer. The irradiated compounds show diminished solubility in water.

3.3.3. Charge Transport Properties

Generally, the irradiated samples show a small but significant increase in electrical conductivity. Variable temperature conductivity and

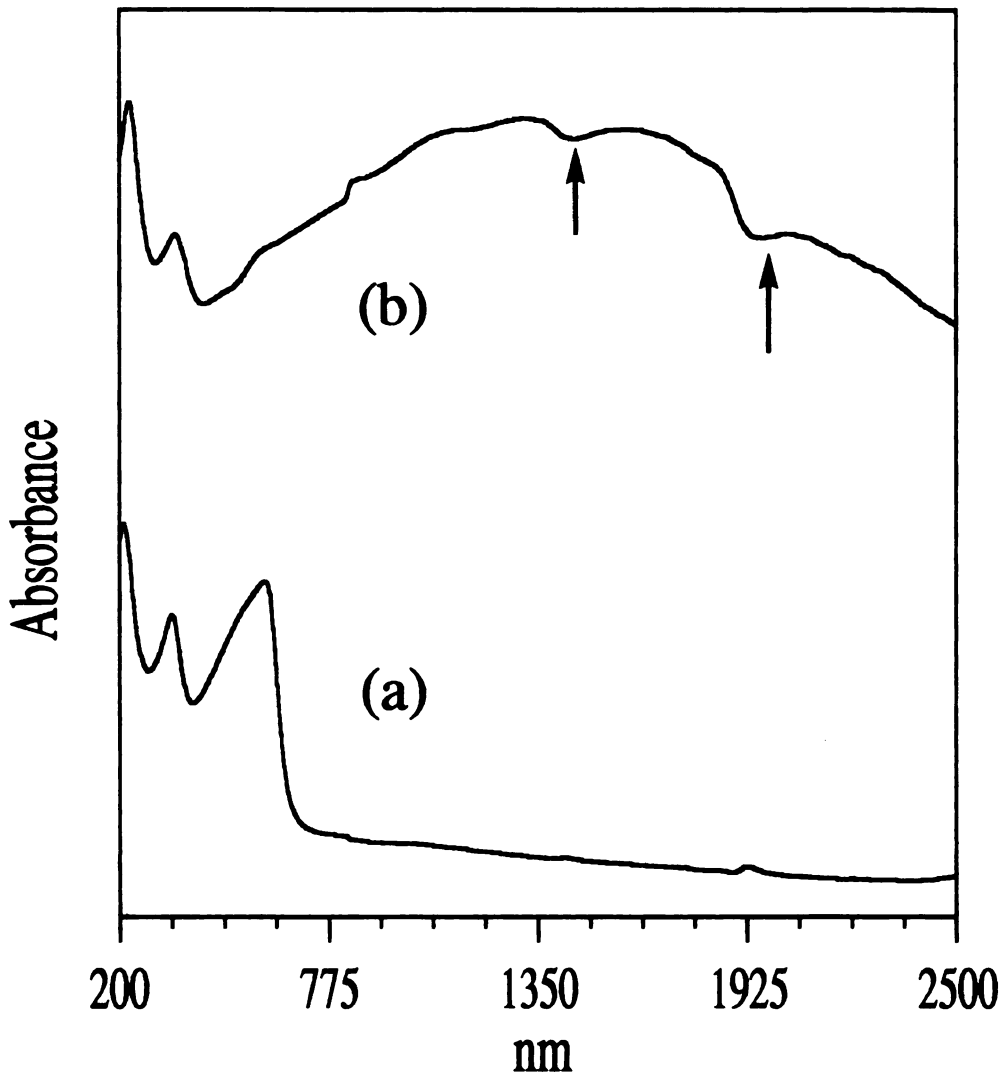

Figure 3.11. Absorption spectra of $(PVP)_{1.0}V_2O_5.nH_2O$ (diffuse reflectance mode) : (a) unirradiated film, (b) irradiated film (12 h). The arrows at 1920 nm and 1440 nm indicate absorptions from water.

thermoelectric power plots of the fresh and irradiated (methyl-cellulose)$_{0.35}V_2O_5.nH_2O$ are shown in Figure 3.12 and Figure 3.13, respectively. The temperature dependence of conductivity suggests semiconducting character. The activation energy of both un-irradiated and irradiated samples calculated from these data is similar at 0.24 eV indicating only minimal structural changes in the V_2O_5 framework. As expected, the Seebeck coefficients are negative and decrease with temperature, similar to those in the PEO/V_2O_5 system. This confirms that these materials are typical small polaron conductors[15] where charge transport is through the vanadium oxide framework. Upon irradiation, the Seebeck coefficient increases dramatically due to the increase of electron carriers. Similar results were obtained from the other materials as summarized in Table 3.2. (PVP)$_{3.0}V_2O_5{\cdot}nH_2O$ has the lowest conductivity of 10^{-9} S/cm at room temperature. The irradiated (PVP)$_{3.0}V_2O_5{\cdot}nH_2O$ shows a nearly 4 orders of magnitude increase in conductivity. In general, compounds with low polymer loading show a higher conductivity than those with high polymer loading. A typical example is shown for the (methyl-cellulose)$_xV_2O_5.nH_2O$ system (for two different x values) in Figure 3.14. the lower conductivities result from the "dilution" of V_2O_5 layers achieved by intercalated, insulating, polymers which hinder the electrical contact between the conducting V_2O_5 layers. Therefore, the electrical conductivity drops as the intercalated polymer loading increases. Similar behavior was observed in PEO/V_2O_5·system.

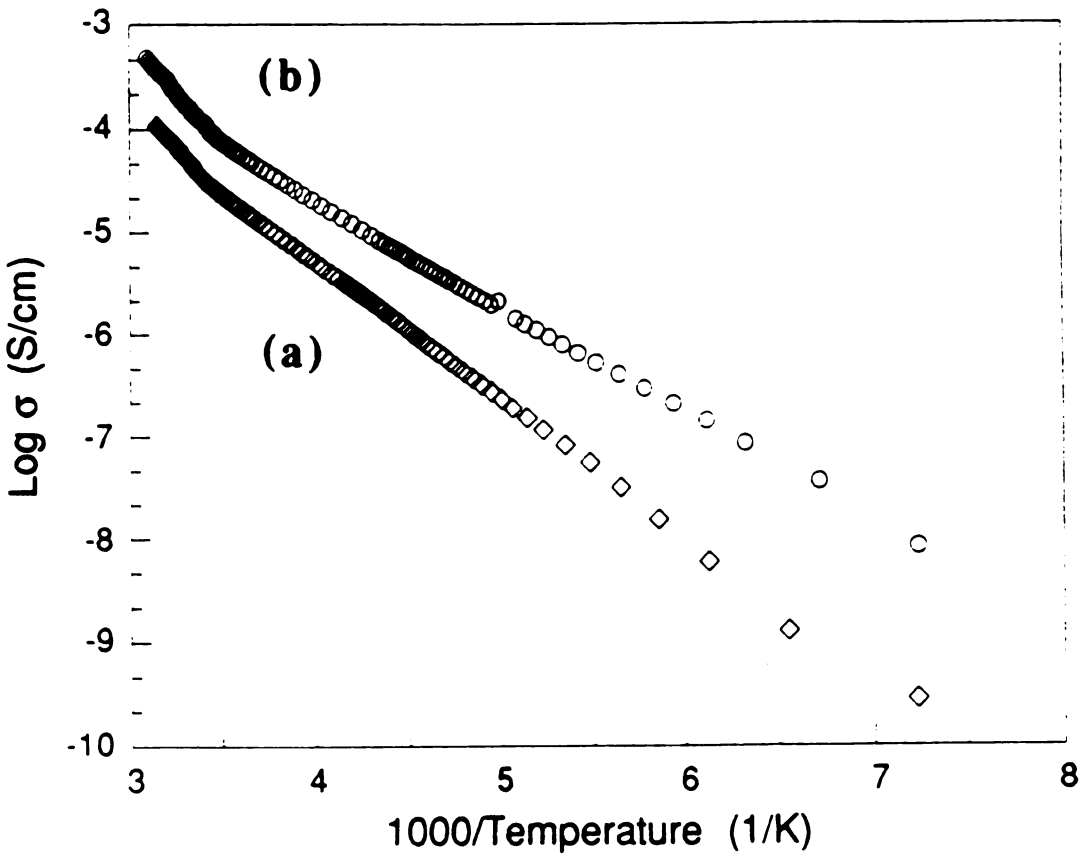

Figure 3.12. Four-probe variable temperature electrical conductivity for films of (a) unirradiated (methyl-cellulose)$_{0.35}V_2O_5.nH_2O$ and (b) irradiated (methyl-cellulose)$_{0.35}V_2O_5.nH_2O$.

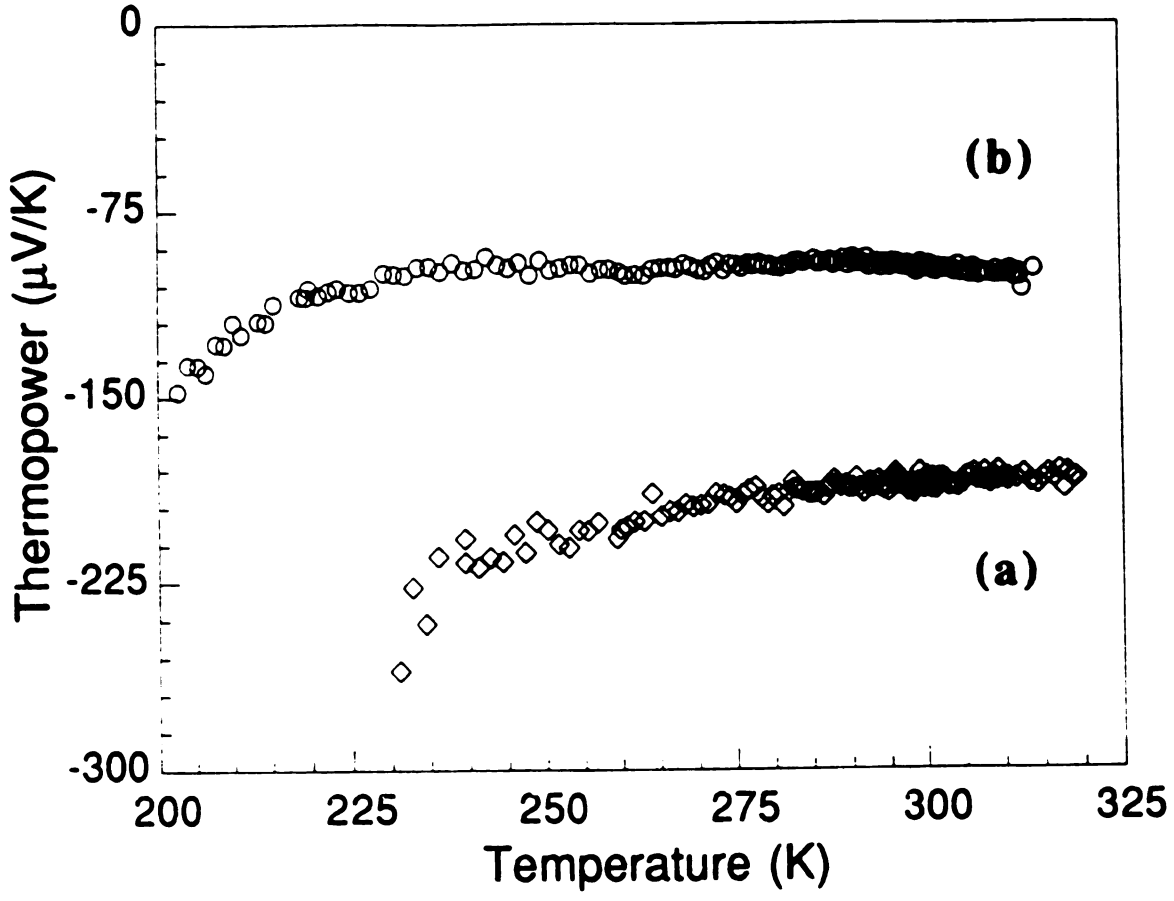

Figure 3.13. Variable temperature thermoelectric power data for films of (a)un-irradiated (methyl-cellulose)$_{0.35}V_2O_5.nH_2O$ and (b) irradiated (methyl-cellulose)$_{0.35}V_2O_5.nH_2O$.

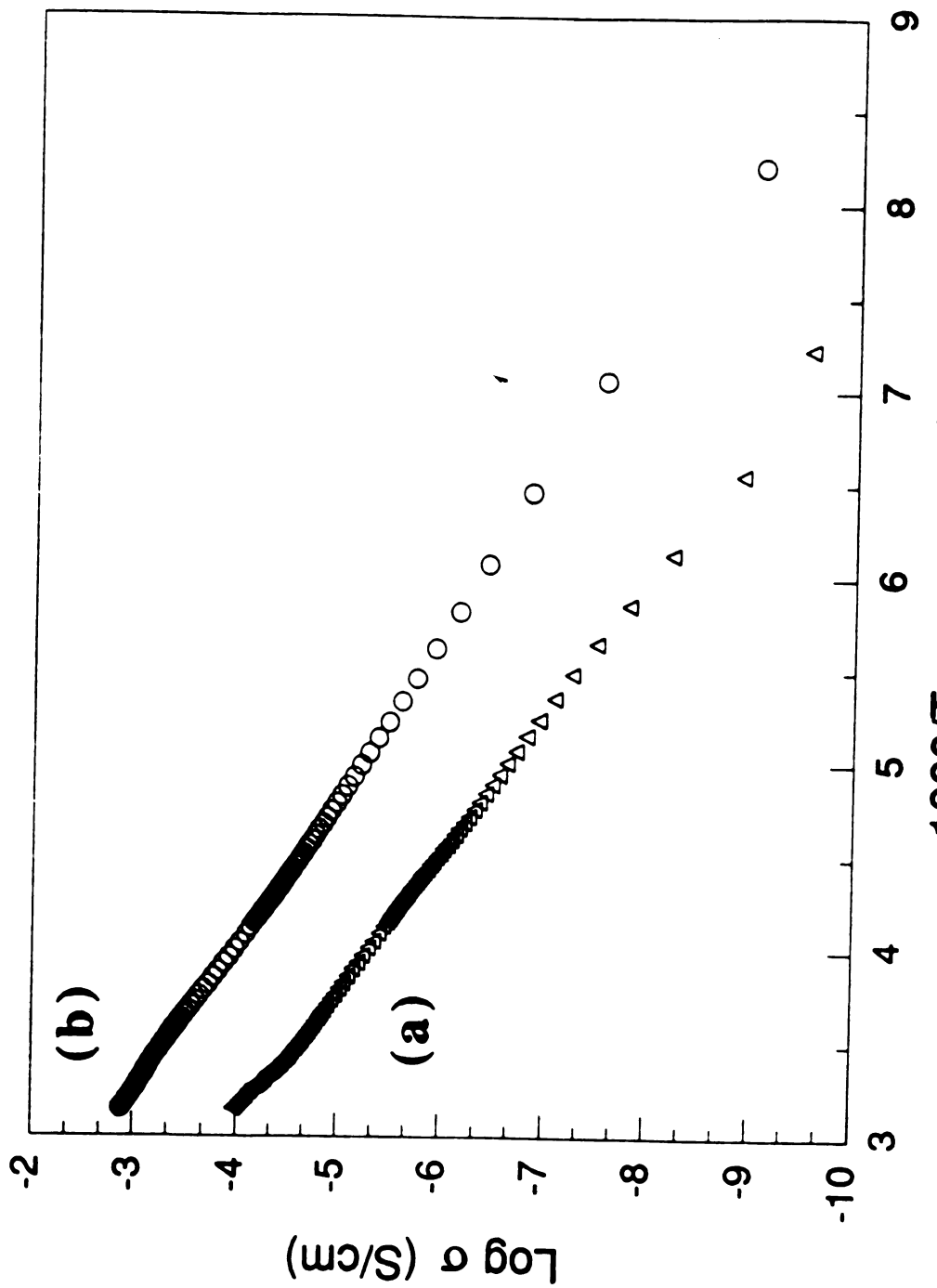

Figure 3.14. Four-probe variable temperature d.c. electrical conductivity data for films of (a) (methyl-cellulose)$_{0.35}V_2O_5.nH_2O$ and (b) (methyl-cellulose)$_{0.05}V_2O_5.nH_2O$.

Table 3.2. Electrical Conductivity and Thermoelectric Power of (Polymer)$_x$$V_2O_5$.$nH_2O$ Materials

		Conductivity (S/cm) at RT		Thermopower (μV/K) at RT	
Polymer	x	Fresh	Irradiated	Fresh	Irradiated
PVP	1.0	$5x10^{-5}$	$8x10^{-5}$	-310	-300
PVP	3.0	10^{-9}	10^{-5}	--	--
Methyl-cellulose	0.05	10^{-3}	$2x10^{-3}$	-200	-100
Methyl-cellulose	0.35	$5x10^{-5}$	10^{-4}	-300	-290

3.4. Conclusion

In summary, we have produced a series of new intercalation compounds of $V_2O_5 \cdot nH_2O$ with saturated water-soluble polymers. The properties of the new materials are similar but not identical to those of the previous PEO/V_2O_5 system. For example, although all of them are light sensitive, the sensitivity decreases from PPG through PEO and methyl-cellulose to PVP. Although the polymer intercalation always changes the physical properties of the V_2O_5 host, the polymer/V_2O_5 films become flexible with PEO and methyl-cellulose but brittle with PPG and PVP. The results reported here warrant further studies on these and other polymers as well as mixed polymers systems, with which we hope to produce a series of inclusion compounds with controlled mechanical properties, light sensitivity and electrical conductivity.

LIST OF REFERENCES

LIST OF REFERENCES

(1) (a) Inoue H.; Yoneyama, H. *J. Electroanal. Chem.* **1987**, 233, 291-295. (b) Enzel P.; Bein, T *J. Phys. Chem.* **1989**, 93, 6270-6272. (c) Okada, A.; Kawasumi, M.; Usuki, A.; Kojima, Y.; Kurauchi, T.; Kamigaito, O. *Mat. Res. Soc. Symp. Proc.* **1989**, 171, 45. (d) Pillion, J.E.; Thompson, M.E. *Chem. Mater.* **1991**, 3, 777-779. (e) Enzel, P.; Bein, T. *Chem. Mater.* **1992**, 4, 819-824.

(2) (a) Kanatzidis, M.G.; Tonge, L.M.; Marks, T.J.; Marcy, H.O.; Kannewurf, C.R. *J. Am. Chem. Soc.* **1987**, 109, 3797-3799. (b) Wu, C.-G.; Kanatzidis, M.G.; Marcy, H.O.; DeGroot, D.C.; Kannewurf, C.R. *Polym. Mat. Sci. Eng.* **1989**, 61, 969-973. (c) Kanatzidis, M.G.; Wu, C.-G.; Marcy, H.O.; DeGroot, D.C.; Kannewurf, C.R. *Chem. Mater.* **1990**, 2(3), 222-224. (d) Wu, C.-G.; Marcy, H.O.; DeGroot, D.C.; Schindler, J.L.; Kannewurf, C.R.; Leung, W.-Y.; Benz, M.; LeGoff, E.; Kanatzidis, M.G. *Synth. Met.* **1991**, 41-43, 797-803. (e) Wu, C.-G.; Marcy, H.O.; DeGroot, D.C.; Schindler, J.L.; Kannewurf, C.R.; Kanatzidis, M.G. *Synth. Met.* **1991**, 41-43, 693-698.

(3) (a) Ruiz-Hitzky, E.; Aranda, P. *Adv. Mater.* **1990**, 2, 545-547. (b) Lagadic, I.; Leaustic, A.; Clement, R. J. *Chem. Soc. Chem. Commun.* **1992**, 1396-1397.

(4) (a) Giannelis, E.P. in press " *Materials Chemistry : An Emerging Subdiscipline*". (b) Yano, K.; Usuki, A.; Okada, A.; Kurauchi, T.;

Kamigaito, O. *Polymer Preprints*, **1991**, 32, #1, 65. (c) Okada, A.; Fukumori, K.; Usuki, A.; Kojima, Y.; Kurauchi, T.; Kamigaito, O. *Polymer Preprints*, **1991**, 32, #3, 540.

(5) (a) Legendre, J.J.; Livage, J. *J. Colloid Interface Sci.* **1983**, 94, 84-89. (b) Aldebert, P.; Haesslin, H.W.; Baffier, N.; Livage, J. *J. Colloid Interface Sci.* **1984**, 98, 478-483. (c) Kittaka, S.; Sasaki, S.; Ogawa, N.; Uchida, N. *J. Solid State Chem.* **1988**, 76, 40-51. (d) Kamiyama, T.; Suzuki, K. *J. Non-Cryst. Solids* **1988**, 100, 466-470. (e) Baffier N.; Aldebert, P.; Livage, J.; Haesslin, H.W. *J. Colloid Interface Sci.* **1991**, 141, 467-474. (f) Livage, J. *Chem. Mater.* **1991**, 3, 578-593.

(6) Liu, Y.-J.; DeGroot, D.C.; Schindler, J.L.; Kannewurf, C.R.; Kanatzidis, M.G. *Chem. Mater.* **1991**, 3, 992-994.

(7) (a) Molyneux, P. in *Water-Soluble Synthetic Polymers* ; CRC press, Inc.: New York, **1983** Vols. 1, 2. (b) Ott, E.; Spurlin, M. in *High Polymers*; Interscience Publishers, Inc. : New York, **1954** Vol. 5.

(8) (a) Oster, G.; Immergut, E.H. *J. Am. Chem. Soc.* **1954**, 76, 1393-1396. (b) Rothschild, W.G. *J. Am. Chem. Soc.* **1972**, 94, 8676-8683.

(9) Aldebert, P.; Baffier, N.; Gharbi, N.; Livage, J. *Mater. Res. Bull.* **1981**, 16, 669-676.

(10) Abello, L.; Husson, E.; Repelin, Y.; Lucazeau, G. *J. Solid State Chem.* **1985**, 56, 379-389.

(11) Lemerle, J.; Nejem, L.; Lefebvre, J. *J. Inorg. Nucl. Chem.* **1980**, 42, 17-20.

(12) Baiker A.; Dollenmeier, P.; Glinski, M.; Reller, A.; Sharma, V.K. J. Catal. 1988, 111, 273-285.

(13) (a) Boudreaux, X.A.; Mulay, L.N. "*Theory and Applications of Molecular Paramagnetism*", John Wiley and Sons: New York **1976**. (b) Drago, R.S. "*Physical Methods in Chemistry*" W.B. Sanders Co.: Philadelphia, **1977**.

(14) Babonneau, F.; Barboux, P.; Josien, F.A.; Livage, J. *J. Chim. Physique* **1985**, 82, 761-766.

(15) Bullot, J.; Cordier, P.; Gallais, O.; Gauthier, M.; Livage, J. *J. Non-Cryst. Solids* **1984**,68, 135-146.

CHAPTER IV

STABILIZATION OF ANILINIUM IN VANADIUM(V) OXIDE XEROGEL AND ITS POST-INTERCALATIVE POLYMERIZATION TO POLY(ANILINE) IN AIR

ABSTRACT

The oxygen-induced polymerization of anilinium to polyaniline in the layered compound $(C_6H_5NH_3)_{0.4}V_2O_5.0.4H_2O$ to form $\{1/n(-C_6H_4NH-)_n\}_{0.4}V_2O_5.0.4H_2O$ is reported. $(C_6H_5NH_3)_{0.4}V_2O_5.0.4H_2O$ was prepared by the reaction of V_2O_5 xerogel with $C_6H_5NH_3I$ in CH_2Cl_2 for two days. X-ray diffraction and infrared spectroscopy confirmed anilinium inside the layers of V_2O_5. Exposure to air resulted in an intra-lamellar polymerization of anilinium to polyaniline. Infrared spectroscopic data show the formation of emeraldine salt of polyaniline. The interlayer expansion (5.6 Å) is consistent with a monolayer of polymer chains in V_2O_5 framework. The oxygen-induced polymerization is activated by vanadium oxide. Magnetic susceptibility measurements and electron paramagnetic resonance spectroscopy indicate that the V_2O_5 framework loses electron during the polymerization process. The electrical conductivity of $\{1/n(-C_6H_4NH-)_n\}_{0.4}V_2O_5.0.4H_2O$ is two orders of magnitude higher than that of its precursor (10^{-5} S/cm) while the thermopower of the former is smaller (-20 μV/K). The MW of the polyaniline formed in the intralamellar space was estimated by gel permeation chromatography.

4.1. Introduction

During the last few years we have investigated in detail the redox intercalative polymerization of several organic molecules such as aniline, pyrrole and 2,2'-bithiophene in vanadium oxide xerogel.[1] The products contain the corresponding conjugated polymers poly(aniline) (PANI), poly(pyrrole) and poly(thiophene) within an electrically conductive mixed-valence V^{4+}/V^{5+} lamellar host. Redox intercalation[2] alters the band structure of vanadium oxide forming bronze-like electrically conductive materials.[3] The formation of PANI from anilinium and vanadium oxide gels is relatively fast and the study of this heterogeneous reaction is difficult. It is presumed that the first step in the insertion of PANI is intercalation of the monomer in V_2O_5 framework. One way to follow the oxidation of aniline by the vanadium oxide would be to trap anilinium between the layers of the host and then observe its conversion to polyaniline (PANI) upon oxidation. The challenge is to prevent anilinium from being oxidized by $V_2O_5.nH_2O$ before controlled polymerization can be initiated. We accomplished this by satisfying the oxidative power of $V_2O_5.nH_2O$ with electrons from a different source such as iodide. In this chapter, we report the successful insertion of intact anilinium molecules in $V_2O_5.nH_2O$ and their intra-lamellar conversion to PANI upon exposure to ambient oxygen.

4.2. Experimental

Materials

$NaVO_3$, NaOH, acetone, methylene chloride, and anilinium iodide were purchased from commercial sources and were used without further purification.

Physicochemical Methods

See chapter two.

Preparation of $V_2O_5 \cdot nH_2O$ Xerogel

See chapter two.

Preparation of $(C_6H_5NH_3)_{0.4}V_2O_5 \cdot 0.4H_2O$

Under a nitrogen atmosphere, powdered 0.5 g (2.37 mmol) of $V_2O_5.1.8H_2O$ reacted with 2.1 g (9.48 mmol) of anilinium iodide in 50 ml of methylene chloride at room temperature. After stirring for two days, the dark-blue product was isolated from filtration and washed with acetone. The composition of the product obtained from thermogravimetric analysis (TGA) under oxygen flow gave $(C_6H_5NH_3)_{0.4}V_2O_5.0.4H_2O$.

Extraction of Polyaniline from $(PANI)_{0.4}V_2O_5.0.4H_2O$

$(PANI)_{0.4}V_2O_5.0.4H_2O$ was added to excess 2 wt% NaOH solution. After one day of stirring at room temperature, the black precipitate was collected by filtration, washed with water and acetone, and dried in air.

4.3. Results and Discussion

4.3.1. Synthesis and Characterization of

$(C_6H_5NH_3)_{0.4}V_2O_5.0.4H_2O$

The anilinium intercalated vanadium oxide gels is formed according to eq (4.1)

$$x\ C_6H_5NH_3^+I^- + V_2O_5{\cdot}nH_2O \longrightarrow (C_6H_5NH_3)_xV_2O_5{\cdot}nH_2O + (x/2)I_2 \qquad (4.1)$$

The V_2O_5 xerogel oxidizes iodide, which is a better reducing agent than anilinium, to iodine. The anilinium is intercalated into the reduced framework to neutralize the negative charges on the layers. The intercalation is confirmed by the net increase of ca. 5.1 Å in the interlayer distance as shown in Figure 4.1(A). The very broad (00l) diffraction peak corresponds to a very short coherence length, perpendicular to the layers stacking axis, which is estimated to be 25Å by using Scherrer formula. This is considerably smaller than the 100Å found in V_2O_5 xerogel itself and indicates considerable disruption of the stacking order of the vanadium oxide layers upon intercalation. The presence of anilinium is unambiguously established by infrared spectroscopy as shown in Figure 4.2(A).

4.3.2. Polymerization of $(C_6H_5NH_3)_{0.4}V_2O_5.0.4H_2O$

Exposure to air induced profound changes in the infrared spectrum of the material, shown in Figure 4.2(B) where the anilinium vibration pattern gradually disappeared and the strong characteristic pattern of the emeraldine salt form of polyaniline became evident.[4] The changes of the position and shape of the stretching vibration peaks of the vanadium oxide

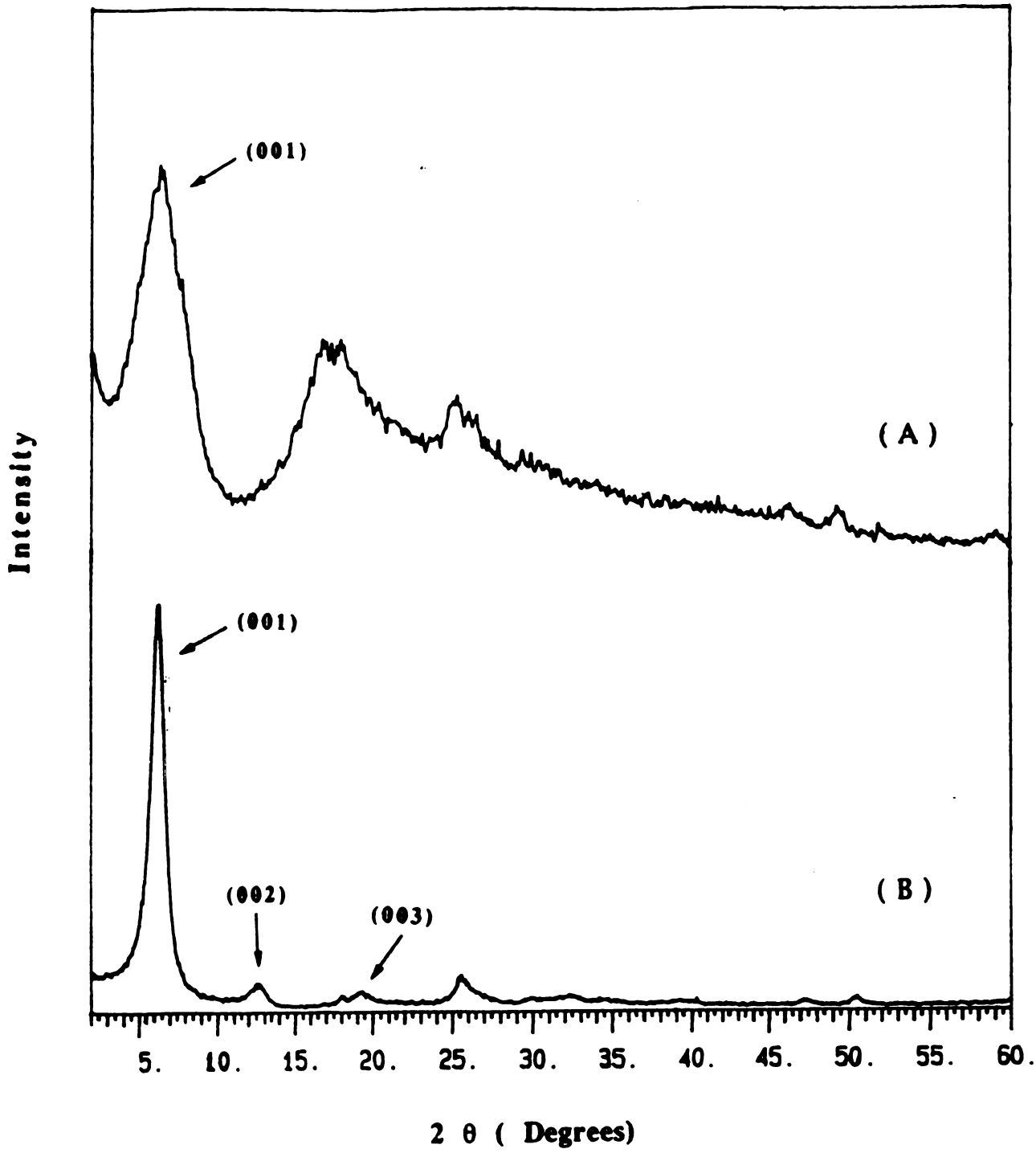

Figure 4.1 X-ray diffraction patterns from (A) $(C_6H_5NH_3)_{0.4}V_2O_5.0.4H_2O$ and (B) $\{1/n(\text{-}C_6H_4NH\text{-})_n\}_{0.4}V_2O_5.0.4H_2O$.

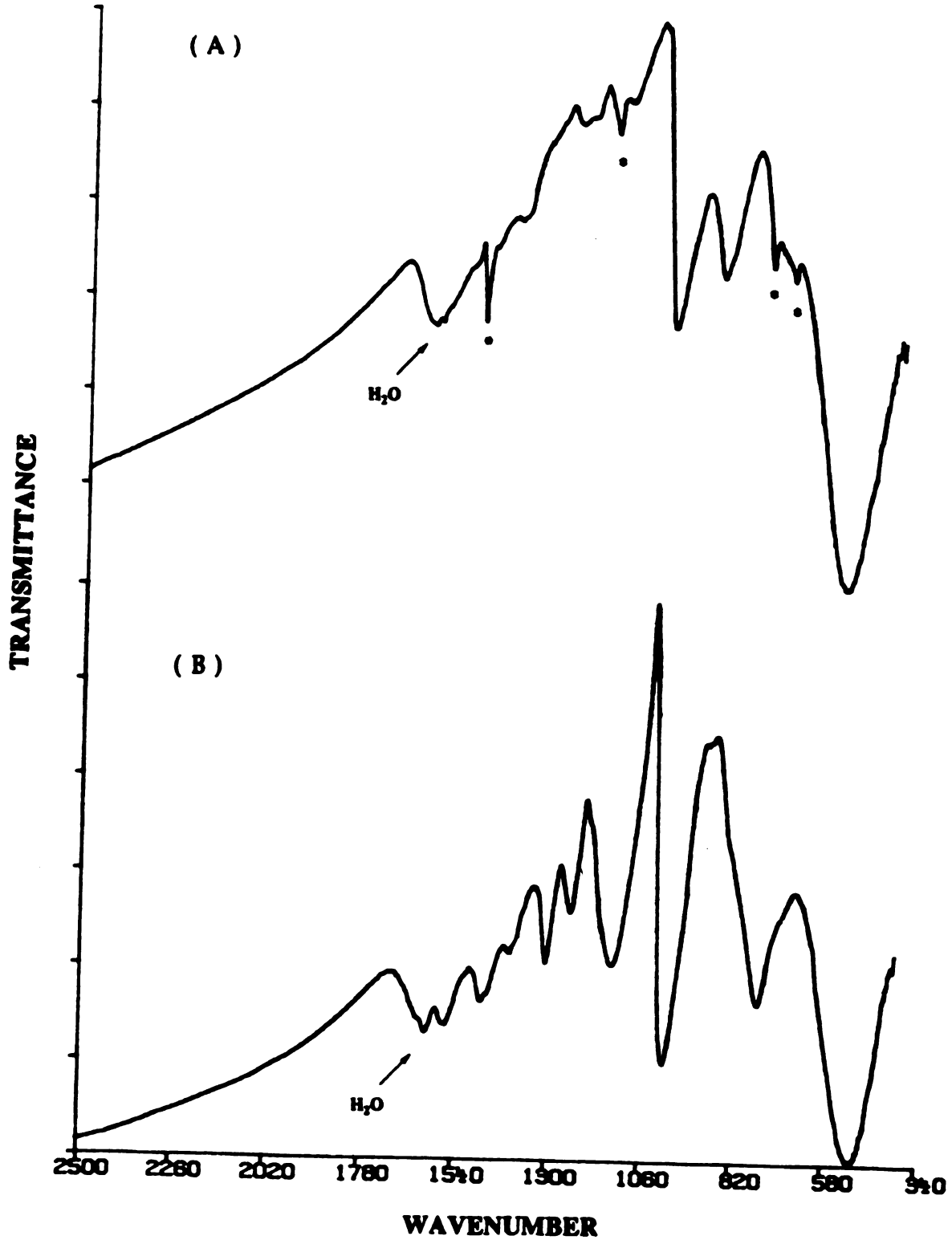

Figure 4.2 Infrared spectra (KBr pellet) of (A) $(C_6H_5NH_3)_{0.4}V_2O_5.0.4H_2O$ and (B) $\{1/n(\text{-}C_6H_4NH\text{-})_n\}_{0.4}V_2O_5.0.4H_2O$. *peaks are from anilinium ion.

framework are also significant. The V=0 vibration peak changes from 990 cm^{-1} to 1000 cm^{-1} and the V-O-V vibration peaks[5] shift from 852 cm^{-1} and 530 cm^{-1} to 750 cm^{-1} and 496 cm^{-1}. This spectroscopic difference is due to the greater degree of reduction in $(C_6H_5NH_3)_{0.4}V_2O_5.0.4H_2O$ **1** than in $\{1/n(\text{-}C_6H_4NH\text{-})_n\}_{0.4}V_2O_5.0.4H_2O$ **2**. This is confirmed by magnetic susceptibility measurements presented below. The infrared absorption peaks of **2** are similar to those of $(PANI)_xV_2O_5.nH_2O$[1a,6] **3**, prepared directly from aniline and $V_2O_5.nH_2O$, as shown in Table 4.1. After digestion of the V_2O_5 framework, the absorptions of the extracted PANI from **2** occur at slightly higher energies than bulk PANI. This suggests that the extracted PANI has lower molecular weight, see below. The (00l) peak in the X-ray diffraction pattern, shown in Figure 4.2(B), of the oxidized product **2** narrows dramatically compared to that of **1** and reveals a small 0.5 Å interlayer expansion. This indicates that the polymerization is intra-lamellar, forming a monolayer of polyaniline chains inside the framework. The conversion is complete in three to four weeks, judged from infrared spectroscopy. The estimated coherence length along the layers stacking axis increases threefold to *ca.* 90 Å, suggesting a significantly improved lattice organization. Compared to **3**, the compound **2** shows additional 0.5 Å expansion. The overall reaction is represented in Scheme 4.1.

The mechanism of this unprecedented post-intercalative oxidative polymerization is complicated but it must be related to the ability of vanadium centers[7] to activate oxygen. Simple anilinium salts are not oxidized to polyaniline under the experimental conditions employed here. Therefore, the vanadium oxide must be implicated. This is consistent with the ability of vanadium oxide to catalyze oxidation of organic molecules.

Table 4.1. IR Vibration Energies of (PANI)$0.4V_2O_5 \cdot 0.4H_2O$ **2**, (PANI)$xV_2O_5 \cdot nH_2O$ **3**, Bulk PANI and Extracted PANI.

	C-C Ring stretching (cm^{-1})	C-H bending or C-N stretching (cm^{-1})	C-H bending (in-plane) (cm^{-1})	C-H bending (out-of-plane) (cm^{-1})	V_2O_5 framework (cm^{-1})
Compound **2**	1567, 1473	1304, 1241	1138		1000, 750, 496
Compound **3***	1566, 1471	1298, 1237	1131		997, 751, 506
Bulk PANI	1560, 1481	1292, 1249	1109	797	
Extracted PANI from **2**	1563, 1491	1301, 1239	1140	802	

*Copy from reference 6.

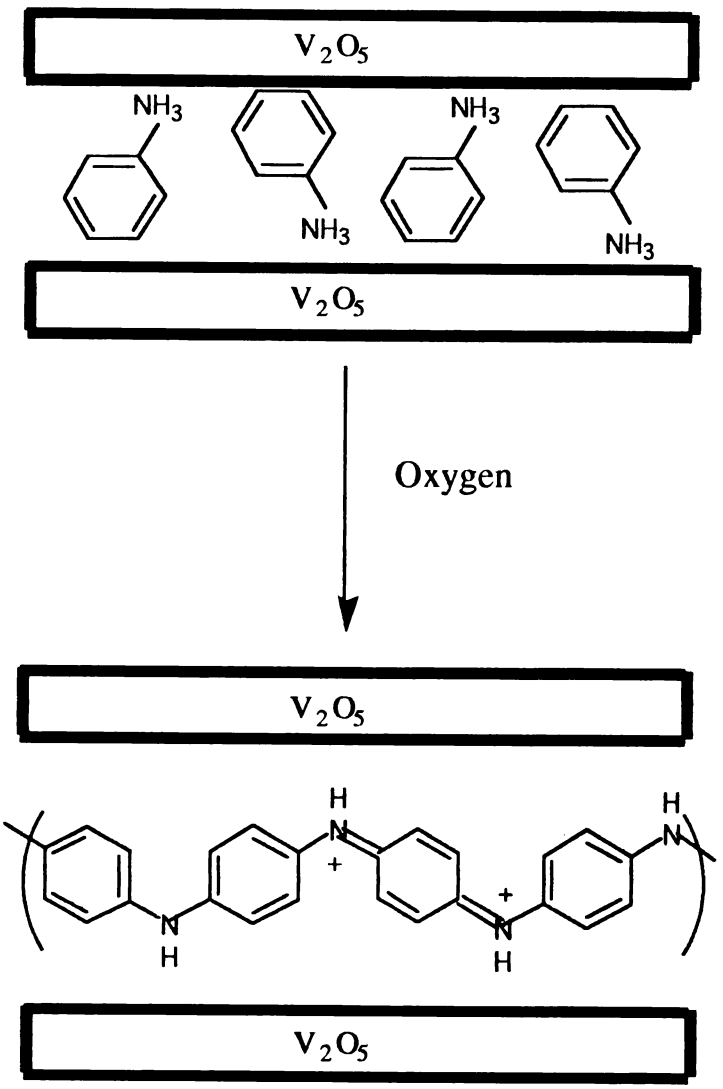

+

H_2O or H_2O_2

Scheme 4.1.

One role for the V_2O_5 framework could be as an electron relay between the reducing guest and oxygen. This is supported by the magnetic susceptibility data of **1** and **2** as shown in Figure 4.3 where **2** shows smaller magnetic susceptibility than **1**. This indicates few unpaired electrons in **2**. Both compounds are paramagnetic exhibiting Curie-Wiess behavior with a contribution of temperature-independent van Vleck paramagnetism (TIP)[8] as represented in eq (4.2).

$$\chi_{(measured)} = \chi_{(Curie\text{-}Weiss)} + \chi_{(TIP)} \qquad (4.2)$$

The TIP term is due to the interaction of the ground state and the excited states in an applied magnetic field and is discussed in chapter five. The $\chi_{(TIP)}$ and μ_{eff} for **1** and **2** are summarized in Table 4.2. Compound **1** has significantly higher μ_{eff} than **2** indicating fewer $V^{4+}(d^1)$ centers in **2**. These data suggest that oxygen removes electrons from the vanadium oxide framework, which in turn removes electrons from anilinium.

Table 4.2. $\chi_{(TIP)}$ and μ_{eff} Values for $(C_6H_5NH_3)_{0.4}V_2O_5.0.4H_2O$ and $\{1/n(\text{-}C_6H_4NH\text{-})_n\}_{0.4}V_2O_5.0.4H_2O$.

Material	μ_{eff}* (BM)	$\chi_{(TIP)}$ (emu/mole)
$(C_6H_5NH_3)_{0.4}V_2O_5.0.4H_2O$	1.30	3.4e-4
$\{1/n(\text{-}C_6H_4NH\text{-})_n\}_{0.4}V_2O_5.0.4H_2O$	0.87	$6.5e^{-5}$

*Calculated from $\chi_{(Curie\text{-}Weiss)}$.

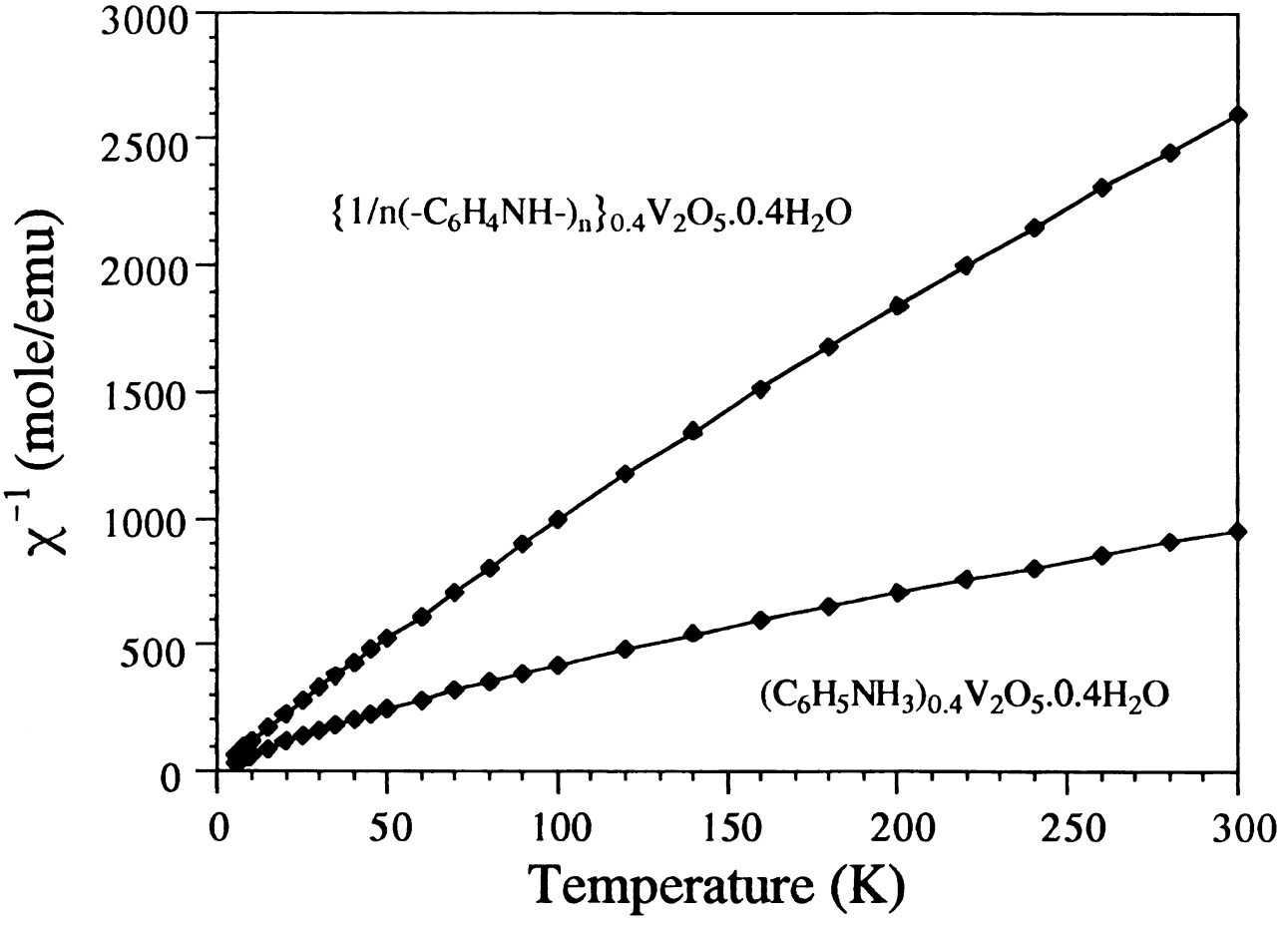

Figure 4.3. Variable temperature magnetic susceptibility of $(C_6H_5NH_3)_{0.4}V_2O_5.0.4H_2O$ and $\{1/n(-C_6H_4NH-)_n\}_{0.4}V_2O_5.0.4H_2O$

4.3.3. Electron Paramagnetic Resonance (EPR)

The room temperature EPR spectra of $(C_6H_5NH_3)_{0.4}V_2O_5.0.4H_2O$ **1** and $\{1/n(\text{-}C_6H_4NH\text{-})_n\}_{0.4}V_2O_5.0.4H_2O$ **2** show symmetric broad signals centered at g ~ 1.96 as illustrated in Figure 4.4. The relatively broad signals derive from the reduced vanadium oxide framework where the V^{4+} centers experience magnetic exchange interactions.[9] The sharp EPR resonance (< 20 G) arising from the polarons of PANI[10] is not observed in **2**, suggesting that magnetic coupling between the PANI and the reduced framework is significant[6]. The peak width (ΔH_{pp}) is 660 G and 130 G for **1** and **2**, respectively. The larger ΔH_{pp} in **1** (increased magnetic exchange broadening) is consistent with larger V^{4+} concentration in this compound compared to **2** and is in agreement with the magnetic susceptibility data for these materials.

4.3.4. Thermogravimetric Analysis (TGA)

TGA diagrams of **1** and **2** under nitrogen flow are shown in Figure 4.5. Both samples lose weight continuously from ~100°C to 900°C. This is due to oxidative degradation of anilinium and PANI by the vanadium oxide framework. Interestingly, **1** shows slightly better thermal stability than **2**, even though **2** contains PAN and is expected to be more stable. This may be because in 2 there are more V^{5+} centers than in **1**, which help to oxidatively degrade PANI. This phenomenon was also observed at fresh and aged $(PANI)_xV_2O_5.nH_2O$ (formed directly from aniline) where fresh samples are more stable than aged samples due to the same reason.

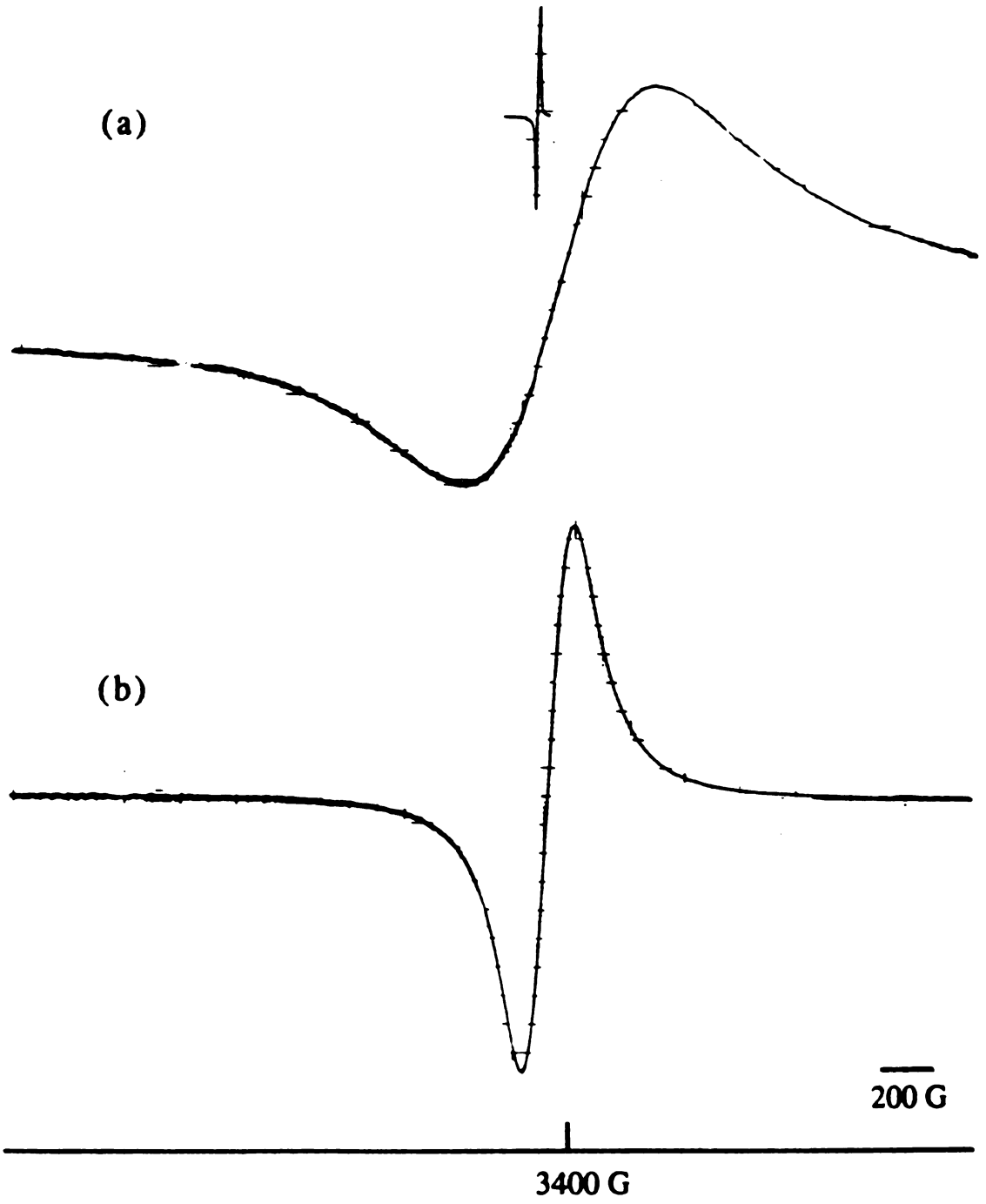

Figure 4.4. Room temperature EPR spectra of (a) $(C_6H_5NH_3)_{0.4}V_2O_5.0.4H_2O$ and (b) $\{1/n(\text{-}C_6H_4NH\text{-})_n\}_{0.4}V_2O_5.0.4H_2O$

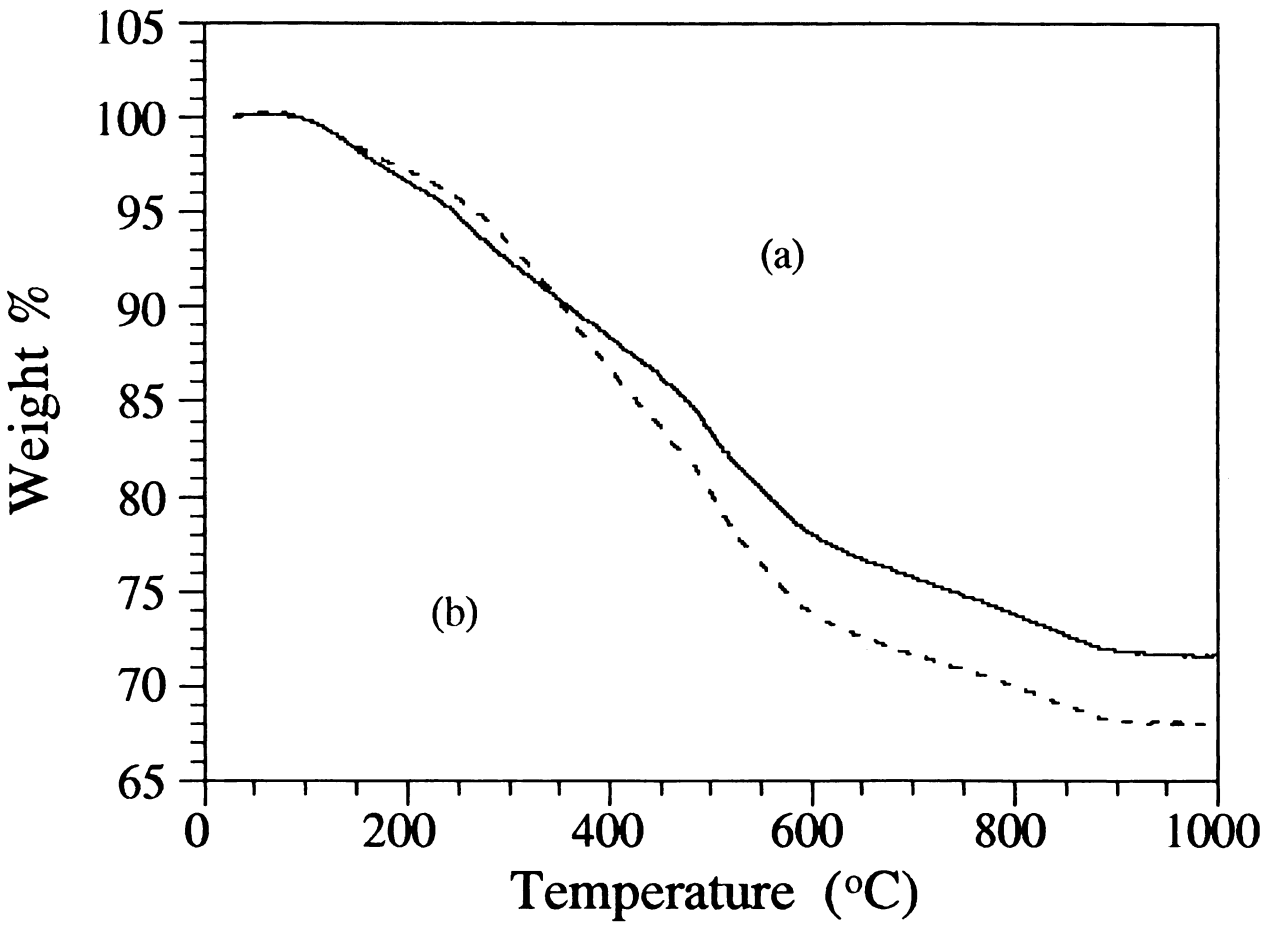

Figure 4.5 TGA diagrams of (a) $(C_6H_5NH_3)_{0.4}V_2O_5.nH_2O$ and (b) $\{1/n(\text{-}C_6H_5NH\text{-})_n\}_{0.4}V_2O_5.nH_2O$ (Samples have been dried under vaccum prior to use)

4.3.5. Molecular Weight Studies

The PANI isolated from **2** is soluble in N-methylpyrrolidinone (NMP) and molecular mass studies using gel permeation chromatography (GPC) were carried simultaneously with similar studies on bulk chemically prepared PANI. The GPC traces reveal a broad monomodal molecular mass distribution, see Figure 4.6, with a peak maximum corresponding to ca. 14,000, compared with 32,000 found for bulk PANI[11], see Table 4.3. By comparison, a molecular mass of 27,000 is obtained from PANI extracted from **3**. The considerably smaller molecular mass of the polymer in **2** is rationalized by the fact that its formation occurred in a structurally constrained environment, in the solid state, in which the polymerization kinetics are slow.

Table 4.3. Molecular Weights of Bulk and Extracted Poly(aniline)

Material	Mp	Mn	Mw
Bulk PANI	32,000	7,700	69,000
Extracted PANI from **2**	14,000	12,300	19,800
Extracted PANI from **3**	27,000	17,700	44,500

M_n (number-average molecular weight) = $(\sum_i N_i M_i)/(\sum_i N_i)$.

M_w (weight-average molecular weight) = $(\sum_i N_i M_i^2)/(\sum_i N_i M_i)$.

M_p : molecular weight at the maximal absorption position.

4.3.6. Charge Transport Properties

Variable-temperature electrical conductivity of **1** and **2** are shown in Figure 4.7. Compound **2** shows enhanced electrical conductivity consistent

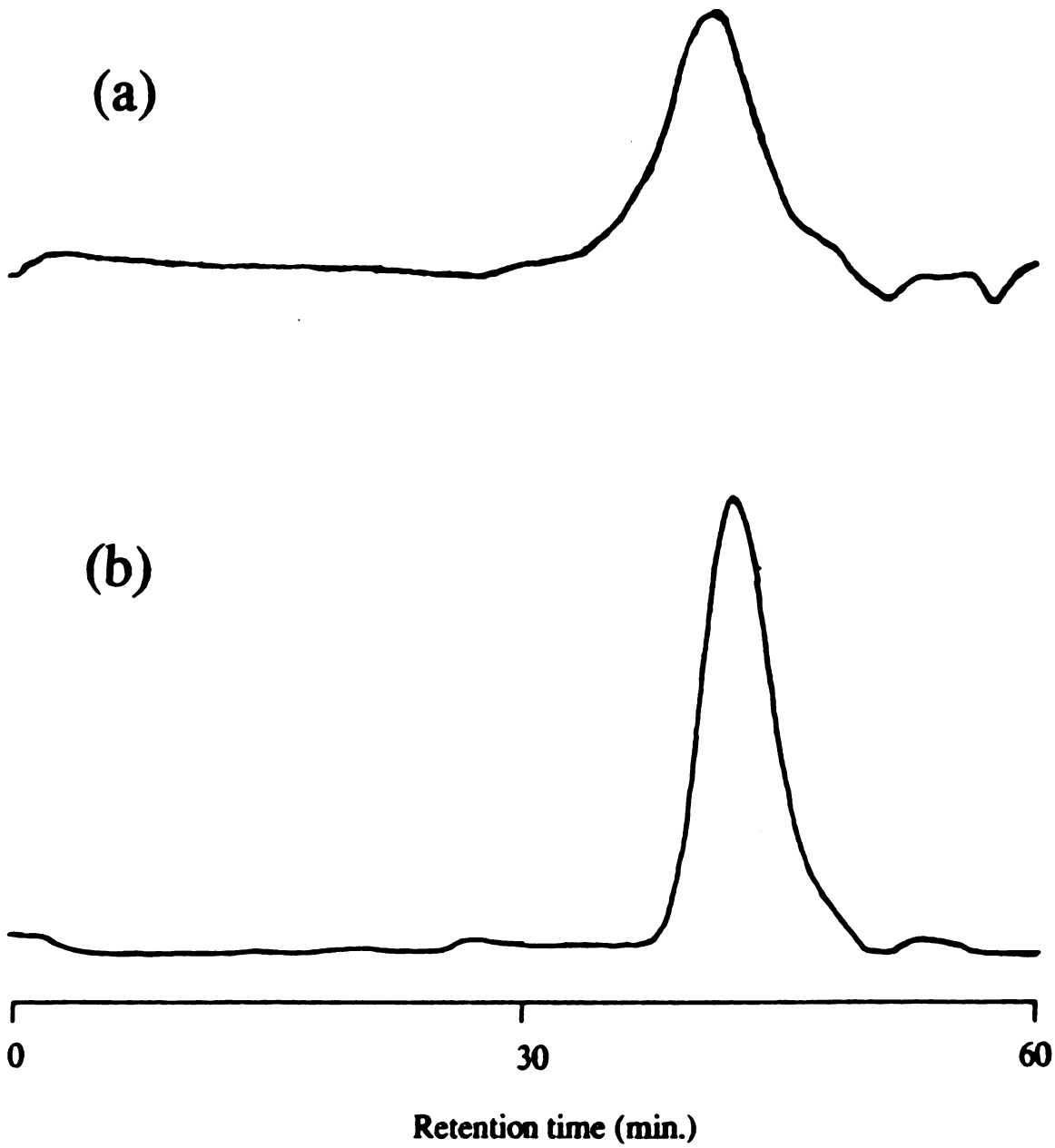

Figure 4.6. GPC diagrams of (a) bulk polyaniline and (b) extracted polyaniline from $\{1/n(-C_6H_4NH-)_n\}_{0.4}V_2O_5.0.4H_2O$.

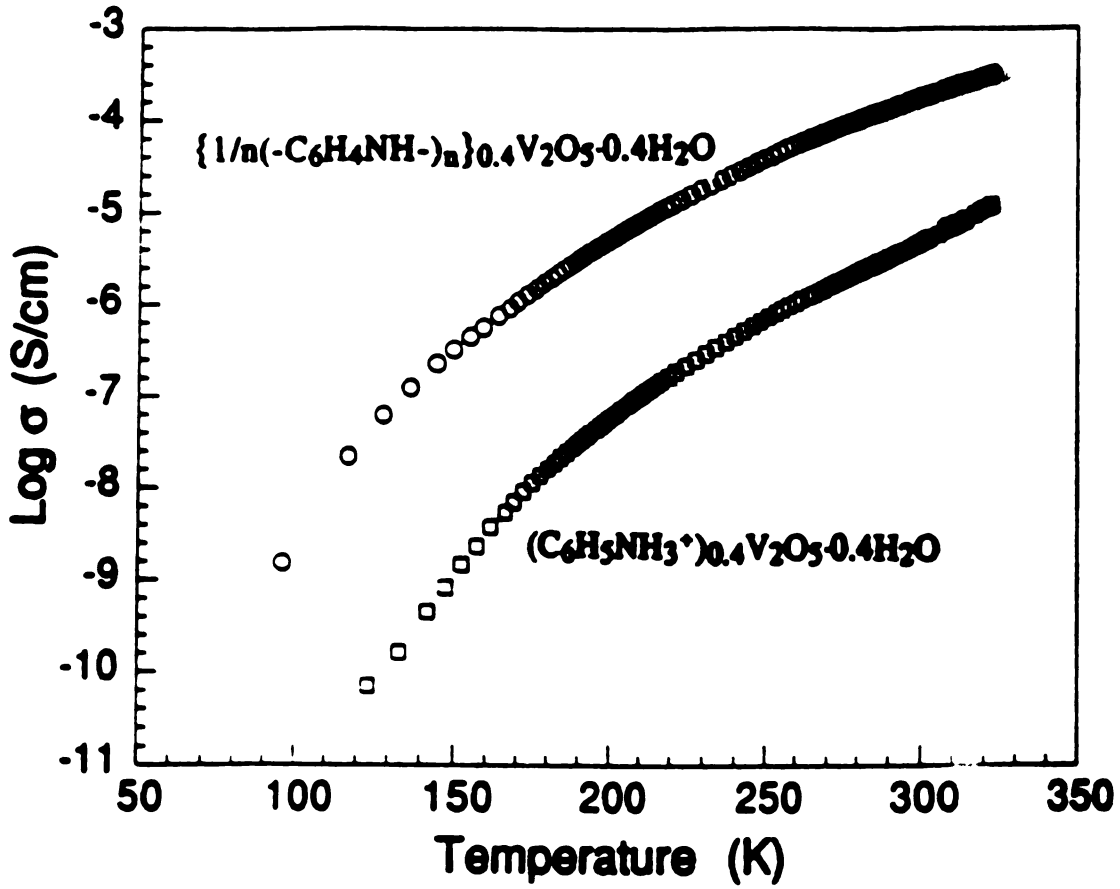

Figure 4.7. Four-probe pressed pellet variable temperature electrical conductivity data of $(C_6H_5NH_3)_{0.4}V_2O_5.0.4H_2O$ and $\{1/n(-C_6H_4NH-)_n\}_{0.4}V_2O_5.0.4H_2O$.

with the presence of PANI. However, the conductivity is approximately two orders of magnitude smaller than that of **3**. This may be due to the smaller chain length of PANI in **2** compared with **3**, described below. The different electrical properties of **1** and **2** are emphasized in the thermoelectric power measurements, see Figure 4.8. At 300K the compound **1** shows a small negative Seebeck coefficient of -15 to -20 μV/K, while **2** exhibits a large negative Seebeck coefficient of -90 to -110 μV/K. The more negative coefficient of **2** is consistent with the fewer charge carriers in the vanadium oxide framework compared with those of **1**, as suggested by the magnetic susceptibility. However, this is inconsistent with the higher conductivity of **2**. The thermally activated temperature dependence of conductivity and the negative Seebeck coefficient suggest n-type semiconducting character for both materials.[12] From these results we conclude that in **2**, despite the presence of PANI, the charge transport properties are dominated by the vanadium oxide. The role of PANI in assisting charge transport is probably significant since the material shows higher conductivity than **1**, but it contains fewer carriers in the vanadium oxide framework.

4.4. Conclusion

The topotactic oxidative polymerization of intercalated anilinium in vanadium oxide xerogel is unprecedented. The reaction itself carriers important implications for studying potentially regioselective intra-lamellar coupling reactions and for the future inclusion synthesis of conjugated polymers in a broad class of layered materials by solid-state polymerization of their corresponding monomer intercalated precursors.

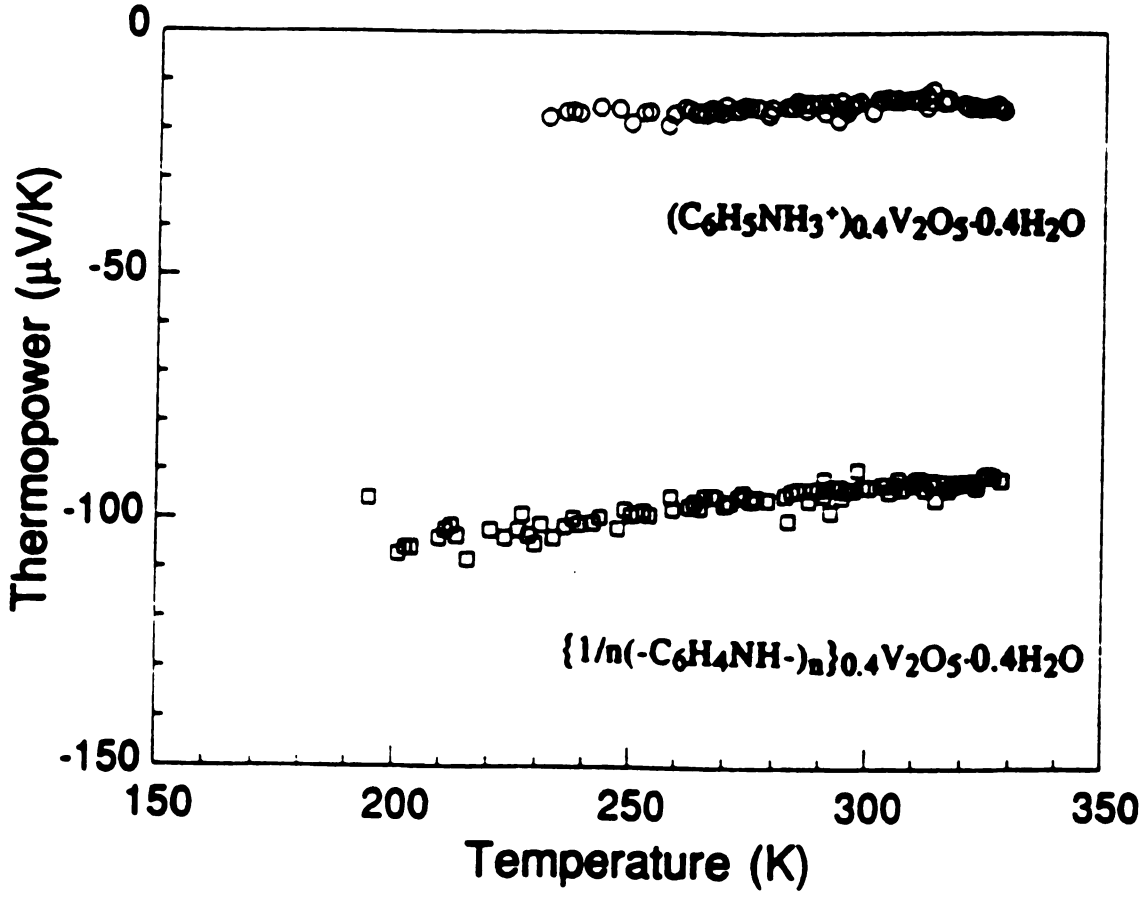

Figure 4.8. Variable-temperature thermoelectric power data of $(C_6H_5NH_3)_{0.4}V_2O_5.0.4H_2O$ and $\{1/n(-C_6H_4NH-)_n\}_{0.4}V_2O_5.0.4H_2O$.

LIST OF REFERENCES

LIST OF REFERENCES

(1) (a) Kanatzidis, M.G.; Wu, C.-G.; Marcy, H.O.; Kannewurf, C.R. *J. Am. Chem. Soc.* **1989**, 111, 4139-4141. (b) Wu, C.-G.; Kanatzidis, M.G.; Marcy, H.O.; DeGroot, D.C.; Kannewurf, C.R. *Polym. Mat. Sci. Eng.* **1989**, 61, 969-973. (c) Wu, C.-G.; Kanatzidis, M.G.; Marcy, H.O.; DeGroot, D.C.; Kannewurf, C.R., NATO Advanced Study Institute "*Lower Dimensional Systems and Molecular Devices*" ed. Metzger, R.M. Plenum Press, Inc. **1991**, pp 427-434.

(2) (a) Lemerle, J.; Nejem, L.; Lefebvre, J. *J. Inorg. Nucl. Chem.* **1980**, 42, 17-20 (b) Legendre, J.-J.; Aldebert, P.; Baffier, N.; Livage, J. *J. Colloid Interface Sci.* **1983**, 94(1), 84-89.

(3) (a) MasBah, H.; Tinet, D.; Crespin, M.; Erre, R.; Setton, R.; Van Damme, H. *Chem. Comm.* **1985**, 935-936 (b) Livage, J. *Chem. Mater.* **1991**, 3, 578-593 (c) Aldebert, P.; Baffier, N.; Gharbi, N.; Livage, J. *J. Mater. Res. Bull.* **1981**, 16, 949-955.

(4) (a) MacDiarmid, A.G.; Chiang, J.-C.; Halpern, M.; Huang, W.-S.; Mu, S.-L.; Somasiri, N.L.D.; Wu, W.; Yaniger, S.I. *Mol. Cryst. Liq. Cryst.* **1985**, 121, 173-180 (b) Snauwaert, PH.; Lazzaroni, R.; Riga, J.; Verbist, J.J. *Synth. Met.* **1987**, 21, 181-187.

(5) Abello, L.; Husson, E.; Repelin, Y.; Lucazeau, G. *J. Solid State Chem.* **1985**, 56, 379-389.

(6) Wu, C.-G. " Ph D. Dissertation" **1992**, Michigan State University.

(7) (a) Genti, G.; Pinelli D.l Trifiro, F. *J. Mol. Catal*, **1990**, 59, 221-231 (b) Ross, R.A.; Fairbridge, C. *Can. J. Chem.* **1984**, 62, 1483-1491.

(8) (a) Drago, R.S. "*Physical Methods in Chemistry*" W.B. Sanders Co.: Philadelphia, **1977** (b) Boudreaux, X.A.; Mulay, L.N. "*Theory and Applications of Molecular Paramagnetism*", John Wiley and Sons: New York **1976**.

(9) (a) Baiker A.; Dollenmeier, P.; Glinski, M.; Reller, A.; Sharma, V.K. J. Catal. 1988, 111, 273-285 (b) Babonneau, F.; Barboux, P.; Josien, F.A.; Livage, J. *J. Chim. Physique* **1985**, 82, 761-766.

(10) (a) Salaneck, W.R.; Liedberg, B.; Inganas, O.; Erlandsson, R.; Lundstrom, I.; MacDiarmid, A.G.; Halpern, M.; Somasiri, N.L.D. *Mol. Cryst. Liq. Cryst.* **1985**, 121, 191-194 (b) Javadi, H.H.S.; Laversanne, R.; Epstein, A.J.; Kohli, R.K.; Scherr, E.M.; MacDiarmid, A.G. *Synth. Met.* **1989**, 29, E439-E444 (c) Cao, Y.; Heeger, A.J. *Synth. Met.* **1990**, 39, 205-214.

(11) (a) Abe, M.; Ohtani, A.; Umemoto, Y.; Akizuki, S.; Ezoe, M.; Higuvhi, H.; Nakamoto, K.; Okuno, A.; Noda, Y. *J. Chem. Soc. Chem. Commun.* **1989**, 1736-1738 (b) Geniès, E.M.; Noël, P. *Synth. Met.* **1992**, 46, 285-292 (c) (b) Scherr, E.M.; MacDiarmid, A.G.; Manohar, S.K.; Masters, J.G.; Sun, Y.; Tang, X.; Druy, M.A.;

Glatkowski, P.J.; Cajipe, V.B.; Fischer, J.E.; Cromack, K.R.; Jozefowicz, M.E.; Ginder, J.M.; McCall, R.P.; Epstein, A.J. *Synth. Met.* **1991**, 41-43, 735-738.

(12) Bullot, J.; Cordier, P.; Gallais, O.; Gauthier, M.; Livage, J. *J. Non-Cryst. Solids* **1984**,68, 135-146.

CHAPTER V

INVESTIGATION OF THE VANADIUM OXIDE XEROGEL BRONZES: $A_xV_2O_5{\cdot}nH_2O$ (A = K AND Cs)

ABSTRACT

The synthesis of bronze-like $A_xV_2O_5{\cdot}nH_2O$ xerogels (A = K and Cs, $0.05 < x < 0.6$) and studies of their chemical, physical and charge transport properties as a function of x are reported. The reduced V_2O_5 xerogels were prepared by the reaction of the xerogel with various amounts of alkali iodide (KI and CsI) in acetone under N_2 atmosphere for three days. X-ray diffraction and spectroscopic data indicate that the V_2O_5 framework in $A_xV_2O_5{\cdot}nH_2O$ maintains the pristine V_2O_5 xerogel structure. The increased V^{4+} (d^1) concentration in the V_2O_5 framework causes the disappearance of EPR hyperfine structure and the increase of magnetic susceptibility and electrical conductivity. The magnetic behavior is best described as Curie-Weiss type coupled with temperature independent paramagnetism (TIP). The Curie constant and EPR peak-width of the $A_xV_2O_5{\cdot}nH_2O$ materials show a maximum value at $x \sim 0.3$, suggesting antiferromagnetic coupling of V^{4+} centers as their population increases. Electrical conductivity slightly increases with V^{4+} concentration, and its temperature dependence indicates a thermally activated process. The thermoelectric power of the $A_xV_2O_5{\cdot}nH_2O$ materials is negative and becomes less negative with increasing V^{4+} concentration. Optical diffuse reflectance spectra are reported.

5.1. Introduction

Recently, it was shown by our group that the redox intercalation of organic monomers such as aniline, pyrrole and 2,2'-bithiophene yields layered materials containing monolayers of conductive polymers in the intralamellar space of V_2O_5 xerogel[1]. The vanadium oxide network and ambient oxygen are reduced to form V^{4+} centers while organic monomers are oxidatively polymerized into electrically conductive polymers. This results in new molecular composites of two electrically active but chemically diverse components: organic conductive polymers and inorganic vanadium bronzes. In order to achieve a better understanding of the role of the conductive polymer inside the oxide sheets, it is important to understand the nature and properties of the reduced V_2O_5 framework alone. Of course, numerous studies have been published on crystalline bronze phases of the type $A_xV_2O_5$[2] but in these materials the V_2O_5 structure is different from that of V_2O_5 xerogels and it varies as a function of A and x. Therefore, these materials are not representative of the reduced xerogel. To our knowledge, complete and systematic studies of compounds with a reduced V_2O_5 xerogel framework are rare.[3] Therefore, a series of reduced V_2O_5 xerogels were prepared by the reaction of the xerogel with various amounts of alkali iodide (KI and CsI). The intercalants are closed-shell K^+ and Cs^+ ions which can be considered as "innocent" species (e.g. diamagnetic and insulating), thus, allowing the properties of the reduced V_2O_5 framework to be studied with no interference from the guests.

In this paper, we report the synthesis of the reduced bronze-like V_2O_5 xerogels as well as their optical, magnetic and charge transport properties as a function x (i.e. V^{4+} concentration).

5.2. Experimental Section

5.2.1. Materials

Sodium metavanadate ($NaVO_3$), potassium iodide (KI), cesium iodide (CsI) were purchased from Aldrich Co., Milwaukee, WI and were used without further purification. Elemental analyses were done by Galbraith Laboratories, Knoxville, TN and Oneida Research Services, Inc., Whitesboro, NY.

5.2.2. Measurements

Infrared spectra were recorded from 4000 to 400 cm^{-1} with a resolution of 1 cm^{-1} on a Nicolet 740 FT-IR spectrometer. Samples were recorded in a pressed KBr matrix under N_2 flow. IR diffuse reflectance spectra were also recorded on the same instrument equipped with a reflectance attachment purchased from Spectra. Tech. Inc. Samples were pressed into pellets and directly put on a sample holder. A gold mirror was used as the reference.

The instruments and experimental setups for X-ray diffraction, EPR, magnetic susceptibility, UV/Vis, electrical conductivity and thermopower are the same as those in chapter 2.

Quantitative elemental analysis was done by the SEM/EDS (Scanning Electron Microscopy/Energy Dispersive Spectroscopy) technique on a JEOL JSM-35C microscope equipped with a Tracor Northern TN 55000

X-ray microanalysis attachment. Samples were glued on an aluminum stub with conductive carbon paint for the dissipation of accumulated charges. Typical experiment conditions are as followed: accelerating voltage, 20 KeV; detector window, beryllium; take-off angle, 27 deg.; accumulation time, 60 sec. A standardless quantitative analysis solfware program was used to analyze the characteristic X-ray peaks of the elements present in the sample. Correction factors for K/V and Cs/V ratios were determined from known compounds such as KVO_3 and $CsVO_3$. The alkali-to-vanadium ratio for each sample obtained by averaging three independent measurements.

The calculation of one-dimensional (1-D) electron density maps was based on the X-ray reflection data using the observed (00l) group of reflections. Eight reflections were used for $Cs_{0.27}V_2O_5 \cdot nH_2O$ out to d_{008} = 1.37Å. The intensities were obtained from the integrated peak areas. The structure factors of these reflections were derived from their intensities and corrected for Lorentz-polarization effects. The signs of the phases for the structure factor calculation were directly obtained from the scattering contributions of the V_2O_5 framework alone. The signs of the phases were also checked by recalculation including the contribution of the Cs^+ ions. All but one reflection changed sign but this did not substantially change the electron density pattern. The calculated and observed structure factors of $Cs_{0.27}V_2O_5 \cdot nH_2O$ are shown in Table 5.1.

5.2.3. Preparation of V_2O_5 Xerogel

See chapter two

5.2.4. Preparation of $A_xV_2O_5 \cdot nH_2O$

Table 5.1. X-ray Diffraction Data, $F_{(obsd)}$ and $F_{(calcd)}$ of $Cs_{0.27}V_2O_5 \cdot nH_2O$

(hkl)	d(obsd). (Å)	d(calcd). (Å)	Intensity (count)	$\|F_{(obsd)}\|$*	$F_{(calcd)}$[1]	$F_{(calcd)}$[2]
001	11.12	11.12	1617	8.900	20.199	13.431
002	5.57	5.54	70	3.735	-7.452	-1.370
003	3.66	3.68	783	19.332	-13.934	-19.024
004	2.74	2.75	78	8.384	-13.611	-9.587
005	2.20	2.19	172	15.993	-10.480	-13.534
006	1.79	1.82	11	5.166	-1.002	1.104
007	1.56	1.55	15	11.330	5.282	3.773
008	1.37	1.35	16	8.622	4.221	5.235

[1]Includes scattering of V_2O_5 only. [2]Includes contributions of V_2O_5 and Cs; R = 0.28, K = 4.5 (Oka's model). R calculated as $R = \sum(|K|F_o|-|F_c||)/\sum(K|F_o|)$. *Corrected by K.

Powdered V_2O_5 xerogel (0.5 g, 3.38 mmol) was added to a 50 ml of acetone with a stoichiometric amount of KI or CsI. The KI/V_2O_5 and CsI/V_2O_5 molar ratios were varied from 0.1 to 1.0 in increments of 0.1. The reaction was stirred under N_2 atmosphere for three days. The dark product was filtered, washed with acetonitrile and then dried under vacuum. The compositions of $A_xV_2O_5{\cdot}nH_2O$ compounds were determined from Elemental analysis and SEM/EDS. An attempt to produce the $A_xV_2O_5{\cdot}nH_2O$ materials with $x > 0.6$ failed, because over-reduction caused amorphization of the V_2O_5 framework. The materials used to calculate the 1-D electron density map were prepared using films of $V_2O_5{\cdot}1.8H_2O$ xerogel. The *n* is ~1.1 when $x < 0.1$ and ~ 0.5-0.6 when $x > 0.1$.

5.3. Results and Discussion

5.3.1. Structure of V_2O_5 Xerogel

The structure of the $V_2O_5{\cdot}nH_2O$ xerogel is not accurately known but two motifs have been proposed. Livage and coworkers suggested a layered structure composed of a single corrugated slab of V_2O_5 with a corrugation step of 2.8 Å.[4] The layers between the steps have the same structure as crystalline V_2O_5. Oka and coworkers support a bilayer model with flat V_2O_5 slabs based on the structure of $Na_xV_2O_5$.[5] These models are shown in Figure 5.1. They mostly satisfy the observed X-ray diffraction data in the reflection mode (00l reflections), although a poor agreement is observed with X-ray diffraction data in the transmission mode. However, based on the observed density of $V_2O_5{\cdot}nH_2O$ xerogel which is ~ 2.5 g/cm^3, Oka's model appears to be most consistent (d_{calcd} ~ 2.87 g/cm^3). The Livage model gives a d_{calcd} ~ 1.5 g cm^3. The density of $A_xV_2O_5{\cdot}nH_2O$

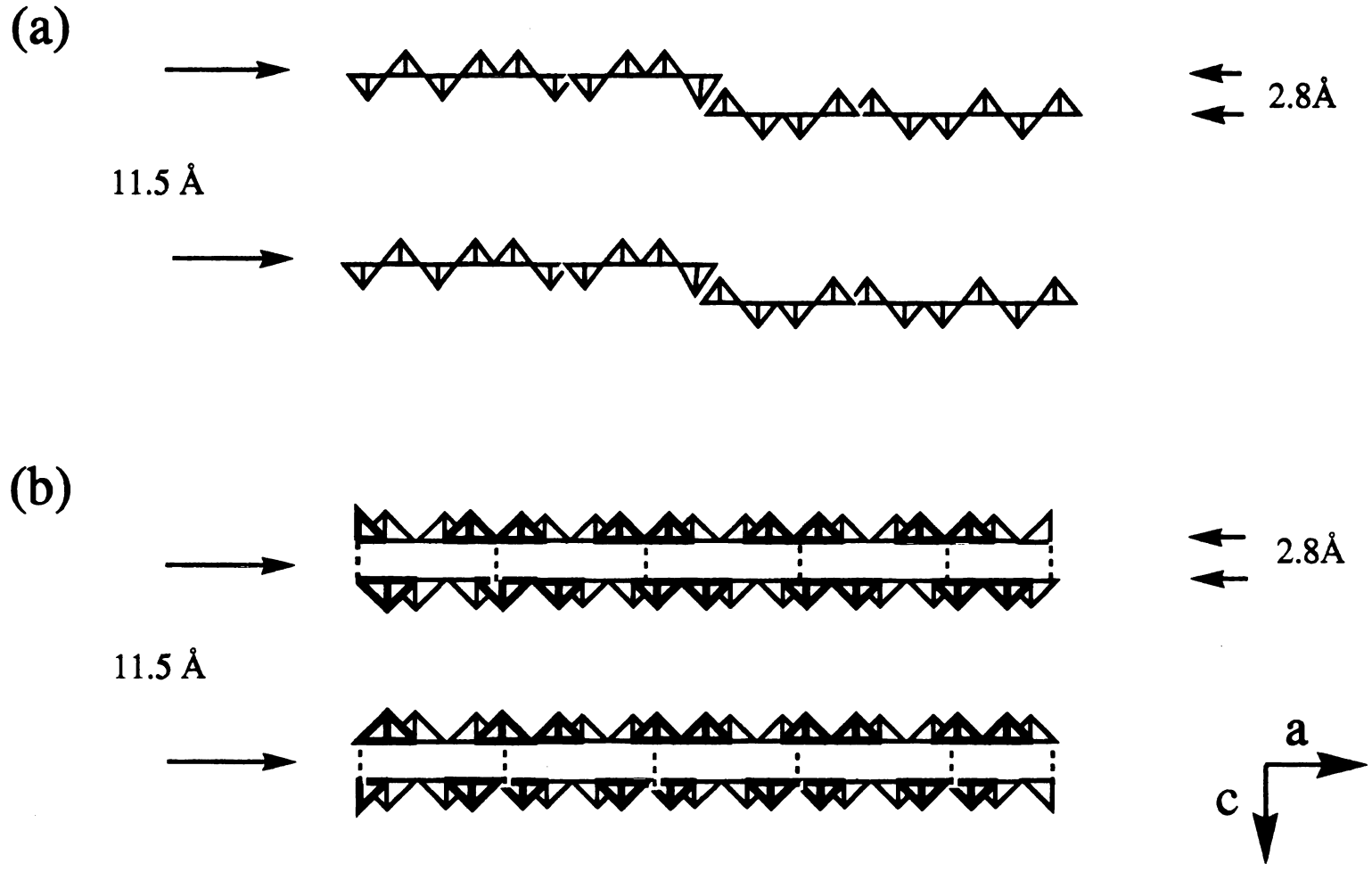

Figure 5.1. Schematic illustration of the proposed structure of V_2O_5 xerogel projected onto the ac plane : (a) from Livage *et al.*, (b) from Oka *et al.*

ranges between 2.7 and 3.3 g/cm^3. Therefore, we prefer to use Oka's model. Incidentally, similar calculations based on Livage's model do substantially change the resulting conclusions

5.3.2. Synthesis and Spectroscopy

The reduced V_2O_5 xerogels were produced according to eq(5.1).

$$y\ AI + V_2O_5.nH_2O \longrightarrow A_yV_2O_5{\cdot}nH_2O + (y/2)\ I_2 \qquad (5.1)$$

$A = K, Cs$

The V_2O_5 xerogel oxidizes iodide to iodine and the alkali ions are intercalated into the reduced framework to achieve electroneutrality. The composition, interlayer distance, and infrared spectroscopic data for $K_xV_2O_5{\cdot}nH_2O$ and $Cs_xV_2O_5{\cdot}nH_2O$ compounds are summarized in Table 5.2 and Table 5.3, respectively. The $A_xV_2O_5{\cdot}nH_2O$ compounds are brown or green when $x < 0.1$ and turn blue when $x \geq 0.1$. The hydrated water, *n*, decreases with the rise of x from 1.8 when $x = 0$ (V_2O_5 xerogel) to ~ 0.6 when $x \sim 0.1$ and becomes constant when $x > 0.1$. Generally, the infrared spectra of the reduced compounds show three characteristic vibration bands from the V_2O_5 framework below 1100 cm^{-1}. A typical infrared spectrum from $K_{0.33}V_2O_5{\cdot}nH_2O$ is shown in Figure 5.2. The band at ~ 1000 cm^{-1} is assigned to the V=0 vibration and the bands at ~750 cm^{-1} and ~500 cm^{-1} are attributed to the in-plane and out-of-plane V-O-V vibrations,[6] respectively. The presence of the three bands suggests that the reduced V_2O_5 framework is intact. The V=O vibration generally shifts to lower energy as the increase of alkali ion concentration increases, see Figure 5.3. The red shift is due to the addition of electrons into antibonding d orbitals

Table 5.2. Summary of Composition, Color, Interlayer Spacing and Infrared Data for $K_xV_2O_5 \cdot nH_2O$

Formula	Color	d-spacing (Å)	Vibration bands (cm^{-1})
$V_2O_5 \cdot 1.8H_2O$	red	11.55	1015, 760, 510
$K_{0.08}V_2O_5.1.1H_2O$	green	11.65	1012, 759, 513
$K_{0.26}V_2O_5 \cdot nH_2O$	dark blue	10.28	999, 762, 527
$K_{0.33}V_2O_5 \cdot nH_2O$	dark blue	10.10	996, 766, 537
$K_{0.39}V_2O_5 \cdot nH_2O$	dark blue	10.05	994,760, 522
$K_{0.44}V_2O_5 \cdot nH_2O$	dark blue	9.87	996, 774, 547
$K_{0.47}V_2O_5 \cdot nH_2O$	dark blue	9.86	996, 761, 530
$K_{0.55}V_2O_5 \cdot nH_2O$	dark blue	9.72	984, 759, 527

1) *n* is in the range of 0.5~0.6.

Table 5.3. Summary of Composition, Color, Interlayer Spacing and Infrared Data for $Cs_xV_2O_5 \cdot nH_2O$

Formula	Color	d-spacing (Å)	Vibration bands (cm^{-1})
$Cs_{0.07}V_2O_5.1.1H_2O$	brown	11.65	1012, 756, 513
$Cs_{0.18}V_2O_5 \cdot nH_2O$	dark blue	11.2	1010, 760, 520
$Cs_{0.26}V_2O_5 \cdot nH_2O$	dark blue	10.8	1006, 762, 532
$Cs_{0.28}V_2O_5 \cdot nH_2O$	dark blue	10.8	999,754, 535
$Cs_{0.35}V_2O_5 \cdot nH_2O$	dark blue	10.8	999, 755, 524
$Cs_{0.38}V_2O_5 \cdot nH_2O$	dark blue	10.8	997, 762, 530
$Cs_{0.41}V_2O_5 \cdot nH_2O$	dark blue	10.7	994, 755, 523

1) *n* is in the range of 0.5~0.6.

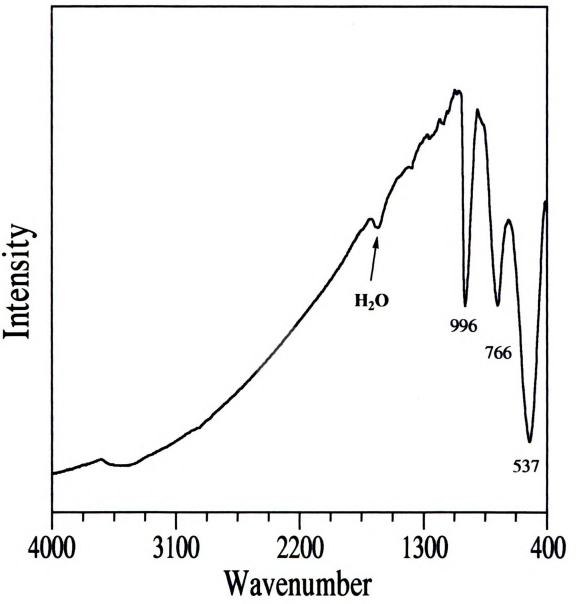

Figure 5.2. Infrared spectrum of $K_{0.33}V_2O_5$ $0.5H_2O$ (KBr pellet).

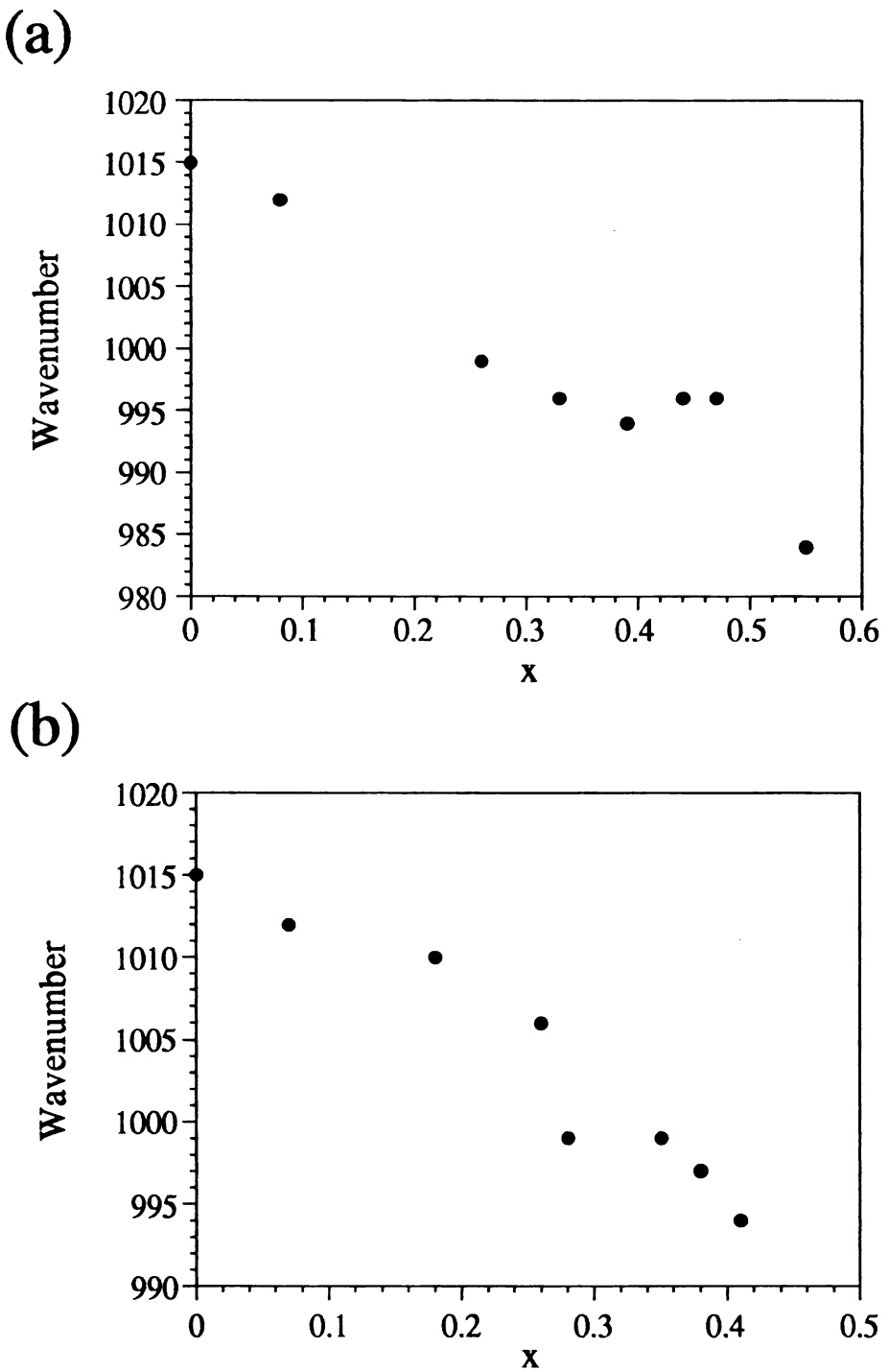

Figure 5.3. Infrared spectral shifts of V=O vibration energy as a function of x : (a) $K_xV_2O_5{\cdot}nH_2O$ and (b) $Cs_xV_2O_5{\cdot}nH_2O$.

of vanadium, probably coupled with ionic interactions between the oxygen of V=O and the alkali ions.

The optical absorption spectra of the $A_xV_2O_5{\cdot}nH_2O$ compounds show a very broad band, centered around 1400 nm with a tail extending into the infrared region (Figure 5.4). The band is described as an intervalence transition from V^{4+} to V^{5+} centers.[3] It is absent in pristine V_2O_5 xerogel due to the very small number of V^{4+} centers. The appearance of this intense intervalence band confirms that the V_2O_5 framework is reduced.

5.3.3. X-ray Diffraction

Figure 5.5 shows a typical X-ray diffraction pattern for the $A_xV_2O_5{\cdot}nH_2O$ compounds in which (00l) peaks dominate, indicating that the layer structure is maintained. The interlayer spacing slightly decreases from 11.65 Å when x = 0.08, to 9.72 Å when x = 0.55 in $K_xV_2O_5{\cdot}nH_2O$, and from 11.65 Å when x = 0.07 Å, to 10.7 Å when x = 0.41 in $Cs_xV_2O_5{\cdot}nH_2O$ (Tables 5.2 & 5.3). The decrease in the interlayer height with increasing x is due to the loss of intercalated water and the increased ionic attractive interactions between the positively charged alkali ions and the negatively charged V_2O_5 layers. For the same x, the $Cs_xV_2O_5{\cdot}nH_2O$ show a slightly higher expansion than the $K_xV_2O_5{\cdot}nH_2O$, consistent with the larger size of Cs^+.

In order to determine the position of alkali ions in the V_2O_5 framework, we performed the 1-D electron density calculation along the layer stacking direction (c axis). Based on Oka's model, a projection of the calculated electron density of $Cs_{0.27}V_2O_5{\cdot}0.5H_2O$ is shown in Figure 5.6. Clearly, the two strong peaks at z = 0.87 and 1.13 are observed with a

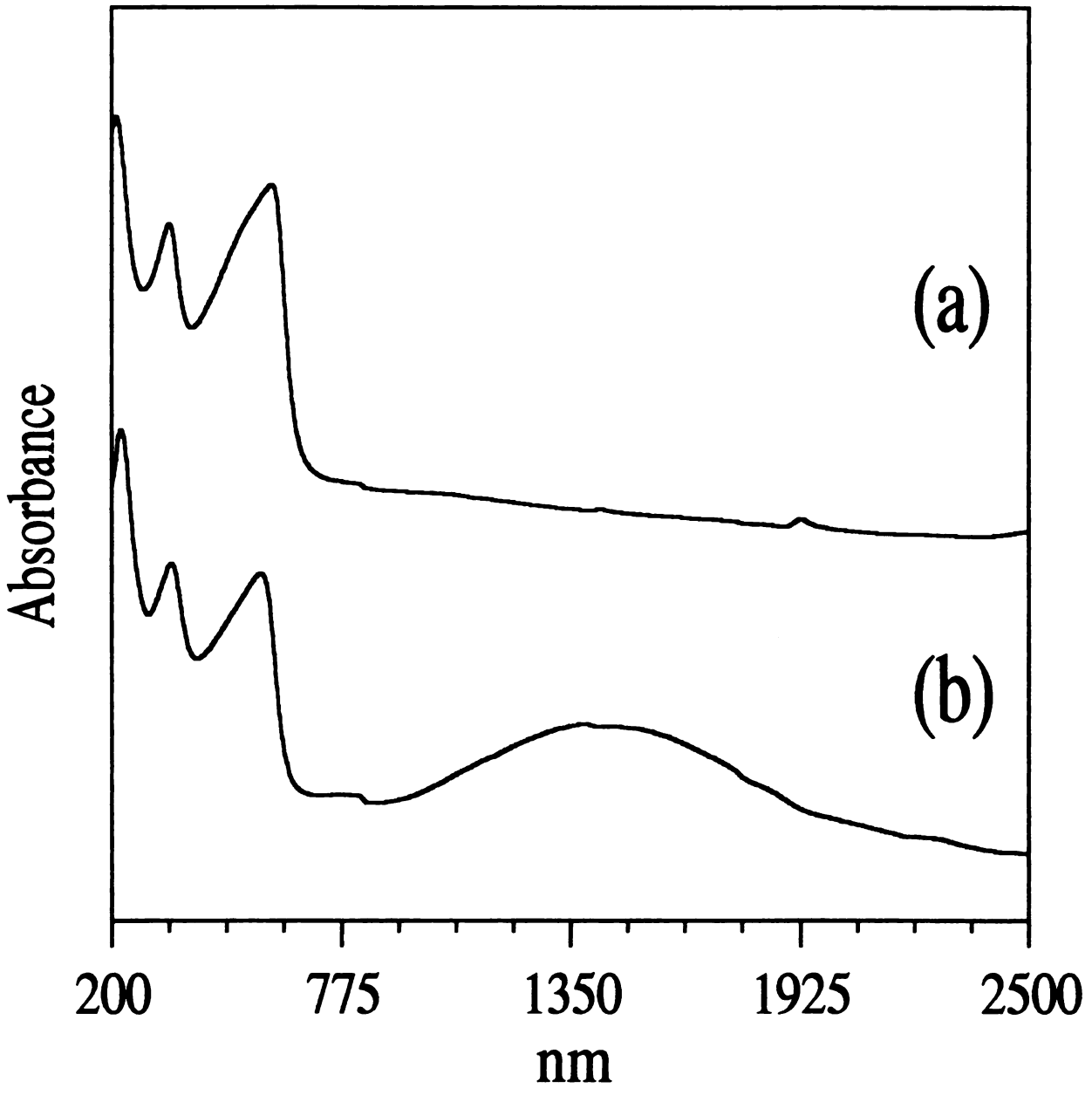

Figure 5.4. Optical absorption spectra of (a) V_2O_5 xerogel and $Cs_{0.27}V_2O_5 \cdot 0.5H_2O$.

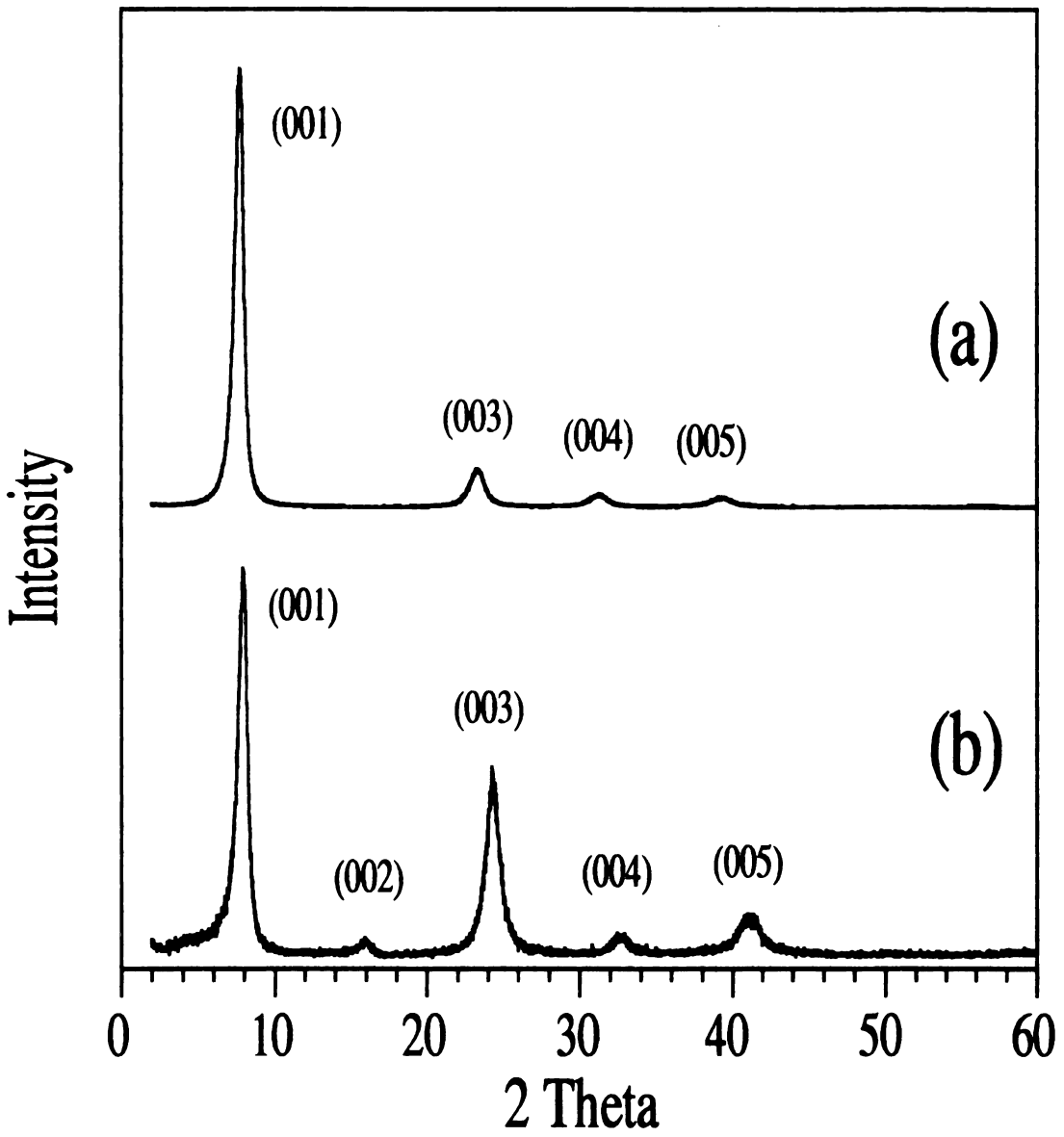

Figure 5.5. X-ray diffraction patterns of (a) V_2O_5 xerogel and (b) $Cs_{0.27}V_2O_5 \cdot 0.5H_2O$.

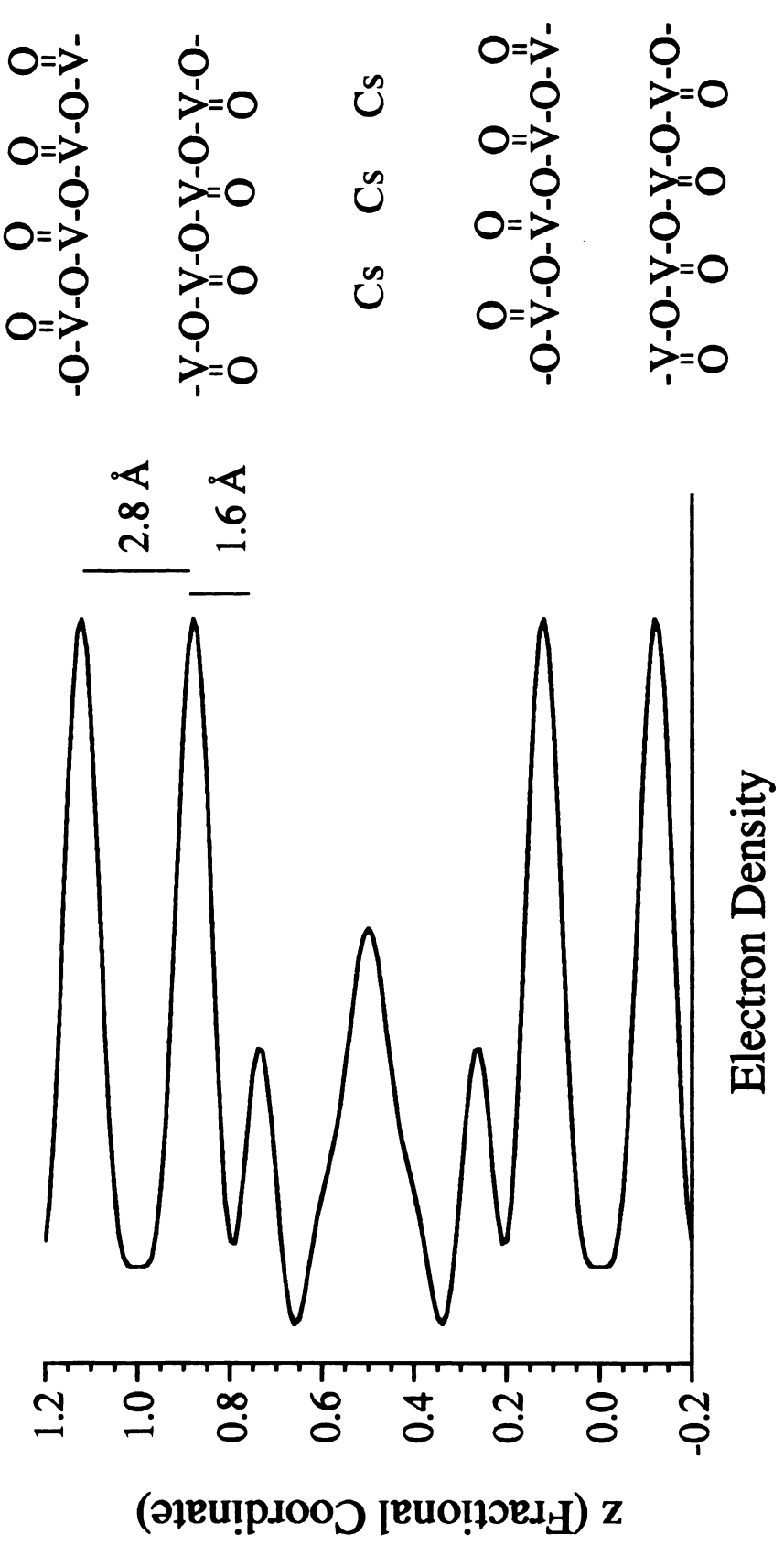

Figure 5.6. Projection of the electron density of $Cs_{0.27}V_2O_5{\cdot}nH_2O$ calculated from Oka's model and illustrations of the deduced arrangement of Cs in the interlayer space.

separation of 2.8 Å. They are readily assigned to the two $VO_{1.5}$ sheets. The peak at z = 0.73 shows a distance of 1.6 Å with the most adjacent $VO_{1.5}$ sheet, consistent with vanadyl groups perpendicular to the $VO_{1.5}$ sheet. This is consistent with the projection of a monolayer of the V_2O_5 structure along this axis. The peak at z = 0.5 is attributed to Cs^+ ions, residing in the middle of the interlayer gallery. Similar results are also observed for the other $A_xV_2O_5 \cdot nH_2O$ compounds with x < 0.3. However, the electron density calculation for the $A_xV_2O_5 \cdot nH_2O$ with x > 0.3 is impossible due to lower crystallinity and insufficient numbers of reflections.

5.3.4. Magnetic Susceptibility Studies

Magnetic susceptibility data as a function of temperature for several $A_xV_2O_5 \cdot nH_2O$ compounds are illustrated in Figure 5.7. The data when plotted as $1/\chi$ vs T, show a slight curvature away from linear dependence, thus deviating from Curie-Weiss law. However, a linear dependence is obtained when a small constant correction is applied to the susceptibility, see Figure 5.8. We interpret the magnetic behavior as Curie-Weiss type with a small amount of deviations due to van Vleck temperature-independent paramagnetism (TIP).[7] Thus, the measured molar magnetic susceptibility (χ_m) can be expressed by eq (5.2).

$$\chi_m = \chi_{(\text{Curie-Weiss})} + \chi_{(\text{TIP})} \qquad (5.2)$$

$$\chi_{(\text{Curie-Weiss})} = \frac{C}{T - \theta} \qquad (5.3)$$

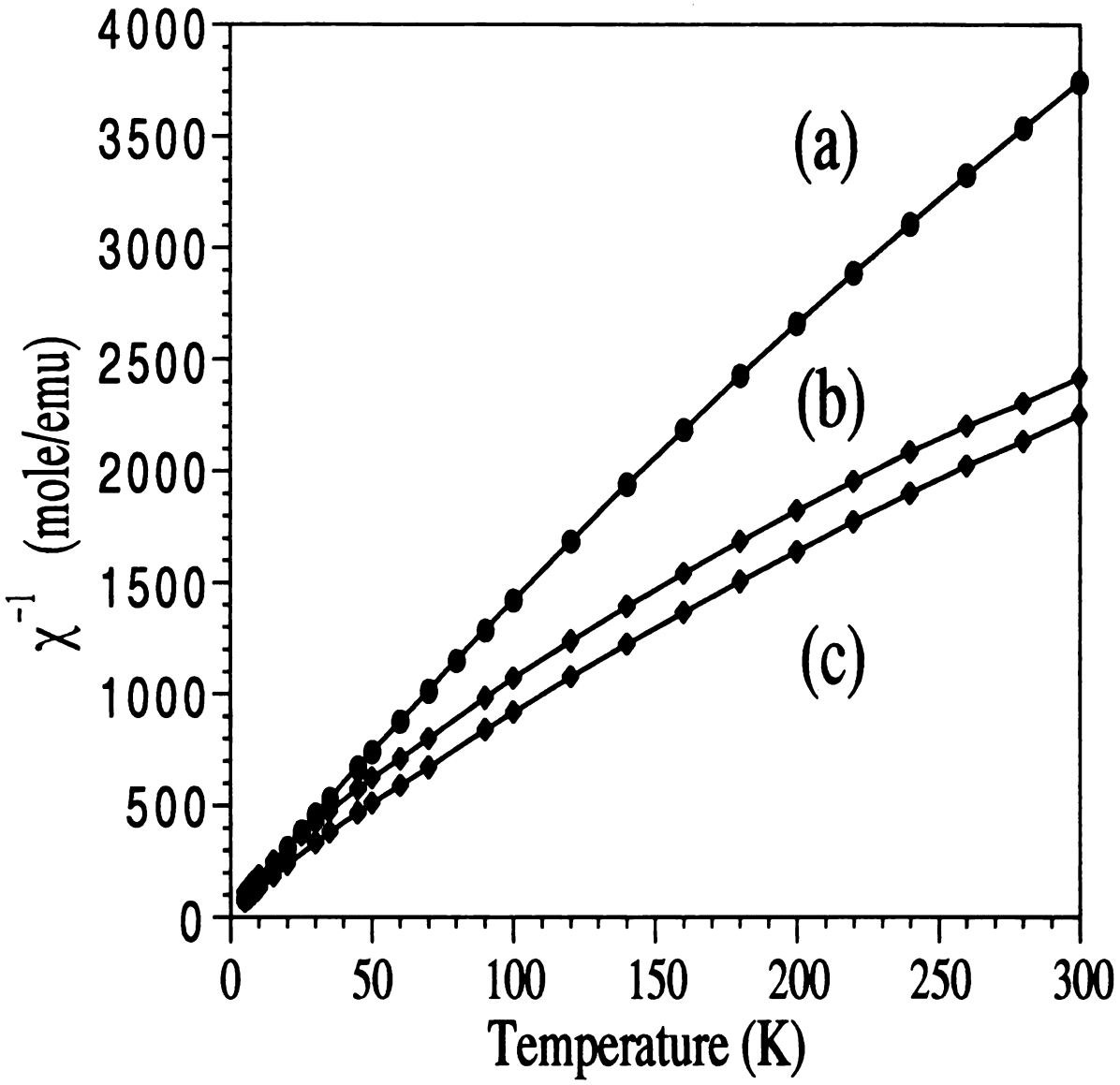

Figure 5.7. Inverse magnetic susceptibility as a function of temperature for (a)$K_{0.08}V_2O_5{\cdot}nH_2O$, (b)$K_{0.26}V_2O_5{\cdot}nH_2O$ and $K_{0.33}V_2O_5{\cdot}nH_2O$.

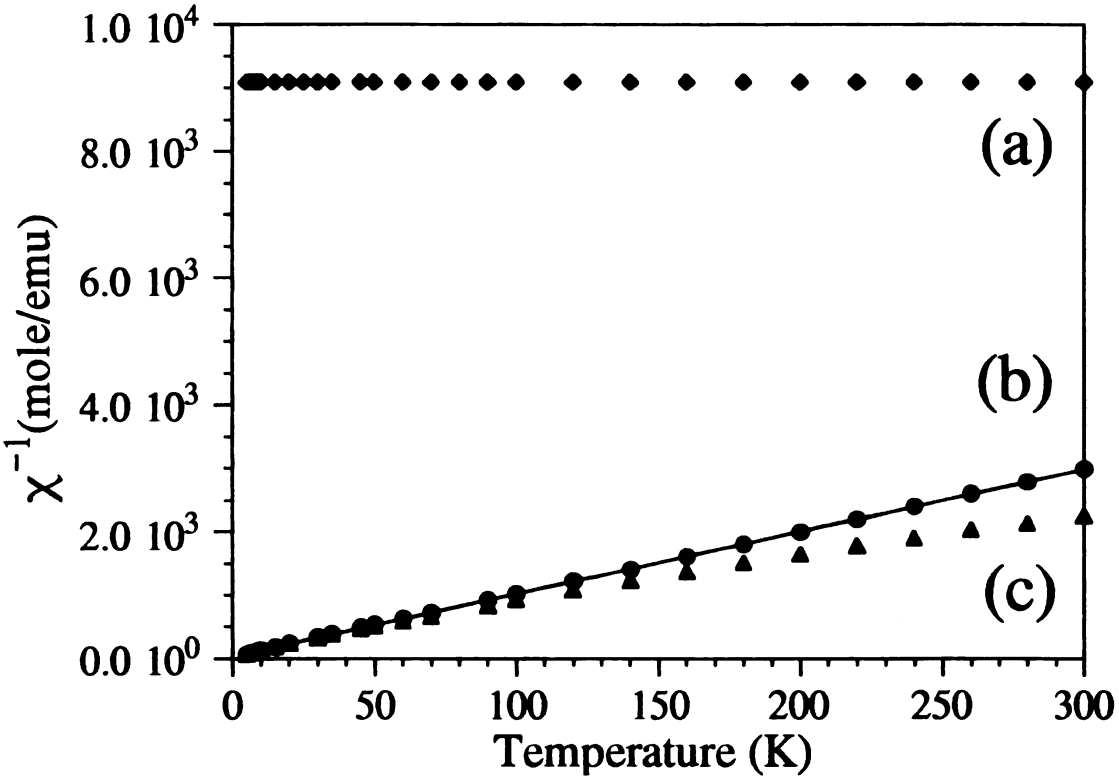

Figure 5.8. Inverse magnetic susceptibility as a function of temperature for $K_{0.26}V_2O_5 \cdot nH_2O$: (a) $\chi_{(TIP)}$, (b) $\chi_{(Curie\text{-}Weiss)}$ and (c) χ_m.

Substituting eq (5.3) for $\chi_{(Curie\text{-}Weiss)}$ in eq (5.2) produces eq (5.4)

$$\chi_m = \frac{C}{T-\theta} + \chi_{(TIP)} \qquad (5.4)$$

where $C = Ng^2\beta^2/4k$ is the Curie constant and θ is the Weiss constant. Fitting the measured magnetic susceptibility data with eq (5.4), the resulting $\chi_{(TIP)}$, C and θ for the $A_xV_2O_5{\cdot}nH_2O$ compounds were extracted and are summarized in Tables 5.4 and 5.5. Depending on x, the μ_{eff} calculated from $\chi_{(Curie\text{-}Weiss)}$ is in the range between 0.6 and 1.0 BM, confirming the increased number of V^{4+} centers in the framework. For comparison, pristine V_2O_5 xerogel has a μ_{eff} of ~ 0.3-0.4 BM because of residual small amounts of V^{4+} impurities which unavoidably form during preparation.

The small correction applied to the susceptibility data is attributed to temperature independence paramagnetism. The TIP term originates from the second-order Zeeman effect which describes the interaction of the ground state and the excited states in an applied magnetic field. The value is inversely proportional to the energy differences ($\Delta E = E_e - E_g$) between the ground and excited state[7], see eq (5.5). Thus the $\chi_{(TIP)}$ to be significant the ΔE must be very small.

$$\chi_{(TIP)} = 2N\beta^2 \sum \frac{\langle \psi_g | \hat{o}p | \psi_e \rangle^2}{\Delta E} \qquad (5.5)$$

N is Avogadro's number, β is the Bohr magneton of the electron, ψ_g and ψ_e are wave functions of the ground and excited states respectively, and $\hat{o}p$

Table 5.4. Magnetic Susceptibility Data for $K_xV_2O_5 \cdot nH_2O$ Compounds

x	χ_m (emu/mole)	$\chi_{(TIP)}$ (emu/mole)	μ_{eff}* (spin only)	C	θ (K)
0.08	2.67e-4	5.6±4.0e-5	0.72±0.07	0.06±0.01	-2±2
0.26	4.44e-4	1.1±0.5e-4	0.89±0.06	0.1±0.01	-3.7±4
0.33	5.30e-4	2.0±0.5e-4	0.88±0.07	0.11±0.01	-5.7±5
0.39	4.14e-4	1.4±0.4e-4	0.83±0.03	0.09±0.01	-6±4.6
0.47	3.98e-4	1.4±0.4e-4	0.78±0.06	0.08±0.01	-7.8±4
0.55	4.32e-4	1.7±0.4e-4	0.78±0.06	0.08±0.01	-9.6±5

*Calculated from (χ_m-$\chi_{(TIP)}$).

Table 5.5. Magnetic Susceptibility Data for $Cs_xV_2O_5 \cdot nH_2O$ Compounds

x	χ_m (emu/mole)	$\chi_{(TIP)}$ (emu/mole)	μ_{eff}* (spin only)	C	θ (K)
0.07	2.13e-4	4.9±2.0e-5	0.62±0.04	0.05±0.01	0.65±3
0.18	3.83e-4	7.0±4.0e-5	0.86±0.06	0.09±0.01	-1.6±3.4
0.26	4.97e-4	1.4±0.6e-4	0.89±0.05	0.11±0.02	-3.9±5
0.28	5.75e-4	2.2±0.5e-4	0.92±0.06	0.10±0.01	-5±5
0.35	5.20e-4	1.9±0.5e-4	0.88±0.06	0.10±0.01	-5±4
0.38	5.14e-4	2.0±0.5e-4	0.86±0.07	0.09±0.01	-5.6±5
0.41	5.38e-4	2.4±0.5e-4	0.83±0.10	0.09±0.01	-7.2±5.5

*Calculated from $(\chi_m - \chi_{(TIP)})$.

is an unspecified operator. In this case the orbitals of interest are the V^{4+} d orbitals. Therefore, if the $\chi_{(TIP)}$ and the orbital ordering in the ground state and excited states are known, ΔE can be calculated. In V_2O_5 xerogel, the vanadium is assumed to be in a distorted square pyramidal geometry with approximate C_{2v} symmetry.[8] Thus, the idealized orbital diagram is shown in Figure 5.9. Based on this scheme the energy difference between the ground (d electron in d_{yz} orbital) and excited (d electron in d_{xz} orbital) states is expected to be quite small. The ordering of d_{xz}, d_{yz} and d_{xy} levels depends on the extend of π acceptor character of d_{xz} and d_{yz} orbitals. In the case of V_2O_5 framework the π character of these orbitals is expected to be substantial because of the filled p_z orbitals of the bridging equatorial oxide ions. Based on this assumption, the eq (5.5) can be simplified into eq (5.6).[7a]

$$\chi_{(TIP)} = \frac{4N\beta^2}{\Delta E} \qquad (5.6)$$

The $\chi_{(TIP)}$ values obtained from the eq (5.2) are in emu per $A_xV_2O_5{\cdot}nH_2O$ which includes both V^{5+} and V^{4+} atoms. Of course, the V^{5+} atoms make no contribution to the $\chi_{(TIP)}$. In order to calculate the ΔE of the V^{4+} ions, the $\chi_{(TIP)}$ was normalized for the concentration of V^{4+}/V^{5+} in the V_2O_5 framework. The latter is known from the alkali ion loading. Using the corrected $\chi_{(TIP)}$ values into the eq (5.6), the ΔE energies were calculated and are shown in Table 5.6. The values fall in the IR range and, remarkably, electronic absorptions in the same range are observed experimentally in the diffuse reflectance IR spectra of the compounds, see

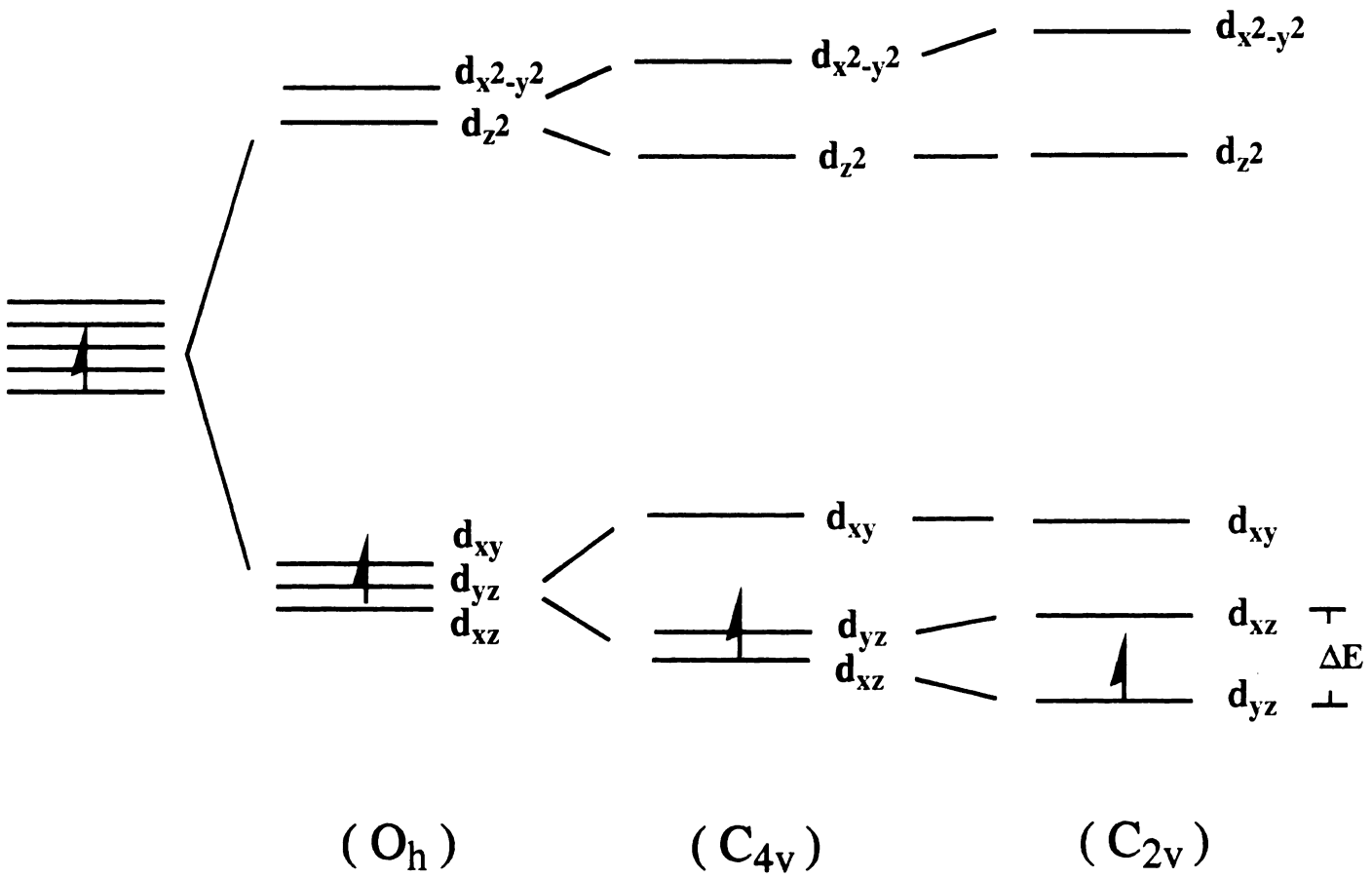

Figure 5.9. Simplified d orbital diagrams of V^{4+} in octahedral , square pyramidal and distorted square pyramidal geometry. The latter geometry is most representative of the V_4+ environment in the reduced V_2O_5 xerogel. (ΔE is the energy separation between d_{xz} and d_{yz} orbitals).

Table 5.6. Temperature-Independent Paramagnetism and Calculated and Observed ΔE for $M_xV_2O_5 \cdot nH_2O$

M	x	$\chi_{(TIP)}$[1] (emu/mole)	$\Delta E_{(calcd)}$ (cm^{-1})	$\Delta E_{(obsd)}$[2] (cm^{-1})
K	0.08	1.4±1.0e-3	2500-420	1900
K	0.26	8.5±3.8e-4	2130-813	2800(w), 1500(s)
K	0.33	1.2±0.3e-3	1100-660	1650
K	0.39	7.2±2.0e-4	1920-1090	1500
Cs	0.18	7.8±4.4e-4	2940-820	2450
Cs	0.28	1.6±0.4e-3	830-520	1650
Cs	0.35	1.0±0.3e-3	1250-720	3000(w), 1590(s)
Cs	0.38	1.1±0.3e-3	1270-760	1500

w : weak; s: strong. [1]Normalized by the concentration of V^{4+}/V^{5+}. [2]Observed spectroscopically.

Figure 5.10. The $A_xV_2O_5{\cdot}nH_2O$ materials show a strong broad band in the region of 1500-2500 cm^{-1} (Table 5.6). Some compounds even have an additional band at ~3000 cm^{-1}, but it is considerably weaker. The bands are absent in the spectra of V_2O_5 xerogel. This strongly supports that the observed absorption bands are electronic d-d transitions associated with the V^{4+} centers. However, two closely spaced transitions are observed in several phases suggesting that the real electronic structure is much more complicated and the presence of possibly two kinds of V^{4+} ions originating from different oxygen environments.

In $A_xV_2O_5{\cdot}nH_2O$, the Curie constant, C, is expected to increase linearly with the V^{4+} concentration. A linear relationship is indeed observed in the range $0< x < 0.3$ but beyond x ~0.3 the Curie constant levels off and then declines somewhat at x ~0.55, see Figure 5.11. It is interesting to speculate on the decline of the magnetic susceptibility beyond x ~ 0.3. In Oka's model, the closest V-V distance is 3.0 Å, involving, dimers of vanadyl ions. As the number of spins introduced into the vanadium oxide framework is increased, the V=O/V=O dimers are populated by electrons. The loss of susceptibility may be due to spin localization in these dimeric units followed by strong antiferromganetic coupling which would lead to a diamagnetic or weakly paramagnetic species. Such V=O/V=O dimers with V^{4+} centers are known in molecular complexes and are all antiferromagnetically coupled. Examples include $[(VO(DANA)]_2$[9] [DANA = 1,5-bis(*p*-methoxyphenyl)-1,3,5-pentanetrione] and $[V_2O_2Se_2(Se_2)_2]$.[10] In fact, these antiferromagnetic d^1-d^1 interactions seem to drive the formation of compounds. At low x values, the d^1 centers are relatively isolated and give rise to Curie paramagnetism. As the number of these centers in the framework increases it is reasonable to

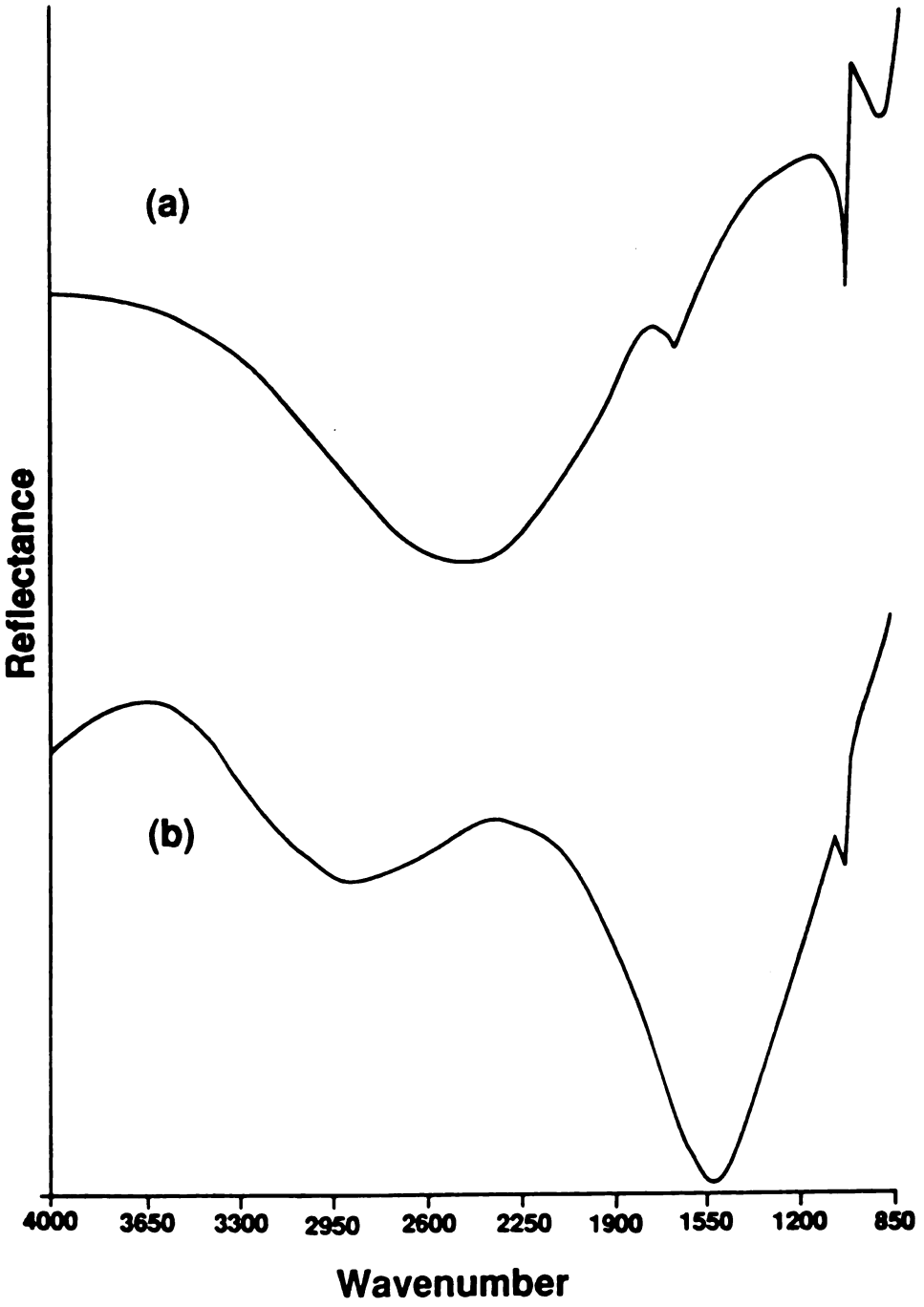

Figure 5.10. Diffuse reflectance IR spectra of (a) $K_xV_2O_5{\cdot}nH_2O$ and (b) $K_xV_2O_5{\cdot}nH_2O$. The broad peaks are assigned to electronic transitions associated with V^{4+} centers.

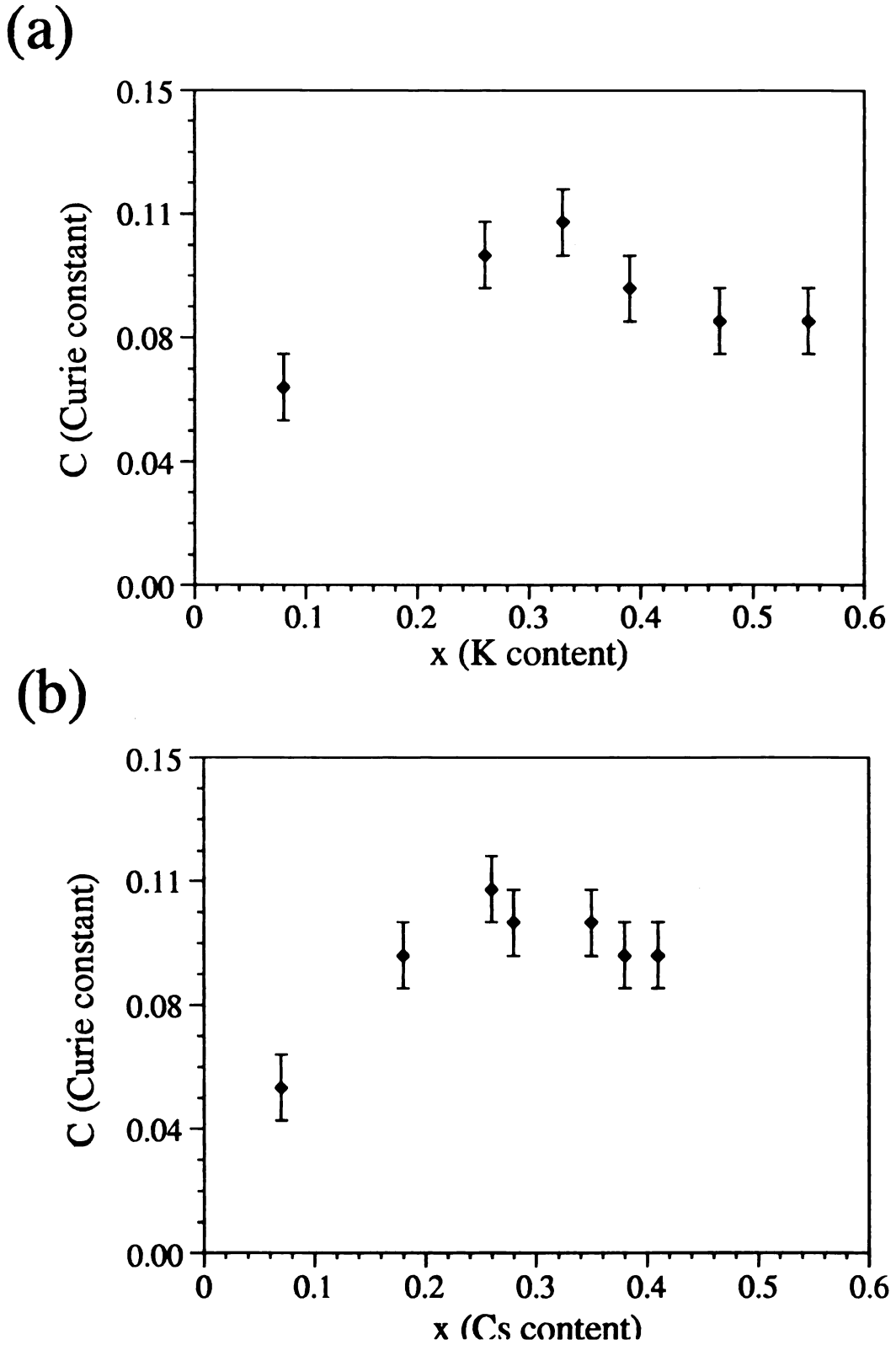

Figure 5.11. Plot of Curie constant, C, vs x (alkali content) for (a) $K_xV_2O_5{\cdot}nH_2O$ and (b) $Cs_xV_2O_5{\cdot}nH_2O$.

expect that beyond some value x, formation of d^1-d^1 dimers will become probable. Being antiferromagnetically coupled, the dimers will not contribute significantly to the susceptibility. This will lead to a leveling off or even a decrease of susceptibility at higher x values.

5.3.5. Electron Paramagnetic Resonance (EPR) Spectroscopy

The increased number of V^{4+} centers in the V_2O_5 framework of $A_xV_2O_5{\cdot}nH_2O$ is also reflected in the EPR spectra of these materials. The pristine V_2O_5 xerogel shows a hyperfine structure due to a small amount of V^{4+} (I= 7/2) impurities in an axially distorted crystal field.[11] In $A_xV_2O_5{\cdot}nH_2O$, the increased V^{4+} centers enhance the spin-spin exchange reaction which converts the original hyperfine structure into a symmetric broad band with a g value centered at *ca.* 1.96. A typical EPR spectrum of $K_{0.33}V_2O_5{\cdot}nH_2O$ is shown in Figure 5.12. The peak-width for all $A_xV_2O_5{\cdot}nH_2O$ materials varies as a function of x as illustrated in Figure 5.13. Interestingly, a maximum peak width is also observed at $x \sim 0.3$, consistent with the magnetic susceptibility data. This indicates that the spin density in the reduced framework is decreasing after $x > 0.3$ due to antiferromagnetic coupling and it is consistent with the magnetic data discussed above.

5.3.6. Charge Transport Measurements

Samples of $A_xV_2O_5{\cdot}nH_2O$ were studied in a pressed pellet form by dc electrical conductivity and thermopower measurements using the four-probe geometry. Compared with V_2O_5 xerogel, the $A_xV_2O_5{\cdot}nH_2O$ materials show at least a one order magnitude increase in electrical

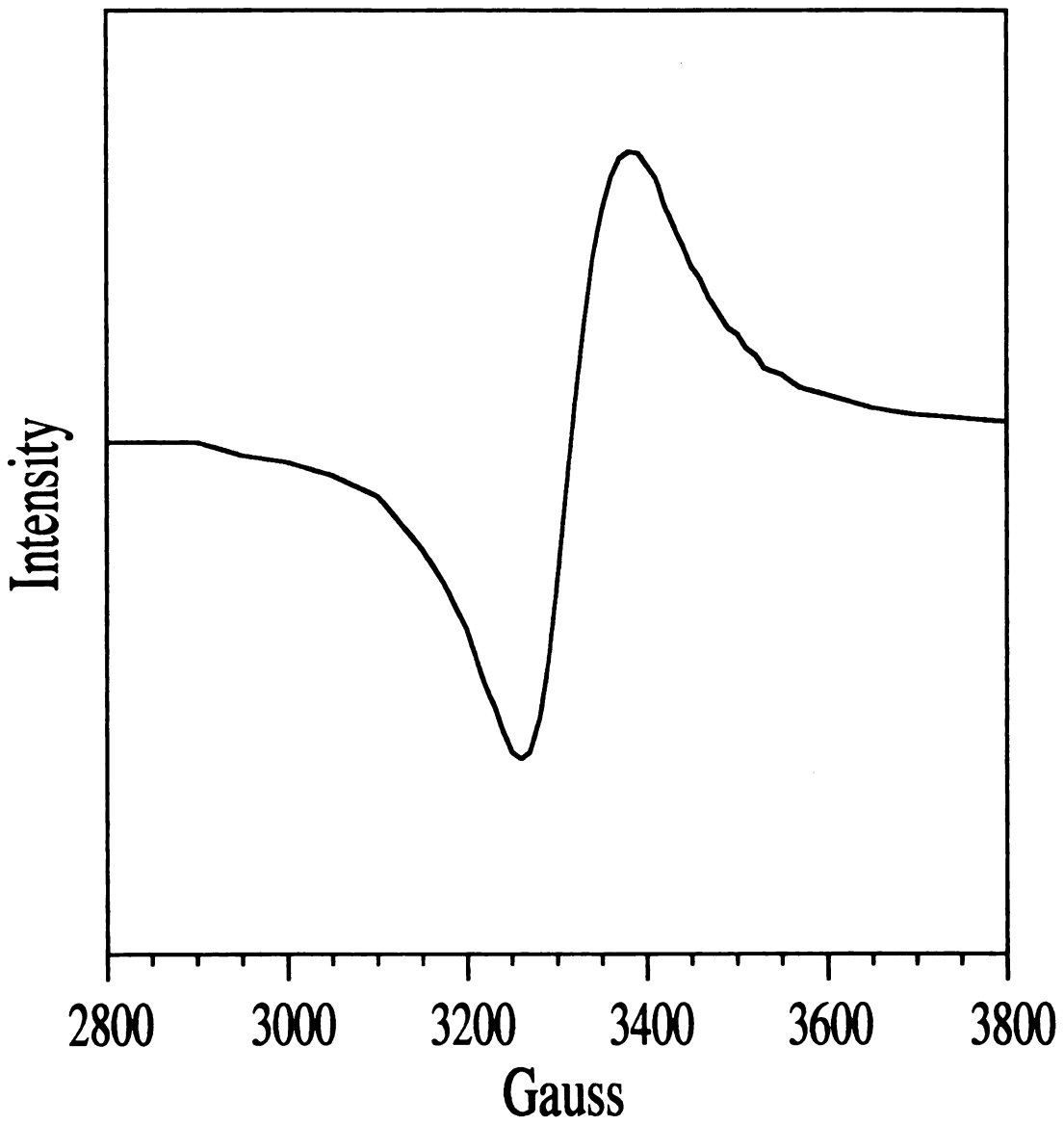

Figure 5.12. Room temperature EPR spectrum of $K_{0.33}V_2O_5 \cdot nH_2O$.

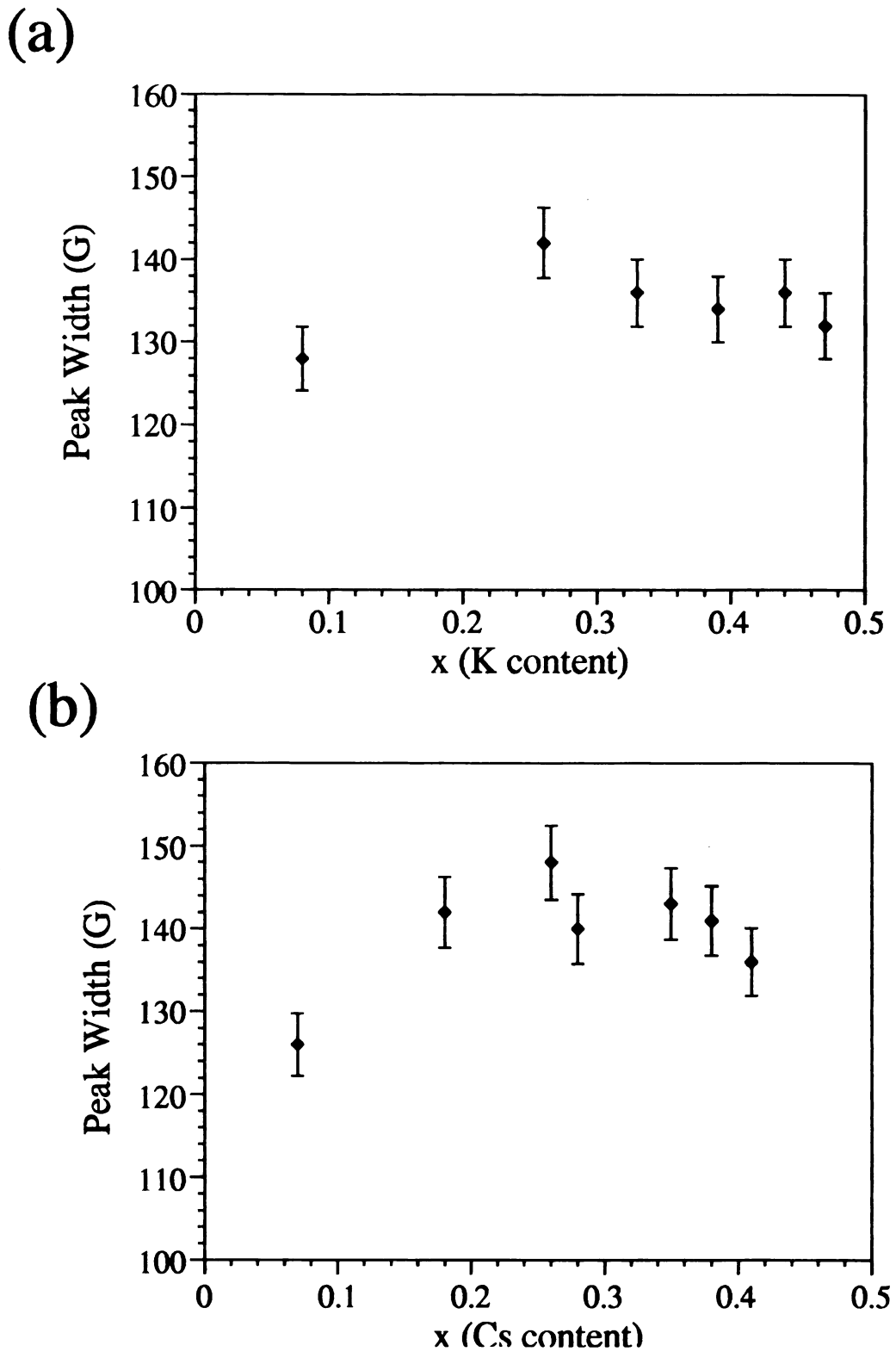

Figure 5.13. Changes of EPR peak width as a function of alkali ion loading for (a) $K_xV_2O_5{\cdot}nH_2O$ and (b) $Cs_xV_2O_5{\cdot}nH_2O$.

conductivity, to 10^{-3} - 10^{-2} S/cm at room temperature. Generally, the conductivity slightly increases with the x as shown in Figure 5.14, consistent with a small polaron semiconductor[12] where charge transport is due to electron hopping. Thus, conductivity increases with the number of charge carriers (V^{4+}) in the framework but levels off at x ~ 0.35. The conductivity measurements on granular samples alone do not unequivocally characterize their electrical behavior. A complementary probe to address this issue is thermoelectric power (TP) measurements as a function of temperature. TP measurements are typically far less susceptible to artifacts arising from the resistive domain boundaries in the material because they are essentially zero-current measurements. This is because temperature drops across such boundaries are much less significant than voltage drops. Figure 5.15 shows typical TP data for $A_xV_2O_5{\cdot}nH_2O$ as a function of temperature. Accurate measurements at low temperature were hindered by the very large sample resistances that developed. The Seebeck coefficients for these materials are negative with big absolute values confirming a n-type semiconductor. The Seebeck coefficients become less negative as the x increases, also confirming the increased number of charge carriers with V^{4+} concentration.

5.4. Conclusion

The use of bronze-like $A_xV_2O_5{\cdot}nH_2O$ phases has allowed the studies of the reduced V_2O_5 xerogel framework without interference from the intercalants. The optical and magnetic properties of these phases are intriguing and associated with the environments and interactions of V^{4+} atoms in the V_2O_5 framework. These phases show relatively low d-d electronic transitions occurring in the infrared range, which leads to small

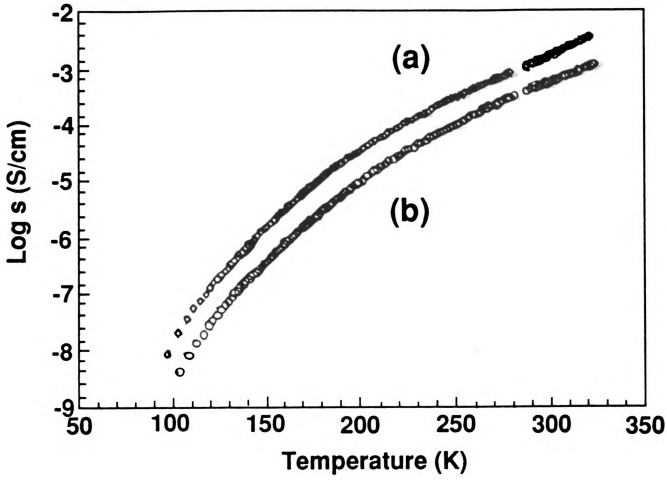

Figure 5.14. Four-probe pressed-pellet variable temperature electrical conductivity data of (a) $K_{0.39}V_2O_5{\cdot}nH_2O$ and (b) $K_{0.08}V_2O_5{\cdot}nH_2O$.

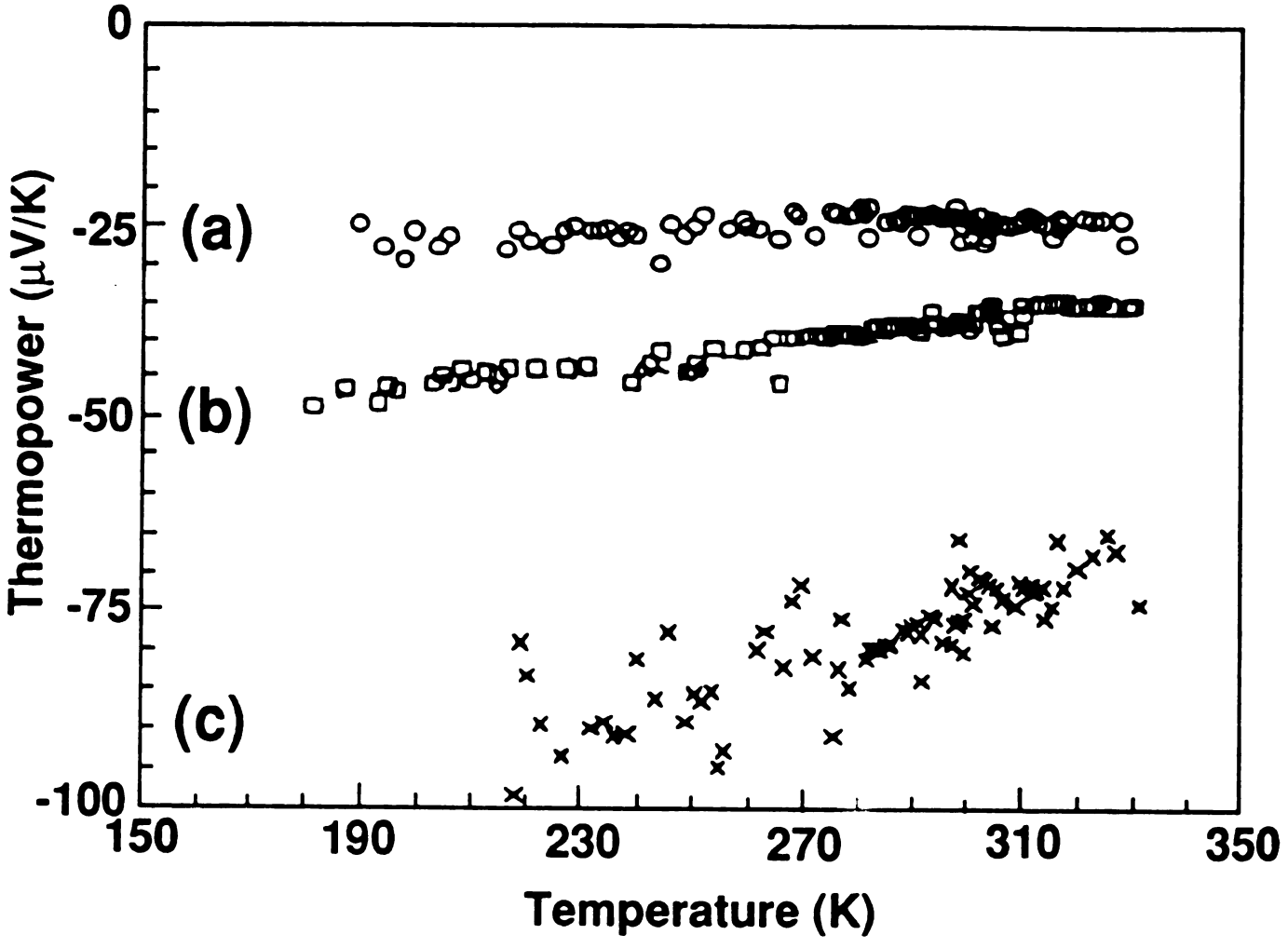

Figure 5.15. Variable temperature thermoelectric power data of $K_xV_2O_5 \cdot nH_2O$: x = 0.39 (a), 0.33 (b) and 0.26 (c).

but significant temperature-independent paramagnetism. Similar phenomena were also observed on all polymer/V_2O_5 intercalation compounds[13]. These studies clarify that these phenomena originate from the reduced V_2O_5 framework, not from the interactions between the polymers and the framework. Interestingly, these $A_xV_2O_5 \cdot nH_2O$ phases show a maximal spin density at $x \sim 0.3$ suggesting the antiferromagnetic coupling between spins when $x > 0.3$. The antiferromagnetic coupling is common in vanadium compounds[2,9,10]. The complicated magnetic behavior of $A_xV_2O_5 \cdot nH_2O$ suggests that it would be very difficult at this time to obtain clear understanding of the spin interactions between conducting polymers and V_2O_5 framework.

LIST OF REFERENCES

LIST OF REFERENCES

(1) (a) Kanatzidis, M.G.; Wu, C.-G.; Marcy, H.O.; Kannewurf, C.R. *J. Am. Chem. Soc.* **1989**, 111, 4139-4141. (b) Wu, C.-G.; Kanatzidis, M.G.; Marcy, H.O.; DeGroot, D.C.; Kannewurf, C.R. *Polym. Mat. Sci. Eng.* **1989**, 61, 969-973. (c) Kanatzidis, M.G.; Wu, C.-G.; Marcy, H.O.; DeGroot, D.C.; Kannewurf, C.R. *Chem. Mater.* **1990**, 2(3), 222-224.

(2) (a) Murphy, D.W.; Christian, P.A.; Disalvo, F.J.; Waszczak, J.V. *Inorg, Chem.* **1979**, 18(10), 2800-2803. (b) Chakraverty, B.K.; Sienko, M.J. *Phys. Rev. B* **1978**, 17(10), 3781-3789. (c) Gendell, J.; Cotts, R.M.; Sienko, M.J. *J. chem. phys.* **1962**, 37(2), 220-225.

(3) (a) Babonneau, F.; Barboux, P.; Josien, F.A.; Livage, J. *J. Chim. Phys.* **1985**, 82, 761-766. (b) Bullot, J.; Cordier, P.; Gallais, O.; Gauthier, M.; Babonneau, F. *J. Non-Cryst. Solids* **1984**, 68, 135-146.

(4) (a) Legendre, J.-J.; Aldebert, P.; Baffier, N.; Livage, J. *J. Colloid Interface Sci.* **1983**, 94(1), 84-89. (b) Livage, J. *Chem. Mater.* 1991, 3, 573-593.

(5) (a) Yao T.; Oka,Y.; Yamamoto, N. *Mat. Res. Bull.* **1992**, 27, 669-675. (b) Yao T.; Oka,Y.; Yamamoto, N. *J. Mater. Chem.* **1992**,

2(3), 331-336. (c) Yao T.; Oka,Y.; Yamamoto, N. *J. Mater. Chem.* **1992**, 2(3), 337-340.

(6) Abello, L.; Husson, E.; Repelin, Y.; Lucazeau, G. *J. Solid State Chem.* **1985**, 56, 379-389.

(7) (a) Drago, R.S. "*Physical Methods in Chemistry*" W.B. Sanders Co.: Philadelphia, **1977**. (b) Boudreaux, X.A.; Mulay, L.N. "*Theory and Applications of Molecular Paramagnetism*", John Wiley and Sons: New York **1976**.

(8) (a) Livage, J.; Gharbi, N.; Leroy, N.C.; Michaud, M. *Mat. Res. Bull.* **1978**, 13, 1117-1124. (b) Stizza, S.; Davoli, I.; Benfatto, M *J. Non-cryst. Solids* **1987**, 95&96, 327-334.

(9) Heeg, M.J.; Mack, J.L.; Glick, M.D.; Lintvedt, R.L. *Inorg. Chem.* **1981**, 20, 833-839.

(10) Liao, J.-H.; Hill, L.; Kanatzidis, M.G. *Inorg. Chem.* **1993**, 32, 4650-4652.

(11) Sanchez, C.; Babonneau, F.; Morineau, R.; Livage, J.; *Bullot, J. Philos. Mag. B*, **1983**, 3, 279-290.

(12) (a) Bullot, J.; Cordier, P.; Gallais, O.; Gauthier, M. *J. Non-Cryst. Solids* **1984**, 68, 123-134. (b) Livage, J.; Jolivet, J.P.; Tronc, E. *J. Non-Cryst. Solids* **1990**, 121, 35-39.

(13) (a) Wu, C.-G. " Ph D. Dissertation" **1992**, Michigan State University. (b) Liu, Y.-J.; DeGroot, D.C.; Schindler, J.L.; Kannewurf, C.R.; Kanatzidis, M.G. *Adv. Mater.* **1993**, 5(5), 369-372.

CHAPTER VI

POLYMERIZATION OF ANILINE AND N-PHENYL-1,4-PHENYLENEDIAMINE IN LAYERED METAL PHOSPHATES BY AMBIENT OXYGEN

ABSTRACT

The formation of polyaniline in the layered metal phosphates, $HUO_2PO_4{\cdot}4H_2O$, α-$Ti(HOPO_3)_2{\cdot}H_2O$ and α-$Zr(HOPO_3)_2{\cdot}H_2O$, is reported. Aniline and N-phenyl-1,4-phenylenediamine (PPDA) are intercalated in the layered phosphates to form the precursors for polymerization. X-ray diffraction patterns show large interlayer expansions with titanium phosphate and zirconium phosphate, indicating that a bilayer of amine molecules are accommodated in the gallery. In contrast, only a monolayer of amine molecules is intercalated in uranyl phosphate. After thermal treatment at 130°C in air, the intercalated aniline and PPDA are slowly polymerized by ambient oxygen. The formation of polyaniline was confirmed by FT-IR, UV/VIS, EPR and magnetic susceptibility. Powder X-ray diffraction shows that, after polymerization, the interlayer spacing slightly increases from 10.46 to 11.8 Å for anilinium/uranyl phosphate, but dramatically decreases from 28.3 to 20.5 Å for PPDA/zirconium phosphate and from 18.87 to 13.25 Å for anilinium/titanium phosphate. The interlayer expansion is consistent with a monolayer of polyaniline present in uranyl phosphate and titanium phosphate, and a bilayer of polyaniline in zirconium phosphate. Gel permeation chromatography shows that the MW of the intercalated polyaniline is much lower than that of bulk polyaniline. Prolonged heating in air results in cross-linked polymer in the galleries. All compounds are insulators.

6.1. Introduction

In recent years, inclusion of conjugated polymers into inorganic host lattices has been the subject of considerable investigation.[1,2] The lattices provide confined spaces which can force the formed polymers into a certain regularity, potentially enhancing charge transport. In such systems the polymer chains are reasonably isolated from one another by the inorganic material and may provide an opportunity to study spectroscopically the properties of single chains.[3]

Polyaniline (PANI), a well-known conducting polymer[4], has been inserted into several inorganic hosts by different methods. One approach uses hosts with sufficient oxidative power to intercalate and polymerize aniline *in situ*. FeOCl[5] and V_2O_5 xerogel[6] are examples of such hosts. However, this type of compounds are comparatively few, while most host materials are non- or weakly oxidizing. Therefore, in order to polymerize monomers inside host materials with insufficient oxidative power, external oxidants must be used. Inoue and coworkers reported an electrochemical polymerization of intercalated aniline in montmorillonite.[7] Bein *et al.* used $(NH_4)_2S_2O_8$ to successfully polymerize the intercalated aniline in zeolites.[8] The same method was also applied to MoO_3.[9] Another method to insert conjugated polymers in host materials is to directly modify the oxidative power of the host by incorporation of oxidants. By pre-intercalating Cu^{2+} in a host, an *in-situ* polymerization of aniline can be accomplished, as in the case of silicates[10] and in zirconium phosphate[11]. Recently, we reported direct inclusion of polyaniline into MoS_2 by taking advantage of the exfoliation property of this dichalcogenide.[12]

Layered metal phosphates are known to possess rich intercalation chemistry.[13] The protons in the layers can be exchanged with cations or neutralized with bases. The resulting intercalation compounds, depending on the guest molecules, can have diverse properties.[13,14] By first, intercalating aniline and N-phenyl-1,4-phenylenediamine (PPDA) molecules, we used oxygen to polymerize them topotactically to polyaniline. In this method, the polymerization is carried out by simple thermal treatment of the amine intercalated compounds in air. Traditional oxidants such as $(NH_4)_2S_2O_8$, $FeCl_3$, lead to ion-exchange reactions which compete with the intralayer polymerization reaction and cause polyaniline to form outside the hosts. With oxygen, the ion-exchange reaction is totally avoided. We have already reported preliminary results from this work in the case of uranyl phosphate.[15] Here, we report the details of this reaction and its application to α-titanium phosphate and α-zirconium phosphate.

6.2. Experimental

6.2.1. Materials

Zirconyl chloride octahydrate ($ZrOCl_2 \cdot 8H_2O$), titanium tetrachloride ($TiCl_4$), aniline, and N-phenyl-1,4-phenylenediamine (PPDA) were used as received from Aldrich Chemical Co., Milwaukee, WI. Uranyl nitrate hexahydrate ($UO_2(NO_3)_2 \cdot 6H_2O$) was obtained from J.T. Baker Chemical Co., Phillipsburg, NJ. Phosphoric acid (85%) and hydrofluoric acid (50%) were purchased from Fisher Scientific Co., Fairlawn, NJ. Catechol was received from Mallinckrodt Inc., Paris, KY.

Elemental analyses were done by Galbraith Laboratories, Knoxville, TN and Oneida Research Services, Inc., Whitesboro, NY.

6.2.2. Measurements

Electronic absorption spectra were measured on a Hitachi U-2000 spectrophotometer from 1100 to 200 nm by spreading a Nujol mull of the samples between two quartz slides.

Thermogravimetric analysis (TGA) was performed on Shimadzu TGA-50. Typically 5-10 mg of samples were heated in a quartz crucible from room temperature to 1000°C with 5°C/min in air or nitrogen.

Differential Scanning Calorimetry (DSC) used Shimadzu DSC-50 thermal analyzer. Samples (3-5 mg) were put in a aluminum pan and heated to 200°C with 5°C/min. An empty aluminum pan was taken as the reference.

Variable temperature magnetic susceptibility data were collected from 5K to 300K on a S.H.E. corporation SQUID system at a magnetic field of 400 gauss. The data were collected by diamagnetic components obtained from the literature[16] or the diamagnetic precursors.

Scanning Electron Microscopy (SEM) was done on JEOL-JSM 35 CF with an accelerating voltage of 15 KV. Samples were glued to the microscope sample holder with conducting graphite paint.

Molecular weights were determined with a Shimadzu LC-10A HPLC system with a PLgel 5μ mix column. The measurements were done at 75°C with NMP (containing 0.5 wt% LiCl) as the eluent. The elution rate was 0.2 ml/min. Polystyrene of known molecular weights was used as standard. The detector was a UV/Vis lamp which was set at 270 nm for polystyrene and 315 nm for polyaniline. Roughly, an amount of 0.1 mg of

polyaniline was dissolved in 5 ml of NMP. The resulting purplish blue solution was pre-filtered with a 4.5 μm of frit and then injected into the column with a volume of 10 μl.

The X-ray coherence length of the crystallites was calculated according to the Scherrer's formula[17]: $L_{hkl} = K\lambda/B\cos\theta$. L is the coherence length along directions perpendicular to the Miller index planes (hkl), λ is the wavelength of the X-rays used, K is Scherrer's constant and has a value of 0.9, θ is the Bragg angle, and B is the peak width at half-height in radians.

The instruments and experimental setups for X-ray diffraction, infrared spectroscopy and electron paramagnetic resonance (EPR) are the same as those in chapter 2.

6.2.3. Preparation of Layered Metal Phosphates

$HUO_2PO_4{\cdot}4H_2O$ (HUP), α-$Zr(HOPO_3)_2{\cdot}H_2O$ (α-ZrP), and α-$Ti(HOPO_3)_2{\cdot}H_2O$ (α-TiP) were prepared according to reported methods.[18,19,20] HUP is a luminous yellow solid which precipitates from H_3PO_4 and $UO_2(NO_3)_2$ in aqueous solution.[18] α-ZrP is a white crystalline powder prepared by adding concentrated H_3PO_4 to $ZrOCl_2$ solution in presence of HF.[19] Crystalline α-TiP was synthesized by refluxing its gel in concentrated H_3PO_4.[20] The gel was prepared by slowly adding $TiCl_4$ into H_3PO_4 solution.

6.2.4. Preparation of $(C_6H_5NH_3)_{1.0}UO_2PO_4{\cdot}0.4H_2O$ (AUP) and $H_{0.12}(C_6H_5NHC_6H_4NH_3)_{0.88}UO_2PO_4$ (A_2UP)

Excess aniline or PPDA was added into a flask containing 1.0 g of $HUO_2PO_4{\cdot}4H_2O$ and 80 ml of distilled water. The mixture was stirred for

one day at room temperature. The product was filtered and then washed with acetone. After drying overnight under N_2, AUP is pale yellow and A_2UP is pale gray. Anal. Calcd for $(C_6H_5NH_3)_{1.0}UO_2PO_4 \cdot 0.4H_2O$: C, 15.40%; H, 1.89%; N, 3.0%. Found: C, 15.48%; H, 1.78%; N, 2.95%. The composition of A_2UP, calculated from thermogravimetric analysis (TGA), is $H_{0.12}(C_6H_5NHC_6H_4NH_3)_{0.88}UO_2PO_4$.

6.2.5. Preparation of $H_{0.6}(C_6H_5NH_3)_{1.4}Ti(PO_4)_2$ (ATiP)

An amount of 1.0 g (3.88 mmol) of $Ti(HOPO_3)\cdot H_2O$ and 1.44 g (15.48 mmol) of aniline were introduced into a 23 ml autoclave. The autoclave was put into a furnace with a constant temperature of 130°C for 3 days. After cooled to room temperature, the white product was filtered and washed with acetone. The composition of ATiP, calculated from TGA, is $H_{0.6}(C_6H_5NH_3)_{1.4}Ti(PO_4)_2$.

6.2.6. Preparation of $H_{0.7}(C_6H_5NH_3)_{1.3}Zr(PO_4)_2$ (AZrP) and $H_{0.6}(C_6H_5NHC_6H_4NH_3)_{1.4}Zr(PO_4)_2$ (A_2ZrP)

Excess PPDA or aniline was added to $Zr(PO_4)_2\cdot H_2O$ (0.5 g) in 50 ml of distilled water, and the mixture was stirred for two days. The reaction temperature was ~25°C for aniline and 80°C for PPDA. The products were removed by filtration, washed with acetone, and then dried under N_2. AZrP is white and A_2ZrP is pale gray. Anal. Calcd. for $H_{0.6}(C_6H_5NHC_6H_4NH_3)_{1.4}Zr(PO_4)_2$: C, 37.3%; H, 3.5%, N, 7.26%. Found: C, 37.6%; N, 7.03%; H, 3.54%. The composition of AZrP, calculated from TGA, is $H_{0.7}(C_6H_5NH_3)_{1.3}Zr(PO_4)_2\cdot 0.1H_2O$.

6.2.7. Preparation of $(PANI)_{0.94}UO_2PO_4 \cdot 0.5H_2O$ (PUP), $(PANI)_{0.8}Ti(PO_4)_2$ (PTiP) and $(PANI)_{2.4}Zr(PO_4)_2$ (PZrP) from AUP, A_2ZrP and ATiP

Quantities of AUP, A_2ZrP and ATiP were introduced into small pyrex containers and the containers were put into a furnace with a constant temperature of 130°C. After several weeks, black products were obtained. Anal. Calcd. for $(PANI)_{0.94}UO_2PO_4 \cdot 0.5H_2O$: C, 14.7%; H, 2.86%, N, 1.24%. Found: C, 14.1%; N, 1.27%; H, 2.83%. Anal. Calcd. for $(PANI)_{2.4}Zr(PO_4)_2$: C, 36.67%; H, 2.7%, N, 7.1%. Found: C, 38.78%; N, 6.52%; H, 2.69%. The composition of PTiP, calculated from TGA, is $(PANI)_{0.8}Ti(PO_4)_2$.

6.2.8. Extraction of Polyaniline from PUP

PUP (0.1 g) was added to excess 20% HCl solution. After one day of stirring at room temperature, the black precipitate was collected by filtration, washed with water then with acetone, and dried in air.

6.2.9. Extraction of Polyaniline from PTiP

PTiP (0.1 g) was added to 50 ml of 20 % HCl solution containing 1.5 g of catechol. The mixture was refluxed for 2 days and then cooled to room temperature. After filtration, the black residue was washed with water and acetone, and dried in air.

6.2.10. Extraction of Polyaniline from PZrP

An amount of 0.2 g PZrP was added to excess 10% HF solution. After ~12 hours of stirring, the black precipitate was filtered, washed with water then with acetone, and dried in air.

6.2.11. Preparation of Base Form of PANI

Extracted PANI was treated with excess 0.1 M NH_4OH for ~12 hours. The product was filtered, washed copiously with distilled water and acetone, and dried in air.

6.3. Results and Discussion

6.3.1. Characterization and Polymerization of Aniline- and PPDA-Intercalated Compounds

The reaction of layered metal phosphates with aniline or derivatives results in intercalation compounds with well defined X-ray powder diffraction patterns. For example, the X-ray diffraction patterns of $H_{0.7}(C_6H_5NH_3)_{1.3}Zr(PO_4)_2$ (AZrP) and $H_{0.6}(C_6H_5NHC_6H_4NH_3)_{1.4}Zr(PO_4)_2$ (A_2ZrP) are given in Figure 6.1. Several strong (00l) peaks, associated with the stacking axis perpendicular to the layers, are observed indicating that the intercalants are highly ordered. The first diffraction peak (001), corresponds to an interlayer distance, of 19Å for AZrP and 28.3Å for A_2ZrP. Subtracting the layer thickness of ~6.6Å, AZrP and A_2ZrP show net expansions of 12.4Å and 21.7Å, respectively, which are consistent with the expected expansion from a bilayer of aniline and PPDA molecules in the interlayer regions. It is likely that the molecules are slightly tilted or interdigitated. The interlayer distances and compositions of all compounds are summarized in Table 6.1. $H_{0.6}(C_6H_5NH_3)_{1.4}Ti(PO_4)_2$ (ATiP) also has bilayered anilinium molecules in the interlayer space. However, no intercalation was observed between

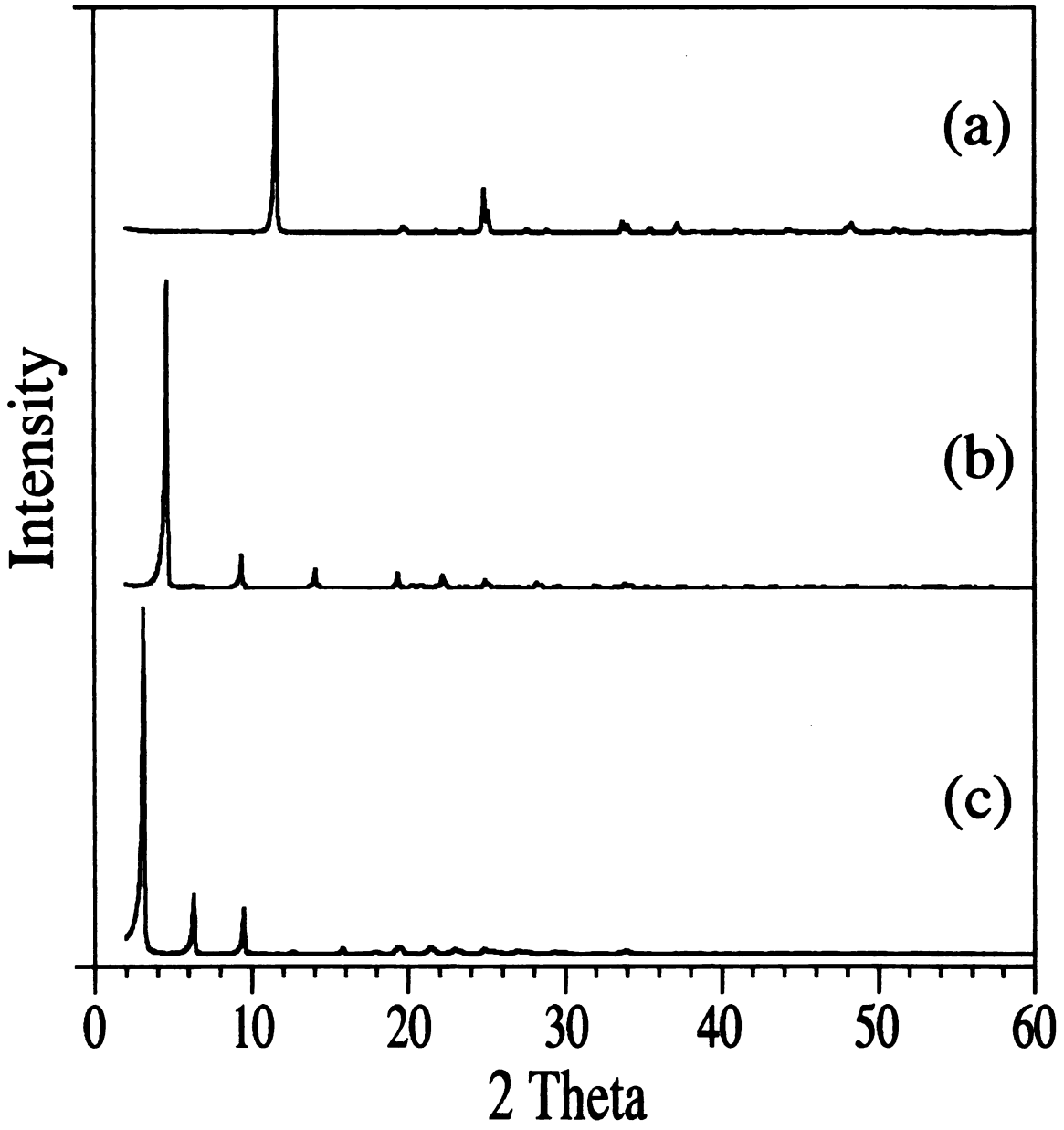

Figure 6.1. Powder X-ray diffraction patterns of (a) α-$Zr(HOPO_3)_2 \cdot H_2O$, (b) $H_{0.7}(C_6H_5NH_3)_{1.3}Zr(PO_4)_2$ and (c) $H_{0.6}(C_6H_5NHC_6H_4NH_3)_{1.4}Zr(PO_4)_2$.

Table 6.1. Summary of Compositions and Interlayer Spacings of Amine Intercalated Metal Phosphates

Inorganic host	Organic guest	Product composition	Interlayer spacing (Å)	Net expansion (Å)
HUP	---	$HUO_2PO_4{\cdot}4H_2O$	8.69	~2.3
HUP	aniline	$(C_6H_5NH_3)_{1.0}UO_2PO_4.0.4H_2O$	10.46	~4.1
HUP	PPDA	$H_{0.12}(C_6H_5NHC_6H_4NH_3)_{0.88}UO_2PO_4$	18.39	~12.0
ZrP	---	$Zr(HOPO_3)_2.H_2O$	7.60	~1.0
ZrP	aniline	$H_{0.7}(C_6H_5NH_3)_{1.3}Zr(PO_4)_2$	19.00	~12.4
ZrP	PPDA	$H_{0.6}(C_6H_5NHC_6H_4NH_3)_{1.4}Zr(PO_4)_2$	28.30	~21.7
TiP	---	$Ti(HOPO_3)_2.H_2O$	7.57	~1.0
TiP	aniline	$H_{0.6}(C_6H_5NH_3)_{1.4}Ti(PO_4)_2$	18.87	~12.3

PPDA = N-phenyl-1,4-phenylenediamine.

PPDA and TiP. In contrast to the group VI phosphates above, $(C_6H_5NH_3)_{1.0}UO_2PO_4 \cdot 0.4H_2O$ (AUP) and $H_{0.12}(C_6H_5NHC_6H_4NH_3)_{0.88}UO_2PO_4$ (A_2UP), show much smaller net expansions suggesting the presence of a monolayer of organic guests.

When these materials were heated at 130°C in air, their color gradually changed from yellow or pale gray to dark green and finally to black. The procedure took 4 days for AUP, 8 days for ATiP, and only one day for A_2ZrP and A_2UP. The color change is, indeed, associated with the polymerization of aniline and PPDA. This is confirmed by FT-IR spectroscopy which shows that the vibration bands of the monomers and dimers gradually decrease in intensity while the vibration bands of PANI quickly dominate the spectra. The changes in the FT-IR spectra of AUP during polymerization are shown in Figure 6.2. Before thermal treatment, AUP shows the characteristic vibrations of anilinium at ~3000, 2600, and 1500 cm^{-1}, consistent with an acid-base intercalation reaction, where the protons transfer from the layers to aniline. However, the appearance in the spectrum of broad vibration bands at 3490 and 3380 cm^{-1}, and a doublet at ~750 and ~690 cm^{-1} also implies the presence of neutral aniline in the layers. After one week, the absorption bands at ~3400-~2800 cm^{-1} (originating from the C-H, NH_3^+, and NH_2 groups) weaken and then are completely masked by a strong electronic transition from PANI, which starts from ~1800 cm^{-1} and extends to the visible region. At the same time, the IR spectrum of PANI is clearly observed. In three weeks, the vibration bands of anilinium disappear. Under the same conditions, the complete polymerization process took ~4 weeks for ATiP, but never went to completion for A_2ZrP and A_2UP. The FT-IR spectra of the last two compounds still show significant amounts of the intercalated dimers. The

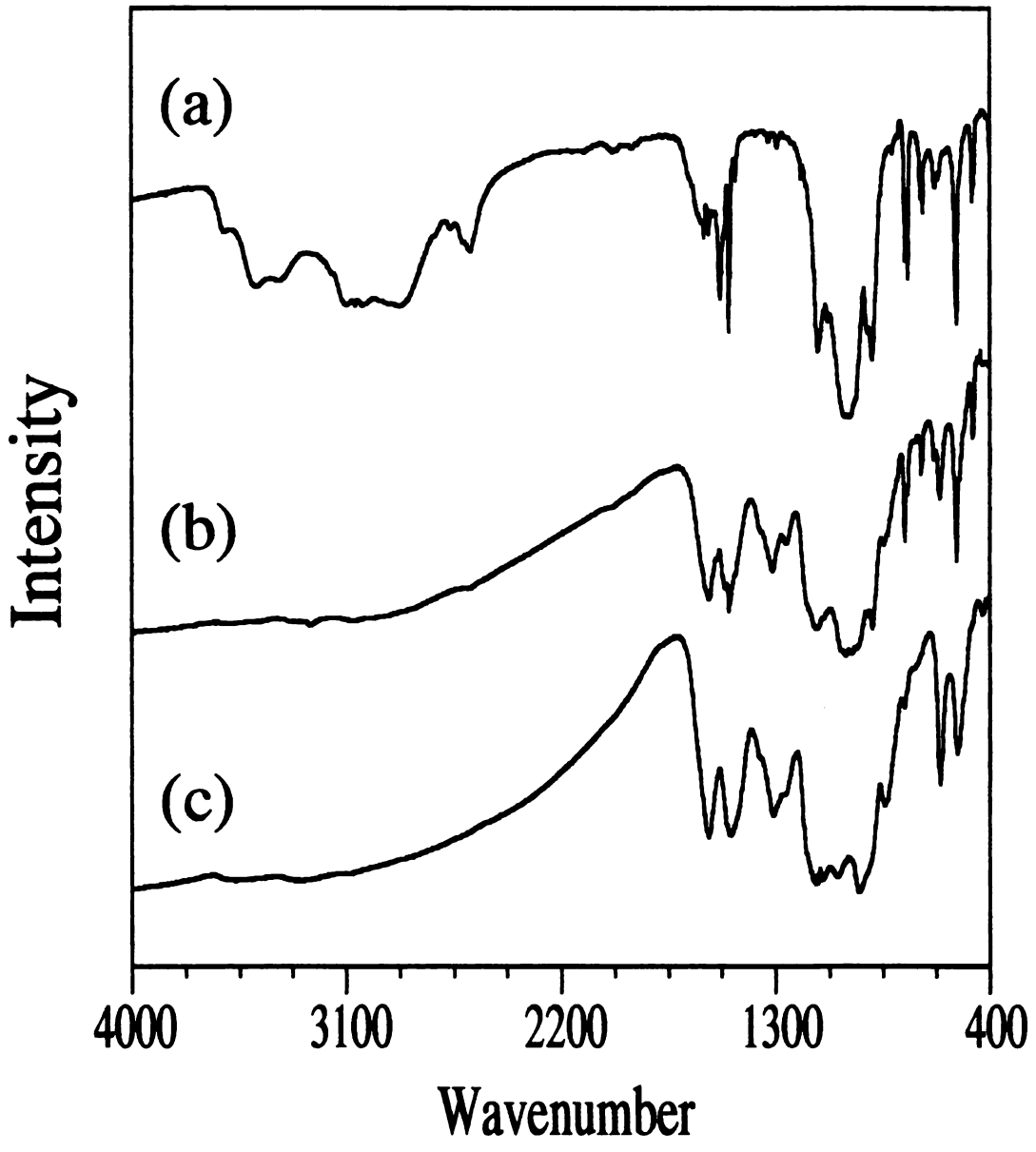

Figure 6.2. FT-IR spectra of $(C_6H_5NH_3)_{1.0}UO_2PO_4{\cdot}0.4H_2O$ (AUP) under thermal treatment for (a) 0 week, (b) one week, and (c) three weeks.

FT-IR spectra of the polymers extracted from the framework are shown in Figure 6.3, where the characteristic vibrations of bulk PANI (emerldine form) are clearly observed in all cases, confirming that they are PANI. Their frequencies and corresponding vibration modes are listed in Table 6.2. Compared with bulk PANI, the frequency and shape of the extracted PANI are respectively slightly higher and sharper. This is either due to the shorter polymer chain length (see below) or to the formation of cross-linked PANI, which has been reported to form when PANI is heated.[20] Although color changes were also observed for AZrP, the FT-IR spectrum of the extracted species, surprisingly, is not PANI. The band at ~1300 cm^{-1} is weak and the bands at ~1100 and ~800cm^{-1} are nearly absent, indicating that the C-H vibration is inhibited. One possibility is that the polymer chains are heavily cross-linked.

Under the same polymerization conditions, these precursors sealed in evacuated tubes show no color changes which indicate no polymerization occurred, confirmed by FT-IR. This can be seen by TGA and DSC experiments under oxygen and nitrogen atmosphere, as shown in Figure 6.4 and Figure 6.5, respectively. The precursors have better thermal stability under oxygen than under nitrogen because of the PANI formation during the experiment. For A_2ZrP, the weight loss begins at 250°C under nitrogen, but mainly at 400°C under oxygen. For ATiP, the weight-loss begins at ~200°C under nitrogen flow. However, under oxygen flow, two decomposition steps were observed at ~200°C and ~400°C. The weight loss starting at 200°C is attributed to aniline and was confirmed by mass spectrometry. The loss of aniline would slow down the intralamellar polymerization and result in incomplete polymerization. In addition, DSC of A_2ZrP shows a slight endotherm to 200°C under N_2 atmosphere

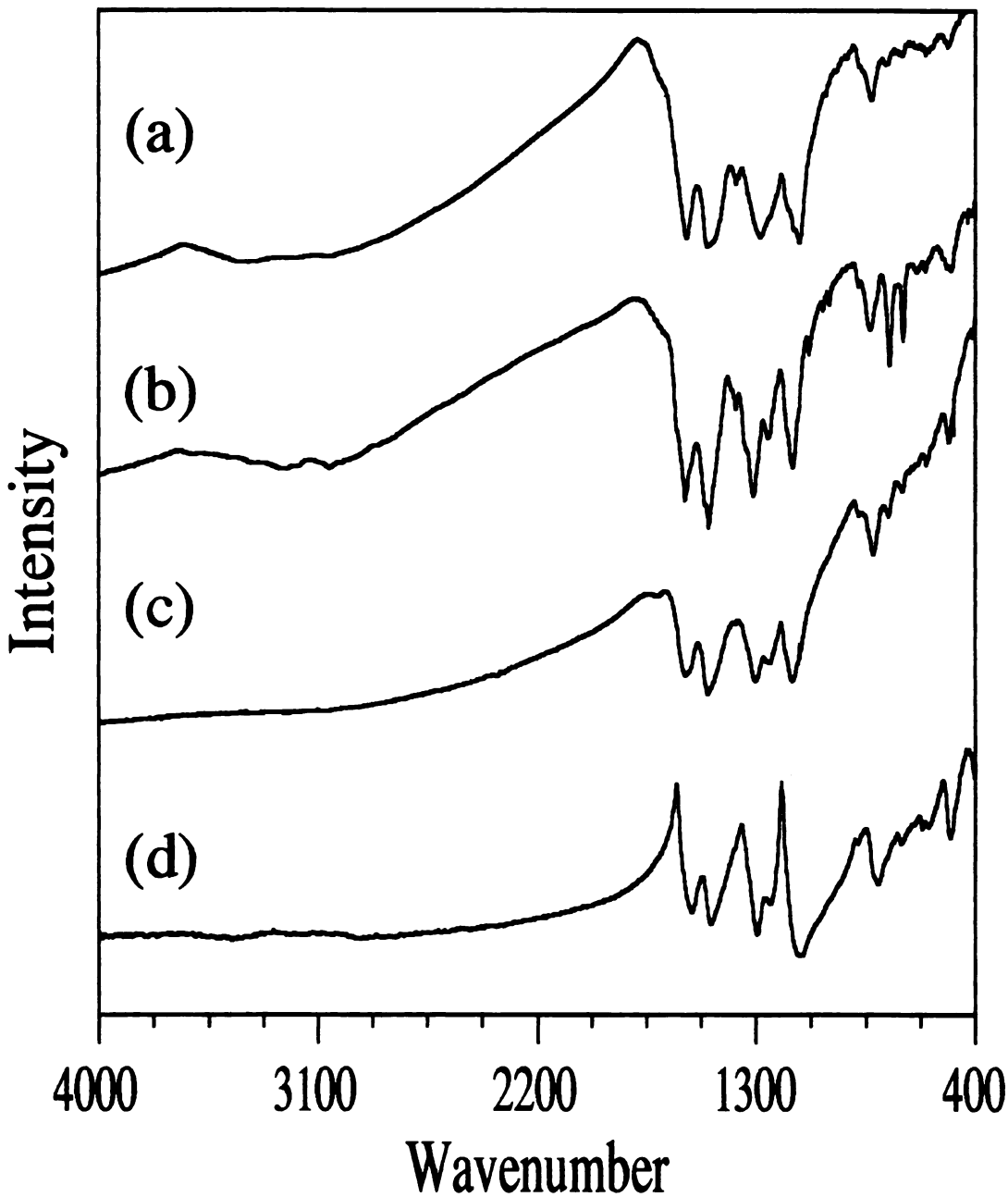

Figure 6.3. FT-IR of extracted PANI from (a) PUP, (b) PZrP and (c) PTiP, and (d) bulk PANI.

Table 6.2. IR Vibration Energies of Extracted Polyaniline from Metal Phosphates

	C-C Ring stretching	C-H bending or C-N stretching	C-H bending (in-plane)	C-H bending (out-of-plane)
Bulk PANI	1560, 1481	1292, 1249	1109	797
PANI from PUP[a]	1576, 1492	1280	1118	815
PANI from PTiP	1582, 1492	1301,1250	1149	817
PANI from PZrP[b]	1594, 1492	1315,1250	1155	830

[a]Polymerized from AUP. [b]Polymerized from A_2ZrP.

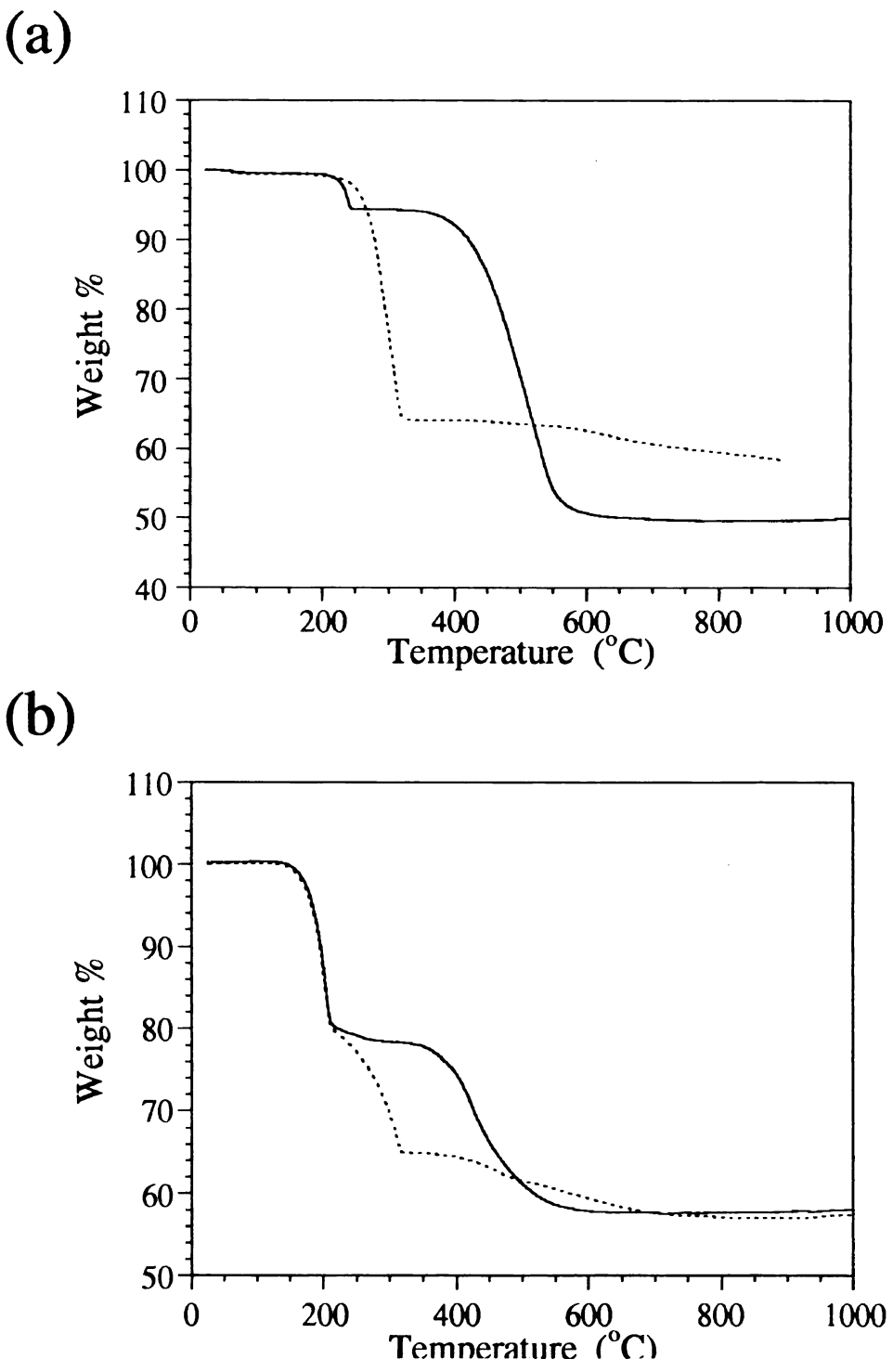

Figure 6.4. Thermogravimetric analysis diagrams of (a) PZrP and (b) PTiP under air (—) and nitrogen flow (-----).

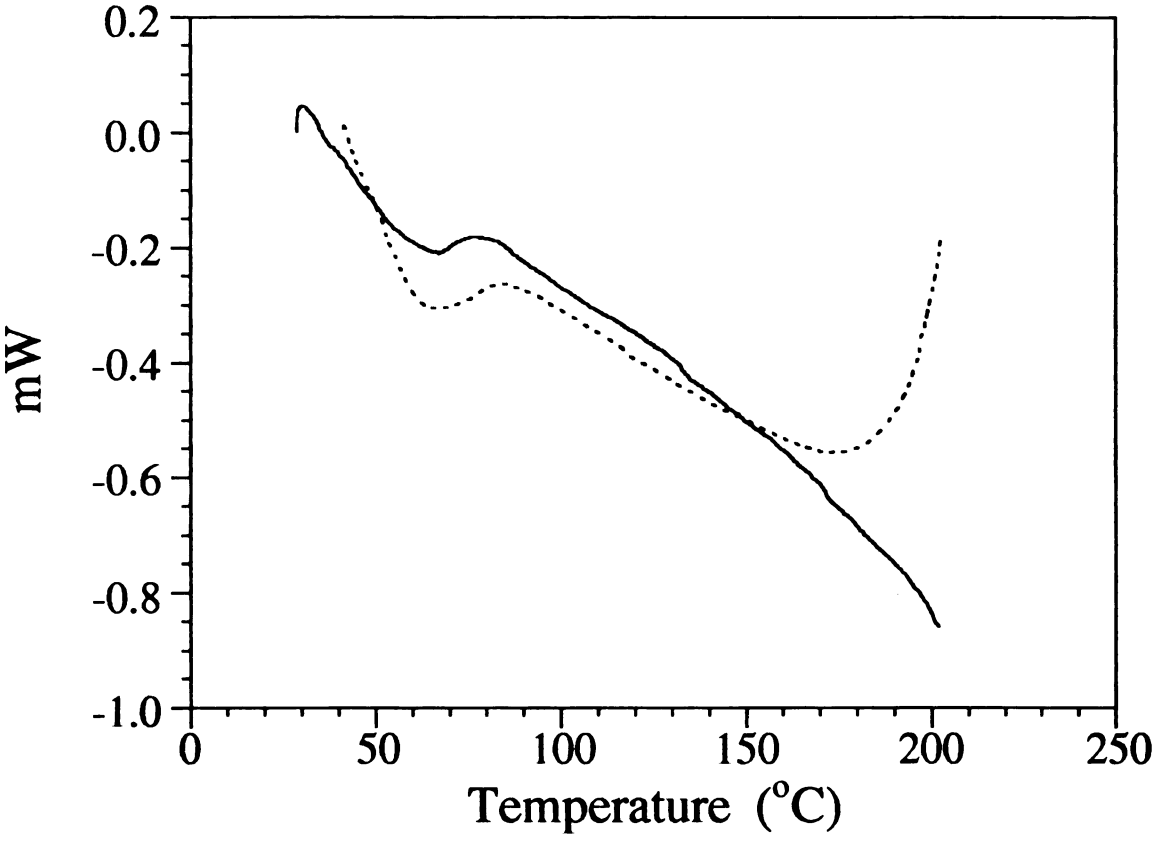

Figure 6.5. Differential scanning calorimetry of A_2ZrP under O_2 (-----) and N_2 (—).

consistent with the loss of PPDA. However, an exotherm was observed at ~ 180°C under oxygen, consistent with polymerization of PANI.

The significant finding was that oxygen is the key for the intralamellar polymerization. Furthermore, attempts to polymerize the intercalated monomers with other oxidants such as $(NH_4)_2S_2O_8$ and $FeCl_3$ did not yield intercalated PANI, instead ion-exchange was observed followed by polymerization on the particle surface.

6.3.2. UV/Vis Spectroscopy

The UV/Vis spectrum of $(PANI)_{0.94}UO_2PO_4 \cdot 0.5H_2O$ (PUP) shows a very broad band at ~ 750 nm as shown in Figure 6.6. The band is the characteristic polaron absorption of protonated PANI.[22] The same band was also observed at ~ 800 nm for $(PANI)_{2.4}Zr(PO_4)_2$ (PZrP) and $(PANI)_{0.8}Ti(PO_4)_2$ (PTiP). This is consistent with infrared spectroscopic data confirming the formation of protonated PANI inside the galleries of layered metal phosphates.

6.3.3. X-ray Diffraction

The intralamellar polymerization changes the orientation of the intercalated molecules and hence leads to a change of the interlayer distance of the host. Therefore, the polymerization can be monitored by X-ray diffraction measurements. The X-ray diffraction patterns of AUP as a function of time are shown in Figure 6.7 where, as the reaction proceeds, the peaks due to AUP gradually disappear and the peaks due to PUP become evident. The peaks due to AUP disappear completely in three weeks, consistent with the infrared spectroscopic data (described above). After polymerization, the interlayer spacing slightly increased to 11.8 Å

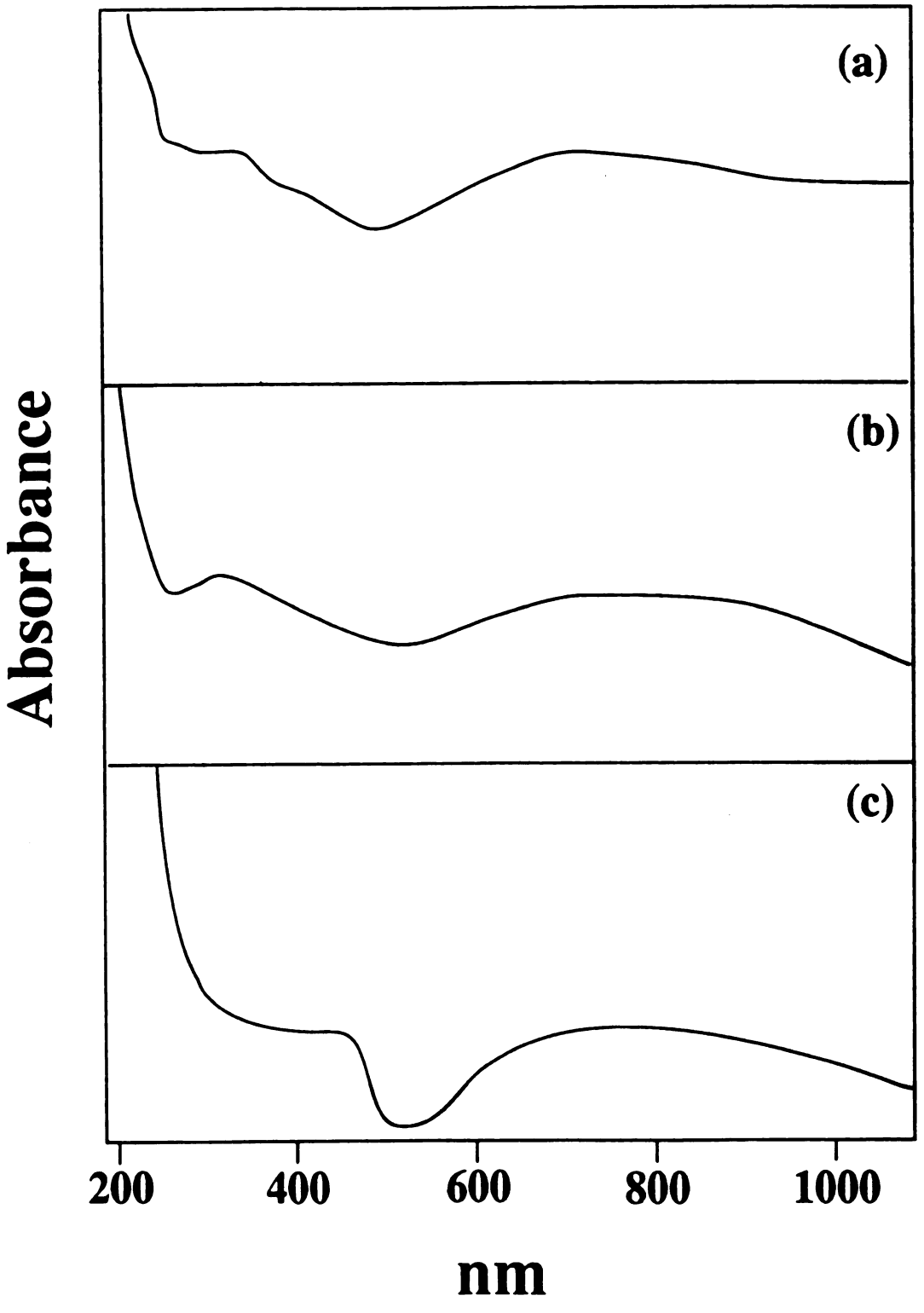

Figure 6.6. Electronic absorption spectra of (a) PUP, (b) PZrP, and (c) bulk PANI.

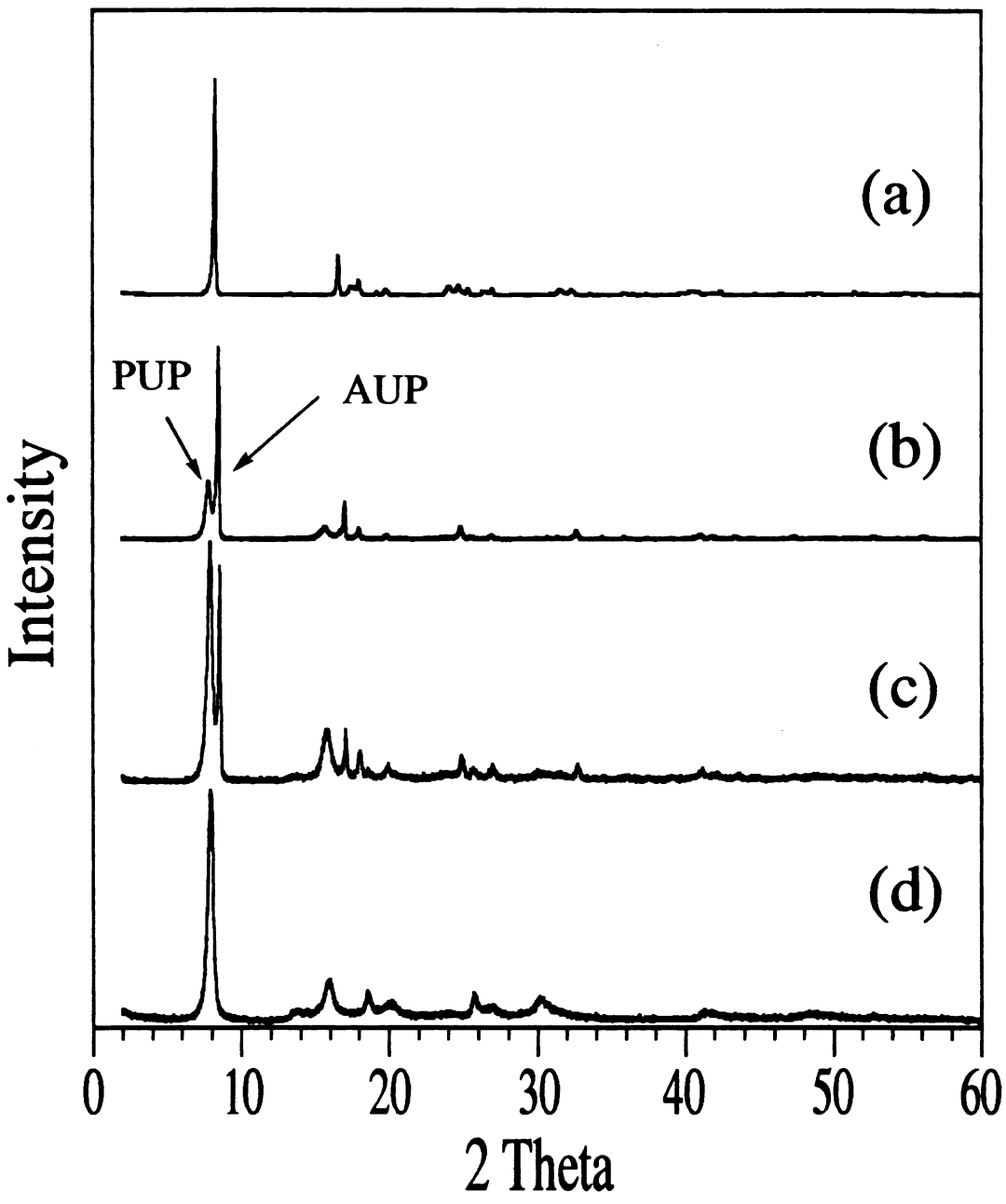

Figure 6.7. Evolution of powder X-ray diffraction patterns of $(C_6H_5NH_3)_{1.0}UO_2PO_4{\cdot}0.4H_2O$ (AUP) under thermal treatment for (a) 0 week, (b) one week, (c) two weeks, and (d) three weeks.

for PUP. However, it dramatically decreased to 20.5 Å for PZrP and 13.25 Å for PTiP. The net expansion of PZrP is ~13.9 Å, comparable with a bilayer of PANI molecules in the interlayer regions as illustrated in Scheme 1. On the other hand, PTiP has a net expansion of only ~6 Å which suggests a monolayer of PANI molecules as illustrated in Scheme 2. In all cases the X-ray diffraction peaks become broader after polymerization due to a decrease in crystallinity. As estimated from the Scherrer formula, the coherence length along the layers stacking axis decreases from ~600 Å in AUP to ~180 Å in PUP, from ~400 Å in ATiP to 180 Å in PTiP and from 260 Å in A_2ZrP to 200 Å in PZrP. This is attributed to the increased stacking disorder during polymerization which involves significant movement of monomers and diffusion of oxygen and water in and out of the materials.

6.3.4. Magnetic Properties

The diamagnetic hosts allow the observation of the evolution of the EPR spectroscopic polaron signal of PANI during the polymerization. All precursor compounds are EPR silent. As the reaction proceeds, the compounds start to show symmetric EPR signals which gradually increase in intensity as shown in Figure 6.8. The peak widths of these signals decrease with reaction time, indicative of extensive electron delocalization and consistent with polaron formation in PANI. Thus, peak width (ΔH_{pp}) decreases from 12 to 8 G in PUP, from 7 to 2 G in TiP, and from 15 to 12 G in ZrP. The g values are close to the free electron value of 2.0023. These observations are consistent with the gradual growth of PANI. Bulk PANI in a protonated form was reported with a peak width about < 3 G,[23]

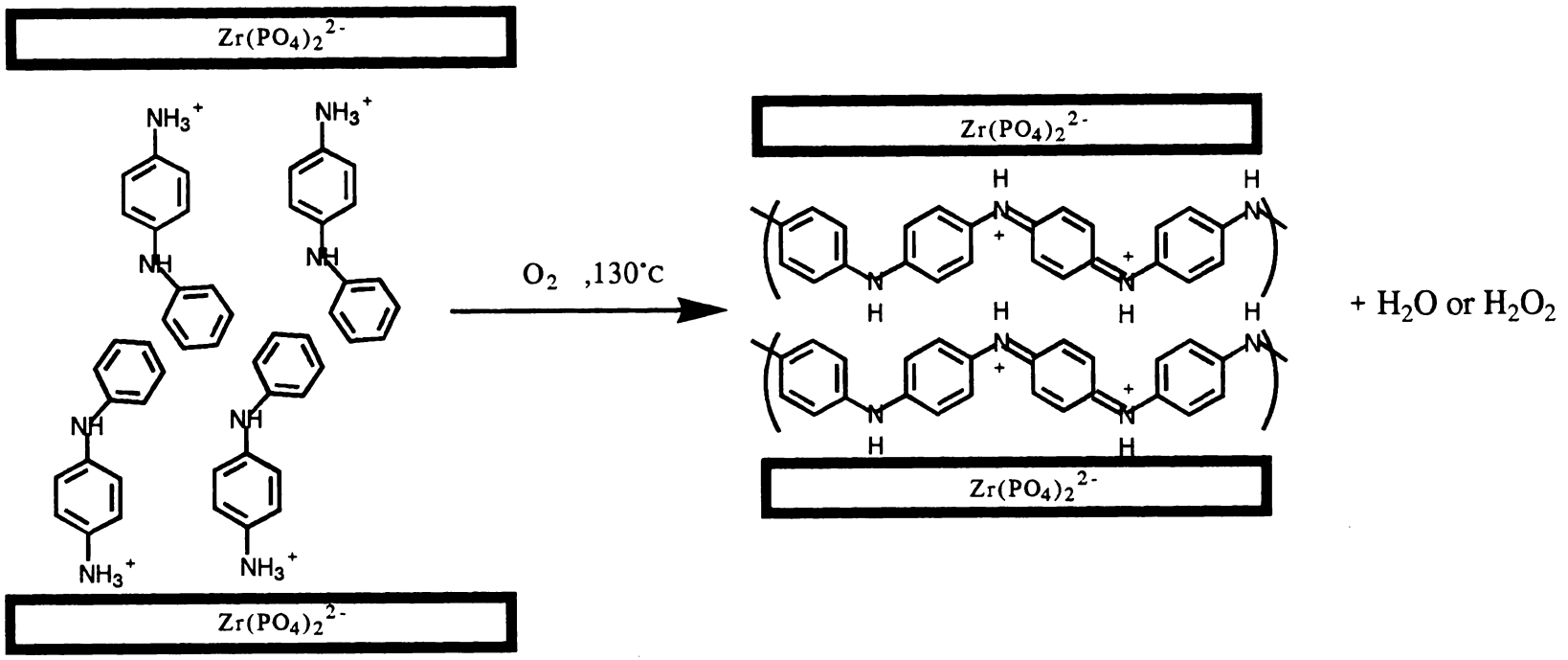

Scheme 6.1 .

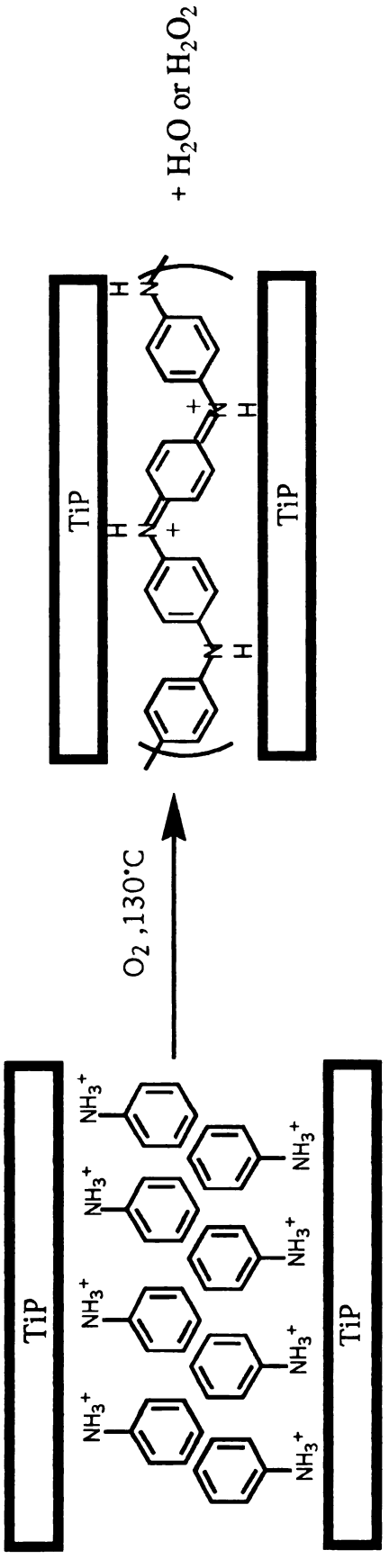

Scheme 6.2.

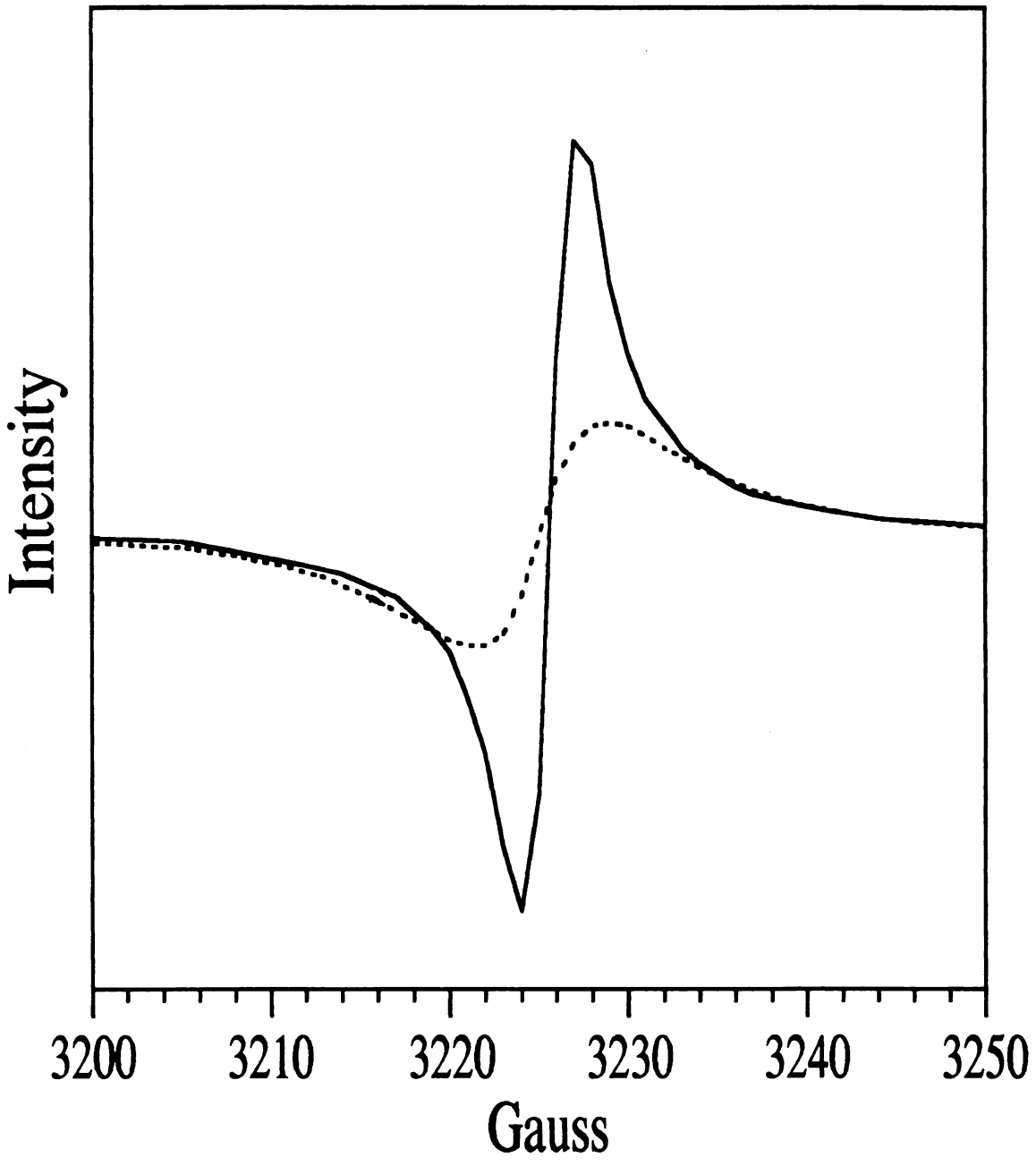

Figure 6.8. Electron paramagnetic resonance spectrum of ATiP after one week (----) and three weeks (—) of thermal treatment.

however, the value can be > 10 G with other dopants[24] and also depends on the relative ambient moisture.

The polymerization process was also monitored with magnetic susceptibility measurements. The evolution of magnetic susceptibility of AUP as a function of reaction time and temperature are shown in Figure 6.9. Before thermal treatment, AUP is diamagnetic. When heated, its magnetic susceptibility begins to increase and shows a temperature-dependent behavior. However, the relationship between magnetic susceptibility (χ_m) and temperature does not follow the Curie-Weiss law. This is probably due to the presence of the Pauli susceptibility which is observed in bulk PANI.[25] Similar data were also obtained for PTiP and PZrP. The Pauli susceptibility and Curie spin density data (calculated from the susceptibility) are summarized in Table 6.3. Except for PUP, the Pauli susceptibility data of PTiP and PZrP are consistent with reported values which increase with protonation and show a range from 0 to $6.0xe^{-5}$ emu/mole. The Curie spin density at PUP and PTiP is approximately one spin per 60 rings and only one spin per 135 rings at PZrP. This is probably because of incomplete polymerization in PZrP where the spin density is diluted by the diamagnetic dimers.

6.3.5. Thermogravimetric Analysis Studies

TGA diagrams of PUP, PTiP and PZrP under O_2 are given in Figure 6.10. PZrP and PTiP show a single-step weight-loss beginning at 400°C. PUP shows a small weight loss below 100°C, attributed to water, and two major weight-loss steps at 400°C and 600°C. The weight-loss step starting at 400°C is attributed to the loss of the intercalated PANI as it thermally breaks up. Compared to bulk PANI in its doped form[26] (<

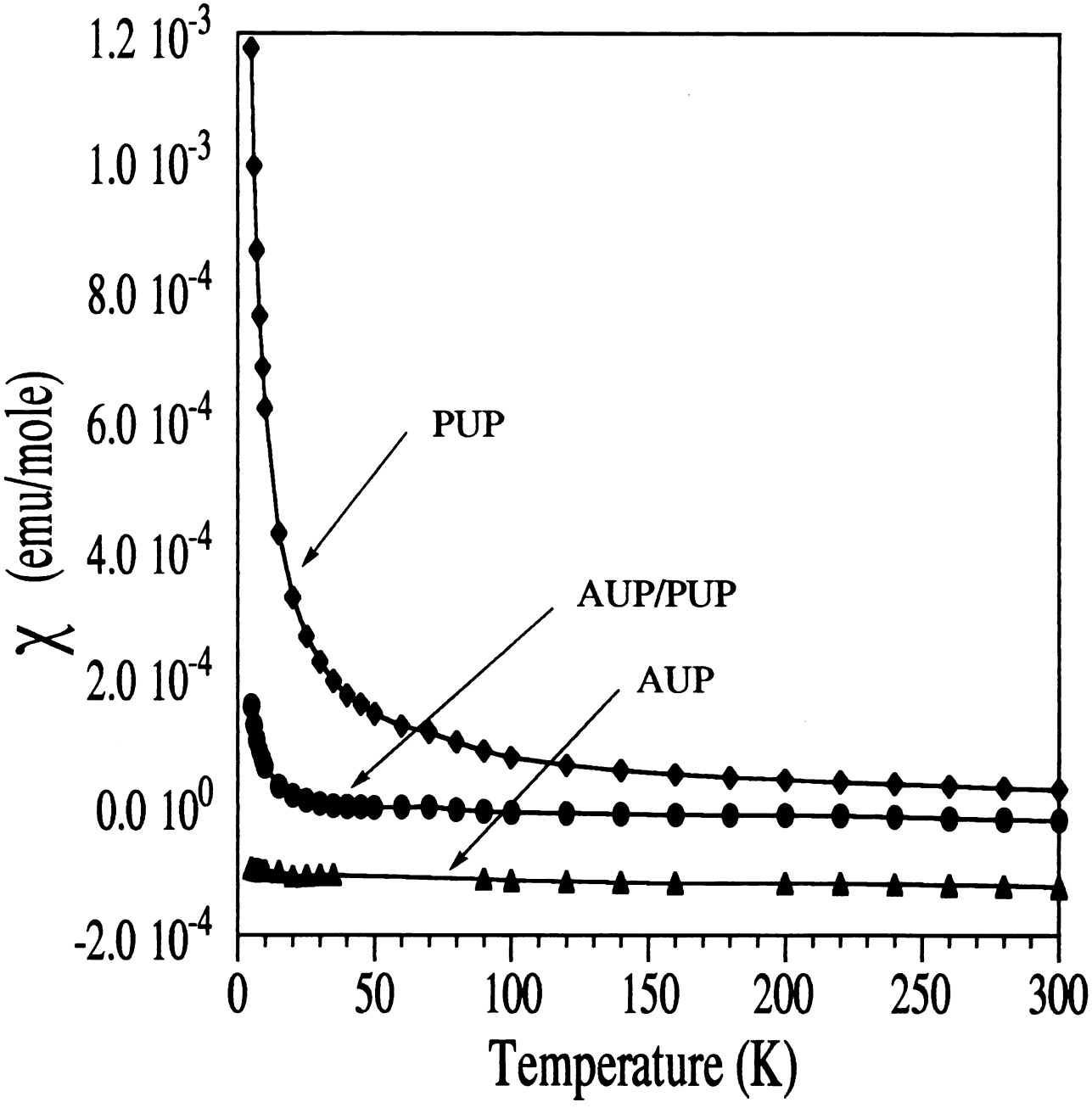

Figure 6.9. Variable temperature magnetic susceptibility data of (a) AUP, (b) AUP/PUP, and (c) PUP.

Table 6.3. Pauli Susceptibility and Curie Spin Density of PANI/Metal Phosphate Intercalates

Compound	Pauli susceptibility (emu/mole)	Curie spin density (ring per spin)
PUP	$1.3e^{-4}$	55
PTiP	$4.4e^{-5}$	66
PZrP	$8.0e^{-5}$	135

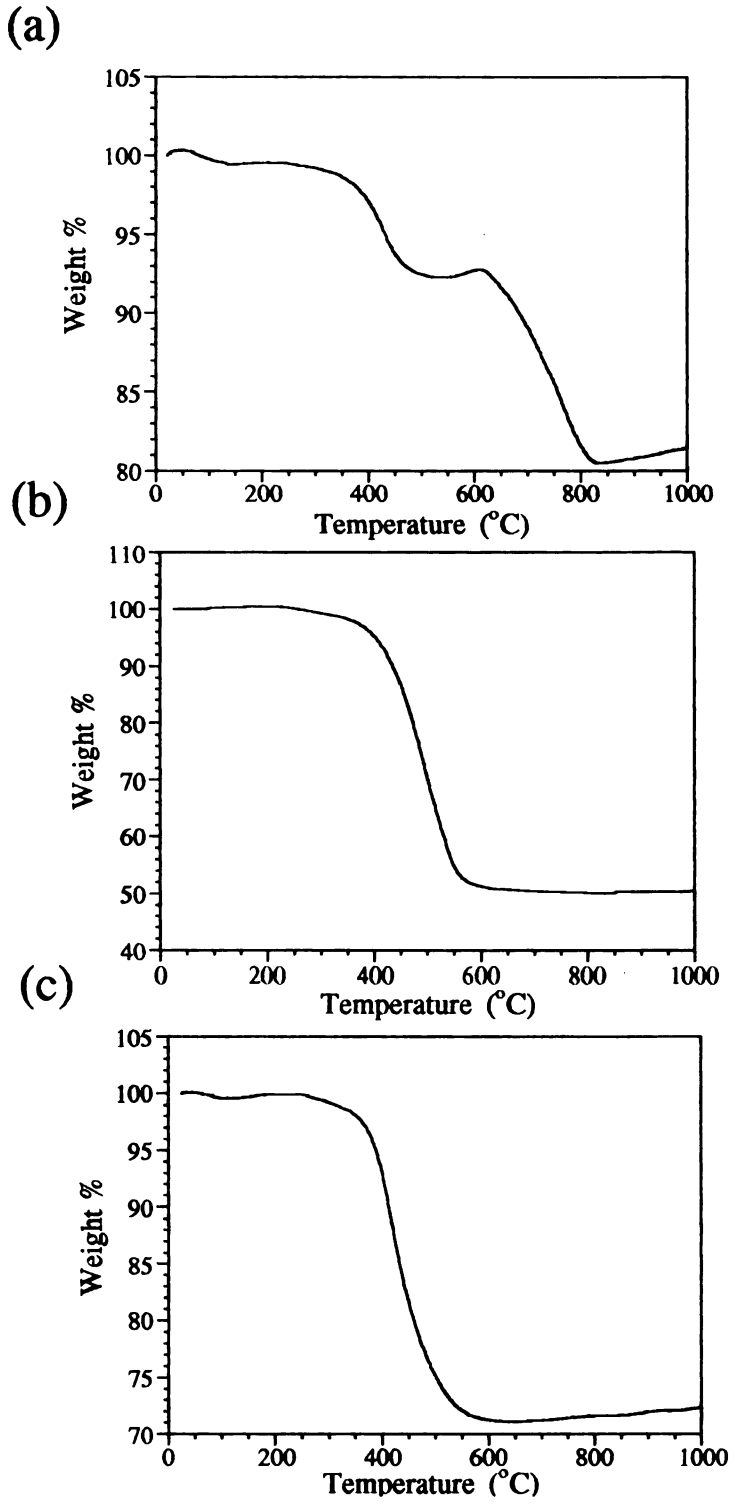

Figure 6.10. Thermogravimetric analysis diagrams under oxygen for (a) PTiP, (b) PZrP, and (c) PUP.

250°C), the intercalated PANI molecules show superior thermal stability, which is due to the spatial confinement and separation of polymer chains by the metal phosphate layers. X-ray diffraction confirms that the final residues at 900°C are $(UO_2)_2(P_2O_7)$, ZrP_2O_7, and TiP_2O_7. Calculated from the diagrams, the composition is $(PANI)_{2.4}Zr(OPO_3)_2$ for PZrP, $(PANI)_{0.8}Ti(OPO_3)_2$ for PTiP, and $(PANI)_{0.94}UO_2PO_4{\cdot}0.5H_2O$ for PUP, consistent with the elemental analyses. Significant amounts of intercalants were lost during polymerization of ATiP and A_2ZrP, but almost none in AUP. This is consistent with the dramatic decrease of the interlayer spacing at PTiP and PZrP.

6.3.6. Scanning Electron Microscopy (SEM)

Figures 6.11 and 6.12 illustrate SEM micrographs of the layered metal phosphates before and after intercalation. Clearly, all metal phosphates show plate-like morphology, consistent with their layered structure. The average particle size of uranyl phosphate is slightly larger than those at zirconium phosphate and titanium phosphate. The particles of the latter are in the sub-micrometer range regime. After intercalation, the plate-like morphology and average particle size are maintained. After oxidative polymerization, the shape and size of the particles, compared with their precursors, were also unchanged, see Figure 6.13. These SEM micrographs confirm the crystalline nature of the inclusion compounds and are consistent with a topotactic polymerization inside the layers.

6.3.7. Gel Permeation Chromatography (GPC) Analysis

The extracted PANI from any of the inorganic hosts was partially soluble in NMP. Therefore, the molecular weight of the soluble portions

Figure 6.11. SEM micrographs of layered metal phosphates before and after intercalation : (a) HUP, (b) α-ZrP and (c) α-TiP.

(a)

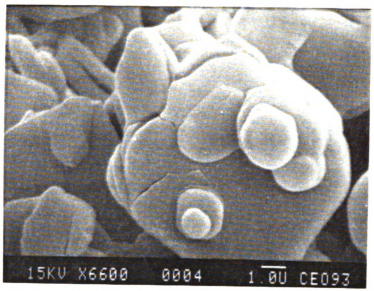
15KV X6600 0004 1.0U CE093

(b)

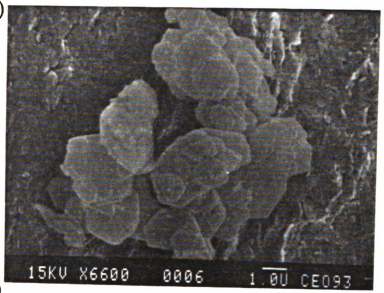
15KV X6600 0006 1.0U CE093

(c)

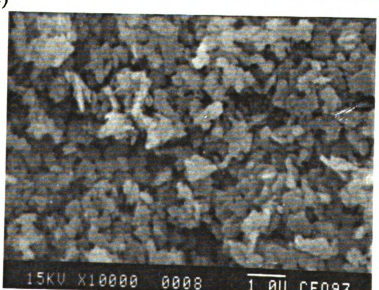
15KV X10000 0008 1.0U CE093

Figure 6.12. SEM micrographs of layered metal phosphates before and after intercalation : (a) AUP, (b) A_2ZrP and (c) ATiP.

(a)

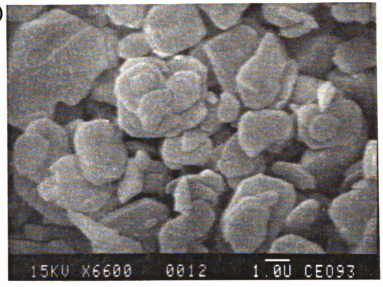
15KV X6600 0012 1.0U CE093

(b)

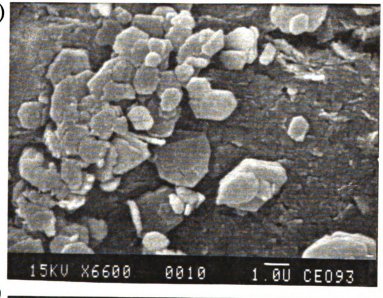
15KV X6600 0010 1.0U CE093

(c)

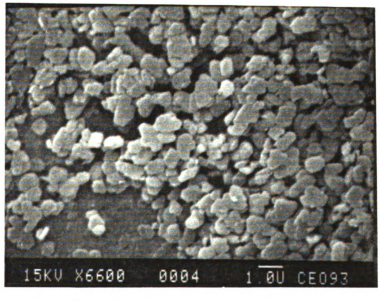
15KV X6600 0004 1.0U CE093

Figure 6.13. SEM micrographs of (a) PUP, and (b) PZrP and (c) PTiP.

(a)

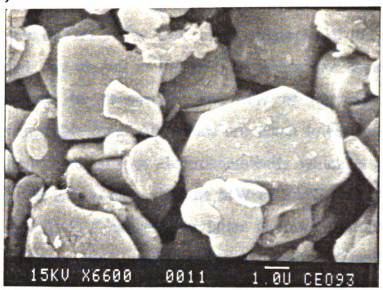
15KV X6600 0011 1.0U CE093

(b)

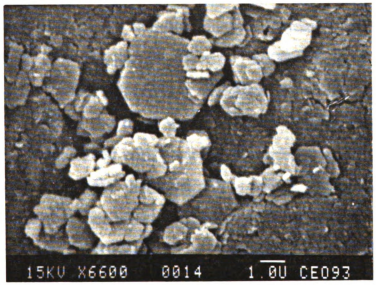
15KV X6600 0014 1.0U CE093

(c)

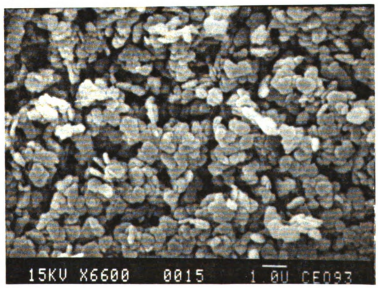
15KV X6600 0015 1.0U CE093

was determined by GPC. The GPC chromatographs of the three extracted PANI materials are shown in Figure 6.14 where one asymmetric elution band is observed in all cases. The MW of the extracted PANI is summarized in Table 6.4. All values are much lower than that of bulk PANI prepared chemically or electrochemically which is in the range of 32,000.[21b,27] It is also clear that the MW of PANI from A_2UP is higher than that from AUP, however, the latter is more uniform. In order to monitor the progress of the polymerization in the intralamellar space of the UO2PO4 we stopped the reaction at regular intervals, extracted the polymer from the host and determined its MW by GPC. Surprisingly, we found that the MW of the soluble fraction decreases with reaction time. For example, PUP shows that the Mw is ~14,000 (Mn = ~4400) in the first week and decreases to ~7400 (Mn = ~4,500) at the second week and only to ~4,500 in the end of the third week. We also observed that the NMP-soluble fraction decreased with prolonged polymerization time. This result suggests that , as the MW increases and a certain amount of cross-linking occurs, the polymer becomes insoluble and that in each case above the soluble fraction is what is left over. The reason the MW of the soluble fraction is smaller in samples that have been heated for a longer time is because it represents kinetically trapped oligomers or short polymer chains in pockets of cross-linked high MW polymer.

6.3.8. Charge Transport Properties

Since the conjugated polymers are embedded in the insulating host and cannot be accessed electrically, all PANI intercalated materials described are insulators. This behavior is similar to that of the systems which involve insulating materials as hosts.[7,8]

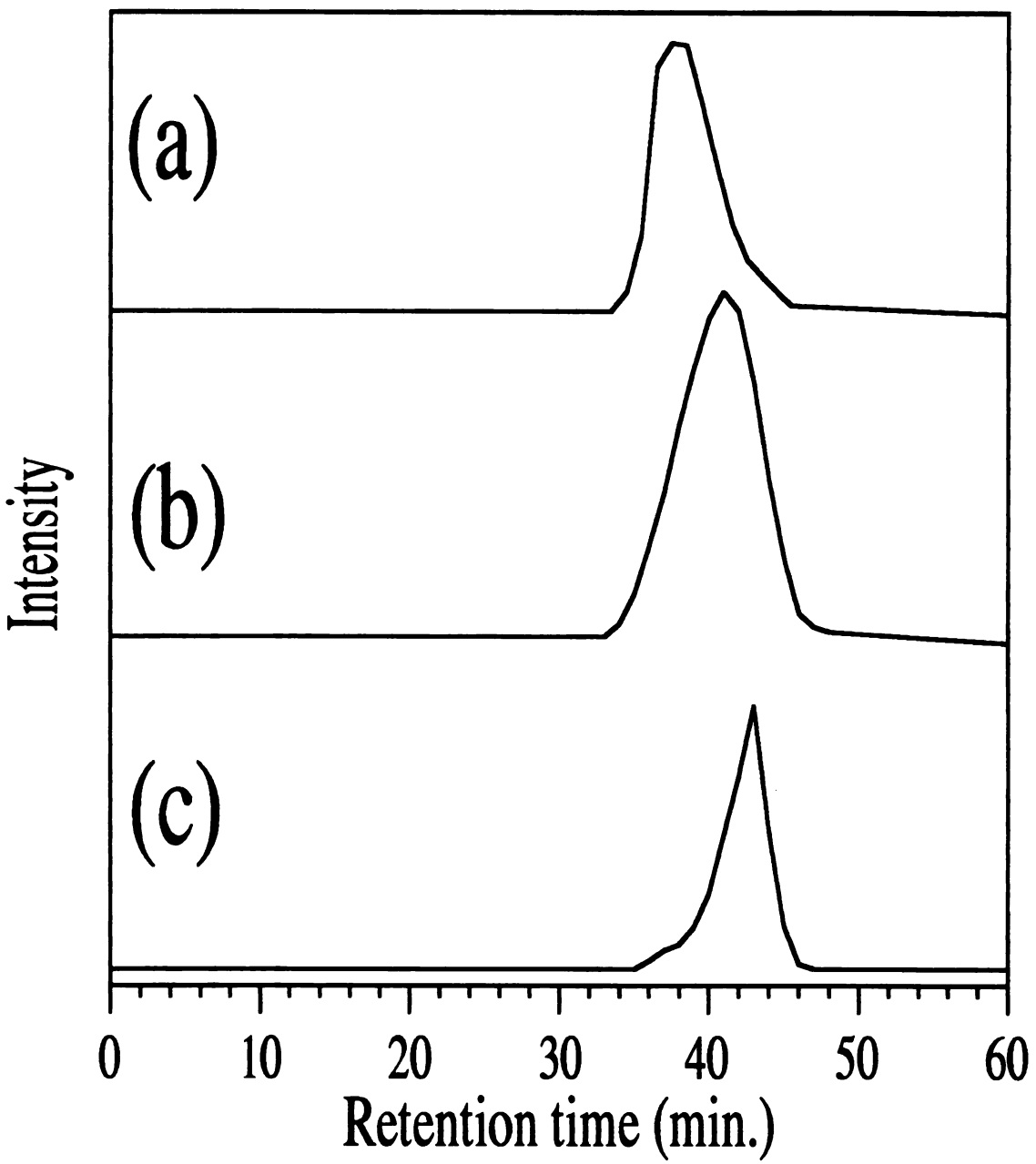

Figure 6.14. GPC chromatographs of extracted PANI from (a) PUP, (b) PTiP and (c) PZrP.

Table 6.4. Molecular Weights of Extracted PANI from Layered Metal Phosphates

	Mn	Mw	Mw/Mn
Bulk PANI[a]	26,000	78,000	3.0
PANI extracted from PUP[b]	4,400	9,200	2.1
PANI extracted from PUP[c]	3,000	4,500	1.5
PANI extracted from PZrP[d]	2,100	2,300	1.1
PANI extracted from PTiP	2,600	3,000	1.2

[a]Adopt from reference 21b. [b]Polymerized from A_2UP. [c]Polymerized from AUP. [d]Polymerized from A_2ZrP.

6.4. Conclusion

We have successfully synthesized polyaniline in layered metal phosphates by thermal treatment in ambient oxygen. The spectroscopic and magnetic data of the extracted PANI are comparable with those of bulk PANI prepared chemically. However, there is evidence of cross-linked between molecules in the intralamellar space. The use of PPDA as a monomer for PANI did not yield shorter reaction times. The results reported here indicate that oxygen may be a convenient and clean reagent for topotactic oxidative polymerization of monomers occluded in inorganic galleries.

LIST OF REFERENCES

LIST OF REFERENCES

(1) (a) Day, P.; Ledsham, R.D. *Mol. Cryst. Liq. Cryst.* **1982**, 86, 163-174. (b) Tieke, B. *Mol. Cryst. Liq. Cryst.* **1983**, 93, 119-145. (c) Pillion, J.E.; Thompson, M.E. *Chem. Mater.* **1991**, 3, 777-779. (d) Enzel, P.; Bein, T. *Chem. Mater.* **1992**, 4, 819-824.

(2) (a) Kanatzidis, M.G.; Tonge, L.M.; Marks, T.J.; Marcy, H.O.; Kannewurf, C.R. *J. Am. Chem. Soc.* **1987**, 109, 3797-3799. (b) Wu, C.-G.; Kanatzidis, M.G.; Marcy, H.O.; DeGroot, D.C.; Kannewurf, C.R. *Polym. Mat. Sci. Eng.* **1989**, 61, 969-973. (c) Kanatzidis, M.G.; Wu, C.-G.; Marcy, H.O.; DeGroot, D.C.; Kannewurf, C.R. *Chem. Mater.* **1990**, 2(3), 222-224. (d) Wu, C.-G.; Marcy, H.O.; DeGroot, D.C.; Schindler, J.L.; Kannewurf, C.R.; Leung, W.-Y.; Benz, M.; LeGoff, E.; Kanatzidis, M.G. *Synth. Met.* **1991**, 41-43, 797-803. (e) Wu, C.-G.; Marcy, H.O.; DeGroot, D.C.; Schindler, J.L.; Kannewurf, C.R.; Kanatzidis, M.G. *Synth. Met.* **1991**, 41-43, 693-698.

(3) Caspar, J.V.; Ramamurthy, V.; Corbin, D.R. *J. Am. Chem. Soc.* **1991**, 113, 600-610

(4) (a) "Handbook of Conducting Polymers"; Skotheim, T.A., Ed.; Marcel Dekker : New York, **1986**; Vol 1 and 2. (b) Huang, W.-S.; Humphrey, B.D.; MacDiarmid, A.G. *J. Chem. Soc. Faraday Trans* **1986**, 82, 2385-2400. (c) Kanatzidis, M.G. *C&EN* **1990**, 68(49),

36-50. (d) Geniès, E.M.; Boyle, A.; Lapkowski, M.; Tsintavis, C. *Synth. Met.* **1990**, 36, 139-182.

(5) Kanatzidis, M.G.; Wu, C.-G. ; Marcy, H.O.; Kannewurf, C.R. *Adv. Mater.* **1990**, 2, 364-366.

(6) Kanatzidis, M.G.; Wu, C.-G.; Marcy, H.O.; Kannewurf, C.R. *J. Am. Chem. Soc.* **1989**, 111, 4139-4141.

(7) Inoue H.; Yoneyama, H. *J. Electroanal. Chem.* **1987**, 233, 291-295.

(8) Enzel P.; Bein, T *J. Phys. Chem.* **1989**, 93, 6270-6272.

(9) Bissessur, R.; DeGroot, D.C.; Schindler, J.L.; Kannewurf, C.R.; Kanatzidis, M.G. *J. Chem. Soc. Chem. Commun.* **1993**, 687-689.

(10) Mehrotra, V.; Giannelis, E.P. *Mater. Res. Soc. Symp. Proc.* **1990**, 171, 39-44.

(11) Bonnet, B.; Meijad, R. EI; Herzog, M.-H.; Jones, D.J.; Roziére, J. *Mater. Sci. Forum*, **1992**, 91-92, 177-182.

(12) Kanatzidis, M.G.; Bissessur, R.; DeGroot, D.C.; Schindler, J.L.; Kannewurf, C.R. *Chem. Mater.* **1993**, 5(5), 595-596.

(13) (a) Clearfield, A. *Comments Inorg. Chem.* **1990**, 10(2&3), 89-128. (b) Clearfield, A. *Chem. Rev.* **1988**, 88, 125-148. (c) Alberti, G.

Acc. Chem. Res. **1978**, 11, 163-170. (d) Cao, G.; Rabenberg, L.K.; Nunn, C.M.; Mallouk, T.E. *Chem. Mater.* **1991**, 3, 149-156. (e) Johnson, J.W.; Jacobson, A.J.; Butler, W.M.; Rosenthal, S.E.; Brody, J.F.; Lewandowski, J.T. *J. Am. Chem. Soc.* **1989**, 111, 381-383.

(14) (a) Olken, M.M.; Biagioni, R.N.; Ellis, A.B. *Inorg. Chem.* **1983**, 22, 4128-4134. (b) Hunsberger, L.R.; Ellis, A.B. *Coord. Chem. Rev.* **1990**, 97, 209-224.

(15) Liu, Y.-J.; Kanatzidis, M.G. *Inorg. Chem.* **1993**, 32(14), 2989-2991.

(16) "*Theory and Applications of Molecular Paramagnetism*" Boudreaux, E.A.; Mulay, L.N., John Wiley &Sons, Inc., **1976.**

(17) Klug, H.P.; Alexander, L.E. "*X-ray Diffraction Procedures for Polycrystalline and amorphous Materials*"; John Wiley & Sons: New York, 1962; 491-538.

(18) Weigel, F.; Hoffmann, G. *J. Inorg. Nucl. Chem.* **1976**, 44, 99-123.

(19) Alberti, G.; Torracca, E. *J. Inorg. Nucl. Chem.* **1968**, 30, 317-318.

(20) Alberti, G.; Cardini-Galli, P.; Costantino, U; Torracca, E. *J. Inorg. Nucl. Chem.* **1967**, 29, 571-578.

(21) (a) Rodrigue, D.; Snauwaert, P.; Demaret, X.; Riga, J.; Verbist, J.J. *Synth. Met.* **1991**, 41-43, 769-773. (b) Scherr, E.M.; MacDiarmid, A.G.; Manohar, S.K.; Masters, J.G.; Sun, Y.; Tang, X.; Druy, M.A.; Glatkowski, P.J.; Cajipe, V.B.; Fischer, J.E.; Cromack, K.R.; Jozefowicz, M.E.; Ginder, J.M.; McCall, R.P.; Epstein, A.J. *Synth. Met.* **1991**, 41-43, 735-738. (c) Epstein, A.J.; MacDiarmid, A.G. in *Lower-Dimensional Systems and Molecular Electronics*, Metzger, R.M.; Day, P.; Papavassiliou, G.C. Ed., Plenum Pess, New York, **1990.**

(22) (a) Ohira, M.; Sakai, T.; Takeuchi, M.; Kobayshi, Y.; Tsuji, M. *Synth. Met.* **1987**, 18, 347. (b) Bloor, D.; Monkman, A. *Synth. Met.* **1987**, 21, 175-179. (c) Epstein, A.J.; MacDiarmid, A.G. *Mol. Cryst. Liq. Cryst.* **1988**, 160, 165-173. (d) Wei, Y.; Focke, W.W.; Wnek, G.E.; Ray, A.; MacDiarmid, A.G. *J. Phys. Chem.* **1989**, 93, 495-499. (e) Ray, A.; MacDiarmid, A.G.; Ginder, J.M.; Epstein. A.J. *Mater. Res. Soc. Symp. Proc.* **1990**, 173, 353-357.

(23) (a) Salaneck, W.R.; Liedberg, B.; Inganas, O.; Erlandsson, R.; Lundstrom, I.; MacDiarmid, A.G.; Halpern, M.; Somasiri, N.L.D. *Mol. Cryst. Liq. Cryst.* **1985**, 121, 191-194. (b) Javadi, H.H.S.; Laversanne, R.; Epstein, A.J.; Kohli, R.K.; Scherr, E.M.; MacDiarmid, A.G. *Synth. Met.* **1989**, 29, E439-E444.

(24) Cao, Y.; Heeger, A.J. *Synth. Met.* **1990**, 39, 205-214.

(25) (a) MacDiarmid, A.G.; Chiang, J.-C.; Richter, A.F.; Epstein, A.J. *Synth. Met.* **1987**, 18, 285-290. (b) Epstein, A.J.; Ginder, J.M.; Zuo, F.; Bigelow, R.W.; Woo, H.-S.; Tanner, D.B.; Richter, A.F.; Huang, W.-S.; MacDiarmid, A.G. *Synth. Met.* **1987**, 18, 303-309. (c) Geniès, E.M.; Boyle, A.; Lapkowski, M.; Tsintavis, C. *Synth. Met.* **1990**, 36, 139-182.

(26) Yue, J.; Epstein, A.J.; Zhong, Z.; Gallagher, P.K.; MacDiarmid, A.G. *Synth. Met.* **1991**, 41-43, 765-768.

(27) (a) Abe, M.; Ohtani, A.; Umemoto, Y.; Akizuki, S.; Ezoe, M.; Higuvhi, H.; Nakamoto, K.; Okuno, A.; Noda, Y. *J. Chem. Soc. Chem. Commun.* **1989**, 1736-1738. (b) Geniès, E.M.; Noël, P. *Synth. Met.* **1992**, 46, 285-292.